DIRECT NUMERICAL SIMULATION OF TURBULENT FLOW OVER A BACKWARD-FACING STEP

By
Hung Le and Parviz Moin

Prepared with support from
the National Science Foundation

Report No. TF-58

Flow Physics and Computational Engineering Group
Department of Mechanical Engineering
Stanford University
Stanford, CA 94305

January 1995

Direct Numerical Simulation of Turbulent Flow Over a Backward-Facing Step

By
Hung Le and Parviz Moin

Prepared with support from
the National Science Foundation

Report No. TF-58

Flow Physics and Computational Engineering Group
Department of Mechanical Engineering
Stanford University
Stanford, CA 94305

January 1995

ABSTRACT

The backward-facing step is frequently employed in the study of turbulent reattachment for its geometrical simplicity. However, in spite of the large amount of experimental work, the physics of the reattachment is not fully understood. A contributing reason is the scarcity of data in the recirculation and reattachment regions. The objective of this study is to conduct a direct numerical simulation of turbulent backward-facing step flow and to provide data in the form of Reynolds stress budgets for Reynolds averaged modeling. Basic statistical data were calculated and compared with experimental data, specifically the concurrent experiment of Jovic & Driver (1994).

Both 2-D and 3-D simulations were performed. In 2-D simulations, three different velocity profiles (parabolic, fully developed turbulent channel, and boundary layer profiles) were applied at the step. The flow is steady at low Reynolds numbers. At high Reynolds number, the flow becomes unsteady and quasi periodic eventhough no fluctuations were imposed at the inlet. The critical Reynolds number, Re_c, beyond which the flow becomes oscillatory varies with the profile shape: a fuller profile (steep velocity gradient at separation) appears to have a lower Re_c. The oscillation can also be resulted from a poor grid resolution. Imposed inlet velocity fluctuations result in periodic solutions. The fundamental frequency of oscillation is the same in all cases with different Reynolds numbers or inlet velocity profiles. The Strouhal number based on the step height and maximum inlet velocity is approximately 0.08. This frequency thus appears to be independent of the input parameters.

The main 3-D simulation was conducted at a Reynolds number of 5100 based on the step height h and inlet free-stream velocity, and an expansion ratio of 1.20. Spanwise-averaged pressure fluctuation contours and reattachment lengths show evidence of an approximate oscillatory behavior of the free shear layer with a Strouhal number of 0.06. The instantaneous velocity fields indicate that the reattachment

location varies in the spanwise direction, and oscillates about a mean of $6.2h$. Statistical results show excellent agreement with experimental data by Jovic & Driver (1994). Of interest are two observations not previously reported for the backward-facing step flow: (a) at the relatively low Reynolds number considered, large negative skin friction is seen in the recirculation region; the peak $|C_f|$ is about 2.5 times the value measured in experiments at high Reynolds numbers; (b) the velocity profiles in the recovery region fall below the universal log-law; the deviation of the velocity profile from the log-law indicates that the turbulent boundary layer is not fully recovered at 20 step heights behind the separation.

The budgets of all Reynolds stress components have been computed. The turbulent kinetic energy budget in the recirculation region is similar to that of a turbulent mixing layer. The turbulent transport term makes a significant contribution to the budget and the peak dissipation is about 60% of the peak production. The velocity pressure-gradient and viscous diffusion are negligible in the shear layer, but both are significant in the near-wall region. This trend is seen throughout the recirculation and reattachment region. In the recovery region, the budgets show that effects of the free shear layer are still present.

A large database from this simulation has been archived. It contains up to third-order statistics, and the budgets of the Reynolds stress tensor.

ACKNOWLEDGMENT

It is with pleasure that the author acknowledges the help and guidance from his advisor Professor Parviz Moin throughout the course of this study.

The author is also grateful to Dr. John Kim for very insightful discussions and technical contributions; and appreciates the cooperation from Drs. Srba Jovic and David M. Driver at NASA-Ames Research Center who performed the concurrent experiment to validate the computational results. Helpful discussions and comments on a draft of this report by Professors John K. Eaton and Peter Bradshaw are gratefully acknowledged.

This study was funded by the National Science Foundation (NSF) and the Center for Turbulence Research (CTR). The computer resources were provided by the NASA-Ames Research Center.

The author wishes to express his deepest gratitude to his parents for their encouragement and support. He owes his inspiration to Professor William C. Reynolds at Stanford University and Dr. Fred J. Moody at GE Nuclear Energy. The continuing support and friendship from his colleagues at GE Nuclear Energy, Stanford University and NASA-Ames Research Center are also greatly appreciated.

TABLE OF CONTENTS

LIST OF TABLES

LIST OF FIGURES

NOMENCLATURE

Roman Symbols

A	Constant in Simpson's (1983) empirical formula for backflow velocity: $U/\|U_N\| = A[y/N - \log(y/N) - 1] - 1$.
$\mathcal{A}_j^{(h)}, \mathcal{B}_j^{(h)}, \mathcal{C}_j^{(h)}$	Coefficients for viscous terms at vertical location j, using central difference (u and w components).
$\mathcal{A}_j^{(\phi)}, \mathcal{B}_j^{(\phi)}, \mathcal{C}_j^{(\phi)}$	Coefficients for Laplace operator at vertical location j, using central difference.
$\mathcal{A}_j^{(v)}, \mathcal{B}_j^{(v)}, \mathcal{C}_j^{(v)}$	Coefficients for viscous terms at vertical location j, using central difference (v component only).
C	Constant in the log law of the wall: $u^+ = \frac{1}{\kappa} y^+ + C$.
$\mathbf{C}$	Capacitance matrix (2-D).
$\mathbf{C}_m$	Capacitance matrix for m^{th} wave number (3-D).
C_f	Coefficient of friction, normalized by the inlet free-stream velocity U_0.
C_{f,U_N}	Coefficient of friction in the recirculation region, normalized by the local maximum mean backflow velocity U_N.
C_{ij}	Convection term in the budget for component ij of the Reynolds stress tensor.
C_k	Convection term in the budget of the turbulent kinetic energy.
C_p	Pressure coefficient, normalized by the inlet free-stream velocity U_0.
$C_{p,BC}$	Borda-Carnot pressure coefficient, $C_{p,BC} = \frac{2}{ER}(1 - \frac{1}{ER})$.
$C_{p,\min}$	Minimum pressure coefficient (recirculation region).
C_p^*	Normalized pressure coefficient: $C_p^* = \frac{C_p - C_{p,\min}}{C_{p,BC} - C_{p,\min}}$.
$\tilde{C}_p$	Normalized pressure coefficient: $\tilde{C}_p = \frac{C_p - C_{p,\min}}{1 - C_{p,\min}}$.

D_{ij}	Viscous diffusion term in the budget for component ij of the Reynolds stress tensor.
D_k	Viscous diffusion term in the budget of the turbulent kinetic energy.
e_i	Residue of a long-time average of the i^{th} mean momentum equation: $e_i = \|\partial U_i/\partial t\|$.
e_{ij}	Residue of a long-time average of the transport equation for the Reynolds stress component ij: $e_{ij} = \|\partial \overline{u_i' u_j'}/\partial t\|$.
E_{uu}, E_{vv}, E_{ww}	One-dimensional energy spectra for the streamwise, vertical and spanwise velocity components, respectively.
E_{ii}	General notation for one-dimensional energy spectra: $E_{11} \equiv E_{uu}$, $E_{22} \equiv E_{vv}$, $E_{33} \equiv E_{ww}$.
ER	Expansion ratio, $ER = L_y/(L_y - h)$.
f	Frequency of oscillation.
G	Clauser shape factor.
$G_{\ell,n}$	Discrete Green's function at boundary node n due to a unit source at ℓ.
h	Step height.
h_c	Channel height.
H	Shape factor, $H = \delta^*/\theta$.
$\mathbf{i}$	Imaginary number: $\mathbf{i} \equiv \sqrt{-1}$.
$\Im$	Imaginary part of a complex expression.
k_y, k_z	Wave numbers associated with y and z directions, respectively (generation of inflow turbulent fluctuations).
k_l', k_m'	Modified wave numbers in x and z directions, respectively (FFT method in solving the Poisson equation).
L_c	Domain length behind the step.
L_i	Length of the development section before the step.

L_x, L_y, L_z	Total dimension of the computational domain in the streamwise, vertical and spanwise directions, respectively.
$L(u_i)$	Linear (viscous) operator in the Navier-Stokes equations; applied to the i^{th} velocity component.
$\mathcal{L}(\phi)$	Laplace operator on ϕ.
$\dot{m}$	Total mass flow rate.
$\dot{M}$	Time averaged mass flow rate.
$\dot{m}'$	Fluctuating mass flow rate.
$\dot{m}_e$	Mass flow rate computed at the exit plane.
$\mathbf{n}$	Notation for spatial direction normal to the domain boundaries.
N	Location of peak mean reverse flow velocity, measured from the bottom wall.
N_c	Total number of velocity points adjacent to the step corner boundary.
N_x, N_y, N_z	Number of cells in the x, y and z directions, respectively.
$N(u_i)$	Non-linear (convective) operator in the Navier-Stokes equations; applied to the i^{th} velocity component.
p	Instantaneous pressure.
P	Mean pressure.
p'	Fluctuating pressure.
$p^\dagger$	Non-dimensionalized pressure, $p^\dagger = p/(\rho U_0^2)$.
P_{ij}	Production term in the budget for component ij of the Reynolds stress tensor.
P_k	Production term in the budget of the turbulent kinetic energy.
P^+	Pressure gradient parameter: $P^+ = \dfrac{1}{Re_h u_\tau^3}\dfrac{\partial P}{\partial x}$.
P_0	Reference pressure.

$Q_{i,j,k}$	Right-hand side of the Poisson equation evaluated at cell i,j,k (divergence of the intermediate velocity field at the 3^{rd} substep).
$\hat{Q}_{l,j,m}$	Fourier coefficient of $Q_{i,j,k}$ at vertical location j, after Fourier transform in the z direction and Cosine transform in the x direction.
r_j	Scaling factor at vertical location j for the inlet turbulent fluctuations.
$\Re$	Real part of a complex expression.
Re_{δ^*}	Displacement-thickness Reynolds number, $Re_{\delta^*} = U_0\delta^*/\nu$.
Re_c	Critical step-height Reynolds number, U_0h/ν, above which the 2-D backward-facing step flow becomes unsteady.
Re_h	Step-height Reynolds number, $Re_h = U_0h/\nu$.
Re_{h_c}	Channel-height Reynolds number, $Re_{h_c} = U_0h_c/\nu$.
Re_θ	Momentum-thickness Reynolds number, $Re_\theta = U_0\theta/\nu$.
R_{uu}, R_{vv}, R_{ww}	Two-point correlations for the streamwise, vertical and spanwise velocity components, respectively.
R_{ii}	General notation for two-point correlations: $R_{11} \equiv R_{uu}$, $R_{22} \equiv R_{vv}$, $R_{33} \equiv R_{ww}$.
St	Strouhal number, $St = \frac{fh}{U_0}$.
St_f	Strouhal number based on the inlet segment period (FFT method to generate turbulent inflow), $St_f = \frac{h}{U_0T_f}$.
t	Time.
$t^\dagger$	Non-dimensionalized time, $t^\dagger = tU_0/h$.
t_f	Time scale for the generation of inlet turbulence.
t_s	Time at start of statistics cummulation.
T	Period of oscillation.
T_f	Segment period for inflow turbulence generation.

T_{ij}	Turbulence transport term in the budget for component ij of the Reynolds stress tensor.
T_k	Turbulence transport term in the budget of the turbulent kinetic energy.
T_r	Selected time interval during which a phase angle φ of the Fourier coefficient is changing at most once (FFT method to generate inflow turbulence).
u, v, w	Streamwise, vertical, and spanwise velocity components, respectively.
u_i	General notation for velocity components; $u_1 \equiv u$, $u_2 \equiv v$, and $u_3 \equiv w$.
u_i'	Fluctuating velocities.
$\tilde{u}_i^{(l)}$	Intermediate velocities at substep l (not divergence-free).
$u_i^{*(l)}$	Approximation of the divergence-free velocities at substep l.
$\hat{u}_i$	Fourier coefficient of u_i' (FFT method to generate inflow turbulence).
$\hat{u}_i^*$	Complex conjugate of $\hat{u}_i$.
u_i^n	Velocity at time step n.
$u_i^\dagger$	Non-dimensionalized velocities, $u_i^\dagger = u_i/U_0$.
u_i^+	Velocities in wall coordinates, $u_i^+ = u_i/u_\tau$.
u_τ	Wall shear velocity.
$u_{\tau 0}$	Wall shear velocity at the inlet.
U_c	Convection velocity.
U_e	Boundary layer mean edge velocity.
U_i	Mean velocities.
U_N	Peak mean backflow velocity.
U_0	Maximum or free-stream mean inlet velocity (reference velocity).

U', V'	Fluctuating velocities in principal coordinates (FFT method to generate inflow turbulence).
x, y, z	Spatial coordinates in the streamwise, vertical and spanwise directions, respectively (x measured from the step, y measured from the bottom wall).
x_i	General notation for spatial coordinates; $x_1 \equiv x$, $x_2 \equiv y$, and $x_3 \equiv z$.
$x_i^\dagger$	Non-dimensionalized spatial coordinates, $x_i^\dagger = x_i/h$.
x_i^+	Wall coordinates, $x_i^+ = x_i u_\tau/\nu$.
x^*	Streamwise distance normalized by the reattachment length, $x^* = (x - X_r)/X_r$.
X_r	Reattachment length.
X, Y	Principal coordinates in which the Reynolds shear stress component is zero (FFT method to generate turbulent inflow).
$\tilde{y}$	Uniform distribution of the vertical grid spacing, mapped onto a non-uniform grid distribution y by a hyperbolic tangent function.

Greek Symbols

α_l, β_l, γ_l, ζ_l	Constants for Runge-Kutta substep l.
γ	Parameter determining the steepness of the transform function $y = f(\tilde{y})$ (degree of grid compression near location of interest).
Γ_h, Γ_v	Horizontal and vertical boundaries adjacent to the step corner.
δ, δ_{99}	Boundary layer thickness.
δ^*	Displacement thickness.
δ_3	Velocity defect thickness: $\delta_3 = -\int_0^\infty \frac{U - U_e}{u_\tau} dy$.
Δt	Time step for the advancement of the Navier-Stokes equations (varied according to the CFL limit).

Δt_f	Time step used in the generation of inlet turbulence (constant).
Δt_s	Time interval between statistical samples.
ΔT_{ave}	Averaging time of turbulence statistics.
Δx, Δy, Δz	Grid spacing in x, y, and z directions, respectively.
ϵ_{ij}	Viscous dissipation term in the budget for component ij of the Reynolds stress tensor.
ϵ_k	Viscous dissipation term in the budget of the turbulent kinetic energy.
κ	von Kármán's constant.
$\lvert\Lambda\rvert_{\max}$	Maximum CFL number.
ν	Dynamic viscosity.
ω_z	Instantaneous spanwise vorticity.
$\overline{\omega_z}$	Mean spanwise vorticity.
ω_z'	Fluctuating spanwise vorticity.
ψ	Stream function.
Π_{ij}	Velocity pressure gradient term in the budget for component ij of the Reynolds stress tensor.
Π_k	Velocity pressure gradient term in the budget of the turbulent kinetic energy.
ω	Frequency number associated with the inflow turbulent fluctuations.
φ	Random phase angle associated with the Fourier coefficients of the inlet turbulent fluctuations.
ϕ	First-order approximation of the pressure (solution of the Poisson equation).
$\hat{\phi}$	Fourier coefficients of ϕ.
$\hat{\phi}^*$	Complex conjugate of $\hat{\phi}$.
ρ	Dynamic viscosity.

ρ_ℓ	Source term placed at location ℓ on the step corner (capacitance matrix method)
θ	Momentum thickness.
θ_p	Angle of rotation between the flow coordinates $[x, y]$ and the principal coordinates $[X, Y]$.
τ	Total shear stress.
τ_w	Wall total shear stress.

Abbreviations

APG	Adverse pressure gradient.
CFL	Courant-Friedrichs-Lewy number.
FFT	Fast Fourier Transform.
LES	Large-eddy simulation.
pdf	Probability density function.
rms	Root-mean-square.

Subscript/Superscript

$()^n$	Variable evaluated at time step n.
$()_i$	Variable associated with velocity component i ($i = 1, 2, 3$).
$()_{ij}$	Variable associated with Reynolds stress component ij ($i = 1, 2, 3$, $j = 1, 2, 3$).
$()_{i,j,k}$	Variable evaluated at node $[i, j, k]$.

Chapter 1
INTRODUCTION

1.1. Motivation

The separation and reattachment of turbulent flows occur in many practical engineering applications, both in internal flow systems such as diffusers, combustors and channels with sudden expansions, and in external flows like flows around airfoils and buildings. In these situations, the flow experiences an adverse pressure gradient, i.e., the pressure increases in the direction of the flow, which causes the boundary layer to separate from the solid surface. The flow subsequently reattaches downstream forming a recirculation bubble.

In some applications such as combustors, the presence of the recirculation and turbulence due to separation can help enhance the mixing of fuel and air. On the other hand, separation in pipe and duct flows causes loss of available energy. Thus, understanding the flow separation and reattachment phenomena is important in engineering design. Among the flow geometries used for the studies of separated flows, the most frequently selected is the backward-facing step. Considerable work has been carried out on the flow over a backward-facing step due to its geometrical simplicity. The separation point is fixed at the step; thus one can avoid the difficulty resulting from the oscillation of the separation point. Furthermore, unlike flow over an obstacle, the backward-facing step produces only one separation bubble; and the streamlines approaching the step are nearly parallel to the wall. Finally, from the computational view point, the rectangular domain of the backward-facing step allows for simple grid structuring.

In spite of the large amount of experimental work on the backward-facing step flows, the physics of the reattachment is still not fully understood. The reason, as pointed out by Eaton & Johnston (1981), lies partially on the inadequacy of cross-wire hot-wire probes in highly turbulent flows used in early studies. Even

with the advent of the laser anemometer and the pulsed-wire anemometer, velocity measurements, particularly in the separated flow region where instantaneous flow reversal occurs, may still be subject to errors caused by velocity bias (Adams & Eaton, 1988).

In general, predictions of separated flows using the Reynolds average equations have not been particularly successful. A comprehensive data base on the budgets of the Reynolds stress tensor is of considerable value for improvement of turbulence models. Generation of such a database is the main motivation for the present work.

Most applications of direct simulations of fully developed turbulent flows have been limited to flows with periodic boundary conditions in the streamwise direction such as channel flow. A new methodology is necessary to incorporate the time-dependent inflow and outflow conditions to simulation techniques. This is a secondary motivation for the current research.

1.2. Survey of Previous Work

Since Bradshaw & Wong (1972) reviewed the experimental data for reattaching flows, there have been many new studies in this area. Eaton & Johnston in 1981 provided an extensive review of available data for turbulent flows over backward-facing steps up to 1980. The following discussion will not repeat their summary, but highlights the findings from some of these studies that are the focus of the present research.

An early study of Abbott & Kline (1961) measured the velocity profiles of both single and double-sided expansion flows for the Reynolds number range of approximately $2 \times 10^4 \leq Re \leq 5 \times 10^4$ based on the inlet channel height. By varying the step height, they established that the reattachment length increased with the expansion ratio. Turbulence intensities were also measured using hot-film anemometers.

The reattachment length variation at low step-height Reynolds numbers ($100 \leq Re_h \leq 480$) was also studied by Goldstein *et al.* (1970). They concluded that, in this

Reynolds number range, the reattachment length increased linearly with Reynolds number.

Bradshaw & Wong (1972) studied the redeveloping boundary layer behind the reattachment and found that the velocity profile did not follow the log-law and still was not fully recovered even at 52 step heights downstream of the separation. The velocity profiles showed a dip below the low-law of the wall. They concluded that the law of the wall and law of the wake were inapplicable behind the turbulent reattachment.

The study by Kim *et al.* (1978, 1980) was an extensive investigation of static pressure distribution, mean velocities, turbulence intensities, Reynolds stresses, and intermittency in the backward-facing step flow. Using a "zonal method," they also developed a computational model for predicting the reattachment point, shape factor, etc.

Eaton & Johnston (1980) used thermal tufts to measure the reattachment length and the pulsed-wall probe for velocity measurement. They provided the first measurements of skin friction in the reattachment region and found that the peak negative skin friction in the recirculation region was large ($C_f \approx -1 \times 10^{-3}$). Low-frequency motions of the shear layer were detected in their study for all Reynolds numbers, but the parameters controlling these motions were not determined. They also observed that the shear layer near the step behaved very much like a plane-mixing layer.

Since the summary by Eaton & Johnston (1981), more experiments using advanced measurement techniques have been performed. In addition, a number of numerical simulations have been conducted. The discussion below summarizes recent findings.

In 1980, Kuehn studied the effect of expansion ratio (ER) on the reattachment length (X_r) of the backward-facing step flow and suggested that X_r increased linearly with expansion ratio. Ra & Chang (1990) varied the streamwise pressure gradient by deflecting the upper wall and showed that an increase in the streamwise

pressure gradient or ER leads to a longer reattachment length. Durst & Tropea (1981) showed that, although X_r increased with ER, the dependency was not linear. The steepest change occurred when $1.0 < ER < 1.3$. They also found a strong Reynolds number dependence for Reynolds number up to 6000 which was also confirmed by Sinha *et al.* (1981).

Armaly *et al.* (1983) studied in details the effect of Reynolds number on the reattachment length. Using a fixed expansion ratio of 2.0, the experiments covered a Reynolds number range of $70 < Re < 8000$. They found that the reattachment length increased monotonically with Reynolds number up to $Re \approx 1200$; then decreased in the transitional range $1200 < Re < 6600$; and remained relatively constant when the flow becomes fully turbulent at $Re > 6600$ which agreed well with findings by Durst & Tropea (1981) and Sinha *et al.* (1981). Their study also included two-dimensional numerical simulations which predicted the reattachment length. However, the simulations underpredicted the reattachment length for $Re > 400$. The discrepancy was attributed to the three-dimensionality observed at $Re > 400$.

In a recent experiment, Ötügen (1990) investigated the effects of expansion ratio on reattachment length and turbulence intensities. The reattachment length was found to decrease with an increase in expansion ratio which contradicted previous findings. The Reynolds number in this study was, however, kept constant based on the inlet channel height, not on the step height. Thus, Re_h varied as well as the expansion ratio.

Durst & Schmitt (1985) used laser Doppler anemometry to measure the mean velocities and turbulence intensities of a high Reynolds number flow over a two-dimensional backward-facing step. The Reynolds number range was $2 \times 10^5 < Re_h < 5 \times 10^5$. They found no significant differences in mean velocity and turbulence intensities in this range.

Adams *et al.* (1984) studied the effects of expansion ratio ER and the upstream boundary layer δ/h. They found that the initial boundary layer state (laminar or

turbulent) as well as its thickness influenced the reattachment length. The reattachment lengths for the cases with an upstream turbulent boundary layer profile were 30% larger than those associated with an upstream laminar boundary layer profile (Adams & Johnston, 1988). The mean friction coefficient C_f was also sensitive to the δ/h (Adams & Johnston, 1985). They also investigated the near-wall flow structure beneath the separation bubble. They concluded that the reverse flow mean velocity profile is similar to a laminar boundary layer but with high level of imposed unsteady fluctuations.

Experiments of Westphal *et al.* (1984) were similar to those of Adams *et al.* (1984), but in addition to the normal backward-facing step configuration, effects of upstream vortex generator and downstream duct angle were also studied. The mean and fluctuating velocity components, and skin friction were measured with a new pulsed-wall probe (Westphal *et al.*, 1981). Similar to measurements by Eaton & Johnston (1980) and Adams *et al.* (1984), the recirculation region showed a high level of negative skin friction.

Vogel & Eaton (1985) included heat transfer in their backward-facing step flow. They provided temperature and velocity profiles and observed that while the boundary layer profile remained disturbed for a long distance downstream of the step, the Stanton number returned quickly to a flat-plate profile.

Driver & Seegmiller (1982, 1985) studied the effect of streamwise adverse pressure gradient on the reattaching shear layer by deflecting the wall opposite the step. Their experiment was the first to use the oil-flow laser interferometer to measure skin friction. They also measured the turbulent triple products. They compared their results with the prediction of two k-ϵ models. The k-ϵ models were shown to overpredict the dissipation in the shear layer. From the same measurements, Driver *et al.* (1983, 1987) investigated the unsteadiness of the reattaching turbulent shear layer. Two types of fluctuations were identified: a random flapping motion of the shear layer, and a periodic vortical motion.

The backward-facing step experiments of Isomoto & Honami (1989) concentrated on the effect of the inlet turbulence intensity on the reattachment process. They found that the reattachment length decreased with an increase in the maximum turbulence intensity near the wall at separation. Furthermore, the turbulence in the region immediately downstream of the step was important in determining the reattachment length.

Recently, Kasagi *et al.* (1992) used a three-dimensional particle tracking velocimeter to measure instantaneous velocity components in the flow over a backward-facing step. The step-height Reynolds number and expansion ratio were 5540 and 1.50, respectively. They established a database of the turbulence statistics which covered a region $-2 < x/h < 12$. Their measurements indicate that, near the reattachment point, the spanwise component of turbulence intensity is the largest of the three normal stresses. This conclusion is not supported by the present computations.

Numerical simulations of the backward-facing step flow have been largely confined to two-dimensional calculations. Armaly *et al.* (1983) and Durst & Pereira (1988) both used the conservative finite volume approach to discretize the Navier-Stokes equations. Their calculated results were compared with experimental results. Their 2-D computations showed that the reattachment lengths were underpredicted for Reynolds numbers larger than 650.

Kaiktsis *et al.* (1991) applied a spectral-element method to both two and three-dimensional simulations of flow over a backward-facing step. Their 2-D study showed that the flow sustained unsteadiness at relatively low Reynolds number; the oscillatory response occurred at $Re \geq 500$ (Reynolds number based on upstream channel height and mean inlet velocity). However, there was no grid refinement study to assure that the oscillations were not due to numerical resolution effects. In their 3-D simulations, an initial perturbation was imposed in the streamwise direction and the flow response was subsequently measured in time. They found sustained unsteady response at $Re \geq 700$.

Friedrich & Arnal (1990) performed a large eddy simulation (LES) of a single-sided backward-facing step flow at $Re_h = 1.65 \times 10^5$ and $ER = 2.0$. An LES of a fully developed channel flow was first performed; and the velocities in a selected vertical plane was used as inflow conditions for the backward-facing step flow. Their results were compared with the experimental data of Durst & Schmitt (1985). Good overall agreement was obtained for statistical quantities but the calculated reattachment length was underpredicted. They also observed a low-frequency temporal oscillation of the shear layer next to the step (Arnal & Friedrich, 1993).

1.3. Objectives

The present research project was conducted with two main objectives:

1. To develop a methodology for direct numerical simulation of turbulent flows which allows for "turbulent" inflow and outflow conditions. The method will be applicable to flow in complex geometries.
2. To generate a well documented database for the backward-facing step flow which can be used for turbulence modeling. The database contains up to third-order statistics at all locations in the flow field, and contains a comprehensive verification of the simulation results by comparison with the experimental data.

Chapter 2
NUMERICAL METHOD

The time-dependent Navier-Stokes equations for an incompressible fluid were solved on a staggered grid. This chapter describes the numerical method used in the two-dimensional (2-D) and three-dimensional (3-D) simulations of the backward-facing step flow. Sections 2.1 and 2.2 describe the non-dimensional governing equations and the flow configuration. The spatial-discretization and time-advancement schemes are presented in Sections 2.3 and 2.4, respectively. The initial conditions are discussed in Section 2.5, and boundary conditions in Section 2.6. Section 2.7 describes the method for solving the Poisson equation on a non-rectangular flow domain.

2.1. Governing Equations

The Navier-Stokes and continuity equations for incompressible viscous flows are:

$$\frac{\partial}{\partial t}u_i = -\frac{\partial}{\partial x_k}u_i u_k + \nu\frac{\partial^2}{\partial x_k \partial x_k}u_i - \frac{1}{\rho}\frac{\partial}{\partial x_i}p, \tag{2.1}$$

$$\frac{\partial}{\partial x_k}u_k = 0, \tag{2.2}$$

where u_i's are the velocity components, p the pressure, ν the kinematic viscosity, and ρ the density. The subscripts i, j, k take on values of 1,2,3 to denote the streamwise (x), vertical (y) and spanwise (z) directions, respectively. All variables are non-dimensionalized by the maximum mean inlet free stream velocity U_0 and the step height h as follows:

$$t^\dagger = \frac{tU_0}{h}, \qquad u_i^\dagger = \frac{u_i}{U_0}, \qquad x_i^\dagger = \frac{x_i}{h}, \qquad p^\dagger = \frac{p}{\rho U_0^2}. \tag{2.3}$$

The Reynolds number, Re_h, is the step-height Reynolds number, $Re_h = U_0 h/\nu$. Unless otherwise indicated, the superscript † will be dropped from subsequent analyses for simplicity.

2.2. Flow Configuration

A single-sided-expansion duct is used for all simulations. A schematic view of a 3-D flow domain is shown in Fig. 2.1. The computational domain for 3-D simulations

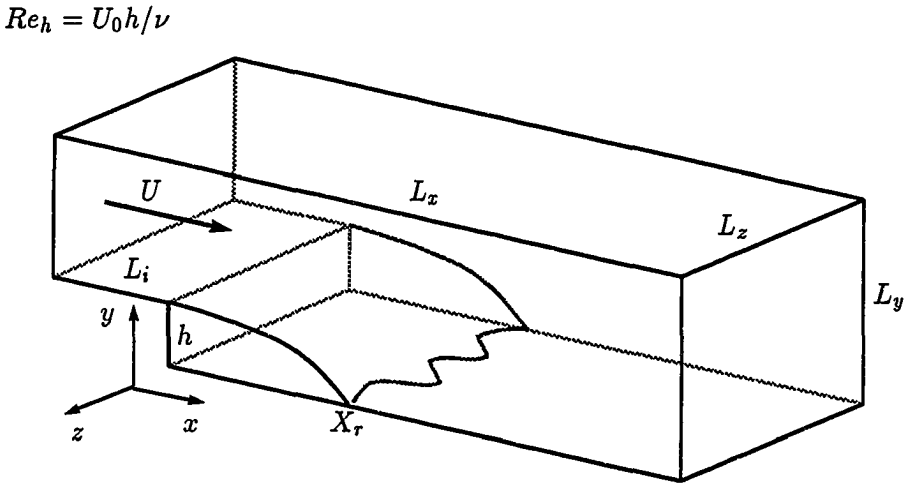

Figure 2.1. Backward-facing step flow configuration.

consists of a streamwise length L_x, including an inlet section L_i prior to the sudden expansion, vertical height L_y and spanwise width L_z, all of which are normalized to the step height h. The coordinate system is placed at the lower step corner as shown in Fig. 2.1. The *mean* inflow velocity profile, $U(y)$, imposed at the left boundary $x = -L_i$, is either a parabolic profile, a fully-developed turbulent channel profile (Kim *et al.*, 1987), or a flat-plate turbulent boundary layer profile (Spalart, 1988), with U_0 being the maximum mean inlet velocity. In the cases of parabolic and turbulent channel flow profiles, the top boundary is a solid wall (no-slip). However, if a boundary layer is used as the inlet profile, a no-stress wall (§2.6) is placed at $y = L_y$. A convective condition is applied at the domain exit, $x = L_x - L_i$ (§2.6.2). Two important parameters used for comparison with other studies are the step-height Reynolds number, Re_h, and the expansion ratio, $ER = L_y/(L_y - h)$.

2.3. Spatial Discretization

All spatial derivatives are approximated with second-order central differences. The grid selection and spatial discretization of Navier-Stokes equations are described below.

2.3.1. Computational Grid

A staggered grid (Harlow & Welch, 1965) is employed in the computations. The computational cell $[i, j]$ for a 2-D domain is illustrated in Fig. 2.2 where the pressure is defined at the center of the cell and the velocity components on the cell surfaces.

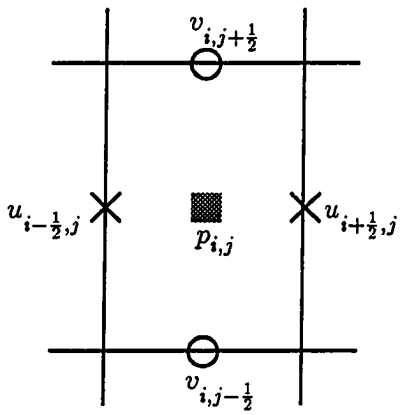

Figure 2.2. Two-dimensional rectangular cell on a staggered grid. × u locations; o v locations; □ p location.

Kim & Moin (1985) successfully applied the staggered grid in their 2-D simulations of flows over a backward-facing step. A 3-D cell is shown in Fig. 2.3. Here the indices i, j, k denote the nodal location of the cell center in the discretized domain; $i = 1, \ldots, N_x$, $j = 1, \ldots, N_y$, $k = 1, \ldots, N_z$, where N_x, N_y and N_z are the number of cells in the x-, y- and z-directions, respectively.

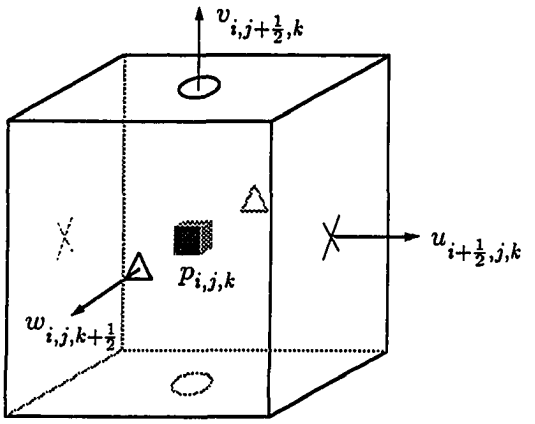

Figure 2.3. Three-dimensional cell on a staggered grid. × u locations; ○ v locations; △ w locations; □ p location.

2.3.2. Grid Spacing

Uniform grid spacings are selected for the streamwise and spanwise directions. For a domain size of $L_x \times L_y \times L_z$, the corresponding cell dimensions are $\Delta x = L_x/N_x$, and $\Delta z = L_z/N_z$, where N_x and N_z are the number of cells in the streamwise and spanwise directions, respectively. The uniform mesh in these directions allows for the application of Fast Fourier Transform (FFT) to the solution of the Poisson equation.

In the vertical direction, strong flow gradients are expected near the wall and in the free-shear layer, and grid clustering is desired at these locations. A coordinate transform function $y = f(\tilde{y})$ is needed to map a uniform grid distribution $\tilde{y}$ onto its non-uniform counterpart, y. This study employs a modified version of the hyperbolic tangent function used by Pauley *et al.* (1988). Presented below is a simple form of $f(\tilde{y})$:

$$y = \xi\left[1 - \frac{\tanh\gamma(\xi - \tilde{y})}{\tanh\gamma\xi}\right] \qquad 0 \le \tilde{y}, y \le L_y. \tag{2.4}$$

In this formula, γ is the curvature of the function determining the degree of grid compression near the wall. The function has an inflection point at $\tilde{y} = \xi$. The value of ξ can be selected between $L_y/2$ and L_y. The grid size will be finest at $y = \tilde{y} = 0$,

and largest at $y = \tilde{y} = \xi$. If $\xi = L_y/2$, the mesh is symmetric about the midpoint, providing fine grids at both $y = 0$ and $y = L_y$; this is applicable to flows with bottom and top no-slip walls. On the other hand, by selecting $\xi = L_y$, a one-sided grid compression is obtained near the lower wall.

Equation (2.4) is applicable to a channel flow ($\xi = L_y/2$) or a flow over a flat plate ($\xi = L_y$). For the current backward-facing step simulation, a more complex coordinate transform function is necessary to provide additional grid compression at the step ($y = h$). Two hyperbolic tangent functions similar to Eq. (2.4) are combined: $y_1 = f_1(\tilde{y})$ for $0 \leq y \leq h$, and $y_2 = f_2(\tilde{y})$ for $h \leq y \leq L_y$. In addition to the constraints at the bottom and top boundaries, f_1 and f_2 must be selected such that the first derivative $dy/d\tilde{y}$ is continuous at the interface of the two functions. Appendix A presents the detailed development of the grid distribution function used in this study.

The selection of the parameters γ and ξ as well as number of computational cells in each direction will be based on the flow domain and the Reynolds number for each case studied. In §3.3, a study of the sensitivity to grid refinement is presented using 2-D simulations.

2.3.3. Evaluation of Spatial Derivatives

Since different velocity components are defined on different cell boundaries, the Navier-Stokes equation for each flow component is applied at the corresponding locations. The Navier-Stokes equation for the streamwise velocity component, for example, is applied at the left-right surfaces of the cell; and equations for y and z components are applied at top-bottom and front-back surfaces, respectively (Fig. 2.3).

Shown below are examples of the finite difference approximations to the first and second derivatives at node $[i+\frac{1}{2}, j]$ of u with respect to the streamwise direction:

$$\left.\frac{\delta u}{\delta x}\right|_{i+\frac{1}{2},j} = \frac{u_{i+1,j} - u_{i,j}}{\Delta x},$$

$$\left.\frac{\delta^2 u}{\delta x^2}\right|_{i+\frac{1}{2},j} = \frac{u_{i+\frac{3}{2}} - 2u_{i+\frac{1}{2},j} + u_{i-\frac{1}{2}}}{\Delta x^2},$$

where $\delta/\delta x$ and $\delta^2/\delta x^2$ are the finite difference operators. If the values of u are required at points where they are not defined, e.g., at the cell center, linear interpolation of values at two adjacent points will be taken. The same procedure is applied in the y- and z-directions. A weighted average is used in the y-direction to account for the non-uniform grid spacing.

The finite difference approximations to each term in the Navier-Stokes equations as well as the Poisson equation are presented in Appendix B.

2.4. Time Advancement

The governing equations are time-advanced using a semi-implicit method. The advancement scheme for the velocity components u_i is a compact-storage three-substep third-order Runge-Kutta scheme (Spalart, 1987 and Spalart *et al.*, 1991) which has an explicit treatment for the convective terms and implicit for the viscous term. The three-substep Runge-Kutta scheme is combined with the fractional step procedure (Kim & Moin, 1985): the method of Le & Moin (1991) is used which allows for the advancement of the velocity field through the substeps without satisfying the continuity equation at each Runge-Kutta substep. The velocities are projected onto the divergence-free field only at the last substep. The convective terms were modified so that the order of accuracy of the scheme remains unaffected. Presented below are the resulting algorithm.

$$\frac{\tilde{u}_i^{(l)} - \tilde{u}_i^{(l-1)}}{\Delta t} = +(\alpha_l + \beta_l) L\left(\tilde{u}_i^{(l-1)}\right) - \frac{\alpha_l}{Re_h}\frac{\delta}{\delta x_i}\left(\frac{\delta \tilde{u}_k^{(l-1)}}{\delta x_k}\right) + \beta_l L\left(\tilde{u}_i^{(l)} - \tilde{u}_i^{(l-1)}\right)$$
$$- \gamma_l N\left(u_i^{*(l-1)}\right) - \zeta_l N\left(u_i^{*(l-2)}\right), \qquad i = 1,2,3, \tag{2.5}$$

$$u_i^{*(l)} = \tilde{u}_i^{(l)} - \Delta t \sum_{m=1}^{l} (\alpha_m + \beta_m)\frac{\delta \phi^n}{\delta x_i}.$$

In Eq. (2.5), $\tilde{u}_i$ represents the intermediate velocity components (not satisfying the continuity equation); u_i^* is the modified velocity in the convective terms to

maintain the order of accuracy of the scheme; the superscript $l = 1, 2, 3$ identifies the Runge-Kutta substeps; $L(u_i)$ and $N(u_i)$ represent second-order finite difference approximations to the viscous and convective terms, respectively:

$$L(u_i) = \frac{1}{Re_h}\frac{\delta^2}{\delta x_k \delta x_k}u_i, \qquad N(u_i) = \frac{\delta}{\delta x_k}u_i u_k. \tag{2.6}$$

The coefficients α_l, β_l, γ_l and ζ_l are constants selected such that the total time advancement between t^n and t^{n+1} is third-order accurate for the convective terms and second-order for the viscous terms (Spalart, 1987). These coefficients are:

$$\begin{aligned}
&\gamma_1 = 8/15, && \gamma_2 = 5/12, && \gamma_3 = 3/4,\\
&\zeta_1 = 0, && \zeta_2 = -17/60, && \zeta_3 = -5/12,\\
&\alpha_1 = \beta_1 = 4/15, && \alpha_2 = \beta_2 = 1/15, && \alpha_3 = \beta_3 = 1/6,
\end{aligned}$$

$$\sum_{l=1}^{3}(\alpha_l + \beta_l) = \sum_{l=1}^{3}(\gamma_l + \zeta_l) = 1.$$

At the first substep ($l = 1$), $\tilde{u}^{(l-2)}$ is ignored and $\tilde{u}_i^{(l-1)} = \tilde{u}_i^{(0)} \equiv u_i^n$. The divergence-free velocity components at time step $n+1$ can be obtained from

$$u_i^{(n+1)} = \tilde{u}_i^{(3)} - \Delta t \frac{\delta \phi}{\delta x_i}, \tag{2.7}$$

where ϕ is the first-order approximation to the pressure and satisfies the Poisson equation,

$$\frac{\delta^2 \phi}{\delta x_k \delta x_k} = \frac{1}{\Delta t}\frac{\delta \tilde{u}_k^{(3)}}{\delta x_k}. \tag{2.8}$$

The time step Δt is determined by the Courant-Friedrichs-Lewy (CFL) number:

$$\Delta t = \frac{CFL}{|\Lambda|_{\max}}, \tag{2.9}$$

where $|\Lambda|_{\max}$ is

$$|\Lambda|_{\max} = \left(\sum_{i=1}^{3}\frac{|u_i|}{\Delta x_i}\right)_{\max}. \tag{2.10}$$

The maximum CFL limit for stability is $\sqrt{3}$ for the third-order Runge-Kutta method. A CFL number of 1.15 was used in the 3-D simulations presented in

this report. At every time step, Δt is adjusted according to Eq. (2.9) except when flow statistics were being accumulated at which time Δt was kept constant (see Chapter 5).

2.5. Initial Condition

For 2-D computations, the desired mean velocity profile $U(y)$ is prescribed at the inlet, and also distributed uniformly in the upper portion of the domain along the streamwise direction. The streamwise velocity was prescribed to be zero in the lower portion (between the lower wall and the step). The vertical velocity component is set to zero over the entire domain. This initial condition, though not physical, does satisfy the global continuity requirement. A minimum of two "flow-through" times ($2(L_x - L_i)/U_c$ where U_c is the mean convection speed) is usually used to remove the initial transients.

For 3-D simulations, the initial flow field is generated by first establishing a corresponding 2-D field following the preceding method. The 2-D velocity components are then duplicated for all N_z vertical planes in the computational domain and a random velocity perturbation is added to the initial flow. In cases where a grid refinement is desired for an existing 3-D flow field, all variables are interpolated and the simulation proceeds from the new field. In either case, a transient period must pass through the domain before any flow statistics can be collected.

2.6. Boundary Conditions

At the upper boundary of the computational domain, either a no-slip or no-stress wall is considered. When a parabolic profile or a fully developed turbulent channel mean profile (Kim *et al.*, 1987) is imposed at the inlet, no-slip boundary condition is applied at $y = L_y$ with $u = v = w = 0$. A no-stress wall is used with a flat-plate boundary layer mean profile (Spalart, 1988) at the inlet. The velocities at the no-stress wall are:

$$v = 0, \qquad \frac{\partial u}{\partial y} = \frac{\partial w}{\partial y} = 0. \tag{2.11}$$

In all 3-D computations, the flow is assumed to be statistically homogeneous in the spanwise direction where periodic boundary conditions are used.

Described below is a method of generating inflow "turbulent" fluctuations, u', v' and w'. The application of the convective outflow boundary condition will also be described.

2.6.1. Inflow Condition

The time-dependent velocities prescribed at the inlet consist of the mean, $U(y)$, and fluctuations, $u_i'(y,z,t)$. Three different mean velocity profiles are considered: parabolic profile, fully developed channel profile from Kim *et al.* (1987), and boundary layer profile from Spalart (1988). In 2-D simulations, these mean profiles are imposed at the step; in 3-D, the inflow conditions are at a distance upstream from the step. Turbulent fluctuations, u', v' and w', are also added to the channel and boundary layer inlet profiles in 3-D simulations. Lee *et al.* (1992) described a method of generating these inflow fluctuations at the inlet plane, $x = 0$. Their method is modified here for wall-bounded incompressible flows.

2.6.1.1. Method

For simplicity, the forgoing development only considers the calculations of the streamwise velocity fluctuations u'. The algorithm of Lee *et al.* (1992) is first summarized below.

At the domain inlet ($x = 0$), the energy spectrum E_{uu} of the signal $u'(y,z,t)$ is prescribed in terms of frequency ω and two transverse wave numbers k_y and k_z: $E_{uu}(k_y,k_z,\omega)$. The Fourier coefficients $\hat{u}(k_y,k_z,\omega,t)$ of u' is related to E_{uu} by the equation

$$\hat{u}\left(k_y,k_z,\omega,t\right) = \left[E_{uu}\left(k_y,k_z,\omega\right)\right]^{\frac{1}{2}} \exp\left[\mathbf{i}\varphi\left(k_y,k_z,\omega,t\right)\right], \qquad (2.12)$$

where $\mathbf{i} = \sqrt{-1}$ and φ is the phase angle. The steps in generating $u'(y,z,t)$ are

(a) Given an energy spectrum E_{uu}, calculate the magnitude of the Fourier coefficient $|\hat{u}(k_y,k_z,\omega)| = [E_{uu}(k_y,k_z,\omega)]^{\frac{1}{2}}$.

(b) Compute the Fourier coefficient $\hat{u}$ in Eq. (2.12) using a random phase angle φ at each frequency ω and wave number $[k_y, k_z]$. The phase angle is varied with time by an amount $\Delta\varphi$ *only once* over a selected time interval T_r. Both $\Delta\varphi$ and the time within T_r at which φ is changed are determined randomly. Furthermore, $|\Delta\varphi|$ is bounded by a prescribed value.

(c) The signal $u'(y,z,t)$ is finally computed by inverse Fourier transforms in y- and z-directions, followed by an inverse Fourier transform from the frequency domain ω.

The inverse Fourier transform from the frequency (ω) to time domain requires a prescribed segment period T_f. Therefore, a zero random phase change ($\Delta\varphi = 0$) will result in a periodic fluctuation signal with a period T_f. On the other hand, a large $\Delta\varphi$ destroys the periodicity but causes further deviation from the target spectrum.

The above procedure is not readily applicable to the generation of inlet turbulence for the backward-facing step flow because of the inhomogeneity in the y-direction. Presented below are modifications made to apply this method to a wall-bounded flow.

For channel or boundary layer flow at the inlet, the fluctuation signals u', v' and w' are generated to conform to the corresponding prescribed turbulence intensities, $\overline{u'^2}$, $\overline{v'^2}$, $\overline{w'^2}$, and the Reynolds shear stress, $\overline{u'v'}$. At a specific discrete j node in the vertical direction, the prescribed streamwise turbulence intensity is $\overline{u_j'^2}$; whereas the calculated value, $\langle u_j'^2 \rangle$, over a period T_f is

$$\langle u_j'^2 \rangle = \sum_{m=0}^{N_z-1} \sum_{l=0}^{N_t-1} \hat{u}_{j,m,l} \hat{u}^*_{j,m,l}, \qquad j = 1, \ldots, N_y, \tag{2.13}$$

where:

T_f is the period of the fluctuation signal;

N_z, N_t are the number of discrete points in spanwise direction and in time period T_f, respectively;

$\hat{u}$, $\hat{u}^*$ are the Fourier coefficient of u' and its complex conjugate, respectively.

Thus to enforce Eq. (2.13) at each vertical location j, the velocity fluctuations at inlet are scaled by a factor $\sqrt{r_j}$ where

$$r_j = \frac{\overline{u_j'^2}}{\langle u_j'^2 \rangle} = \frac{\overline{u_j'^2}}{\sum_{m=0} \sum_{l=0} \hat{u}_{j,m,l} \hat{u}^*_{j,m,l}}. \tag{2.14}$$

This in effect leads to a deviation from the target spectrum $E_{uu}(k_x, k_y, \omega)$ in the vertical direction.

The same procedure is repeated to compute v' and w'. However, since u', v' and w' are computed independently, the results will be a set of uncorrelated signals, i.e., $\overline{u'v'} = 0$. Thus, the calculated fluctuations conform to the turbulence intensities, $\overline{u'^2}$, $\overline{v'^2}$ and $\overline{w'^2}$, but not to the Reynolds shear stress, $\overline{u'v'}$. The remedy is to rotate the flow coordinates $[x, y]$ to coincide with the principal coordinates $[X, Y]$ where the corresponding velocities U' and V' are uncorrelated, i.e., $\overline{U'V'} = 0$. The fluctuation signals are thus calculated in the $[X, Y]$ coordinates, then are rotated back to the flow coordinates. This method is described below.

The velocities in the two coordinate systems are related through the angle of rotation θ_p as follows:

$$u' = U' \cos\theta_p + V' \sin\theta_p, \tag{2.15a}$$

$$v' = -U' \sin\theta_p + V' \cos\theta_p. \tag{2.15b}$$

Multiplying Eqs. (2.15a) and (2.15b), then averaging gives:

$$\overline{u'v'} = \left(\overline{V'^2} - \overline{U'^2}\right) \frac{\sin(2\theta_p)}{2} + \overline{U'V'} \cos(2\theta_p) \tag{2.16}$$

By setting $\overline{U'V'} = 0$, for U' and V' are in the principal coordinates, Eq. (2.16) becomes

$$\overline{u'v'} = \left(\overline{V'^2} - \overline{U'^2}\right) \frac{\sin(2\theta_p)}{2}. \tag{2.17}$$

Equations (2.15a) and (2.15b) also provide a relationship among the turbulence intensities:

$$\overline{u'^2} = \overline{U'^2}\cos^2\theta_p + \overline{V'^2}\sin^2\theta_p,$$
$$\overline{v'^2} = \overline{U'^2}\sin^2\theta_p + \overline{V'^2}\cos^2\theta_p,$$

or,

$$\overline{U'^2} = \frac{\overline{u'^2}\cos^2\theta_p - \overline{v'^2}\sin^2\theta_p}{\cos^2\theta_p - \sin^2\theta_p}, \tag{2.18a}$$

$$\overline{V'^2} = \frac{\overline{v'^2}\cos^2\theta_p - \overline{u'^2}\sin^2\theta_p}{\cos^2\theta_p - \sin^2\theta_p}. \tag{2.18b}$$

The angle θ_p is found by combining Eqs. (2.17) and (2.18):

$$\theta_p = \frac{1}{2}\tan^{-1}\left[\frac{2\overline{u'v'}}{\overline{v'^2} - \overline{u'^2}}\right]. \tag{2.19}$$

Given a set of $\overline{u'^2}$, $\overline{v'^2}$ and $\overline{u'v'}$, the angle θ_p can be determined; the corresponding set of $\overline{U'^2}$ and $\overline{V'^2}$ are then calculated from Eq. (2.18).

The steps in generating inflow turbulence for a given set of turbulence intensities and Reynolds shear stress are summarized below.

One-time calculations:

(A) At every j location, calculate the angle of rotation θ_p using Eq. (2.19).

(B) Obtain $\overline{U_j'^2}$ and $\overline{V_j'^2}$ in principal coordinates using Eq. (2.18).

(C) Calculate the magnitude of the Fourier coefficients $|\hat{u}_{n,m,l}|$ from the energy spectrum $E_{uu}(k_y, k_z, \omega)$.

Calculations at every time step:

(D) At a randomly assigned instant, change the phase angle $\varphi_{n,m,l}$ by a random amount $\Delta\varphi_{n,m,l}$ and apply to $|\hat{u}_{n,m,l}|$ to obtain $\hat{u}_{n,m,l}$.

(E) Inverse Fourier transform in the vertical direction to obtain $\hat{u}_{j,m,l}$.

(F) Calculate $\sum_l \sum_m \hat{u}_{j,m,l}\hat{u}^*_{j,m,l}$, and the mean-square ratio r_j:

$$r_j = \frac{\overline{U_j'^2}}{\sum_l \sum_m \hat{u}_{j,m,l}\hat{u}^*_{j,m,l}}.$$

(G) Inverse Fourier transform in k_z direction and sum over all frequencies to obtain $U'_{j,k}(t)$. Scale $U'_{j,k}(t)$ with $\sqrt{r_j}$ to match $\sqrt{\overline{U'^2_j}}$ from step (B).

(H) Repeat steps (D) through (G) for $V'_{j,k}(t)$ and $w'_{j,k}(t)$.

(I) Rotate $U'_{j,k}(t)$ and $V'_{j,k}(t)$ back to $u'_{j,k}(t)$ and $v'_{j,k}(t)$ in the flow coordinates using Eq. (2.15).

The procedure described above gives a set of stochastic signals that satisfy a prescribed set of second-order statistics at the inlet. The use of Lee *et al.*'s (1992) procedure ensures that the resulting signals do not contain excessive small scale motions which would have resulted if simply random numbers were used to generate u', v' and w'. An example of a signal $u'(t)$ generated by this method at a selected inlet location is shown in Fig. 2.4. The Reynolds shear stress and

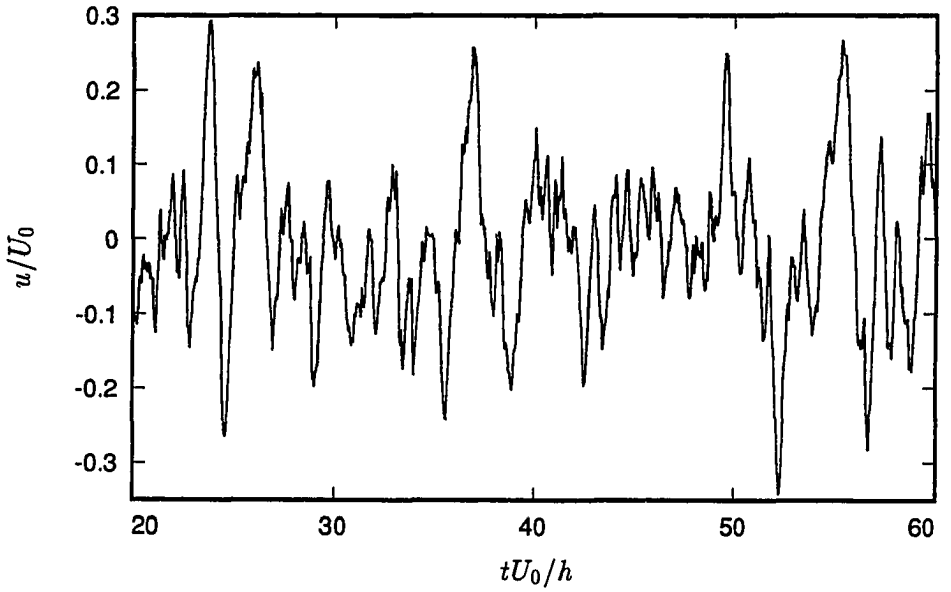

Figure 2.4. Inlet turbulent signal $u'(t)$.

turbulence intensity profiles from the channel simulation of Kim *et al.* (1987) were used in this case. The segment period is $T_f = 6.4h/U_0$ (Strouhal number based on

h and U_0 is $St_f = h/(U_0 T_f) = 0.156$) using $N_t = 128$ discrete intervals per period (time step $\Delta t_f = 0.05 h/U_0$). At any spectral location, the random phase change is allowed only once over an interval $T_r = 10\Delta t_f = 0.5 h/U_0$ with $-0.2\pi < \Delta\varphi < 0.2\pi$. These prescribed parameters, which ensure an aperiodic signal as shown in Fig. 2.4, will be used in subsequent 2-D and 3-D simulations (Chapters 3, 4 and 5).

When the turbulent signals are imposed at the inlet plane, the compatibility condition required for the solution of the Poisson equation must also be considered. This condition for a Poisson equation with Neumann boundary conditions (§2.7) is equivalent to a global mass conservation:

$$\dot{m} = \iint_{\text{inlet}} u\,(y,z)\; dzdy = \iint_{\text{exit}} u\,(y,z)\; dzdy. \tag{2.20}$$

Two methods are considered to maintain a global mass conservation. In one method, the mass flux at the inlet plane is kept constant, equal to the mean flow rate, $\dot{M}$, from the mean velocity profile $U(y)$. This implies that the net mass inflow resulting from the streamwise fluctuations must be zero. This is accomplished in step (D) above, setting to zero the value of the Fourier coefficients at $k_z = 0$ wave number: $\hat{u}(k_y, 0, \omega) = 0$.

The total mass inflow can also be allowed to fluctuate in time, $\dot{m} = \dot{M} + \dot{m}'$, where the mass flow fluctuation is

$$\dot{m}' = \int_y \int_z u'\,(y,z)\; dzdy. \tag{2.21}$$

The global continuity condition is then satisfied by adjusting the exit velocities, at every time step. Calculations of exit velocities are discussed in §2.6.2.

Simulations with a variable mass flow rate indicated that the fluctuation $\dot{m}'$ is less than 0.1% of the mean flow rate. As a result, negligible differences are observed in the statistical quantities calculated from these two methods. All 3-D simulations in this study maintain a constant mass flow rate.

2.6.1.2. Validation

The above method of generating inflow turbulence was used to simulate spatially evolving plain channel flow. The inlet mean velocity, Reynolds shear stress and

turbulence intensity profiles were obtained from the channel simulation of Kim *et al.* (1987). The Reynolds number was 6600 based on the peak inlet velocity U_0 and channel height, h_c. The first and second order statistics were collected at all points along the channel. The comparison between the calculated Reynolds stress components at the inlet and the target profiles is presented in Fig. 2.5.

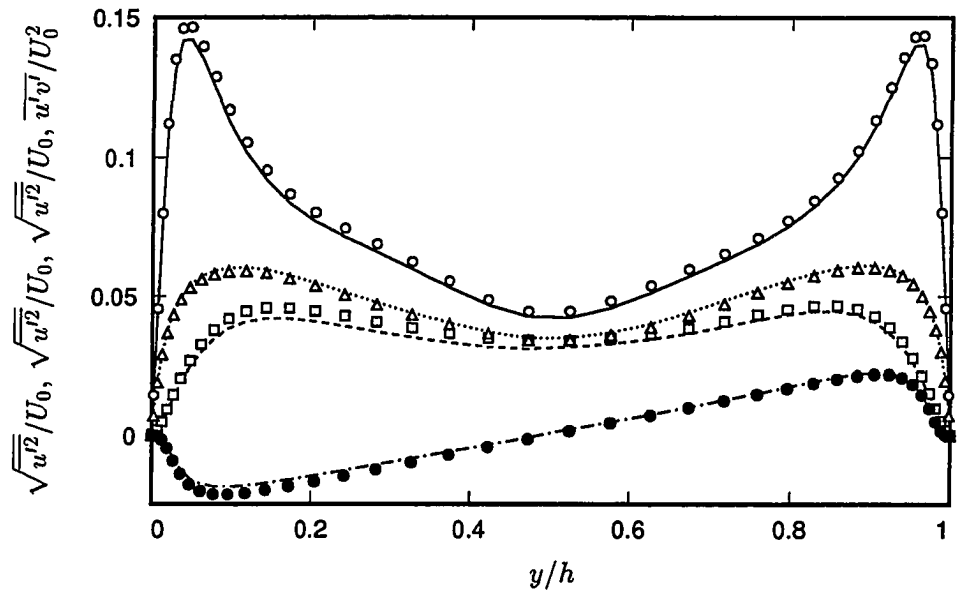

Figure 2.5. Validation of inflow turbulence. $\sqrt{\overline{u'^2}}$: —— computed ; ○ target. $\sqrt{\overline{v'^2}}$: ---- computed; △ target. $\sqrt{\overline{w'^2}}$: ····· computed; □ target. $\overline{u'v'} \times 10$: —·— computed; • target.

As expected, the turbulence intensities and Reynolds shear stress are recovered at the inlet. However, the flow quickly loses its statistical characteristics within the first few channel heights from the inlet. Figure 2.6 shows the mean velocity profiles, U, for the distance $x/h_c < 3.0$ in wall coordinates. The profile follows the log-law at the inlet, but deviates upward from the log-law downstream. The rise above the log-law indicates a drop in the wall shear velocity, u_τ. The evolution of the friction coefficient C_f with the streamwise distance is plotted in Fig. 2.7. From the inlet value of 6×10^{-3}, the friction coefficient loses approximately 33% of its channel flow

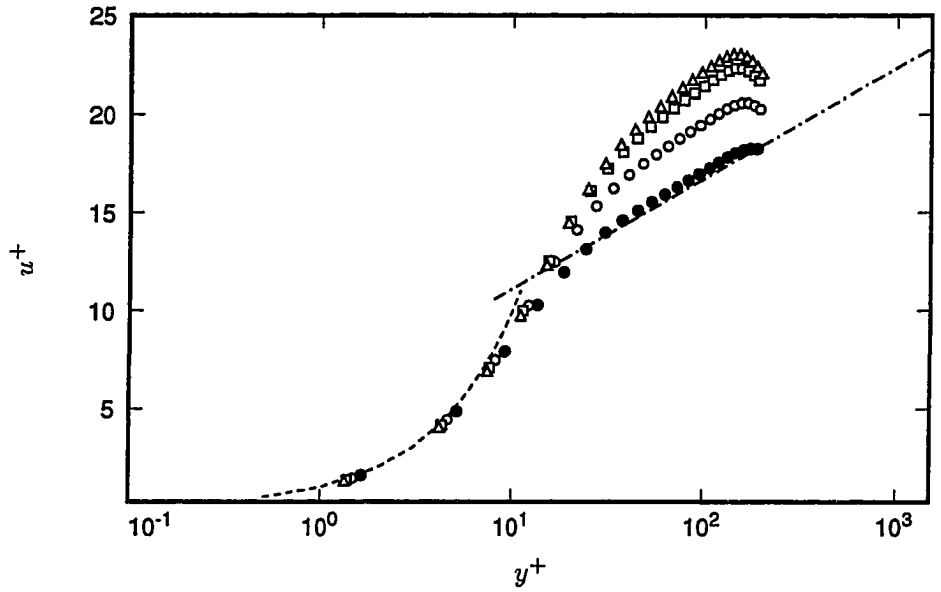

Figure 2.6. Near-wall mean velocity profiles; turbulent channel flow. ---- $u^+ = y^+$; —·— $u^+ = \frac{1}{0.41}\log y^+ + 5.5$; • $x/h_c = 0$ (inlet); ○ $x/h_c = 1.0$; □ $x/h_c = 2.0$; △ $x/h_c = 3.0$.

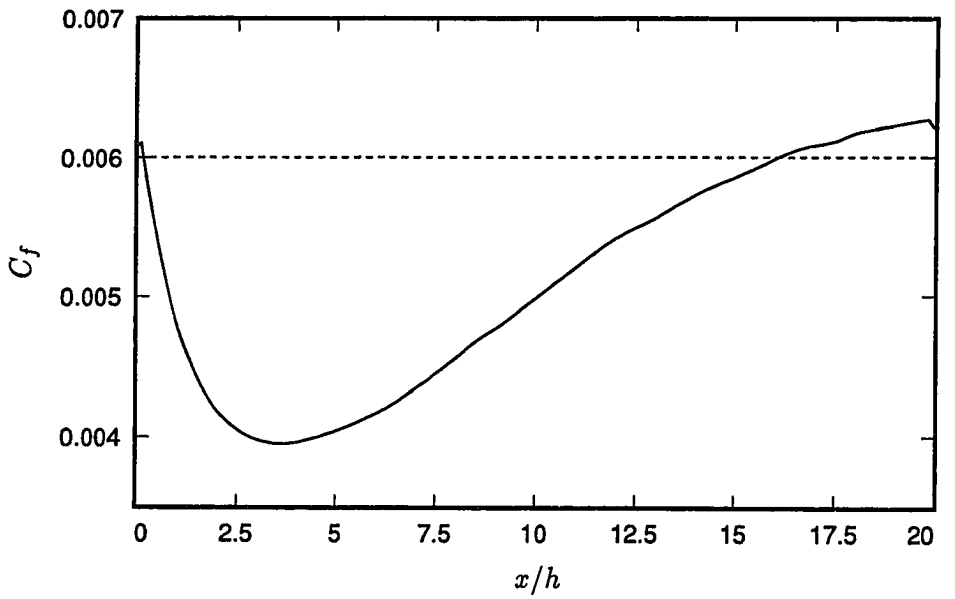

Figure 2.7. Development of mean friction coefficient; turbulent channel flow. —— computed C_f; ---- target C_f.

value within the first $3h_c$. This initial transition and apparent laminarization is due to the unphysical inlet turbulence which is a result of the randomized phase angles. The turbulent characteristics are, however, recovered slowly downstream and the C_f stays within 5% of the target value as $x > 14h_c$.

The domain size used in the above test was $20h_c \times h_c \times 5h_c$ in x-, y- and z-directions, respectively. The corresponding grid was $256 \times 40 \times 64$. To assure that the observed behavior is not a result of grid resolution or domain size, several simulations with varying streamwise and spanwise dimensions as well as grid spacing were performed. The results indicate that, although the recovering distance is somewhat reduced ($< 10\%$) with higher resolution, a substantial transition length is unavoidable.

The channel simulations demonstrate that, although the turbulent signal generated by the present method has the correct first and second order flow statistics, its turbulent structures are missing. The test also provides information on the necessary development length to recover the target flow. In the 3-D simulations of the backward-facing step flow, a transition distance of $10h$ is used. This inlet section length with a fine streamwise grid spacing brings the flow statistics to less than 6% of the target values after approximately 7 step heights (Chapter 5).

2.6.2. Outflow Condition

Several exit boundary conditions applied to an unsteady separated boundary layer were tested by Pauley *et al.* (1988). For unsteady problems, the convective boundary condition was best suited for moving structures out of the computational domain. The convective boundary condition was used by Lowery & Reynolds (1986) in numerical simulations of spatially evolving mixing layers. The time-dependent condition of any velocity component u_i at the exit plane ($x = L_x$) is taken as

$$\frac{\partial u_i}{\partial t} + U_c \frac{\partial u_i}{\partial x} = 0, \tag{2.22}$$

where U_c is the convection velocity. Pauley *et al.* (1988) showed that the inclusion of one or more viscous terms in Eq. (2.22) leads to instability. In this work, Eq. (2.22)

is used, but tests were conducted to determine the proper selection of the convection velocity U_c.

Application of Eq. (2.22) to the streamwise velocity at the exit (see Fig. 2.8) leads to

$$u^{n+1}_{N_x+\frac{1}{2},j,k} = u^{n}_{N_x+\frac{1}{2},j,k} - \frac{\Delta t}{\Delta x} U_c \left(u^{n}_{N_x+\frac{1}{2},j,k} - u^{n}_{N_x-\frac{1}{2},j,k} \right), \tag{2.23}$$

where, a first-order backward difference approximation of $\partial/\partial x$ is employed.

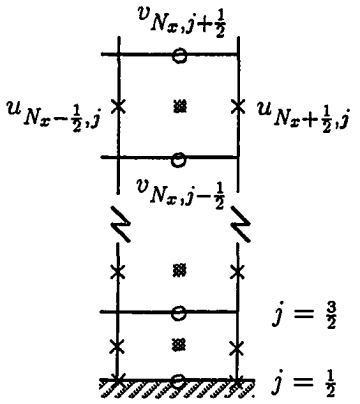

Figure 2.8. Cells adjacent to the flow exit.

Han *et al.* (1983) proposed a similar boundary condition for laminar wakes using the instantaneous local speed as the convection speed. In their formation, the velocity U_c was the streamwise exit velocity at the current time step which varies with y. This formulation may violate the compatibility condition (Eq. (2.20)) discussed in §2.6.1. A U_c which is a function of space does not guarantee the balance between the mass inflow and outflow at each time step. This difficulty can be avoided, for example, by multiplying the streamwise exit velocities by the mass ratio $\dot{m}/\dot{m}_e$, where the exit mass flow rate is

$$\dot{m}_e = \sum_{j=1}^{N_y} \sum_{k=1}^{N_z} u^{n+1}_{N_x+\frac{1}{2},j,k} \Delta z \Delta y_j,$$

and $\dot{m}$ is the inlet mass flow rate. This approach works well if $|\dot{m} - \dot{m}_e|$ is small. Tests showed that the mass flow imbalance may grow unbounded, and leads to numerical instability if the convective speed becomes negative; this was also observed by Han *et al.* (1983). Thus, if the instantaneous velocity $u^n_{N_x+\frac{1}{2},j,k}$ is negative, the convective speed is set to zero. The mass flow difference, $|\dot{m} - \dot{m}_e|$, with this approach is maintained within 0.02%.

A simpler method to maintain a global mass conservation is to use a constant mean exit velocity as the convection speed. Tests with both variable and constant U_c showed negligible differences in the statistical results. This will be shown in the preliminary 3-D simulations (§4.2). A constant U_c was used in all simulations presented in this report.

Besides satisfying the global conservation of mass, the upstream influence of the convective boundary condition was also studied in 2-D simulations of unsteady flows. These simulations are reported in Chapter 3. The exit boundary condition causes some distortion of structures convecting out of the computational domain; but the most severe distortion is contained within one step height upstream from the exit.

Numerical errors due to the convective boundary condition are also apparent in 2-D steady flows (Pauley *et al.*, 1988), or in time-averaged flow fields of unsteady flows (2-D or 3-D). In such cases, the time derivative, $\partial/\partial t$, vanishes. Equation (2.22), applied to the time-averaged streamwise velocity U, becomes

$$\left.\frac{\partial U}{\partial x}\right|_{N_x+\frac{1}{2},j} = 0.$$

It follows from the continuity equation that $\partial V/\partial y$ is also zero, which implies,

$$V_{N_x,j+\frac{1}{2}} = V_{N_x,\frac{1}{2}} = 0 \quad \text{for all } j = 1,\ldots,N_y.$$

This is shown in Fig. 2.9 for 3-D simulations where the time-averaged velocity component V is forced to zero at all vertical exit locations although small vertical motions are still expected (Chapter 5). Examining all statistical quantities from 3-D simulations indicate that the exit convective boundary condition can have some

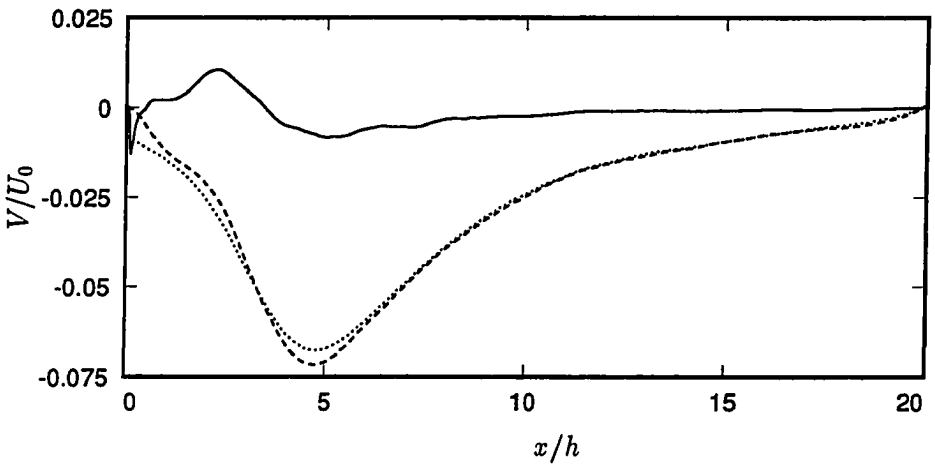

Figure 2.9. Time-averaged velocity V as a function of streamwise distance. —— $y/h = 0.1$; ---- $y/h = 1.0$; ····· $y/h = 1.5$.

adverse effect on the results at locations several step heights upstream, but the most severe effects are within one step height from the exit.

In 2-D backward-facing step simulations, this condition forced the exit streamlines to be parallel to the x-axis. This is seen in the streamlines of steady flows with parabolic profiles at the entrance in the Reynolds number range $500 < Re_h < 2000$ (see §3.1), where a top-wall separation bubble is located near or at the exit. All streamlines are parallel to the horizontal axis even though streamline curvatures are expected near the bubble. The convective boundary condition therefore must be applied sufficiently far from any location with streamline curvatures, e.g., separation bubbles.

2.7. Solution to Poisson Equation

2.7.1. Formulation of Equation and Boundary Condition

The discrete Poisson equation (Eq. (2.8)) applied to an interior cell $[i, j, k]$ is

$$\left(\frac{\delta^2}{\delta x^2} + \frac{\delta^2}{\delta y^2} + \frac{\delta^2}{\delta z^2}\right)\phi_{i,j,k} = \frac{1}{\Delta t}\left(\frac{\delta}{\delta x}\tilde{u} + \frac{\delta}{\delta y}\tilde{v} + \frac{\delta}{\delta z}\tilde{w}\right)\Bigg|_{i,j,k},$$

$$= Q_{i,j,k}, \tag{2.24}$$

$$i = 1, \ldots, N_x, \quad j = 1, \ldots, N_y, \quad k = 1, \ldots, N_z.$$

Kim & Moin (1985) showed that the set of equations arising from enforcing the continuity equation in the fractional step method is equivalent to a Poisson equation with Neumann boundary conditions. The compatibility condition, or solvability, of the Neumann problem is

$$\int_\Omega Q \, dxdydz = \int_\Gamma \frac{\delta\phi}{\delta \mathbf{n}} \, d\Gamma, \tag{2.25}$$

where Ω and Γ denote the domain volume and its boundary surface, respectively; and $\delta/\delta\mathbf{n}$ is the gradient normal to Γ. The compatibility condition is satisfied only if the global continuity is preserved, i.e. a zero net mass flux.

The boundary condition on $\delta\phi/\delta\mathbf{n}$ at each individual boundary node can be selected arbitrarily as along as the global continuity is maintained. In the current study, $\delta\phi/\delta\mathbf{n}$ is selected to be zero at both x and y boundaries. It should be noted here that, by selecting $\delta\phi/\delta\mathbf{n} = 0$, the no-slip condition also requires a zero boundary condition on $\hat{u}$ and $\hat{v}$, i.e., $\hat{v} = 0$ at the lower wall, and $\hat{u} = 0$ at the step vertical wall ($x/h = 0$, $0 \leq y/h \leq 1.0$).

2.7.2. Solution on a Rectangular Domain Using Fourier Transform

A Fourier method for the solution of the Poisson equation was developed by Hockney (1965) and Door (1970) to solve Eq. (2.24) directly on a rectangular domain. Door (1973) also introduced a direct algorithm specifically for the solution of the Poisson equation with Neumann conditions on a staggered grid. The basic solution scheme used in the current simulations was developed by Kim & Moin (1985) which is a modification of an algorithm by Schumann & Sweet (1988). This method combines discrete Fourier transform (Hockney, 1965) with the staggered grid (Door, 1973). A brief summary is presented here.

The central-difference approximation of the Laplace operator in Eq. (2.24) using a 3-point stencil produces an $(N_x N_y N_z) \times (N_x N_y N_z)$ block tridiagonal matrix. The

Fourier method uncouples the streamwise and spanwise directions and reduces this matrix to a set of $N_x N_z$ independent tridiagonal matrices of size $N_y \times N_y$. A full Fourier transform is applicable in the z-direction for its periodic boundary condition and uniform grid spacing. In the x-direction, a half-range Fourier expansion using only cosine functions is suitable. The orthogonal property of cosine and exponential functions in the Fourier expansion reduces Eq. (2.24) to a set of Helmholtz equations in Fourier space:

$$\left(\frac{\delta^2}{\delta y^2} - k_l' - k_m'\right)\hat{\phi}_{l,j,m} = \hat{Q}_{l,j,m}, \qquad l = 0,\ldots,N_x-1, \quad m = -\frac{N_z}{2}+1,\ldots,\frac{N_z}{2}, \tag{2.26}$$

k_l' and k_m' are the modified wave numbers defined as:

$$k_l' = \frac{2}{\Delta x^2}\left[1 - \cos\left(\frac{\pi l}{N_x}\right)\right], \tag{2.27a}$$

$$k_m' = \frac{2}{\Delta z^2}\left[1 - \cos\left(\frac{2\pi m}{N_z}\right)\right]. \tag{2.27b}$$

$\hat{Q}_{l,j,m}$ is the Fourier coefficient of $Q_{i,j,k}$ at wave number $[l,m]$ defined as:

$$\hat{Q}_{l,j,m} = \frac{1}{N_x N_z}\sum_{i=1}^{N_x}\sum_{k=1}^{N_z} Q_{i,j,k}\cos\left[\frac{\pi l}{N_x}(i-\tfrac{1}{2})\right]\exp\left[-\mathbf{i}\frac{2\pi m}{N_z}(k-\tfrac{1}{2})\right], \tag{2.28}$$
$$l = 0,\ldots,N_x-1, \quad m = -\frac{N_z}{2}+1,\ldots,\frac{N_z}{2},$$

where $\mathbf{i}$ is $\sqrt{-1}$. The Fourier coefficient of the solution, $\hat{\phi}_{l,j,m}$, is similarly defined.

Equation (2.26) becomes a linear system of equations in y for each set of wave number $[l,m]$,

$$\mathbf{M}_{l,m}\hat{\mathbf{\Phi}}_{l,m} = \hat{\mathbf{Q}}_{l,m}, \quad l = 0,\ldots,N_x-1, \quad m = -\frac{N_z}{2}+1,\ldots,\frac{N_z}{2}. \tag{2.29}$$

$\mathbf{M}_{l,m}$ is an $N_y \times N_y$ tridiagonal matrix of the form

$$\mathbf{M}_{l,m} = \left[\mathcal{A}_j^{(\phi)}, \quad \mathcal{B}_j^{(\phi)} - k_l' - k_m', \quad \mathcal{C}_j^{(\phi)}\right], \tag{2.30}$$

where $\mathcal{A}_j^{(\phi)}$, $\mathcal{B}_j^{(\phi)}$ and $\mathcal{C}_j^{(\phi)}$ are the coefficients derived for the Laplace operator $\delta^2/\delta y^2$ at the pressure node point j (see Appendix B). The solution vector $\hat{\mathbf{\Phi}}_{l,m}$ is solved at

each wave number $[l, m]$ by inversion of $\mathbf{M}_{l,m}$ and the final solution $\phi_{i,j,k}$ obtained by inverse Fourier transforms. A special treatment of Eq. (2.29) is necessary when $k_l' = k_m' = 0$, because $\mathbf{M}_{0,0}$ is singular.

2.7.3. Solution on a 2-D L-Shape Domain

In this section, the direct solution method for the Poisson equation with Neumann boundary conditions in the backward-facing step geometry is described. Several methods have been proposed for the solution of the Poisson and Helmholtz equations in domains consisting of connected rectangles. Hockney (1970), Buzbee *et al.* (1970, 1971), and Dryja (1978) all presented different variations of a two-iteration technique called the *capacitance matrix* method. These algorithms, however, were derived primarily for problems with Dirichlet boundary conditions. Proskurowski & Widlund (1976), and later, Schumann & Benner (1982) applied the capacitance matrix method to Neumann problems. The capacitance matrix method presented in this section follows that of Schumann & Benner (1982), but is tailored to the specific configuration and boundary conditions of the backward-facing step. Also for simplicity, the derivation below focuses on a 2-D domain with the governing equation,

$$\left(\frac{\delta^2}{\delta x^2} + \frac{\delta^2}{\delta y^2}\right)\phi_{i,j} = \frac{1}{\Delta t}\left(\frac{\delta}{\delta x}\tilde{u} + \frac{\delta}{\delta y}\tilde{v}\right)\Big|_{i,j},$$
$$= Q_{i,j}, \qquad i = 1, \ldots, N_x, \quad j = 1, \ldots, N_y. \tag{2.31}$$

2.7.3.1. Concept

Figure 2.10 shows a rectangular domain Ω that covers both the flow field and the step corner. The boundary of this region is $\partial\Omega$. The flow region and the solid corner Ω_c share the common boundary Γ which consists of a vertical section Γ_{v} and a horizontal section Γ_{h}. The Poisson equation (2.31) is only solved on the entire rectangular domain, Ω. Difficulties arise when the no-slip velocity condition is enforced at the step boundary Γ, i.e., $v = 0$ on Γ_{h} and $u = 0$ on Γ_{v}. This is shown by examining the cells adjacent to Γ in Fig. 2.11. Since the treatment of the

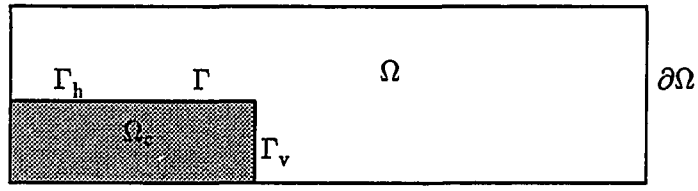

Figure 2.10. Flow domain with solid corner.

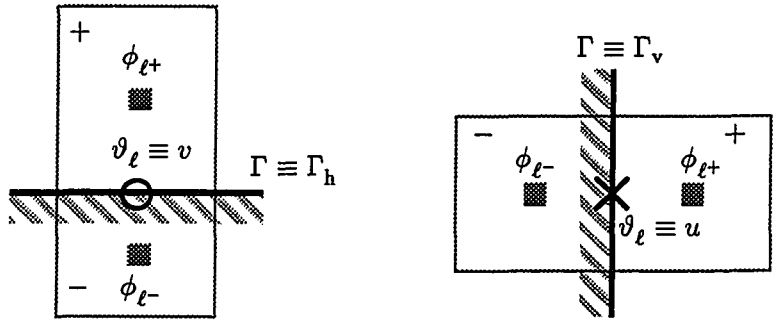

Figure 2.11. Cells adjacent to step boundary.

velocities is the same for v on Γ_h as for u on Γ_v, the following common nomenclature is used in the subsequent development.

ϑ	Velocity component on the step boundary Γ: $\vartheta \equiv u$ on Γ_v and $\vartheta \equiv v$ on Γ_h.
η	Spatial coordinates normal to Γ: $\eta \equiv x$ on Γ_v and $\eta \equiv y$ on Γ_h).
$\delta\phi/\delta\eta$	Gradient of ϕ normal to Γ: $\delta\phi/\delta\eta \equiv \delta\phi/\delta x$ on Γ_v and $\delta\phi/\delta\eta \equiv \delta\phi/\delta y$ on Γ_h.
N_c	Total numbers of ϑ points on Γ.

ℓ^+, ℓ^- Index denoting cells adjacent to Γ at location ℓ ($\ell = 1, \ldots, N_c$). ℓ^+ designates cells in the flow region; ℓ^- designates cells in the solid corner.

The velocity at the step boundary is

$$\vartheta_\ell = \tilde{\vartheta}_\ell - \Delta t \left.\frac{\delta\phi}{\delta\eta}\right|_\ell, \qquad \ell = 1, \ldots, N_c. \tag{2.32}$$

$\tilde{\vartheta}_\ell$, $\ell = 1, \ldots, N_c$, are set to zero which are the $\tilde{u}$ and $\tilde{v}$ boundary conditions in the intermediate fractional steps (see §2.7.1). The solution ϕ, obtained by solving the Poisson equation over the entire domain Ω, does not guarantee zero gradients across Γ ($\partial\phi/\partial\eta \neq 0$). Therefore,

$$\vartheta_\ell = -\Delta t \left.\frac{\delta\phi}{\delta\eta}\right|_\ell \neq 0, \qquad \ell = 1, \ldots, N_c. \tag{2.33}$$

which violates the no-slip condition on Γ.

In the *capacitance matrix* method, the Poisson equation is solved twice. The final solution is the superposition of the solutions from these two passes. This superposition method takes advantage of the linear property of the Laplace operator: if $\phi^{(\mathrm{I})}$ and $\phi^{(\mathrm{II})}$ are solutions of Eq. (2.31), then $\phi^{\mathrm{final}} = \phi^{(\mathrm{I})} + \phi^{(\mathrm{II})}$ is also a solution. The two-pass procedure is shown schematically in Fig. 2.12 and outlined below.

(I) In the first pass, Eq. (2.31) is solved with $\tilde{\vartheta}_\ell^{(\mathrm{I})}$ ($\ell = 1, \ldots, N_c$) prescribed to be zero (boundary conditions on $\tilde{u}$ and $\tilde{v}$, §2.7.1). Non-zero gradients $\delta\phi_\ell^{(\mathrm{I})}/\delta\eta$ across Γ are obtained, and the no-slip condition on Γ will not be satisfied,

$$\vartheta_\ell^{(\mathrm{I})} = -\Delta t \left.\frac{\delta\phi^{(\mathrm{I})}}{\delta\eta}\right|_\ell \neq 0, \qquad \ell = 1, \ldots, N_c. \tag{2.34}$$

(II) In the second pass, a new set of *non-zero* $\tilde{\vartheta}_\ell^{(\mathrm{II})}$ ($\ell = 1, \ldots, N_c$) is calculated. The Poisson equation is then solved with only $\tilde{\vartheta}_\ell^{(\mathrm{II})}$ placed on Γ and zero elsewhere. The non-zero set $\tilde{\vartheta}_\ell^{(\mathrm{II})}$ is obtained such that, the superposition of the first and second pass velocities results in a zero wall velocity:

$$\vartheta_\ell^{\mathrm{final}} = \vartheta_\ell^{(\mathrm{I})} + \vartheta_\ell^{(\mathrm{II})} = 0, \qquad \ell = 1, \ldots, N_c.$$

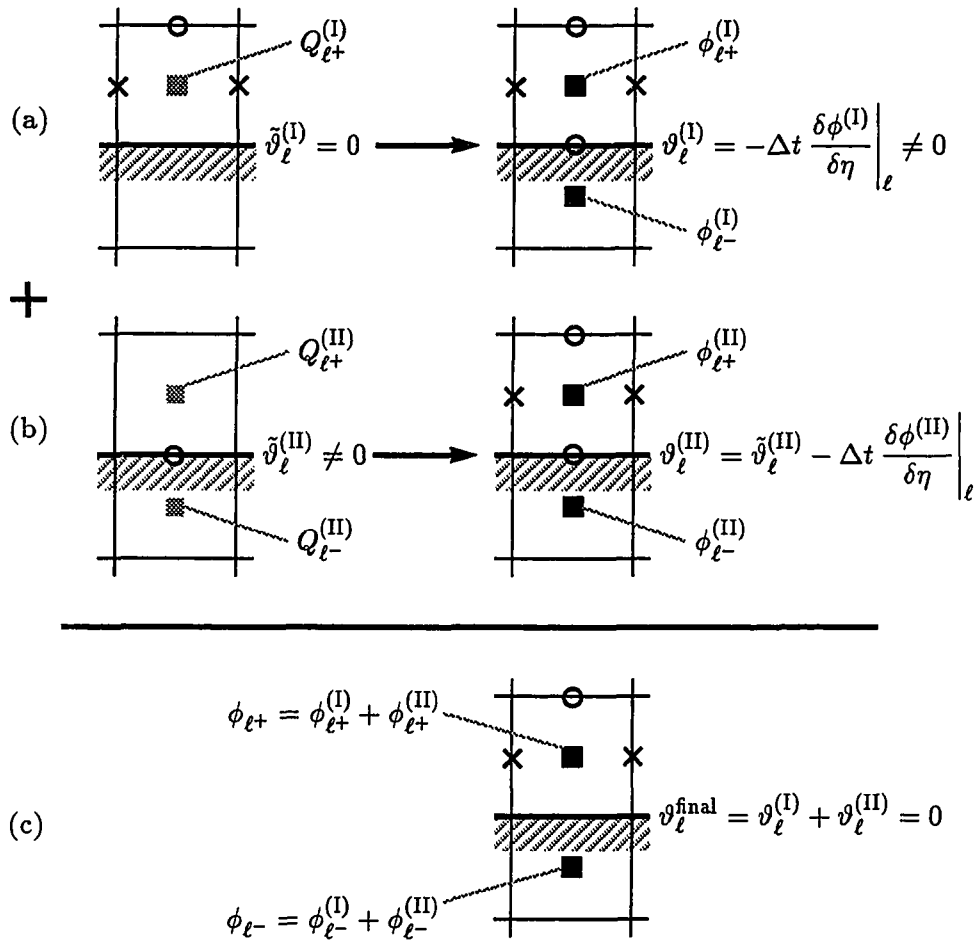

Figure 2.12. Superposition of two Poisson solutions. (a) First pass (I) with $\tilde{\vartheta}_\ell = 0$. (b) Second pass (II) with $\tilde{\vartheta}_\ell \neq 0$. (c) Final solution.

Section 2.7.3.2 discusses the procedure to obtain $\tilde{\vartheta}_\ell^{(II)}$ for the second pass based on the error in Eq. (2.34).

2.7.3.2. Capacitance Matrix

It is desired to calculate the set of non-zero $\tilde{\vartheta}_\ell^{(II)}$ for the second pass, given the error on $\vartheta_\ell^{(I)}$ obtained from the first pass (Eq. (2.34)). This section describes the

so-called *capacitance matrix* which relates $\tilde{\vartheta}_\ell^{(\mathrm{II})}$ to $\vartheta_\ell^{(\mathrm{I})}$. The velocities calculated from the two passes are

$$\vartheta_\ell^{(\mathrm{I})} = -\Delta t \left.\frac{\delta\phi^{(\mathrm{I})}}{\delta\eta}\right|_\ell, \qquad \ell = 1,\ldots,N_c, \tag{2.35a}$$

$$\vartheta_\ell^{(\mathrm{II})} = \tilde{\vartheta}_\ell^{(\mathrm{II})} - \Delta t \left.\frac{\delta\phi^{(\mathrm{II})}}{\delta\eta}\right|_\ell, \qquad \ell = 1,\ldots,N_c. \tag{2.35b}$$

A superposition of the two solutions in Eqs. (2.35a) and (2.35b) gives

$$\vartheta_\ell^{\mathrm{final}} = \vartheta_\ell^{(\mathrm{I})} + \vartheta_\ell^{(\mathrm{II})} = -\Delta t \left.\frac{\delta\phi^{(\mathrm{I})}}{\delta\eta}\right|_\ell + \tilde{\vartheta}_\ell^{(\mathrm{II})} - \Delta t \left.\frac{\delta\phi^{(\mathrm{II})}}{\delta\eta}\right|_\ell. \tag{2.36}$$

To satisfy the no-slip condition, the right-hand side of Eq. (2.36) is set to zero,

$$-\Delta t \left.\frac{\delta\phi^{(\mathrm{I})}}{\delta\eta}\right|_\ell + \tilde{\vartheta}_\ell^{(\mathrm{II})} - \Delta t \left.\frac{\delta\phi^{(\mathrm{II})}}{\delta\eta}\right|_\ell = 0. \tag{2.37}$$

Equation (2.37) is rearranged and discretized to yield

$$\Delta\phi_\ell^{(\mathrm{II})} - \Delta\eta_\ell \frac{\tilde{\vartheta}_\ell^{(\mathrm{II})}}{\Delta t} = -\Delta\phi_\ell^{(\mathrm{I})}. \tag{2.38}$$

where $\Delta\phi_\ell = \phi_{\ell+} - \phi_{\ell-}$ and $\Delta\eta_\ell$ is the distance across Γ between the two cell centers (see Fig. 2.11).

$\Delta\phi_\ell^{(\mathrm{II})}$ in Eq. (2.38) is the solution of the Poisson equation with $\tilde{\vartheta}_\ell^{(\mathrm{II})}$ ($\ell = 1,\ldots,N_c$) on Γ, and zero elsewhere. Using the Green's function, $G(\Gamma)$, for the Neumann problem (Hildebrand, 1976 and Proskurowski & Widlund, 1976), $\Delta\phi^{(\mathrm{II})}$ can be expressed in terms of $\tilde{\vartheta}^{(\mathrm{II})}$:

$$\Delta\phi^{(\mathrm{II})} = \int_\Gamma G(\Gamma)\tilde{\vartheta}^{(\mathrm{II})} d\Gamma,$$

or, in finite difference form:

$$\Delta\phi_\ell^{(\mathrm{II})} = \sum_{n=1}^{N_c} G_{\ell,n}\tilde{\vartheta}_n^{(\mathrm{II})}, \qquad \ell = 1,\ldots,N_c. \tag{2.39}$$

The discrete Green's functions $G_{\ell,n}$, $n = 1,\ldots,N_c$, is the Poisson solution, $\Delta\phi$, at location n on Γ if a value $\tilde{\vartheta} = 1$ is placed at location ℓ only, and zero elsewhere. The detailed procedure to calculate $G_{\ell,n}$ for all ℓ's is presented in Appendix C.

Substituting Eq. (2.39) into Eq. (2.38) yields a matrix equation:

$$\mathbf{C}\mathbf{r}^{(\mathrm{II})} = [\mathbf{G} + \mathbf{d}]\,\mathbf{r}^{(\mathrm{II})} = -\Delta\mathbf{\Phi}^{(\mathrm{I})}, \tag{2.40}$$

where:

- $\Delta\mathbf{\Phi}^{(\mathrm{I})}$ is the error vector of length N_c: $\Delta\phi_\ell^{(\mathrm{I})}$, $\ell = 1, \ldots, N_c$, calculated from the first pass;
- $\mathbf{r}^{(\mathrm{II})}$ is the desired solution vector $\tilde{\vartheta}_\ell^{(\mathrm{II})}/\Delta t$, $\ell = 1, \ldots, N_c$;
- $\mathbf{d}$ is an $N_c \times N_c$ diagonal matrix with elements $-\Delta\eta_\ell$, $\ell = 1, \ldots, N_c$;
- $\mathbf{G}$ is an $N_c \times N_c$ matrix, elements of which are the discrete Green's functions $G_{\ell,n}$, $\ell, n = 1, \ldots, N_c$.
  The combined $N_c \times N_c$ matrix $\mathbf{C} = \mathbf{G} + \mathbf{d}$ is called the *capacitance matrix.*

Since the capacitance matrix requires solving the Poisson equation N_c times, the computational cost of $\mathbf{C}$ is substantial with a large N_c. However, $\mathbf{C}$ only needs to be calculated and stored once because elements of $\mathbf{C}$ depend only on the geometry and mesh spacing of the domain.

2.7.4. Solution on a 3-D L-Shape Domain

In 3-D simulations, the computational cost to calculate $\mathbf{C}$ is greatly reduced by taking advantage of the Fourier transform method. The Poisson equation (2.24) is first Fourier transformed in the z-direction leading to a Helmholtz equation in the x-y plane,

$$\left(\frac{\delta^2}{\delta x^2} + \frac{\delta^2}{\delta y^2} - k_m'\right)\hat{\phi}_{i,j,m} = \hat{Q}_{i,j,m}, \tag{2.41}$$
$$i = 1, \ldots, N_x, \quad j = 1, \ldots, N_y, \quad m = 0, \ldots, \frac{N_z}{2},$$

where m is the Fourier wave number. The system now has a set of $N_z/2 + 1$ independent capacitance matrices, $\mathbf{C}_m$, each corresponding to one wave number. At each wave number m the formulation of $\mathbf{C}_m$ is that of a 2-D problem presented in §2.7.3. Each $\mathbf{C}_m$ is an $N_c \times N_c$ matrix with real elements. In a 2-D domain, the

capacitance matrix is always singular due to the Neumann boundary condition. In a 3-D domain, $\mathbf{C}_m$ is non-singular if $m \neq 0$. At the zeroeth wave number, $k'_m = 0$, the Helmholtz equation (2.41) becomes a 2-D Poisson equation, and $\mathbf{C}_0$ is a singular matrix.

Chapter 3
TWO-DIMENSIONAL SIMULATIONS

Although 3-D simulation of a turbulent flow over a backward-facing step is the focus of the current research, 2-D computations can provide some insight into the characteristics of the flow reattachment, and establish grid-selection guidelines for the 3-D simulations. The flow response to steady inlet velocity profiles are discussed in §3.1. The flow response to an inlet velocity profile with superimposed fluctuations are reported in §3.2. Studies of flow sensitivity to grid refinement are described in §3.3. The 2-D simulations were also used to study the effect of the convective boundary condition at the exit; the results of which are presented in §3.4. Finally, the mechanics of the unsteady reattachment are discussed in §3.5. In the 2-D simulations presented, the inflow boundary was located at the step, and an expansion ratio of 2.0 was used. The Reynolds number is based on the step height h and the maximum mean inlet velocity U_0. The boundary conditions were either no-slip (parabolic and channel inlet profiles) or no-stress (boundary layer inlet profile) at the top wall, and convective at the exit.

3.1. Two-Dimensional Simulations with Steady Inflow

The behavior of the reattachment length as a function of Reynolds number was established using a series of 2-D simulations. Both steady and unsteady flow responses are observed.

3.1.1. Low Reynolds Numbers: Steady Flow Responses

At low Reynolds numbers, an unperturbed inlet velocity profile results in a steady flow response. A series of simulations were conducted using flow conditions from Armaly *et al.* (1983): parabolic velocity profile at the inlet and expansion ratio $ER = 2.0$. The reattachment length, X_r, as a function of Reynolds number, is compared to the data of Armaly *et al.* (1983) in Fig. 3.1. (It should be noted that

Armaly *et al.* (1983) used a Reynolds number based on $2h$ and the averaged inlet velocity, $\frac{2}{3}U_0$ which corresponds to $\frac{4}{3}Re_h$. Their data was rescaled for this plot.)

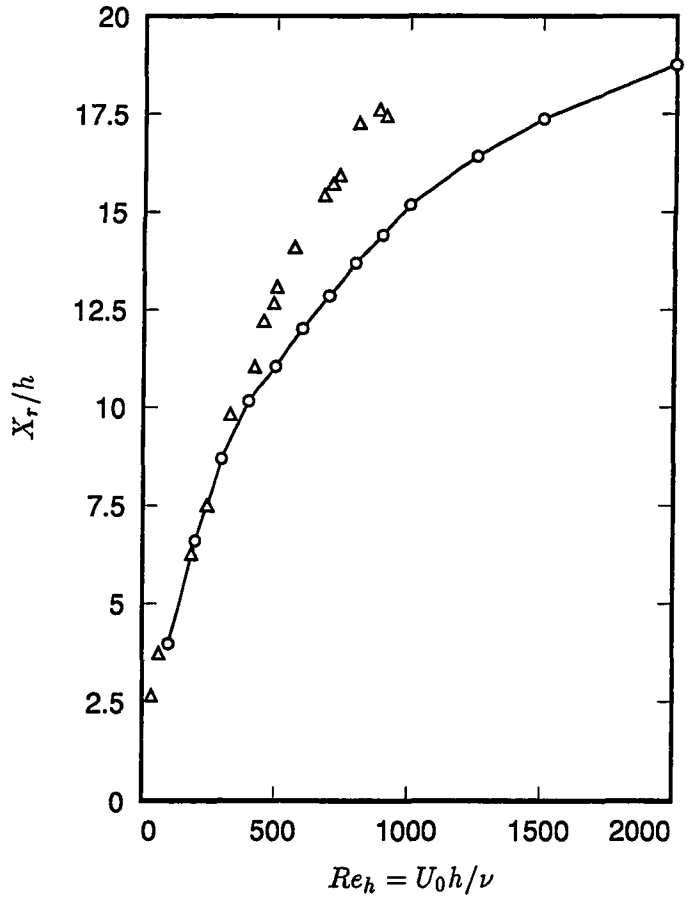

Figure 3.1. Reattachment length as a function of Reynolds number with laminar inlet flow: comparison between Armaly *et al.* (1983) and 2-D simulations. △ Armaly *et al.* (1983); o 2-D computation.

As expected the computational results are identical to those of Kim & Moin (1985). The calculated X_r's in Fig. 3.1 are in good agreement with experimental data only up to $Re_h \approx 400$. Beyond this point, the calculated reattachment lengths deviate from the experimental values. As in the study of Kim & Moin (1985),

varying the streamwise domain length, CFL number for time advancement, or grid spacing did not reduce this difference.

Typical streamlines of the steady flows are shown in Fig. 3.2. Table 3.1 lists computational parameters for all simulations with an inlet parabolic velocity profile.

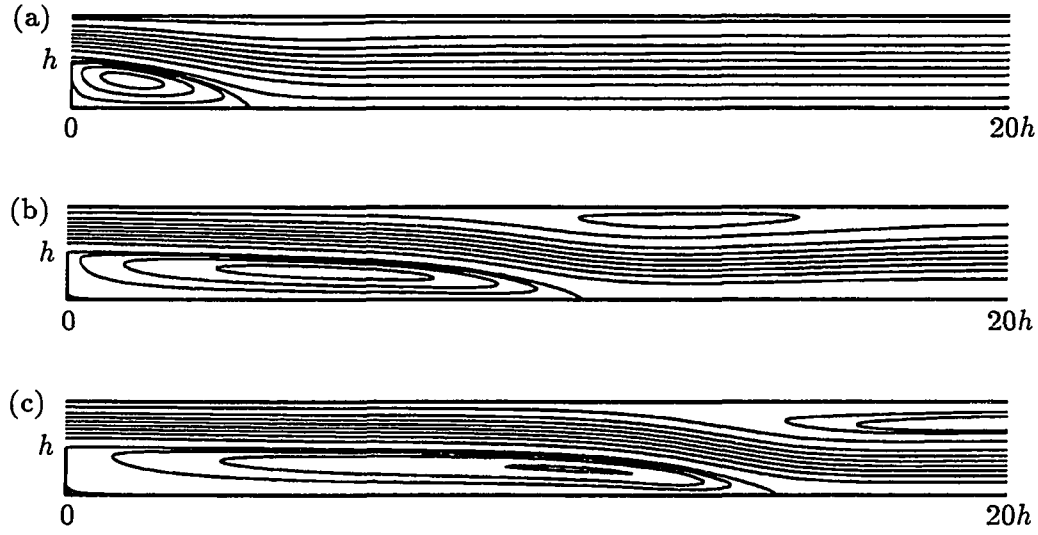

Figure 3.2. Streamline contours of steady backward-facing step flows, parabolic inlet profile. (a) $Re_h = 100$; (b) $Re_h = 500$; (c) $Re_h = 1000$.

At $Re_h \approx 300$, a separation bubble at the no-step wall is observed. This bubble grows in length and moves downstream as Re_h and the corresponding step-side reattachment length increase (Fig. 3.2(b) and 3.2(c)); this observation was also reported by Armaly *et al.* (1983) and Kim & Moin (1985). As the Reynolds number increases to about 1000, a small secondary vortex at the step corner becomes visible. These well known secondary corner bubbles are perhaps too small ($\approx 0.2h$) to measure and were not observed by Armaly *et al.* (1983).

Above $Re_h \approx 600$, the top wall separation bubble moves across the exit plane (Fig. 3.2(c)) creating reverse flow at the exit. Furthermore, as discussed in §2.6.2, the convective outflow boundary condition is not applicable near a separation bubble. Thus, the validity of the results in this region is questionable, particularly

Table 3.1. 2-D simulations at low Reynolds number with parabolic inlet profile

Case	Re_h	Grid	L_x	X_r
1	100	128 × 64	$20h$	$3.98h$
2	200	128 × 64	$20h$	$6.60h$
3	300	128 × 64	$20h$	$8.69h$
4	400	128 × 64	$20h$	$10.16h$
5	500	192 × 96	$20h$	$11.05h$
6	600	192 × 96	$20h$	$12.02h$
7	700	192 × 96	$20h$	$12.85h$
8	800	192 × 96	$20h$	$13.69h$
9	900	192 × 96	$20h$	$14.40h$
10	1000	256 × 128	$20h$	$15.18h$
11	1250	384 × 128	$20h$	$16.42h$
12	1500	400 × 128	$20h$	$17.37h$
13	2000	766 × 192	$30h$	$18.76h$

in cases where the reattachment location is only a few step heights from the exit ($Re_h > 1250$). Case 12 with $Re_h = 1500$ was recomputed with a longer streamwise domain ($L_x = 40h$). The resulting reattachment length was increased to $18.42h$. However, at $x/h = 40$, there is still a small amount of reverse flow very close to the top wall.

Another simulation at $Re_h = 1500$ was also conducted with an inlet section of $10h$ whereas the post-expansion length remains at $20h$. The reattachment length

in this case is $18.63h$ which indicates that the inlet section has some influence on the down stream development.

For comparison, 2-D simulations were carried out with the inlet mean velocity profile of fully-developed turbulent channel of Kim *et al.* (1987). This profile was a result of their channel flow simulation at $Re = 3300$ based on the channel half-height. Table 3.2 shows the parameters of these simulations. The dependency

Table 3.2. 2-D simulations at low Reynolds number with mean channel profile at inlet

Case	Re_h	Grid	L_x	X_r
1	300	128×64	$20h$	$7.38h$
2	600	192×96	$20h$	$10.05h$
3	900	192×96	$20h$	$11.60h$
4	1500	400×128	$20h$	$14.41h$

of X_r on Re_h is similar to that of parabolic profiles. However, at comparable Reynolds numbers, flows with a mean turbulent profile at inlet consistently possess shorter reattachment lengths than with the parabolic profile. On the other hand, the secondary corner vortex is larger ($0.54h$ for $Re_h = 1500$). Kaiktsis *et al.* (1991) also found that a fuller inlet profile results in a shorter reattachment length.

3.1.2. High Reynolds Numbers: Unsteady Flow Responses

When the Reynolds number is sufficiently high, the flow becomes unsteady and oscillatory even if the inlet velocity profile remains unperturbed. The critical Reynolds number, Re_c, at which the flow over a backward-facing step begins exhibiting this unsteady behavior depends on the inlet profile. Tests using both parabolic and fully-developed turbulent channel profiles (Kim *et al.*, 1987) show that a steeper velocity gradient at separation causes the flow to become oscillatory

at a lower Re_c. For the mean turbulent channel profile at the inlet, Re_c is found to be close to 2000, whereas the flow remains steady with a parabolic profile at this Reynolds number (Table 3.1).

The focus of this section is not to identify a specific Re_c for each profile, but to investigate the oscillatory nature of the flow once it becomes unsteady. The 2-D simulation conducted for this purpose was at $Re_h = 3000$ using a fully-developed turbulent channel profile at the inlet. The time history of the streamwise velocity component at a point near the bottom wall ($x/h = 5.0$, $y/h = 0.01$) for this case is shown in Fig. 3.3. A quasi-periodic response of the flow is clearly discernible with a period of approximately $T \approx 12h/U_0$.

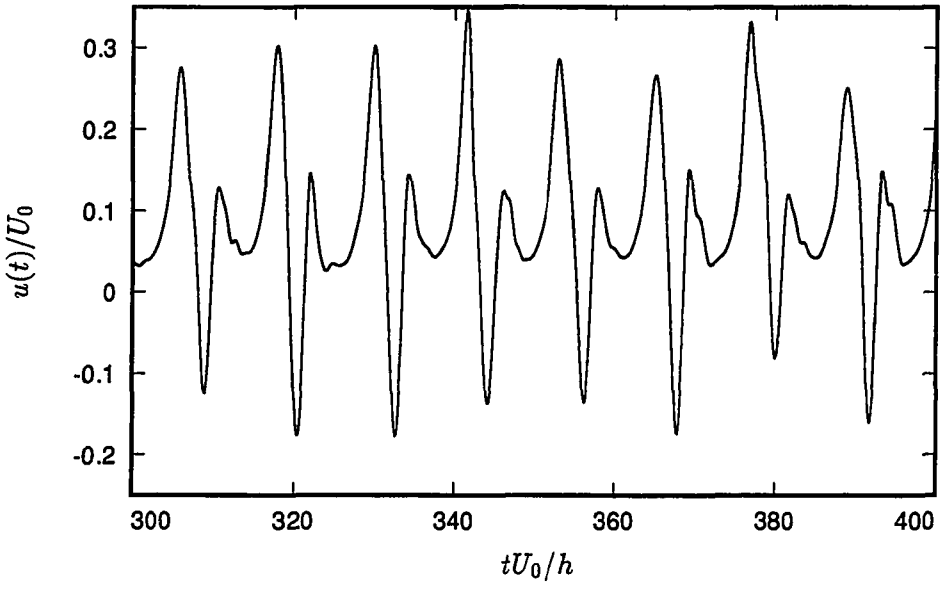

Figure 3.3. Time history of streamwise velocity component at $x/h = 5.0$, $y/h = 0.01$; $Re_h = 3000$, steady turbulent channel inlet profile.

However, the time oscillation of the flow response could be an artifact of insufficient spatial resolution. This is illustrated by simulations at $Re_h = 1500$ using two different grid resolutions: 128×32 and 400×128. With 400×128 computational cells, the flow at $Re_h = 1500$ has a steady response. When the grid is reduced to

128×32, the flow does exhibit an oscillatory behavior. This is shown in a time history plot of the streamwise velocity at $x/h = 5.0$, $y/h = 0.01$ in Fig. 3.4. The periodicity is not sharply defined, but a dominant frequency similar to that seen in Fig. 3.3 is discernible. Recent work by Gresho *et al.* (1993) have independently shown that insufficient resolution will result in an unsteady numerical solutions in backward-facing step simulations.

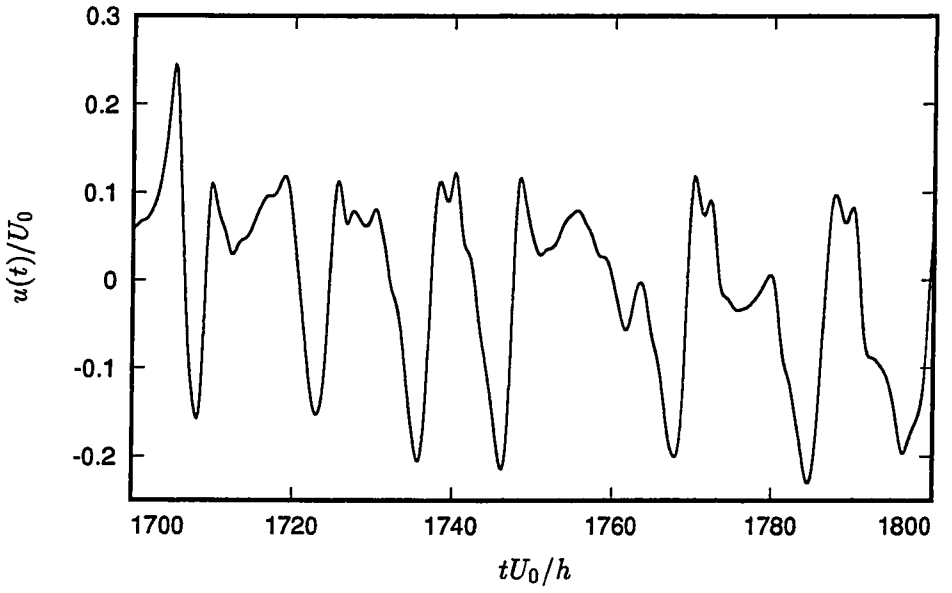

Figure 3.4. Time history of streamwise velocity component at $x/h = 5.0$, $y/h = 0.01$; $Re_h = 1500$, steady turbulent channel inlet profile with coarse grid (128×32).

To ensure that the oscillatory behavior in Fig. 3.3 was not induced by a coarse resolution, several simulations were performed for the case of $Re_h = 3000$ with increasing grid points in both directions. These simulations are tabulated in Table 3.3. Figure 3.5 compares the time history plots of the streamwise velocity at the same location for 320×128 and 640×192 grids. Although there are shifts in the numerical results among these simulations (possibly due to the presence of small superimposed chaotic behavior), the periodic (two-torus) behavior, especially the

Table 3.3. Sensitivity of oscillation to grid refinement: $Re_h = 3000$, steady turbulent channel inlet profile.

Case	Grid	$\Delta x/h$	$\Delta y_{\min}/h$
1	320 × 128	0.06250	0.006674
2	320 × 256	0.06250	0.003282
3	640 × 128	0.03125	0.006674
4	640 × 192	0.03125	0.004401

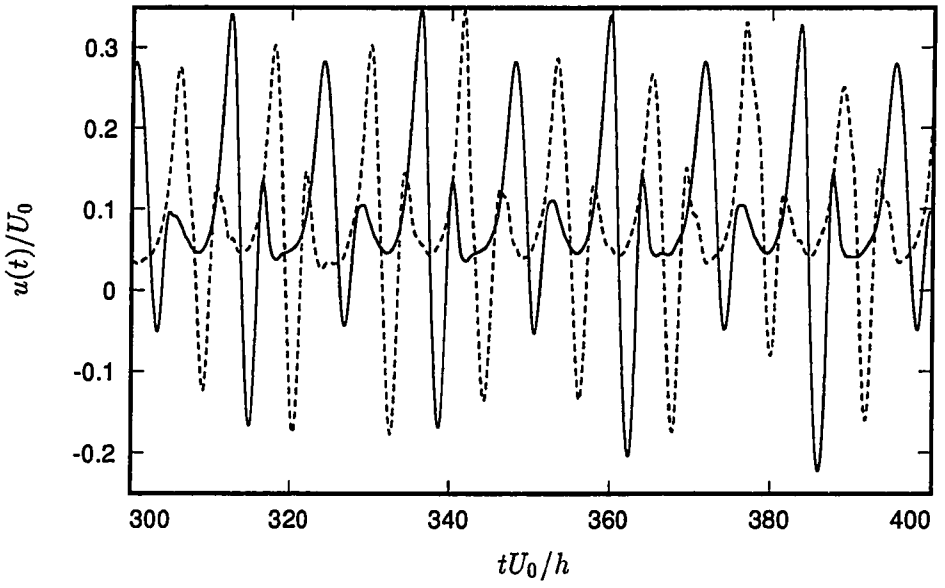

Figure 3.5. Time history of streamwise velocity component at $x/h = 5.0$, $y/h = 0.01$; $Re_h = 3000$, steady turbulent channel inlet profile. —— , 640 × 192; ---- 320 × 128.

frequency, is essentially unchanged implying that the unsteadiness is not a result of grid resolution. However, the slight increase of regularity in the higher resolution calculation may be an indication of periodic (or even fixed point) behavior with further refinements. Thus, additional grid refinements may prove to be instructive.

The quasi-periodic response is a result of vortex shedding at the separation point. The instantaneous streamline contours for the $Re_h = 3000$ case are shown in Fig. 3.6 illustrating the movement of the vortices, both at the bottom and at the top walls. The mechanics of this vortex shedding and how it affects the unsteady reattachment will be discussed in detail in §3.5.

Figure 3.6. Streamline contours, $Re_h = 3000$, steady turbulent channel inlet profile.

3.2. Two-Dimensional Simulations with Unsteady Inflow

In all 2-D simulations presented in §3.1, only an unperturbed mean velocity profile is prescribed at the inlet. The effects of inlet "turbulence" is now investigated by superimposing fluctuating components $u'(y,t)$ and $v'(y,t)$ onto the mean profile following the method outlined in §2.6.1. For this purpose, the fully-developed turbulent channel velocity profile of Kim *et al.* (1987) is used. The selected Reynolds number in this study is 1500 where the flow is known to be steady if there are no inlet fluctuations (§3.1.1). The simulation was conducted with a steady inflow until a steady state was reached; the computations were then continued with velocity fluctuations imposed at the inlet. The streamlines of the flow with steady and unsteady inlet profiles are compared in Fig. 3.7. In both cases the streamwise box length is $20h$. The mean reattachment length in the unsteady case is approximately $3.6h$ compared to $17.4h$ in the steady case.

Figure 3.8 shows the corresponding time history of the streamwise velocity component at point $x/h = 5.0$, $y/h = 0.01$. A quasi-periodic response is discernible which is similar to the response in the case with a steady inlet profile at high Reynolds number (Fig. 3.3). It is also interesting to note that, although the velocity

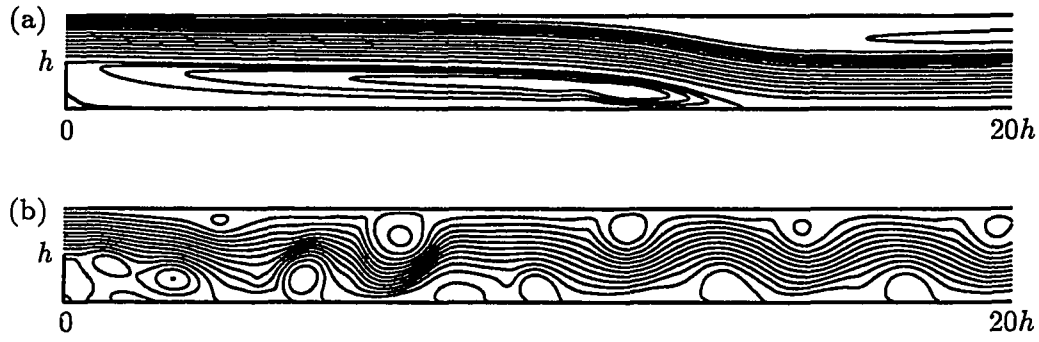

Figure 3.7. Streamline contours. $Re_h = 1500$, turbulent channel inlet profile. (a) Mean profile at inlet; (b) Mean profile with imposed fluctuations at inlet.

fluctuations at the inlet are generated from a prescribed broad-band energy spectrum, the flow appears to select the same frequency observed in the high Reynolds number case (Fig. 3.3). Further discussion of the flow oscillation frequencies will be presented in §3.5 and §5.7.1.

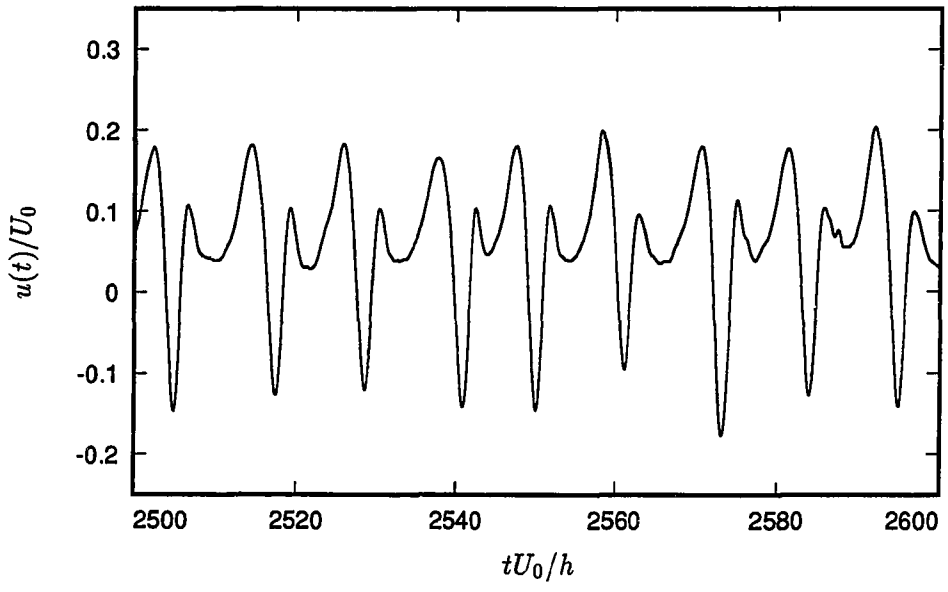

Figure 3.8. Time history of spanwise velocity component at $x/h = 5.0$, $y/h = 0.01$. $Re_h = 1500$, unsteady turbulent channel inlet profile.

3.3. Effect of Grid Refinement on Unsteady Flow Structures

The objective of the 2-D simulations in this section is to establish, for the range of Reynolds numbers considered, an acceptable grid spacing in the streamwise and vertical directions. The Reynolds number for this study was set at 4000, and the inlet velocity profile was that of a flat plate boundary layer (Spalart, 1988) with a relatively thin boundary layer thickness, $\delta = 0.20h$. In all of the following 2-D simulations, a no-stress boundary condition was applied at the top, and a grid clustering at the bottom wall. The simulations were performed with five different grid sizes. The five cases studied are summarized in Table 3.4 in which the grid 256×128 is the base case. All five simulations were started from an identical initial flow field and run through the same non-dimensional time period. The spanwise vorticity contours at one instant in time were obtained for all five cases and compared in Fig. 3.9.

Table 3.4. Grid refinement study: 2-D simulations at $Re_h = 4000$, steady boundary layer inlet profile.

Case	Grid	$\Delta x/h$	$\Delta y_{\min}/h$
1	256 × 128 †	0.0781	0.004506
2	256 × 256 †	0.0781	0.002241
3	512 × 128 †	0.0391	0.004506
4	512 × 256 †	0.0391	0.002241
5	576 × 256 ‡	0.0260	0.002241

† Streamwise domain $L_x = 20h$

‡ Streamwise domain $L_x = 15h$

It is clear from Fig. 3.9 that some improvement is observed when the number of vertical cells were doubled from 128 to 256 (the minimum $\Delta y/h$ at the wall changes from 0.0045 to 0.0022). However, doubling the resolution in the streamwise direction

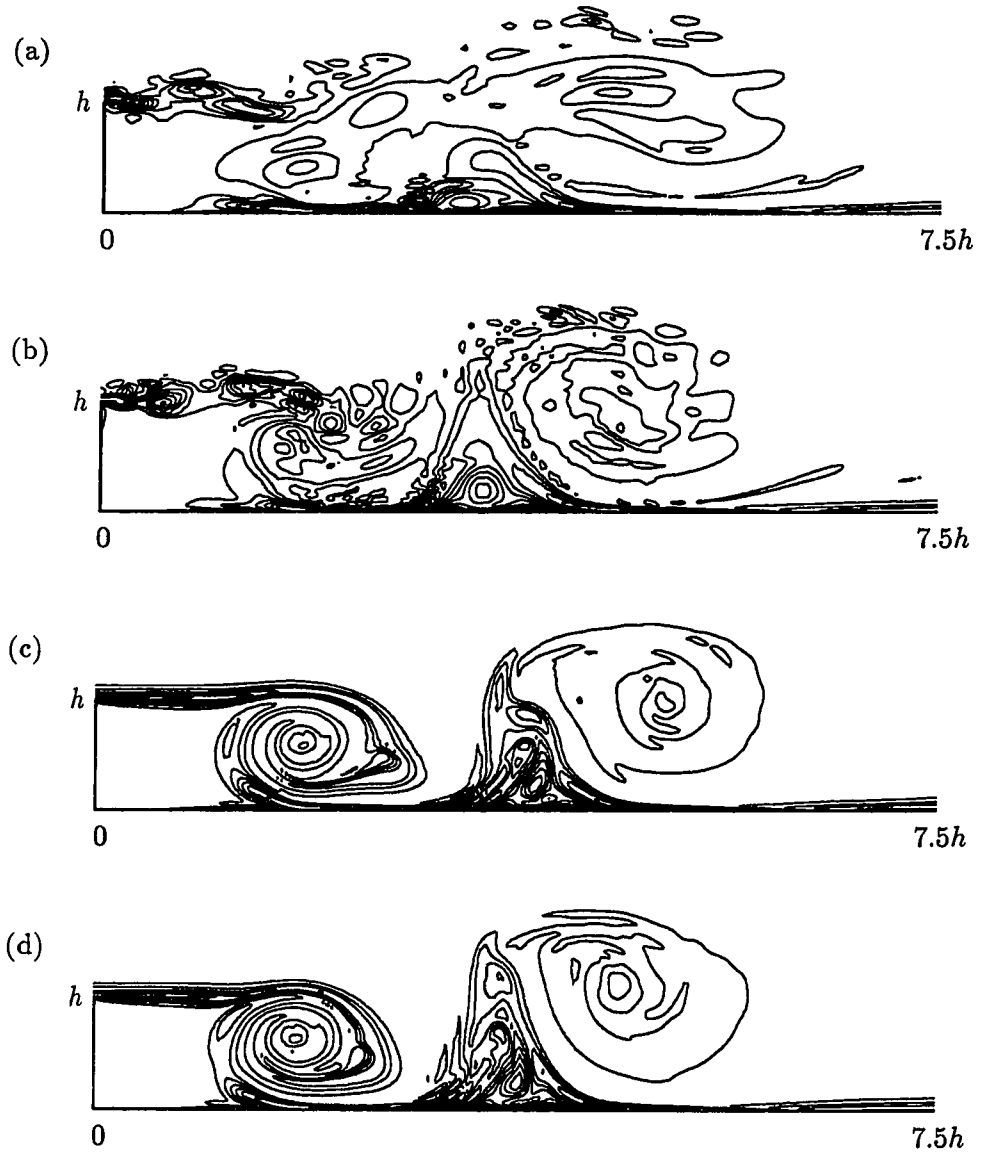

Figure 3.9. Grid refinement study: spanwise vorticity contours, steady boundary layer inlet profile, $Re_h = 4000$. (a) 256 × 128; (b) 256 × 256; (c) 512 × 128; (d) 512 × 256.

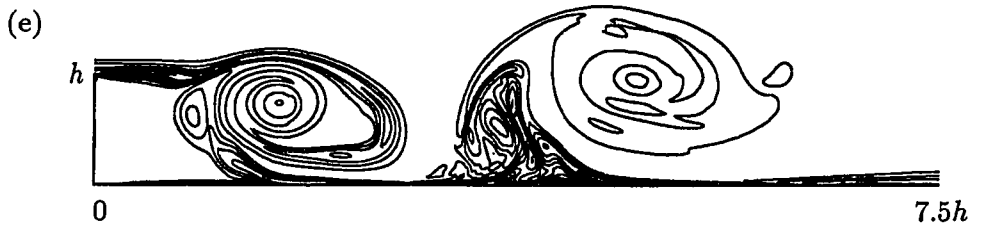

Figure 3.9. (Cont.) Grid refinement study: spanwise vorticity contours, steady boundary layer inlet profile, $Re_h = 4000$. (e) 576×256, $L_x = 15h$.

results in a substantial improvement (Fig. 3.9(c)). Fig. 3.9(d) shows the vorticity contours when the number of cells are doubled in both directions (512×256) from the base case; a further 33% reduction in the streamwise grid size only gives a modest change in the vorticity contours (Fig. 3.9(e)). Therefore, at $Re_h \approx 4000$, the recommended grid and domain sizes should follow the following guidelines: $\Delta x \leq 0.039h$ and $\Delta y_{\text{wall}} \leq 0.0022h$. These correspond to $\Delta x^+ \approx 8.5$ and $\Delta y^+_{\text{wall}} \approx 0.48$ using an inlet friction velocity of $u_{\tau 0} = 5.4 \times 10^{-2} U_0$ (Spalart, 1988). This is the basis for the preliminary grid selections for computations reported in Chapters 4 and 5.

3.4. Effect of Convective Boundary Condition

The convective boundary condition at the exit was discussed in §2.6.2. Pauley *et al.* (1988) documented the extent of the upstream influence of this boundary condition. In this section the effect of the downstream boundary condition on the flow structures is examined in the backward-facing step geometry. The base simulation is case 4 in Table 3.4 in which the streamwise domain length was $L_{x1} = 20h$ with the grid of 512×256. The domain length was then reduced to $L_{x2} = 15h$ in the second simulation but maintaining the same grid resolution; hence the number of cells in the second simulation was 384×256. The flow structures as well as numerical results near $x/h = 15$ are compared to their respective values in the base simulation.

The spanwise vorticity contours at the same instant for these two simulations are compared in Fig. 3.10. As previously reported by Pauley *et al.* (1988), the convective boundary condition does allow vortical structures to exit the shorter domain (Fig. 3.10(b)) smoothly with a slight distortion compared to the same location in the longer domain (Fig. 3.10(a)). Visual inspection of Fig. 3.10, however, does not convey accurately the extent of the region affected by the convective boundary condition. Using the results of the base case ($L_{x1} = 20h$) as a benchmark, the errors in velocity components, as the domain is shortened to $15h$, are plotted in Fig. 3.11. Three vertical locations are selected for the comparison: $y/h = 0.0079$, 0.9946, and 1.9013. Compared to the results from the base simulation, the error in u drops below 1% for $x/h < 13$ ($2h$ from the exit boundary). For the vertical component, large relative errors are observed up to $5h$ from the exit boundary. The error in v appears to be very large at many locations because the corresponding values of v in the base simulation are very close to zero. Nevertheless, the existing vortex structure in Fig. 3.10(b) remains unaffected since v is negligible in this region compared to u.

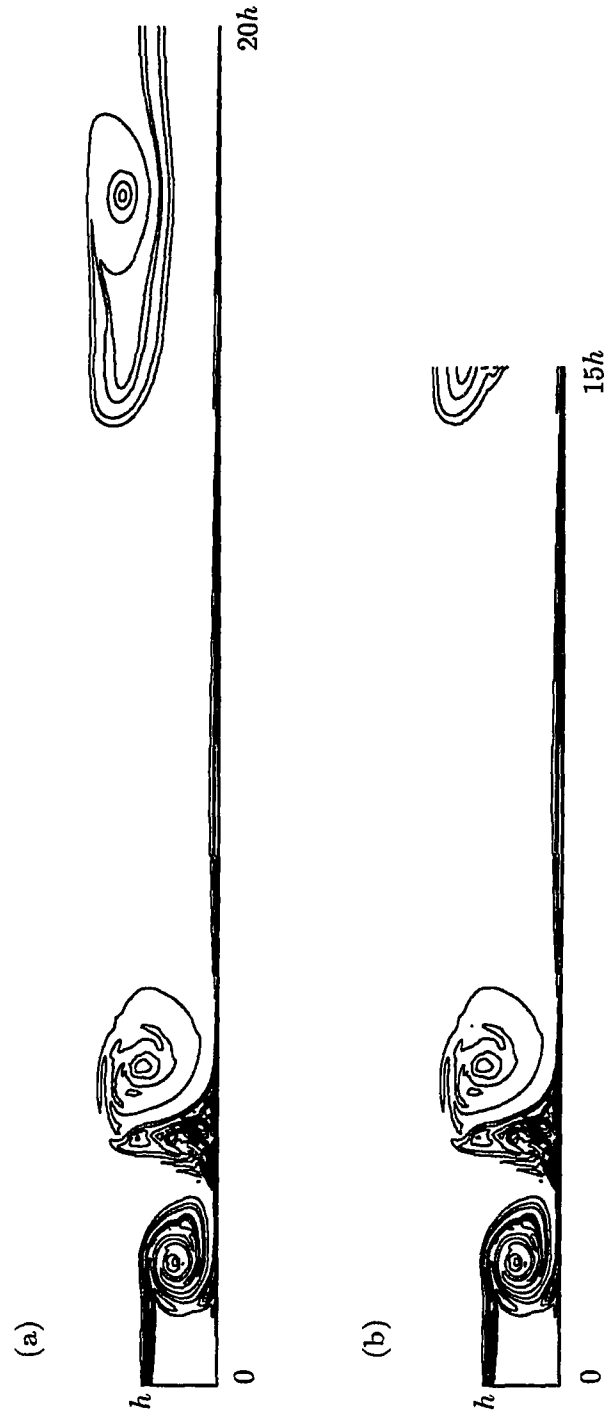

Figure 3.10. Effects of convective boundary condition: 2D spanwise vorticity contours, steady boundary layer inlet profile, $Re_h = 4000$. (a) $L_x = 20h$, grid: 512×256; (b) $L_x = 15h$, grid: 384×256.

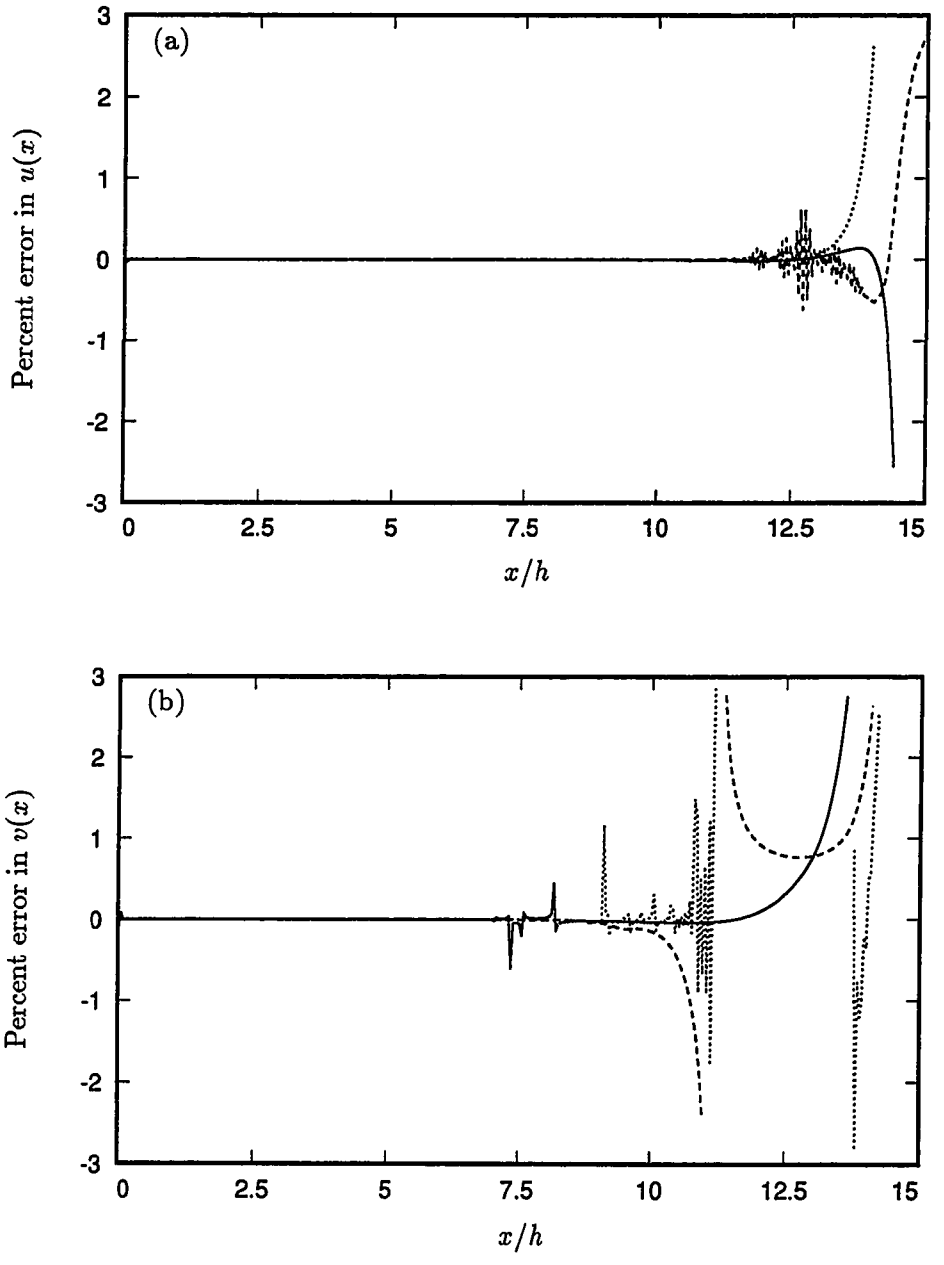

Figure 3.11. Error in velocities (in %) for $L_x = 15$ due to effect of convective outflow condition. (a) $u(x)$; (b) $v(x)$. —— $y/h = 0.0079$; ---- $y/h = 0.9946$; ····· $y/h = 1.9013$.

3.5. Mechanics of Unsteady Reattachment

The variation of the backward-facing step flow reattachment length as a function of Reynolds number was documented in details by Armaly *et al.* (1983). Figure 3.12 reproduces their X_r measurements for Re_h up to 5500. From this curve, the laminar regime is identified as $Re_h < 900$ where the reattachment length increases monotonically up to $17.5h$. The reattachment length drops sharply in the transitional regime ($900 < Re_h < 4900$), and remains relatively constant at approximately $8h$ for $Re_h > 5000$.

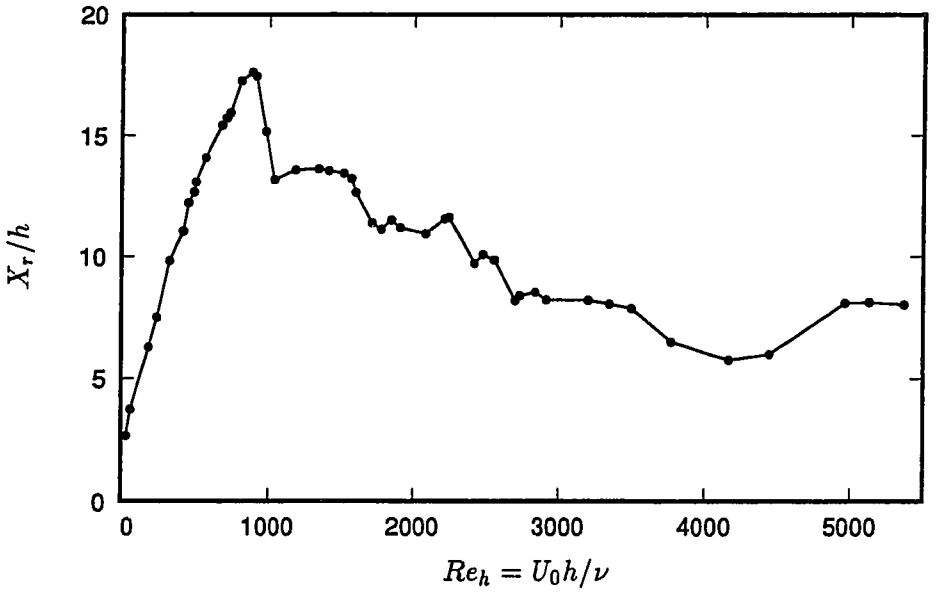

Figure 3.12. Reattachment length as a function of Reynolds number, Armaly *et al.* (1983).

Although the shorter reattachment length in the turbulent regime compared to those observed at lower Reynolds numbers has been confirmed by many studies, e.g., Durst & Tropea (1981), there has not been an explanation for this phenomenon. Some insight into the unsteady reattachment process can be gained by examining the quasi-periodic shedding of the vortices at the step in a two-dimensional unsteady

flow. Figure 3.13 presents a time sequence of spanwise vorticity shed from the step corner. For this case, a steady mean boundary layer velocity profile (Spalart, 1988) is imposed at the inlet at a Reynolds number of 4000. In Fig. 3.13(a), a clockwise vortex (negative vorticity) is shedding at the step and grows as it travels downstream. As this first vortex interacts with the lower wall, the no-slip wall condition induces a counter-clockwise rotating vortex (positive vorticity) traveling upstream (Fig. 3.13b); this vortex encounters a second negative vortex that is shed from the step. The interaction between the two counter-rotating vortices shown in Fig. 3.13(c) induces strong motion toward the step corner. This induced motion periodically brings down the free shear layer and is probably responsible for the shortening of the mean reattachment location.

The *unsteady* 2-D backward-facing step flows studied are: (a) $Re_h = 4000$, steady inlet boundary layer profile (hereinafter referred to as BL4000s), (b) $Re_h = 3000$, steady inlet turbulent channel profile (CH3000s), and (c) $Re_h = 1500$, unsteady inlet channel profile (CH1500u). All of these flows exhibit a quasi-periodic oscillatory behavior. Furthermore, the surprisingly similar period of oscillation of all flows suggests a correspondence to a natural frequency independent of the inlet profile. This same period of oscillation is also observed in the low Reynolds number flow with coarse grid (CH1500c). Power spectra are computed for the streamwise velocity signal at point $x/h = 5.0$, $y/h = 0.01$ in all four cases and shown in Fig. 3.14. Distinct frequencies are presented in the form of Strouhal number based on U_0 and h, $St = fh/U_0$, in Table 3.5. The most energetic frequency (fundamental) in all cases is at $St \approx 0.08$, corresponding to an oscillation period of $12.5U_0/h$. The five lowest frequencies in BL4000s are within 5% of those in CH3000s. When the inlet fluctuations are prescribed, only the two lowest peaks are distinctly visible (Fig. 3.14(c)). The two lowest frequencies are again excited in the simulation with coarse grid (Fig. 3.14(d)), but some additional modes have also been excited. Other points in the flow field also present similar results. Comparison of the dominant frequencies in Table 3.5 indicates that these are the natural frequencies of the flow,

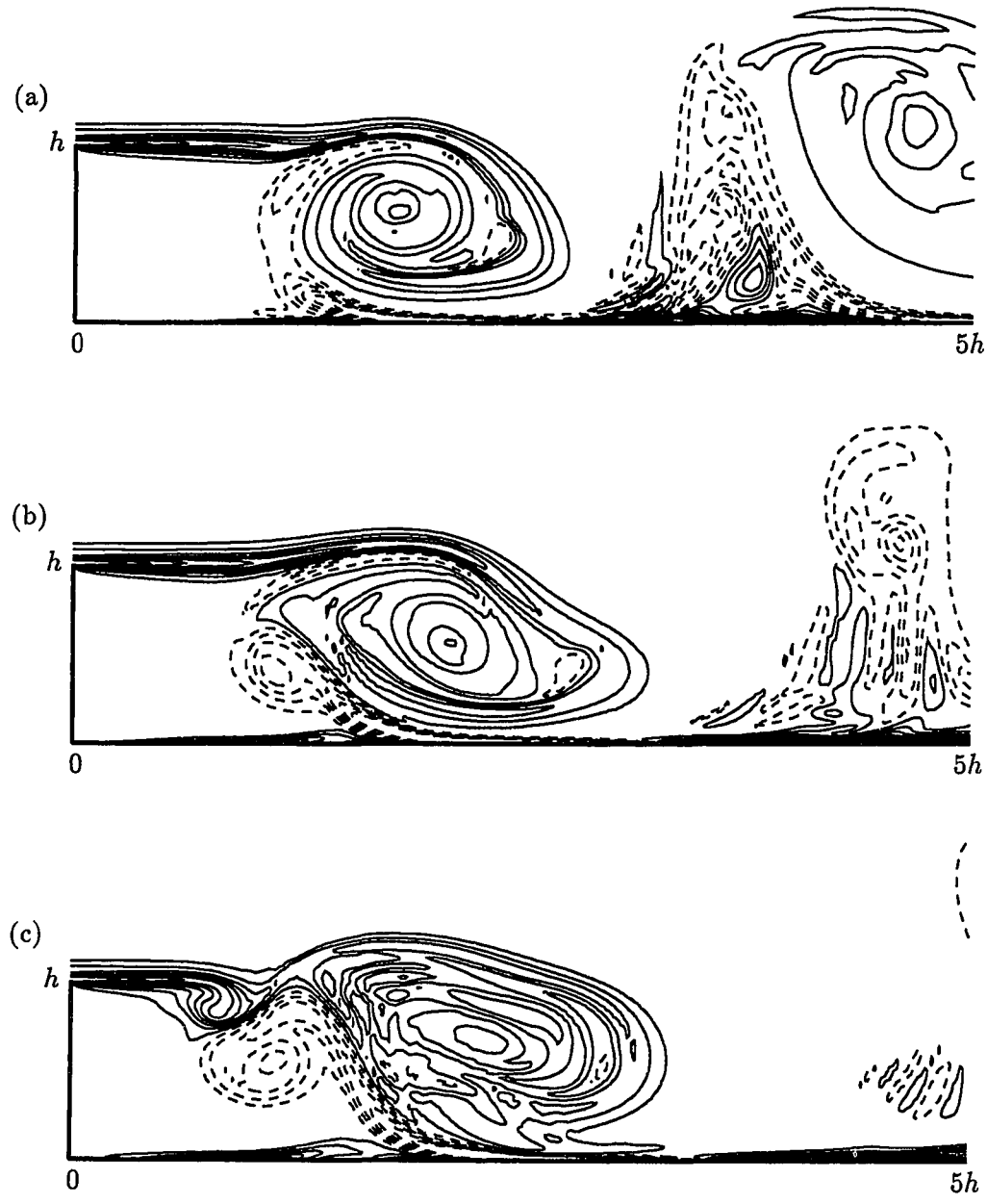

Figure 3.13. Spanwise unsteady vortex shedding, steady inlet boundary layer profile, $Re_h = 4000$. (a) $t = 20h/U_0$; (b) $t = 21h/U_0$; (c) $t = 22h/U_0$. —— negative vorticity; ---- positive vorticity.

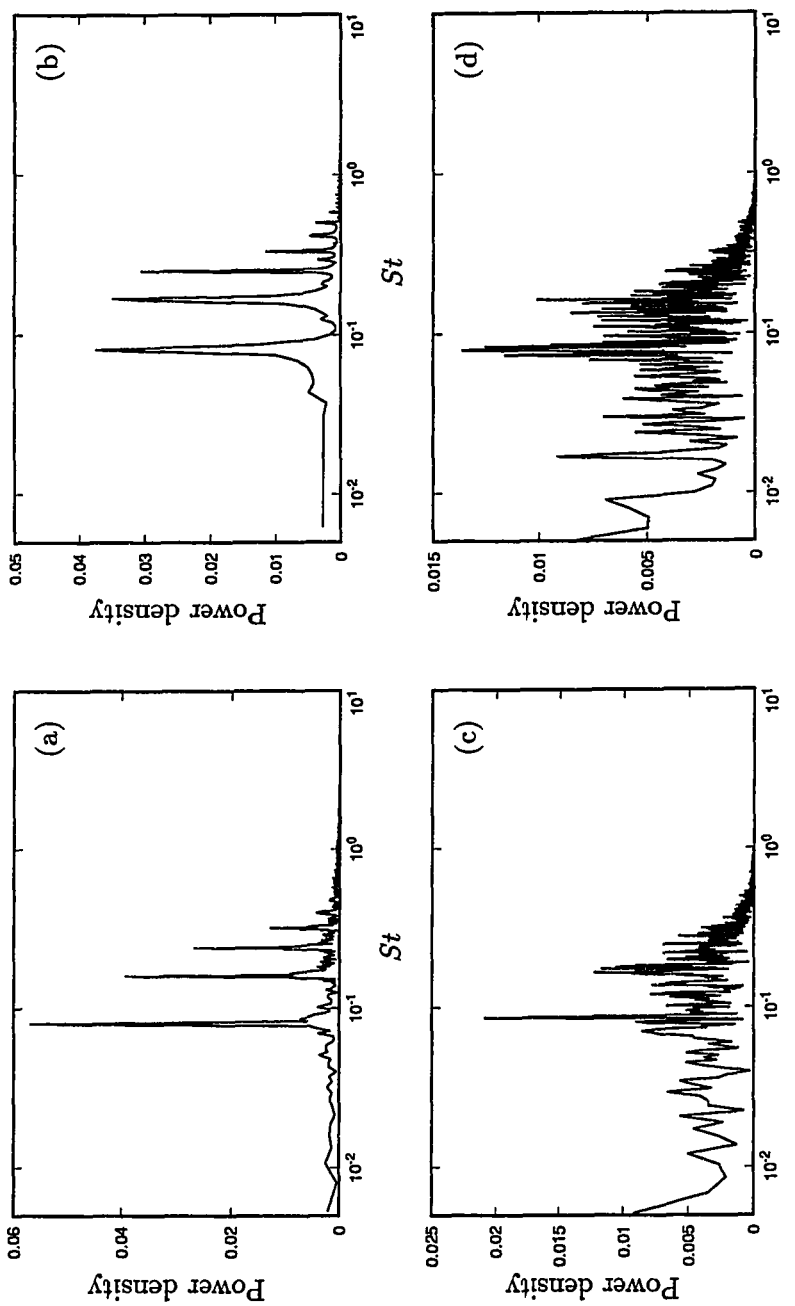

Figure 3.14. Power spectra at $x/h = 5.0$, $y/h = 0.01$; $St = fh/U_0$. (a) Steady turbulent boundary layer profile at inlet, $Re_h = 4000$; (b) Steady turbulent channel profile at inlet, $Re_h = 3000$; (c) Unsteady turbulent channel profile at inlet, $Re_h = 1500$; (d) Steady turbulent channel profile at inlet, $Re_h = 1500$, course resolution.

and they are not directly associated with Reynolds numbers or inlet profiles. Introducing turbulent fluctuations at the inlet appears to mask the higher modes, but reduces the power density amplitude. The study also establishes that the oscillation frequency is independent of the inlet segment frequency of the turbulent fluctuations (see §2.6.1) in CH1500t.

Table 3.5. Comparison of frequencies with different inlet conditions

	BL4000s	CH3000s	CH1500t	CH1500c
$f_1 h/U_0$	0.080	0.081	0.086	0.079
$f_2 h/U_0$	0.160	0.168	0.165	0.162
$f_3 h/U_0$	0.240	0.250	-	-
$f_4 h/U_0$	0.320	0.330	-	-
$f_5 h/U_0$	0.400	0.412	-	-

Although the dominant frequencies appear to be independent of Reynolds number and inlet boundary condition, the flow characteristics do depend on these parameters. For example, the time-average statistics show that the mean reattachment lengths are different for different inlet profiles. Case BL4000s has a mean reattachment length of $2.68h$, whereas $X_r = 3.62h$ in case CH3000s. This is consistent with earlier findings showing a decrease in reattachment length with an increase in velocity gradient at separation.

Chapter 4
PRELIMINARY 3-D SIMULATIONS

A series of preliminary 3-D simulations were conducted with various grid resolutions, domain lengths, Reynolds numbers, inlet velocity profiles and expansion ratios. The parameters for the final simulation were selected based on the information gained from the preliminary studies. This chapter describes the preliminary simulations and their results.

The preliminary simulations were carried out only long enough to obtain a reasonably steady mean velocity profile (approximately two "flow through" times). These simulations are divided into two categories according to the inlet velocity profiles – fully developed turbulent channel or turbulent boundary layer profile. It should be noted that in the course of the simulations, several modifications of the computer program were incorporated to accomplish the desired change in parameters; e.g., the inclusion of the inlet section prior to the step. Therefore, the grouping of the simulations into these two categories here is for convenience only, and the simulations presented are not necessarily in chronological order. Simulations with turbulent channel and boundary layer velocity profiles are described in §§4.1 and 4.2, respectively. Section 4.3 summarizes what has been learned from the preliminary simulations.

4.1. Simulations With Fully Developed Turbulent Channel Profile

The fully developed channel velocity profile from Kim *et al.* (1987) (hereinafter referred to as KKM) was used in category CH. Table 4.1 summarizes the simulations in this category. In Table 4.1, ER is the expansion ratio and X_r is the reattachment length. CH1 did not have an inlet section whereas the remaining cases had an entry section length of $10h$. The spanwise and post-expansion lengths for all cases are $4h$ and $20h$, respectively. In addition, CH4 had a refined mesh at the step.

Table 4.1. Simulations with fully developed turbulent channel inflow

Case	Re_h	ER	Inlet section	Post-expansion	X_r/h
CH1	5000	2.00	-	$256 \times 80 \times 64$ †	6.5
CH2	5000	2.00	$128 \times 40 \times 64$ †	$256 \times 80 \times 64$ †	9.2
CH3	6600	2.00	$128 \times 40 \times 64$ †	$256 \times 80 \times 64$ †	9.7
CH4	6600	2.00	$128 \times 40 \times 64$ ‡	$256 \times 80 \times 64$ ‡	9.3

† Refined mesh at the bottom and top walls.

‡ Refined mesh at the bottom and top walls and at the step.

The lower wall skin friction coefficient, C_f, is selected for comparison among the CH cases and is shown in Fig. 4.1. First, the effect of the entry section can be

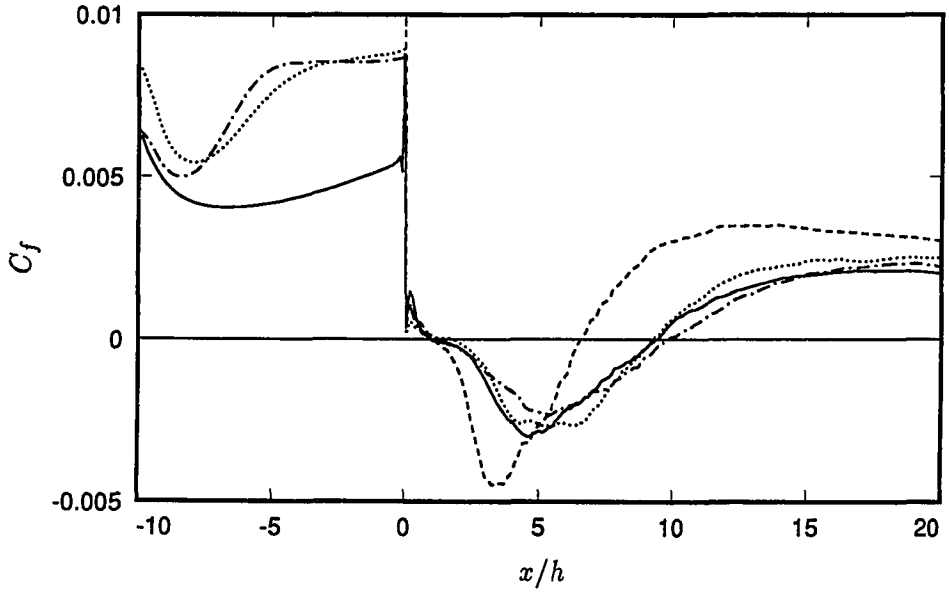

Figure 4.1. Step-wall skin-friction coefficient, channel profile at inlet. ---- case CH1; ····· case CH2; —·— case CH3; —— case CH4. $x/h = 0$ is the step location.

evaluated by comparing CH1 and CH2. Without the entry section, CH1 shows a very high $|C_f|$ in the recirculation region (the peak negative C_f is $\approx 4.5 \times 10^{-3}$; this is about 4 times larger than values reported by previous experiments, e.g. Westphal *et al.*, 1984 and Adams *et al.*, 1984). This can be explained in part by inadequate turbulence characteristics due to the random phase generation at the step (see §2.6.1). For cases with a leading section, the flow quickly loses its prescribed statistical characteristics within a few grid points from the inlet; and the wall shear stress in the leading section reduces to that of a laminar flow before recovering. The magnitude of the recirculation C_f in CH1 is comparable to the 2-D simulation results in Chapter 3 where no turbulent fluctuations are imposed. With the addition of the development section in CH2, the flow develops its structure as it approaches the separation; the wall skin friction returns to the level imposed at the inlet (the dotted line in Fig. 4.1). The result is a reduction in the peak backflow C_f by approximately 40%. The recirculation zone, measured by the reattachment length X_r, is also expanded from $6.5h$ to $9.2h$.

The peak negative C_f in CH2, however, remains high compared to earlier experimental results. It was conjectured at this point that this high C_f peak was a result of the incorrect application of $Re_h = 5000$ to the KKM velocity profile. The KKM profile is of a channel flow with $Re = 3300$ based on the *channel half-height*; thus for the expansion ratio $ER = 2$ considered here, the correct step-height Reynolds number should be $Re_h = 6600$. The result is a higher C_f value at the inlet for the same velocity profile (KKM: $C_f = 6.04 \times 10^{-3}$; CH1 and CH2: $C_f = 7.97 \times 10^{-3}$). Therefore CH3 was conducted with $Re_h = 6600$ to provide the correct inlet C_f. Nevertheless, a comparison of the C_f plots shows that the skin friction is the same in the recirculation zone for both CH2 and CH3 as the flow develops near the separation.

Since a no-slip top wall was used in all CH simulations, the mean flow through the inlet channel was expected to be symmetrical. However, in CH2 and CH3, C_f symmetry was not observed between the bottom and top walls ($y = h$ and $2h$) in

the development channel, a likely result of an uneven mesh distribution between the two walls. This was the reason for a fourth simulation, CH4, where a fine mesh was distributed at all horizontal walls. An improvement in the skin friction in the inlet section can be seen by the solid line in Fig. 4.1. Nevertheless, corrections in the inlet C_f and vertical mesh refinement have no significant impact on the skin friction after the expansion.

In all three cases with an entry section, the C_f plots show a sharp spike at the separation ($x/h = 0$) which is a singular point in the back-step computations. Simulations in §4.2 and in Chapter 5 indicate that this is due to an insufficient streamwise grid refinement near the step.

Another quantity of interest is the mean streamwise velocity profile, U, in the recovery region. Plotted in Fig. 4.2 are the velocities at $x/h = 19.0$ for all four cases in Table 4.1, normalized by the local shear velocity u_τ. The near-wall profiles of all

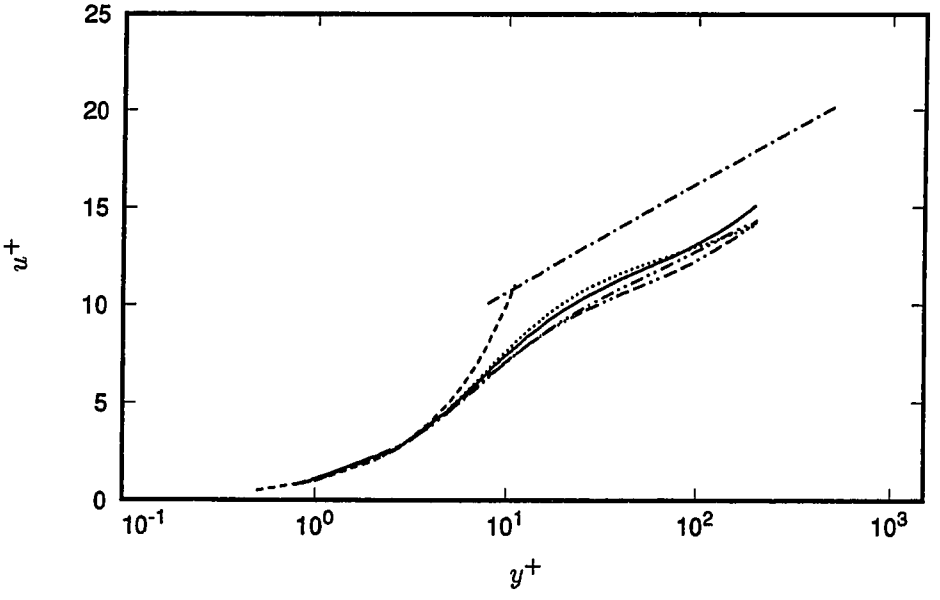

Figure 4.2. Mean streamwise velocity profiles in wall coordinates at $x/h = 19.0$, channel profile at inlet. ---- $u^+ = y^+$; —·— $u^+ = \frac{1}{0.41}\log y^+ + 5.0$; ····· case CH1; —·— case CH2; –·– case CH3; —— case CH4.

CH cases are well below the universal log-law, $u^+ = \frac{1}{\kappa}\log y^+ + C$, where $\kappa = 0.41$ and $C = 5.0$. All profiles appear to have the correct slope, $1/\kappa$, but a lower value of the intercept ($C < 3$). Similar to the C_f plots, this behavior in the recovery region is not significantly affected by the different conditions among the four CH cases.

4.2. Simulations With Turbulent Boundary Layer Profile

In the second category, BL, the inlet velocity profile is that of a turbulent boundary layer (Spalart, 1988). The BL simulations are listed in Table 4.2. Not listed in

Table 4.2. Simulations with turbulent boundary layer inflow

Case	Re_h	ER	Grid	δ/h	X_r/h
BL1	4000	2.00	$512 \times 128 \times 64$ †	0.20	7.44
BL2	4000	2.00	$512 \times 128 \times 128$ †	0.20	7.52
BL3	4000	1.54	$512 \times 160 \times 64$ †	0.20	6.74
BL4	5000	1.33	$512 \times 160 \times 64$ †	1.00	7.30
BL5	5100	1.20	$480 \times 128 \times 32$ ‡ *	1.20	6.89

† Refined mesh at the bottom wall.

‡ Refined mesh at the step and bottom wall.

* Inlet section: $160 \times 78 \times 32$, post-expansion section: $320 \times 128 \times 32$

Table 4.2 is the final simulation, BL6, which will be analyzed in detail in Chapter 5. The nomenclature in Table 4.2 is the same as Table 4.1 with the addition of δ, the inlet boundary layer thickness (δ_{99}). All cases had spanwise and post-expansion lengths of $4h$ and $20h$, respectively. Only BL5 had an inlet section of $10h$. The first two cases, BL1 and BL2, in this category investigated the effect of resolution in the spanwise direction; BL3 and BL4 provided different expansion ratios and inlet

boundary layer thicknesses; case BL5 had an entry section and the same flow condition as that of the final simulation, but with lower resolution. All BL simulations except BL5 were conducted before an algorithm was developed for the inclusion of an entry section. Thus the backflow $|C_f|$ is expected to be high as in cases CH1 and CH2 of §4.1. Furthermore, as in CH1 and CH2, Spalart's (1988) profile was not correctly applied in conjunction with the Reynolds number Re_h and boundary layer thickness δ for BL1 through BL4. In the first four BL cases, Spalart's (1988) profile with $Re_{\delta^*} = 500$ was used, where δ^* is the displacement thickness. The correct Reynolds number corresponding to this profile and $\delta/h = 0.2$ is approximately $Re_h = 13500$. Another profile with $Re_{\delta^*} = 1000$ was applied to BL5 and the final simulation, BL6. Only in BL5 and BL6 were the parameters Re_h and δ/h selected to correctly match Spalart's (1988) profile. Despite these deficiencies, useful information was learned from the BL simulations. The bottom-wall skin friction and the mean streamwise velocity profiles are again used to compare the results of the BL preliminary simulations in Figs. 4.3 and 4.4.

The only difference between BL1 and BL2 is the spanwise resolution; $\Delta z^+ = 12$ in BL1 and $\Delta z^+ = 6$ in BL2 based on the inlet u_τ. The dashed and dotted lines in Fig. 4.3 indicate that, in the recirculation region, there is no change in the skin friction by doubling the spanwise resolution from 64 to 128. It was also initially believed that the spanwise resolution might have been responsible for the deviation from the standard log-law of U in the recovery region. However, the near-wall profiles do not appear to be affected by the change in resolution (the dotted and chain-dot-dot lines in Fig. 4.4). The calculated reattachment length also varies less than 1.5%.

Not presented in Table 4.2 is a repeat of case BL1 (referred to as BL1x) with a modified exit boundary condition. As discussed in §2.6.2, the convective outflow condition can be applied with an instantaneous convective speed U_c if the global mass conservation is preserved. This method would result in a fluctuation of the total mass flow rate. Case BL1x was used as a test of this modified boundary

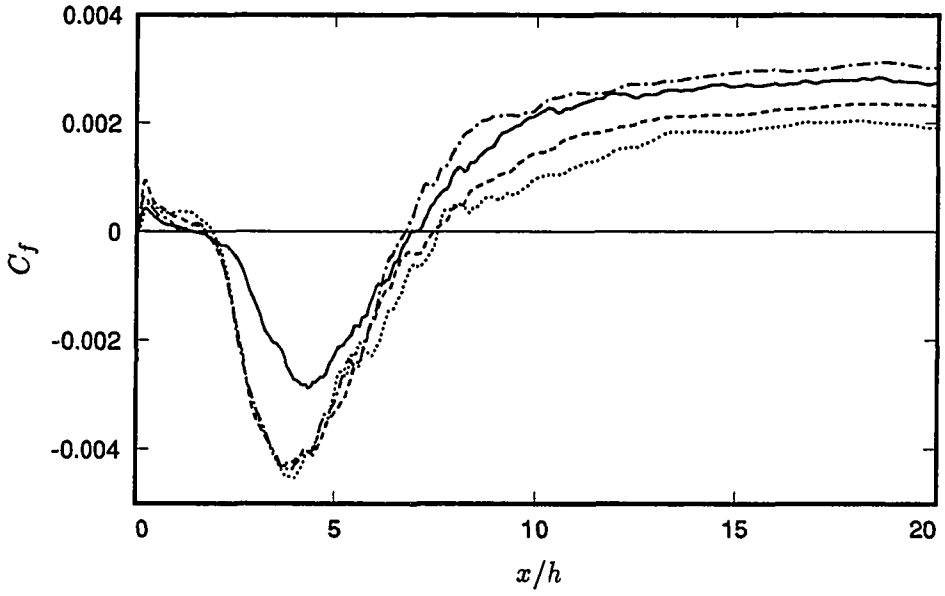

Figure 4.3. Step-wall skin-friction coefficient, boundary layer profile at inlet. ---- case BL1; ····· case BL2; —·— case BL3; —— case BL5.

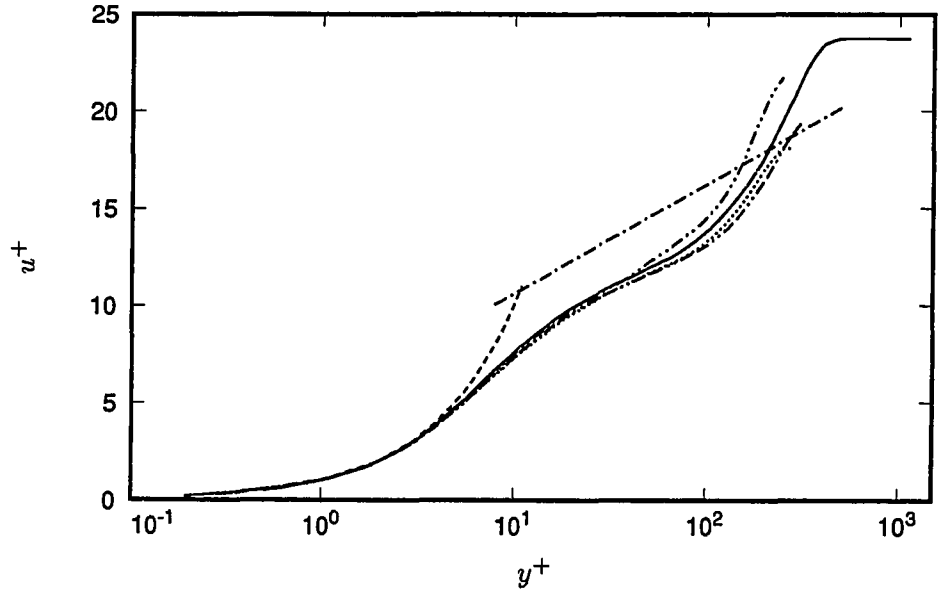

Figure 4.4. Mean streamwise velocity profiles in wall coordinates at $x/h = 19.0$, boundary layer profile at inlet. ---- $u^+ = y^+$; —·— $u^+ = \frac{1}{0.41}\log y^+ + 5.0$; ····· case BL1; —·— case BL2; —·— case BL3; —— case BL5.

condition. The simulation shows that the mass flow fluctuation is less that 2% of the mean flow; and there is negligible change in the statistical results as compared to BL1 with a constant U_c (<0.1%).

In BL3, the expansion ratio was reduced to 1.54 from 2.0 in BL1 and BL2 by extending the top boundary. All other parameters remained the same as of BL1. Again, neither the bottom-wall C_f, nor the near-wall U/u_τ in the recovery region is significantly affected by the difference in ER. However, the reattachment length, X_r, is reduced from $7.44h$ in BL1 to $6.74h$ in BL3. This concurs with previous experimental studies (Kuehn, 1980) stipulating that, for the low Reynolds number range considered, X_r decreases with decreasing ER.

Asides from the above observations, the BL simulations also test the applicability of the no-stress boundary condition at the top wall. Plots of the turbulence intensity $\sqrt{\overline{u'^2}}$ near the exit ($x/h = 19.0$) are presented in Fig. 4.5. In BL1 and

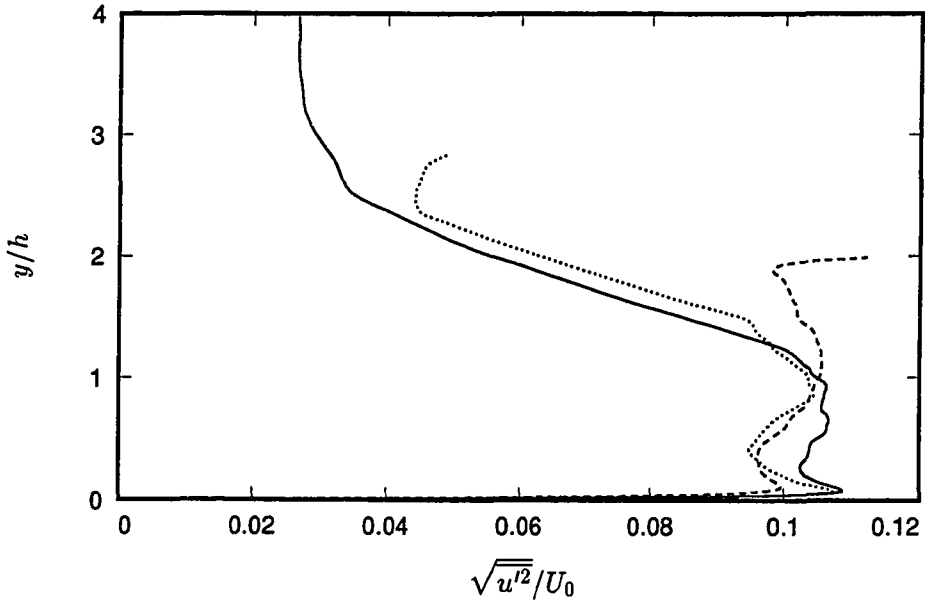

Figure 4.5. Effect of no-stress wall on streamwise turbulence intensity ($\sqrt{\overline{u'^2}}/U_0$) at $x/h = 19.0$. ---- $ER = 2$ (BL1); ····· $ER = 1.54$ (BL3); —— $ER = 1.33$ (BL4).

BL3, the turbulence intensity decreases toward the outer edge of the free shear layer, but increases again near the top wall. The unphysical behavior of $\sqrt{u'^2}$ near the no-stress upper wall in BL1 and BL3 indicates that the width of the free shear layer has spread to the no-stress boundary. The no-stress boundary condition (see §2.6) appears to be a reasonable approximation for cases with sufficiently low expansion ratio where the upper boundary does not interfere with the flow near the step wall. Case BL4 was thus conducted with a further reduced expansion ratio ($ER = 1.33$) by raising the domain height to $L_y/h = 4$. At $y/h > 3.5$, the no-stress boundary appears sufficiently far from the free shear layer (Fig. 4.5) to allow the turbulence intensity to monotonically decrease to nearly a constant value. The Reynolds number and inlet boundary layer thickness were also altered in BL4.

Finally, case BL5 was conducted as the first coordinated effort between numerical simulations and the concurrent experiment by Jovic & Driver (1994) using the same flow condition. The flow parameters for BL5 (Table 4.2) were selected to satisfy constraints in both experimental apparatus and computational resources. Spalart's (1988) profile with $Re_{\delta^*} = 1000$ was used in this simulation. A relatively coarse grid in all three directions were employed. Unlike previous simulations, BL5 was carried out to more than five "flow through" times. Selected results of BL5 will be compared to the final simulation, BL6, in Chapter 5, which had identical initial conditions but with higher resolution.

4.3. Conclusions From The Preliminary 3-D Simulations

In summary, the preliminary simulations CH and BL led to the following observations:

(a) The turbulent inflow conditions, with random phase generation, imposed at the step result in a large skin friction coefficient in the recirculation region. An entry section is thus essential for the development of turbulence prior to the step. The addition of the entry section also increases the computed reattachment length.

(b) The near-wall mean velocity profile in the recovery region falls below the universal log-law. This behavior is not a result of resolution, boundary or initial conditions.

(c) Despite the inclusion of the inlet section, the backflow $|C_f|$ remains high compared to previous experimental results.

(d) The vertical grid refinement is necessary at the step ($y = h$). This is essential for the correct development of the near-wall turbulence in the entry section.

(e) The spanwise resolution of 64 cells ($\Delta z^+ \approx 12$ based on the inlet u_τ) appears to be sufficient for the Reynolds numbers considered. Doubling the spanwise grid points did not improve the first order statistics, e.g. U, C_f.

(f) There is no change in statistical results if an instantaneous convective velocity profile is used in the convective outflow condition.

(g) For the Reynolds number range considered, the reattachment length decreases with decreasing expansion ratio which is in agreement with a conclusion by Kuehn (1980).

(h) To apply the no-stress condition at the top wall, the expansion ratio must be sufficiently low ($ER < 1.33$) such that the upper boundary does not interfere with the turbulent free shear layer.

Chapter 5
THREE-DIMENSIONAL SIMULATION – RESULTS

This chapter discusses the results of the main three-dimensional simulation with an inlet turbulent boundary layer profile, referred to as BL6. BL6 is the key simulation in this work and is central to all flow analyses presented in this report. The flow conditions of BL6 are the same as BL5 (see §4.2) but with higher grid resolution in all three directions. Table 5.1 compares the conditions of BL5 and BL6.

Table 5.1. 3-D simulations at $Re_h = 5100$

Case	Re_h	ER	Grid	δ/h	L_i/h	X_r/h
BL5	5100	1.20	$480 \times 128 \times 32$	1.20	$10h$	6.89
BL6	5100	1.20	$768 \times 192 \times 64$	1.20	$10h$	6.28

These conditions were selected to match, as closely as possible, those of a concurrent experiment by Jovic & Driver (1994) at NASA Ames Research Center (hereinafter referred to as "JD" experiment). Long time statistical averages were obtained for both BL5 and BL6 and compared with JD data. Although this chapter focuses on the analyses of the BL6 results, selected statistical quantities are also compared with BL5 to present the effect of grid resolution.

The selection of parameters for BL6, e.g., entry section, expansion ratio, boundary layer thickness, etc., is discussed in §5.1. Sections 5.2 and 5.3 describes the performance of the computer program and the statistics calculations, respectively. The configuration of the JD experiment is also described briefly in §5.4. Section 5.5 discusses the energy spectra and two-point correlations. In §5.6, the instantaneous velocity fields and oscillatory behavior of the flow are presented. Statistical results are compared with the JD experiment and discussed in §5.7 which includes: reattachment length (§5.7.1), coefficient of friction (§5.7.2), pressure distribution

(§5.7.3), velocity profiles (§5.7.4), and turbulence intensities (§5.7.5). Section 5.8 presents the budgets of the momentum equations. Finally, the Reynolds stress and turbulent kinetic energy budgets are presented in §5.9.

5.1. Flow Parameters for Computations

The flow conditions and parameters were selected based on information learned from the preliminary 2-D and 3-D simulations (Chapters 3 and 4). Also taken into consideration were the limitations of computational resources, and experimental constraints in velocity and skin friction measurements at low Reynolds numbers. Discussed below are the flow conditions selected for both BL6 and JD experiment.

5.1.1. Inlet Velocity Profiles

The mean inlet velocity profile for case BL6 was obtained from Spalart's (1988) boundary layer simulation at $Re_\theta = 670$ ($Re_{\delta^*} = 1000$), where θ and δ^* are the momentum and displacement thicknesses, respectively. For this particular profile, the boundary layer thickness is $\delta \approx 6.1\delta^*$ (Spalart, 1988). The boundary layer thickness here is δ_{99}, and was selected to be $1.2h$. This was also the δ_{99} used in the JD experiment. Thus, the step-height Reynolds number corresponding to this profile is

$$Re_h = Re_{\delta^*} \left(\frac{\delta}{\delta^*}\right) \left(\frac{h}{\delta}\right) \approx 5100.$$

The inlet fluctuations were generated such that, after long time averaging, the Reynolds stress components of the Spalart's (1988) profile are recovered (see §2.6.1). The turbulence intensity and Reynolds shear stress profiles at the inlet ($x/h = -10$) after an averaging time $\Delta T_{\text{ave}} \approx 109h/U_0$ are compared to the target profiles in Fig. 5.1.

5.1.2. Computational Domain and Grid Spacing

An inlet section length of $10h$ was selected for BL6. According to the method validation discussed in §2.6.1, the inlet section should ideally be approximately

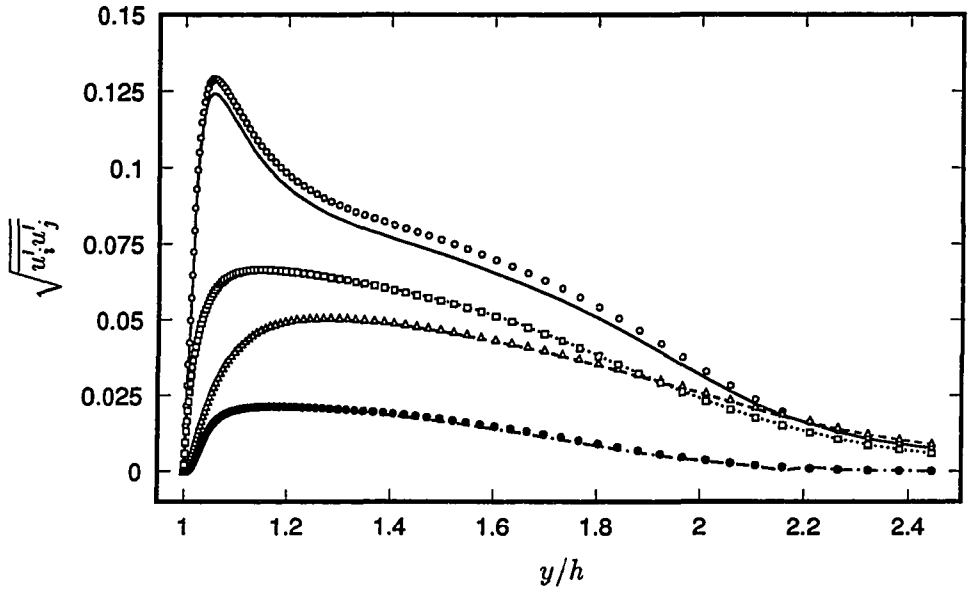

Figure 5.1. Inlet turbulence intensity and Reynolds shear stress profiles, normalized to mean free-stream velocity U_0. o target $\sqrt{\overline{u'^2}}$; —— calculated $\sqrt{\overline{u'^2}}$; △ target $\sqrt{\overline{v'^2}}$; ---- calculated $\sqrt{\overline{v'^2}}$; □ target $\sqrt{\overline{w'^2}}$; ····· calculated $\sqrt{\overline{w'^2}}$; • target $-\overline{u'v'} \times 10$; —·— calculated $-\overline{u'v'} \times 10$.

$20h$. However, with the computer resource restrictions, $10h$ was the affordable length of the development section. This section is $\frac{1}{3}$ of the total domain length. The numerical results show that, after an adjustment period, the inlet velocity profile and the friction coefficient are recovered in a distance $\approx 7h$ from the inlet boundary. Figure 5.2 compares the velocity profiles at $x/h = -10$, $x/h = -7.5$, and at $x/h = -3$. The streamwise distribution of the friction coefficient in the development section is shown in Fig. 5.3. The rapid departure from the inlet C_f value (4.8×10^{-3}) is due to unphysical random phase distributions (see §2.6.1.2). Note also in Fig. 5.3 that, compared to the C_f data in §4.1, the high resolution in BL6 greatly reduces the sharp spike in C_f near the singular point ($x/h = 0$).

The post-expansion channel length is $20h$. The number of grid points selected in the section behind the step was 512. Thus including the development section,

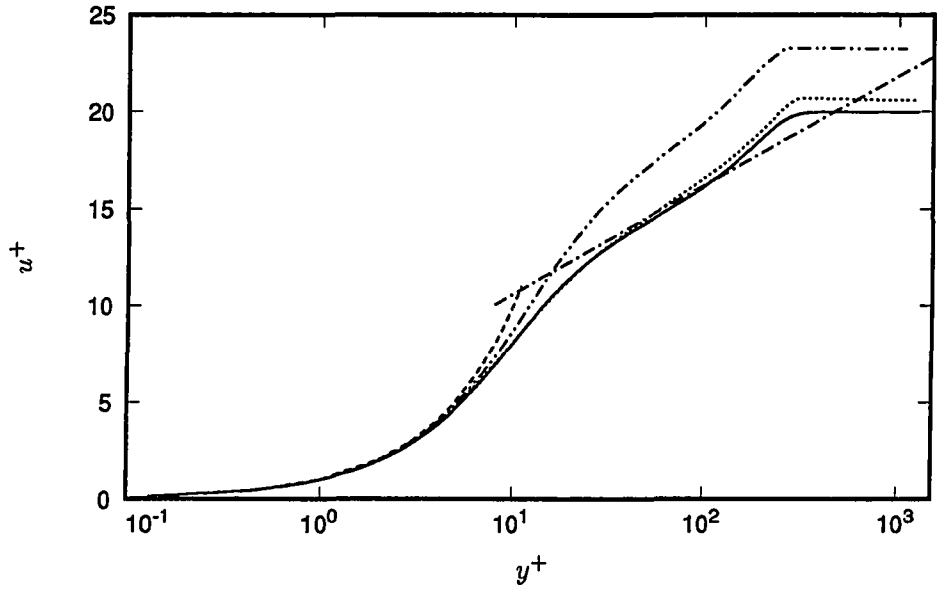

Figure 5.2. Near-wall velocity profiles in entry section. ---- $u^+ = y^+$; —·— $u^+ = \frac{1}{0.41}\log(y^+) + 5.0$; —— $x/h = -10$ (inlet); —··— $x/h = -7.5$; ····· , $x/h = -3$.

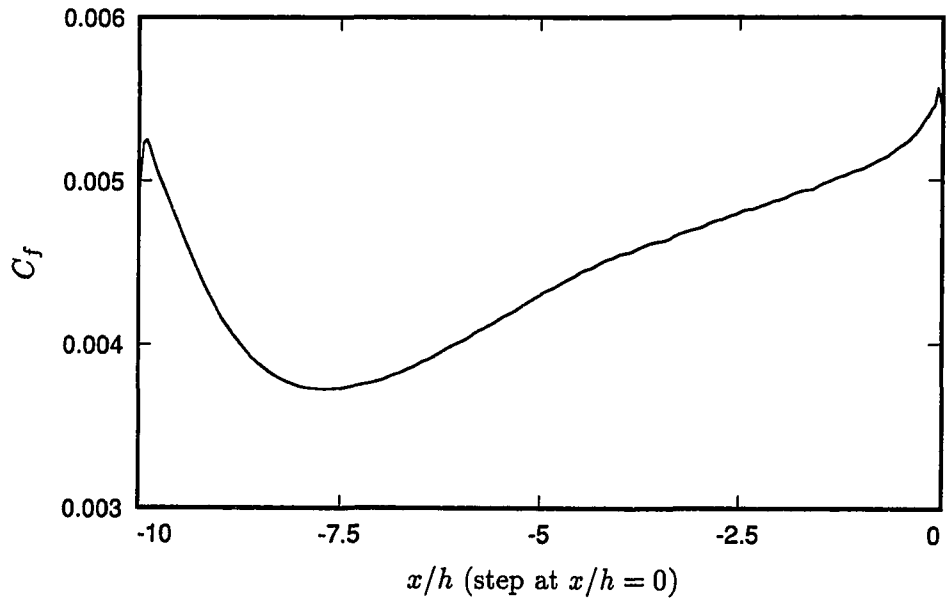

Figure 5.3. Coefficient of friction in entry section, target $C_f = 4.8 \times 10^{-3}$.

768 computational cells were selected for the x-direction. Based on the inlet wall shear velocity $u_{\tau 0} = 4.9 \times 10^{-2} U_0$, where U_0 is the mean inlet free stream velocity, the grid spacing in the streamwise direction is $\Delta x^+ \approx 10$ in wall units.

In the vertical direction, an expansion ratio of 1.20 was chosen which corresponds to the domain height $L_y/h = 6$. A non-uniform mesh distribution was used with fine grid spacing near the lower wall and at the location of the step (see Appendix A). The spacing at these two locations is $\Delta y^+_{\min} \approx 0.3$; and the maximum grid spacing is at the no-stress wall ($y = L_y$), $\Delta y^+_{\max} \approx 31$; both are normalized by the inlet shear velocity $u_{\tau 0}$. The total number of computational cells in the vertical direction is 192, of which 70 are placed within the step ($y < h$).

In the spanwise direction, the size of the computational box is $L_z/h = 4$ with 64 cells. This gives a spanwise grid spacing $\Delta z^+ \approx 15$ in wall units (normalized by $u_{\tau 0}$ at the inlet). Kim *et al.*'s (1987) direct simulations of channel flow were performed with $\Delta z^+ \approx 7$. However, to improve the spanwise resolution in this study, an increase in number of computational cells or a reduction in L_z is required, neither of which was feasible. As discussed below, even a dimension of $4h$ in the z-direction is inadequate to assure uncorrelated turbulent fluctuations at a separation of $L_z/2$. Thus, it would be highly desirable to increase the number of grid points in the z-direction by at least a factor of 2.

The total number of grid points used in this study was 8,290,304.

5.2. Performance of Computer Program

The computer program was first run on the CRAY Y-MP, and later on the CRAY C-90 at NASA Ames Research Center. On the CRAY C-90, approximately 450 time steps were taken in each 4-hour batch job. The velocity and pressure fields were saved at the end of each batch job and used as the restart fields for the next run. Although the CFL limit for the third-order Runge-Kutta scheme is $\sqrt{3}$, $CFL = 1.15$ was selected for BL6. In the early batch runs, the time step, Δt, was allowed to vary according to this CFL limit, and fluctuated around $0.002h/U_0$. In later runs

when the flow has approached statistical equilibrium and instantaneous motions were recorded for animation purposes, the time step was fixed at $\Delta t = 0.0018h/U_0$.

The program required approximately 13 mega-words of memory. Each time step used 22 CPU seconds (CRAY C-90), about 10 seconds of which was devoted to solving the Poisson equation. The efficiency rating of the program was approximately 450 mega-flops on the CRAY C-90. The size of the velocity and pressure fields saved at the conclusion of each batch job is approximately 364 mega-bytes.

5.3. Statistical Calculations

Statistical quantities are averaged over the spanwise direction and time. On a staggered grid, the pressure is defined at the cell center whereas velocities are at the cell surfaces. However, all variables are interpolated to the cell centers for statistical calculations. Statistical data are sampled at equal time intervals, $\Delta t_s = 0.018h/U_0$, apart, or every 10 time steps.

The total simulation time for BL6 is $t_{\text{end}} = 382h/U_0$. The initial time, $t_s = 273h/U_0$, or approximately 11 "flow-through" times, was discarded to allow for the passage of initial transients. The "flow-through" time here is defined as the convection time through the post-expansion section of $20h$ at the mean convective speed, $U_c \approx 0.8U_0$. The necessity of using a large initial transient period is due to the large residence time of fluid particles in the recirculation zone. The statistical data set accumulated over the remaining time, $\Delta T_{\text{ave}} = t_{\text{end}} - t_s = 109h/U_0$, was carefully examined to determine the convergence of turbulence statistics. The convergence is monitored by the relative magnitude of the Navier-Stokes equations residues and the Reynolds-stress equations residues.

The residues are the unsteady terms of the mean Navier-Stokes and Reynolds-stress equations, denoted respectively by e_i and e_{ij}:

$$e_i = \left| \frac{\partial U_i}{\partial t} \right|; \qquad e_{ij} = \left| \frac{\partial \overline{u_i' u_j'}}{\partial t} \right|.$$

The budget of the mean normal momentum equation is shown in Figs. 5.4 where a negligible residue is evident. The residue of the streamwise momentum equation is also negligible. The budget of the normal momentum equation was found to be most sensitive to the statistical sample used.

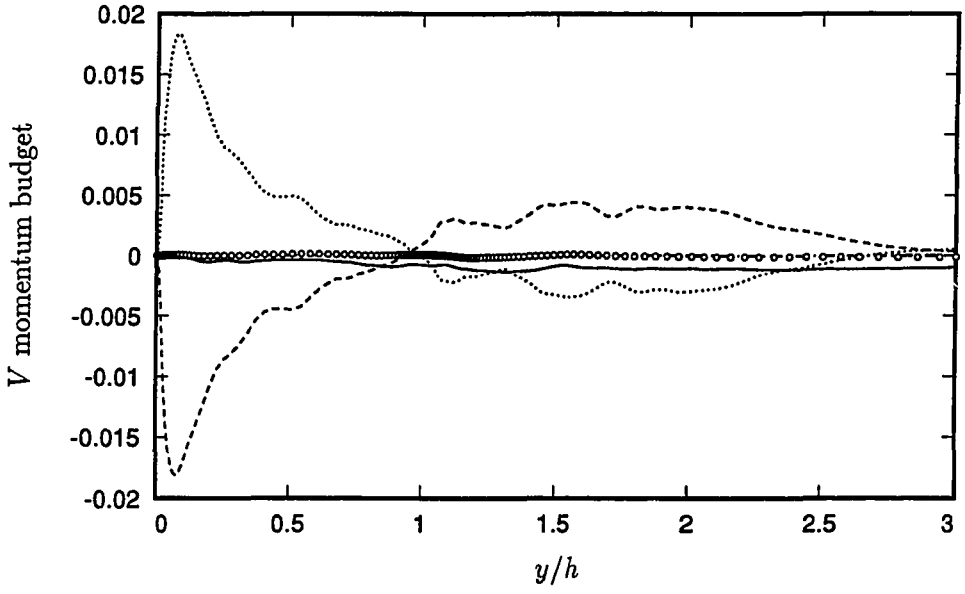

Figure 5.4. Vertical momentum budget at $x/h = 18.0$, $\Delta T_{\text{ave}} = 109h/U_0$. —— convection term; ---- Reynolds stress term; —·— viscous term; ····· pressure gradient term; o balance of terms, e_2. Terms are normalized by U_0^2/h.

Figure 5.5 shows the $\overline{v'v'}$ budget at $x/h = 18.0$, eventhough a good balance of the equation was achieved after $\Delta T_{\text{ave}} = 109h/U_0$, large scale fluctuations still persist in three terms (turbulence transport, velocity pressure-gradient, and convection terms). The fluctuations are observed only in the free shear layer region ($y^+ > 50$). These fluctuations are seen in all budgets, but are most pronounced in the $\overline{v'v'}$ budget near the domain exit (Fig. 5.5). One possible cause of these fluctuations is the limited number of samples as the start time of statistical calculations was

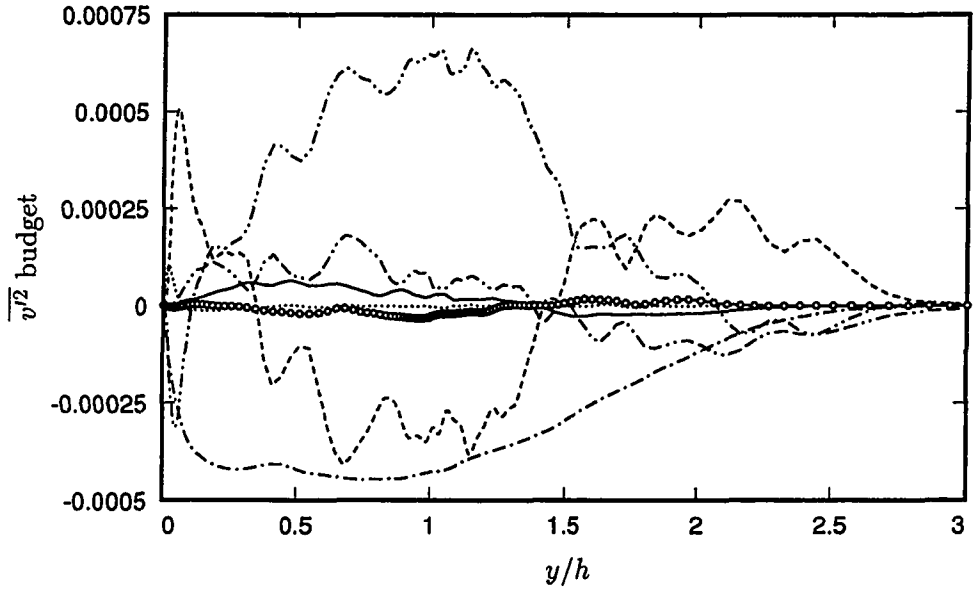

Figure 5.5. Vertical Reynolds-stress budgets at $x/h = 18.0$, $\Delta T_{\text{ave}} = 109h/U_0$. ——·— convection; —— production; ---- turbulence transport; ····· viscous diffusion; —·— viscous dissipation; —··— velocity pressure-gradient; o balance of terms, e_{22}. Terms are normalized by U_0^3/h.

delayed to $t_s = 273h/U_0$. However, the reduction in the magnitude of fluctuations was proven to be very slow with increasing averaging time.

Both the residues of the equations and fluctuations decrease, albeit extremely slowly, as more samples are added to the ensemble average, although the overall shape of all terms do not change. It is not economical to further continue the simulation beyond $t_{\text{end}} = 382h/U_0$. Thus, largely for aesthetic reasons and for use in turbulence modeling, in plots of budgets presented in this chapter, a piecewise least-square method using the Savitzky-Golay filter (Press *et al.*, 1992) is applied to data points away from the wall. Figures 5.6 and 5.7 compare several budgets with and without curve fitting. The least-square fit is not applied to plots of first and second-order statistics, nor to any budget terms near the wall ($y^+ < 50$) or at streamwise locations before the step ($x/h < 0.0$). In subsequent sections, plots using least-square fit will be so indicated.

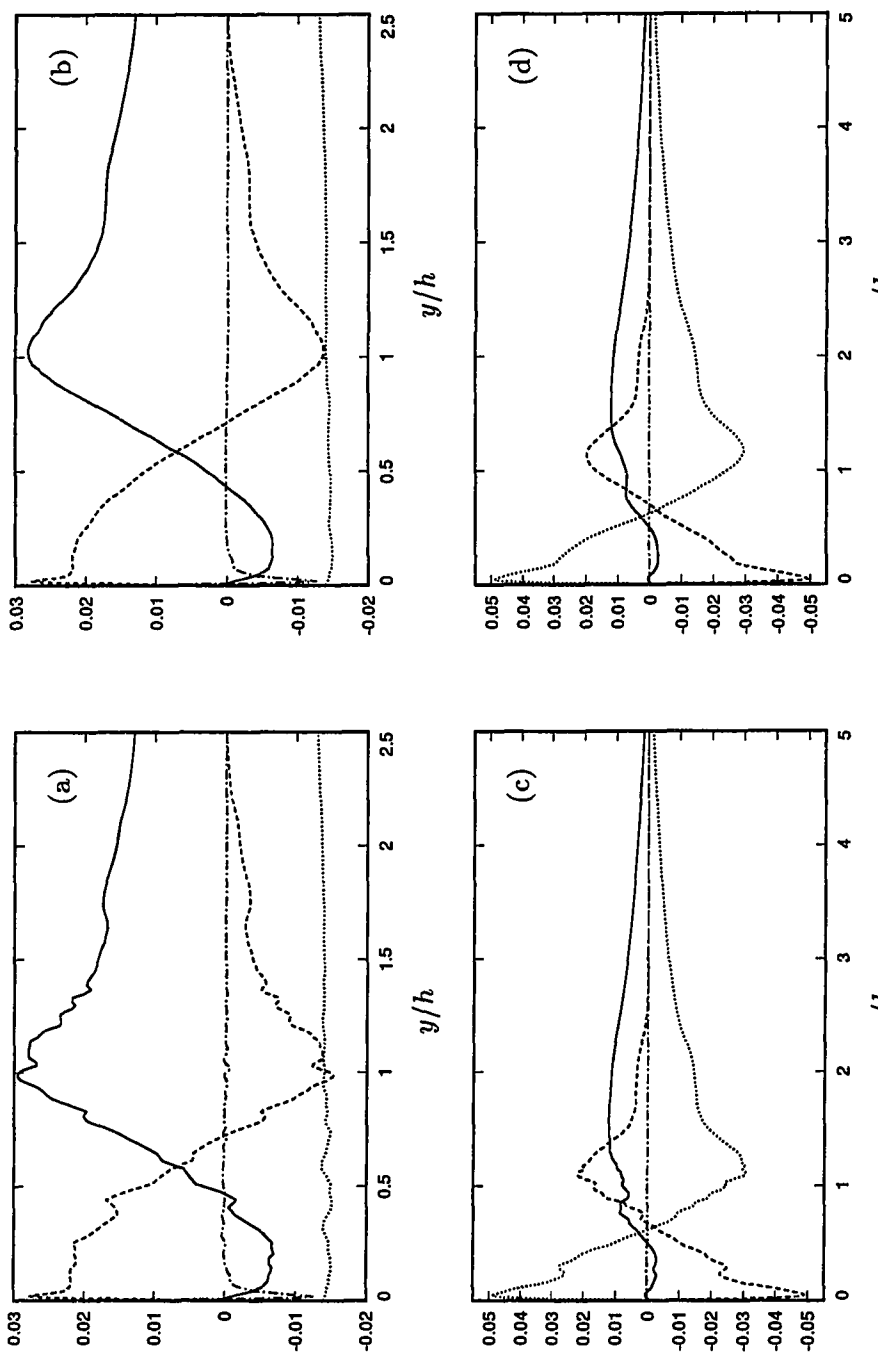

Figure 5.6. Effects of curve fitting on momentum budgets. U budget at $x/h = 7.0$: (a) raw data; (b) least-square fit. V budget at $x/h = 4.0$: (c) raw data; (d) least-square fit.

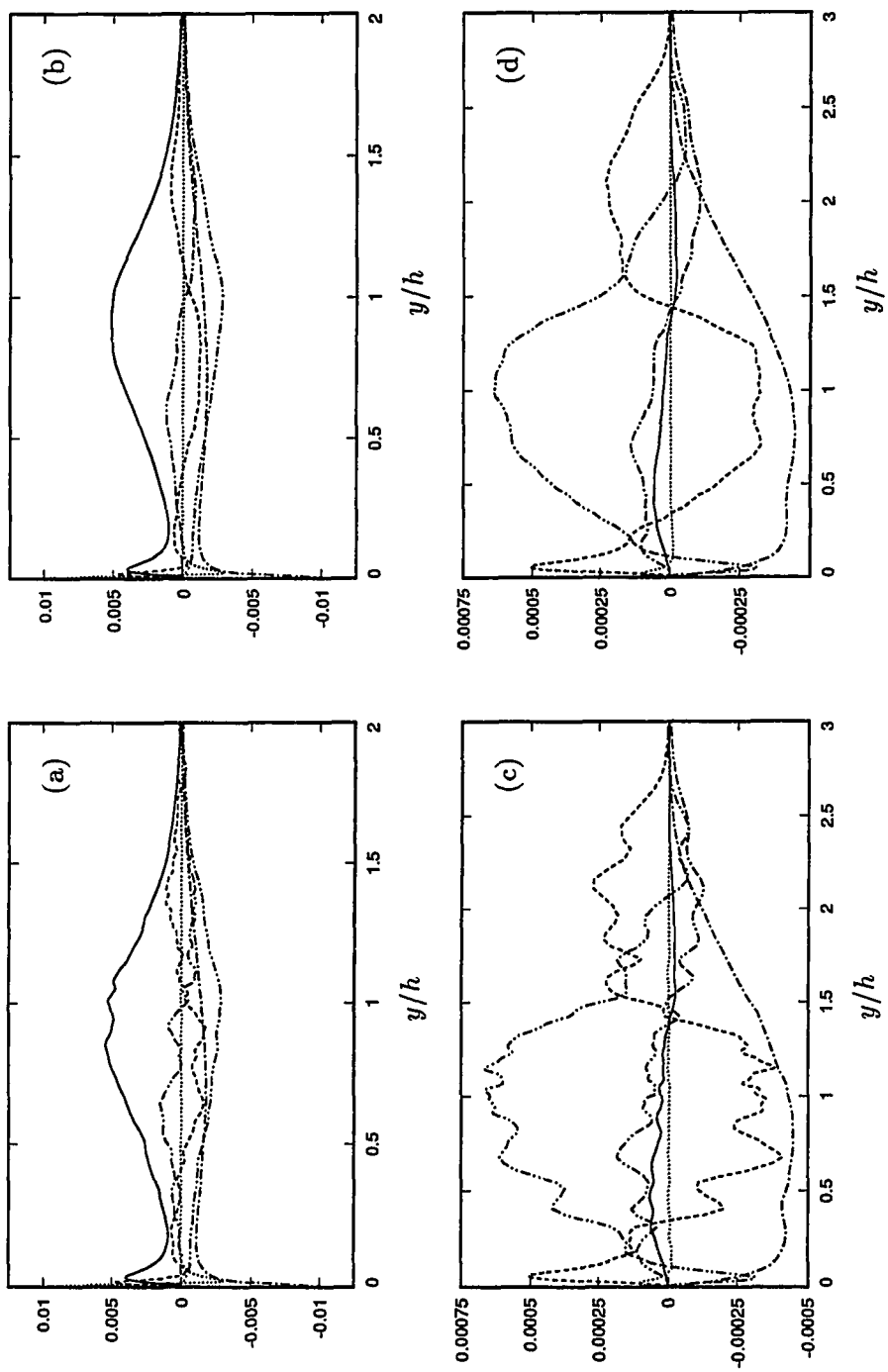

Figure 5.7. Effects of curve fitting on Reynolds-stress budgets. $\overline{u'u'}$ budget at $x/h = 10.0$: (a) raw data; (b) least-square fit. $\overline{v'v'}$ budget at $x/h = 18.0$: (c) raw data; (d) least-square fit.

5.4. Jovic & Driver's Experiment

The JD experiment configuration is briefly discussed below. The reader is referred to Jovic & Driver (1994) for a more detailed description.

A low-speed wind tunnel at the NASA Ames Research Center was used. A double-expansion channel was used to produce symmetry in the mean flow, which was simulated by the no-stress upper wall in BL6. The step height, h, was $9.65mm$; and the expansion ratio was 1.20. The aspect ratio of the tunnel was $L_z/h = 11$, where L_z is the spanwise dimension. The boundary layer was tripped at the end of the wind tunnel contraction to promote transition. The distance from the trip to the step location was $381mm$. The mean inlet free stream velocity, U_0, is $7.65m/sec$, measured at a reference point upstream of the step. The fully developed turbulent boundary layer thickness, $\delta = \delta_{99}$, at the reference point was $11.60mm$ which gives $\delta/h \approx 1.20$. The inlet free stream velocity and the step height corresponded to a Reynolds number, Re_h, of approximately 5000.

A set of constant-temperature anemometers in conjunction with X-wire probes were used to perform turbulence measurements. The skin friction was directly measured with a laser interferometer.

5.5. Energy Spectra and Two-Point Correlations

Figures 5.8–5.10 examine the one-dimensional energy spectra in the spanwise direction at four streamwise locations: $x/h = -2.5$ (before the step), 5.0 (recirculation region), 10.0 (reattachment region), and 18.0 (recovery region). Shown in Fig. 5.8 are the spectra for locations near the walls. The distance from the wall in wall coordinates are $y^+ \approx 9$ ($y/h = 1.04$) before the step, and $y^+ \approx 4$ ($y/h = 0.017$) behind the step. The shear velocities, u_τ, used in y^+ are based on local values. There is sufficient energy drop at high wavenumbers for E_{uu} and E_{ww} to indicate adequate grid resolution. However, E_{vv} shows that higher spanwise resolution is needed near the walls to resolve the small-scale structures at $y^+ < 10$. The spectra are presented for points in the free shear layer ($y/h \approx 1$) in Fig. 5.9, and at the edge

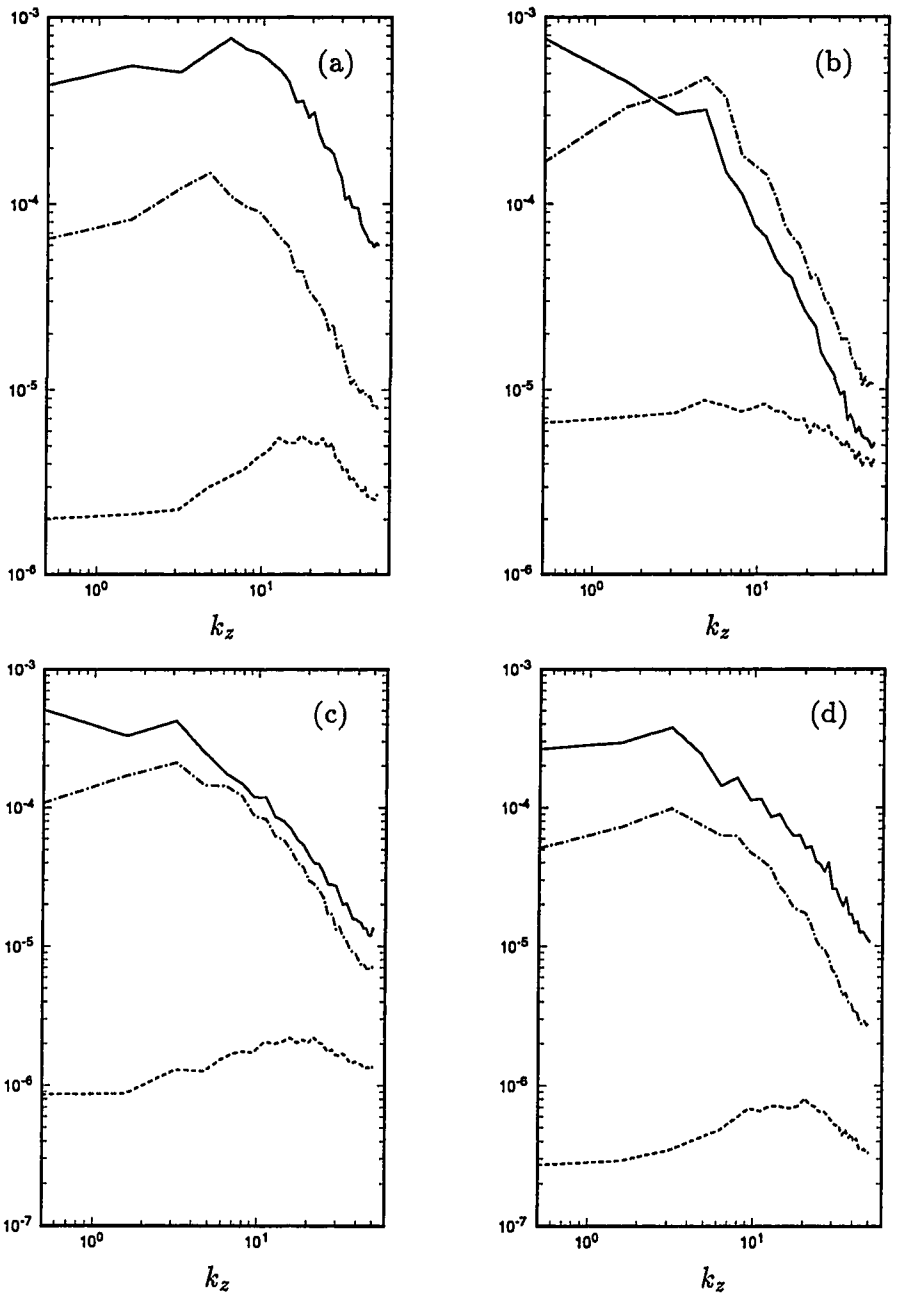

Figure 5.8. One-dimensional spanwise energy spectra near the walls. —— E_{uu}; ---- E_{vv}; —·— E_{ww}. (a) $x/h = -2.5$, $y/h = 1.04$; (b) $x/h = 5.0$, $y/h = 0.017$; (c) $x/h = 10.0$, $y/h = 0.017$; (d) $x/h = 18.0$, $y/h = 0.017$.

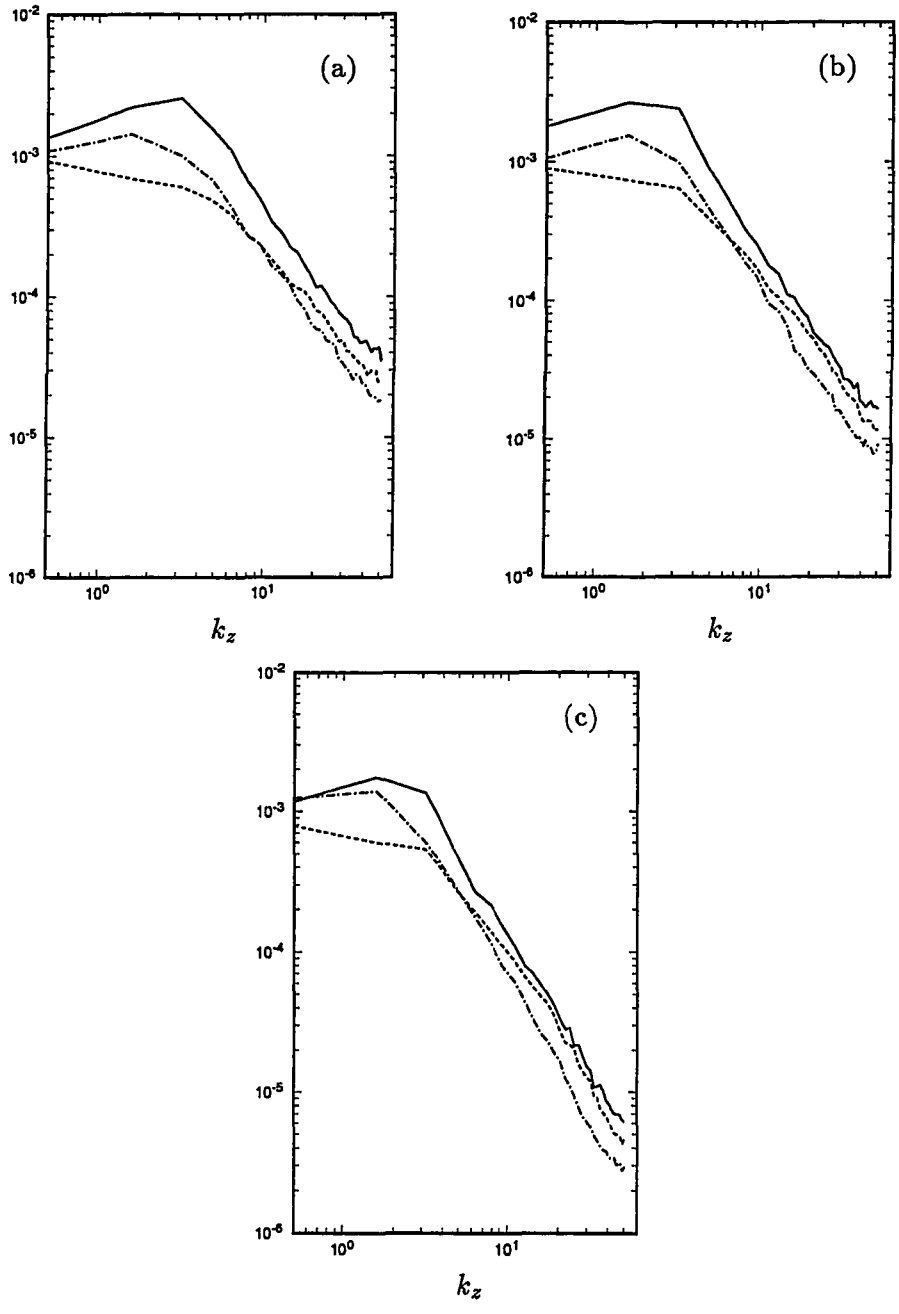

Figure 5.9. One-dimensional spanwise energy spectra at $y/h = 1.04$. —— E_{uu}; ---- E_{vv}; —·— E_{ww}. (a) $x/h = 5.0$; (b) $x/h = 10.0$; (c) $x/h = 18.0$.

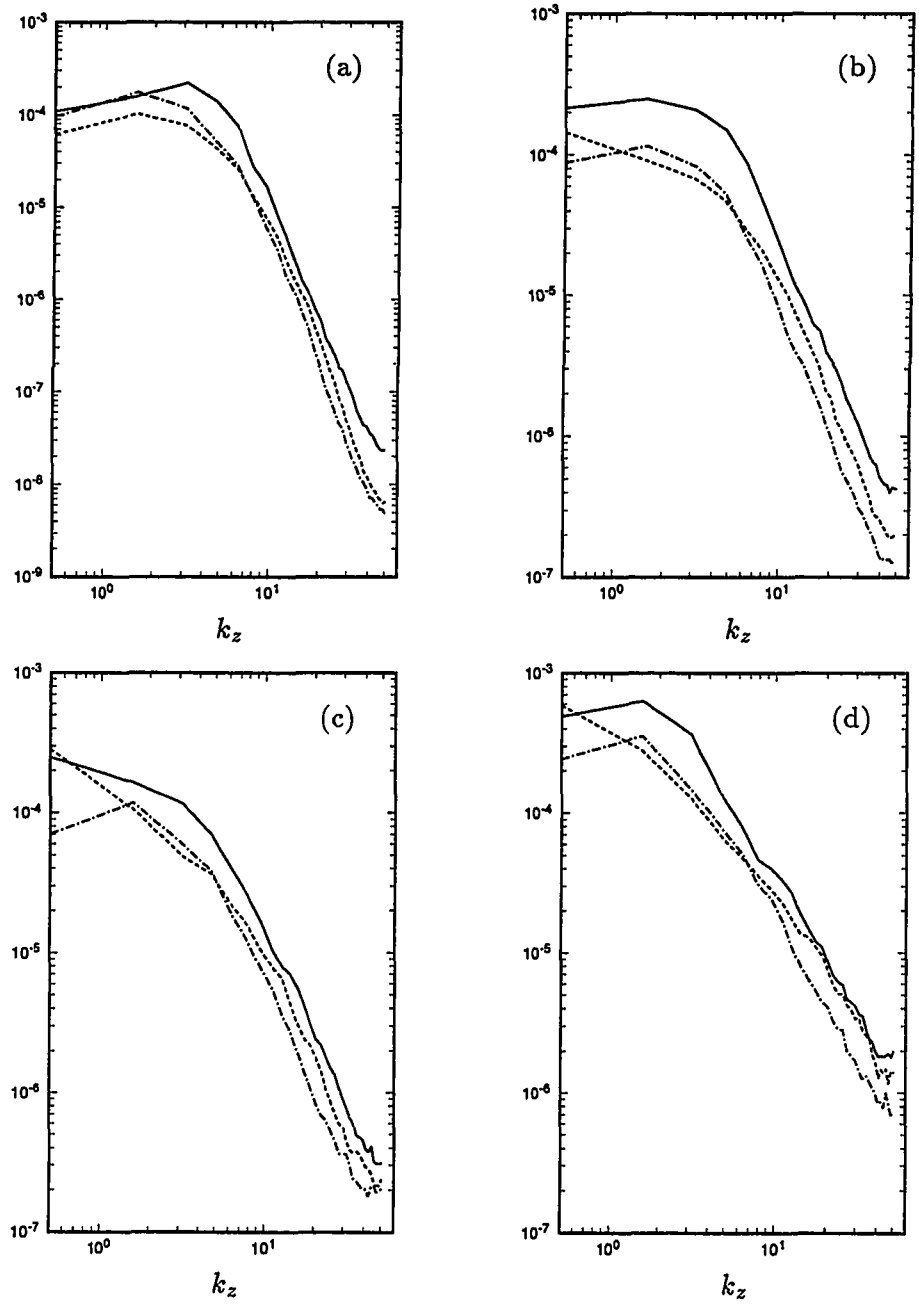

Figure 5.10. One-dimensional spanwise energy spectra at $y/h = 2.03$. —— E_{uu}; ---- E_{vv}; —·— E_{ww}. (a) $x/h = -2.5$; (b) $x/h = 5.0$; (c) $x/h = 10.0$; (d) $x/h = 18.0$.

of the boundary layer ($y/h \approx 2$) in Fig. 5.10. Both figures indicate the adequacy of the spanwise resolution for all points away from the wall.

The two-point correlations at the same locations are illustrated in Figs. 5.11–5.13, and at $y/h = 2.50$ in Fig. 5.14. Again, the lack of resolution to resolve the small-scale structures near the wall is evident in R_{vv} plots in Fig. 5.11. The correlations drop off to zero at large separations for all points near the wall. This is not true, however, as one moves away from the wall. In Fig. 5.12, the correlations remain at 10% at the largest separations for points in the free shear layer. The increased correlation lengths in the free shear layer may be attributed to the presence of the spanwise rollers. The correlations at $L_z/2$ increase to approximately 20% at $y/h = 2.03$ (Fig. 5.13). It appears that a larger domain size may be desirable.

The correlation lengths for all three velocity components grow even larger as one moves well into the free stream ($y/h = 2.50$) where the turbulent fluctuations are expectedly negligible (Fig. 5.14). The increasingly large correlations seen from $y/h = 1.03$ to $y/h = 2.50$ could be the effect of irrotational fluctuations (see Bradshaw, 1967). To verify whether or not the flow in this region is dominated by irrotational fluctuations, the spanwise vorticity fluctuations, $\sqrt{\overline{\omega_z'^2}}$, at four streamwise locations are calculated and plotted in Fig. 5.15. Note that the origin of the y-axis in the leading section is at $y/h = 1$. At $y/h = 2.03$, $\sqrt{\overline{\omega_z'^2}}$ at all x-locations is about 6% to 8% of its maximum value. At $y/h = 2.50$, the level of fluctuation drops to less than 0.5% of $\sqrt{\overline{\omega_z'^2}}_{\max}$. The turbulent free shear layer extends beyond $y/h = 2.0$, especially near the exit; but at $y/h = 2.50$, the large correlations appear to be due to irrotational fluctuations.

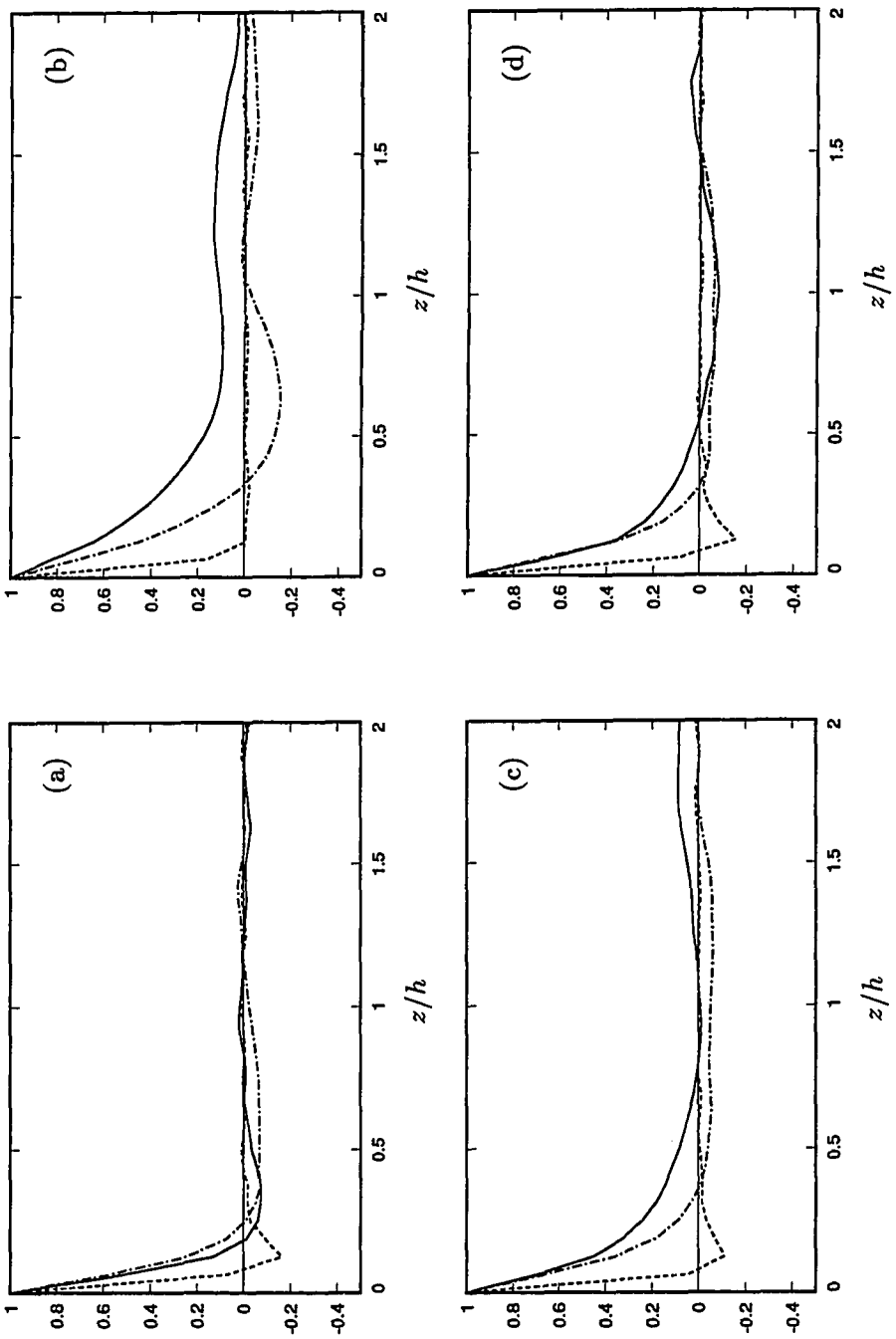

Figure 5.11. Two-point correlations near the walls. ——— , R_{uu}; ---- , R_{vv}; —·— , R_{ww}. (a) $x/h = -2.5$, $y/h = 1.04$; (b) $x/h = 5.0$, $y/h = 0.017$; (c) $x/h = 10.0$, $y/h = 0.017$; (d) $x/h = 18.0$, $y/h = 0.017$.

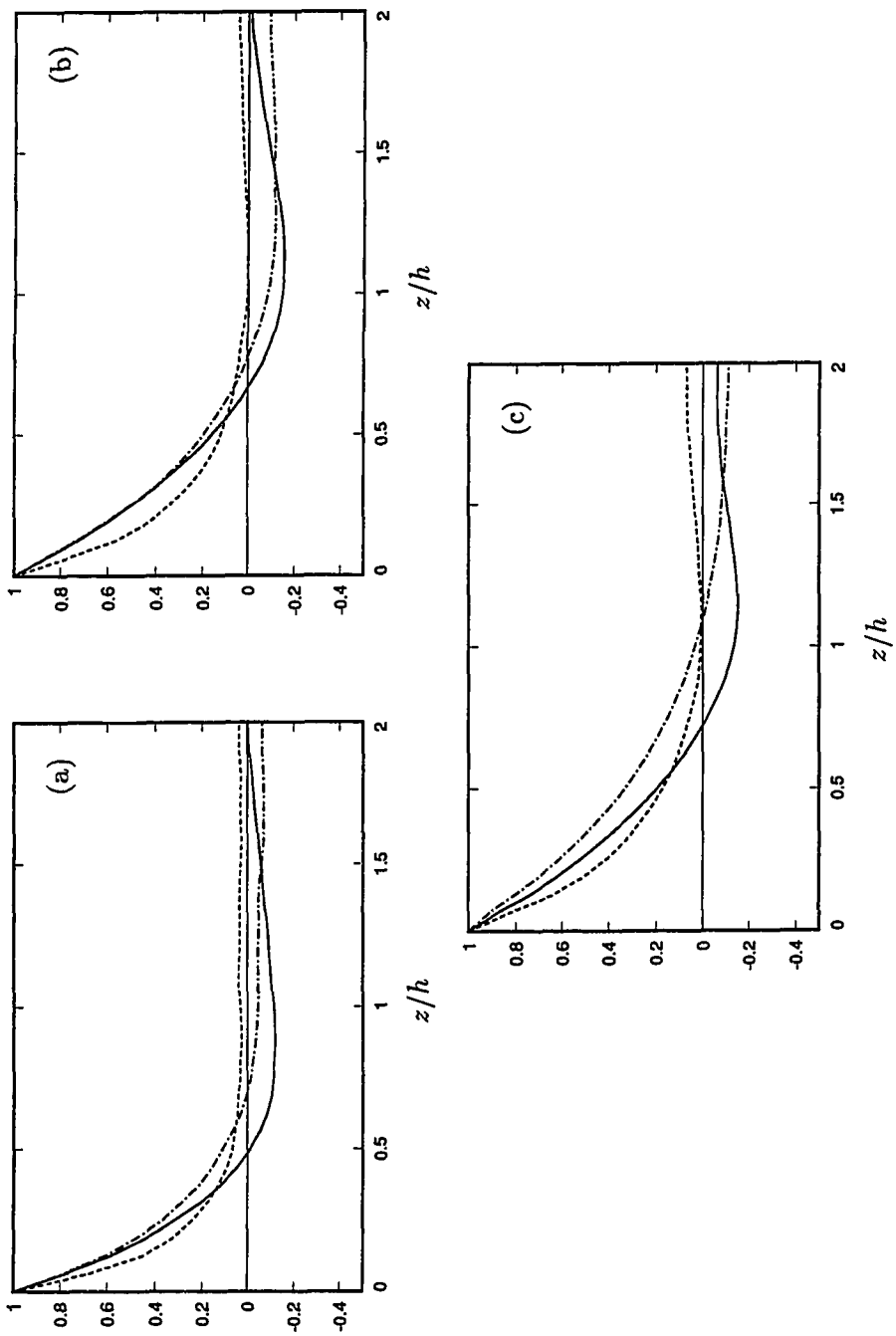

Figure 5.12. Two-point correlations at $y/h = 1.04$. ——, R_{uu}; ---- , R_{vv}; —·— , R_{ww}. (a) $x/h = 5.0$; (b) $x/h = 10.0$; (c) $x/h = 18.0$.

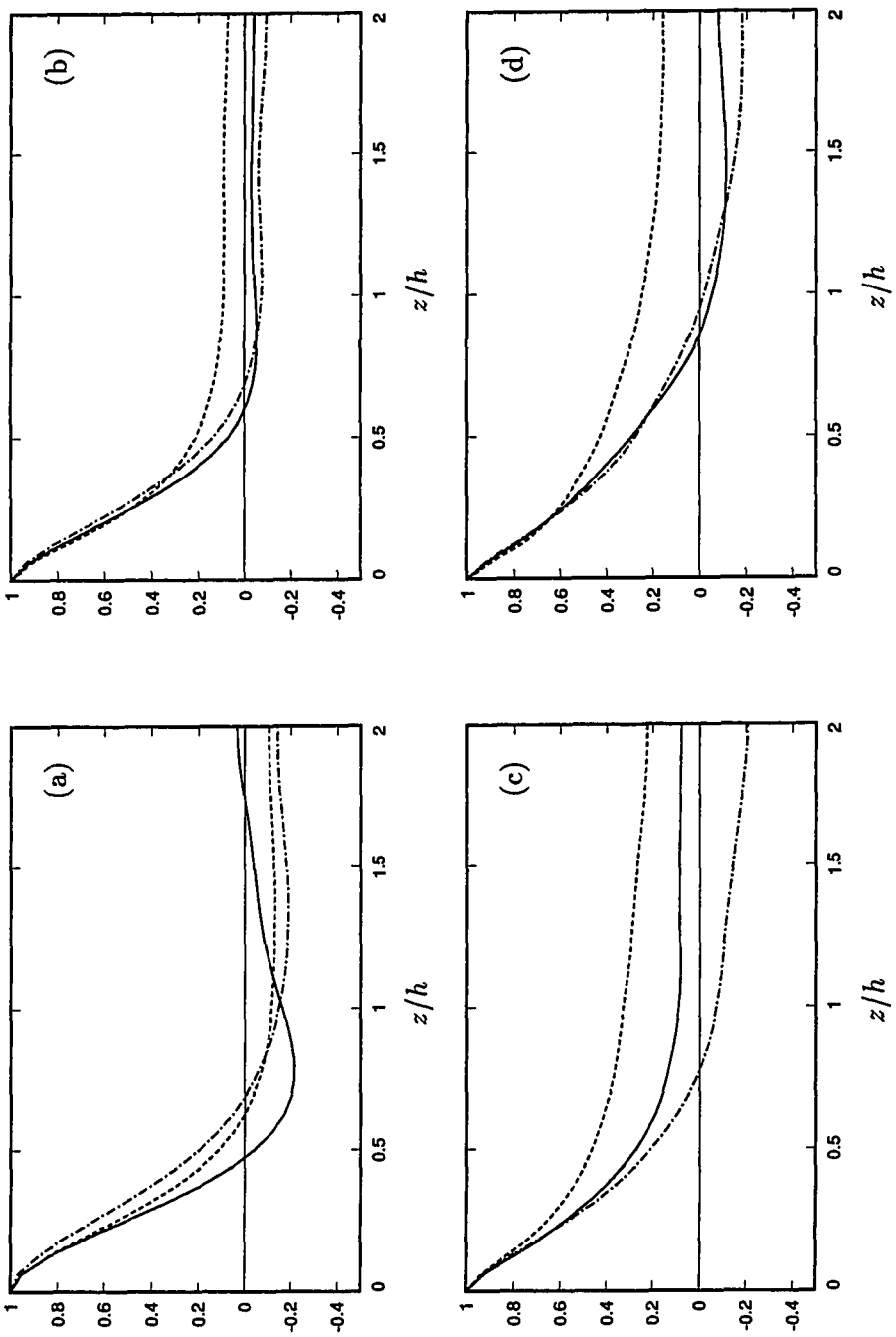

Figure 5.13. Two-point correlations at $y/h = 2.03$. ——— , R_{uu}; ---- , R_{vv}; —·— , R_{ww}. (a) $x/h = -2.5$; (b) $x/h = 5.0$; (c) $x/h = 10.0$; (d) $x/h = 18.0$.

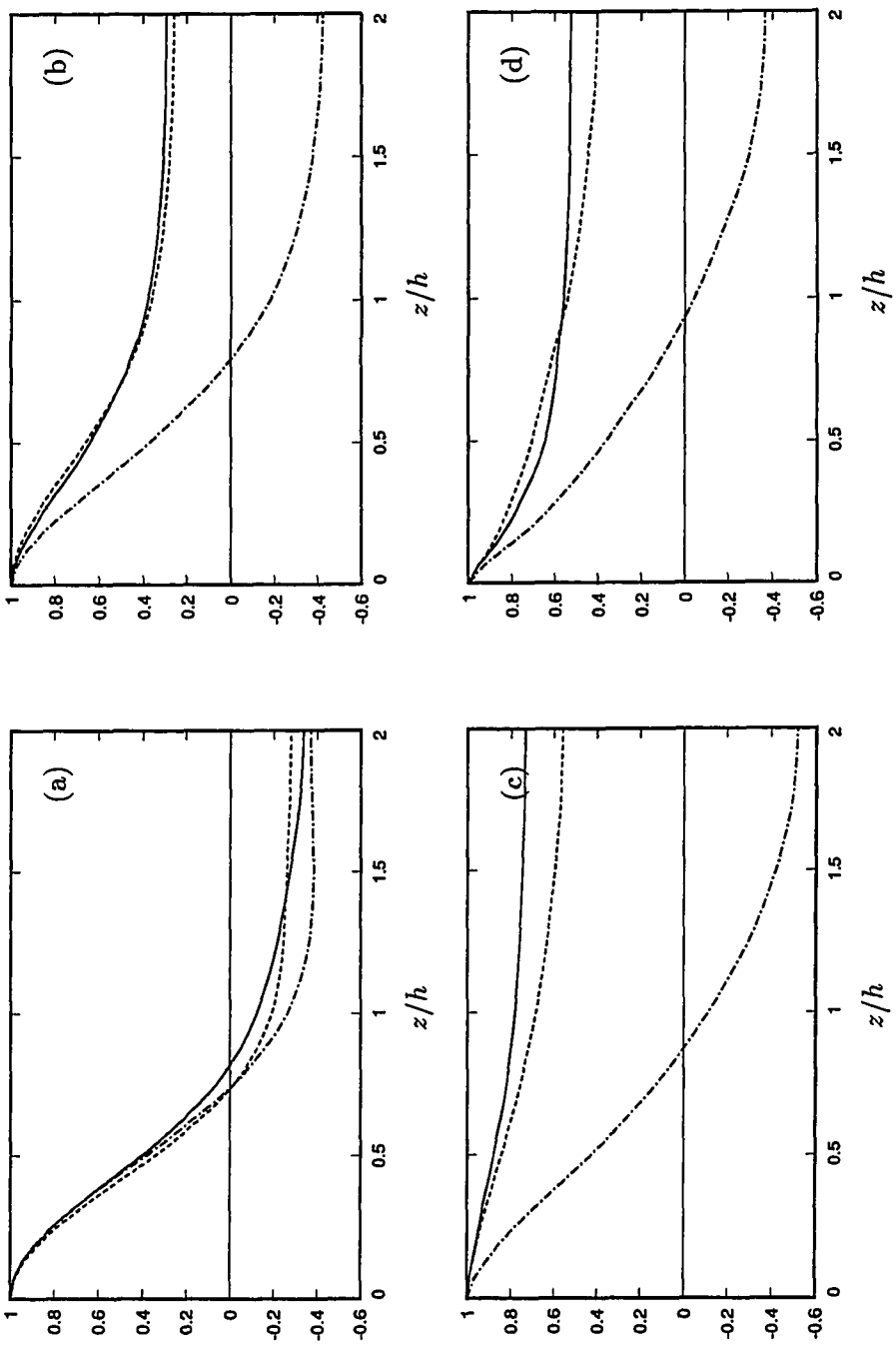

Figure 5.14. Two-point correlations at $y/h = 2.50$. ——— , R_{uu}; ----- , R_{vv}; —·— , R_{ww}. (a) $x/h = -2.5$; (b) $x/h = 5.0$; (c) $x/h = 10.0$; (d) $x/h = 18.0$.

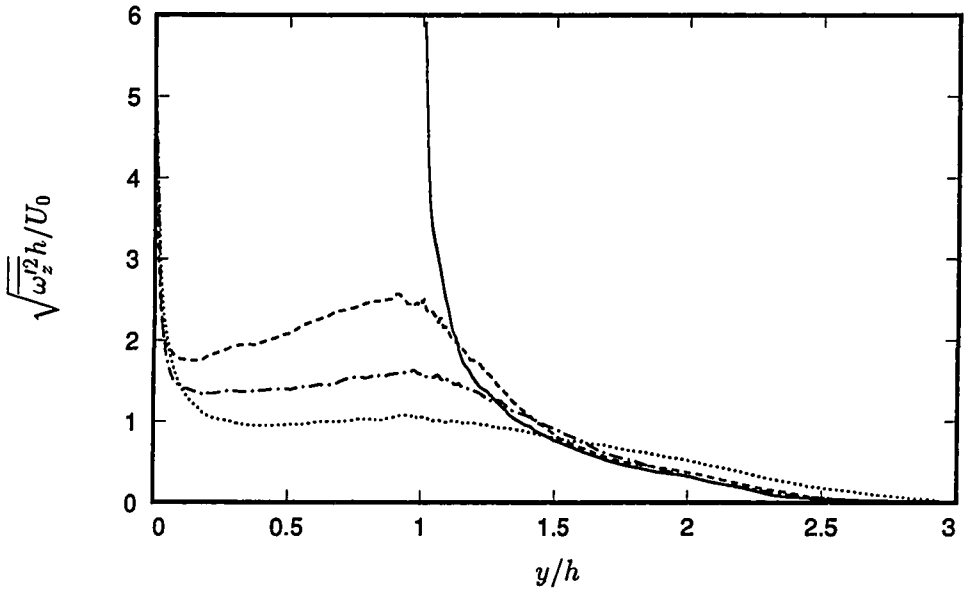

Figure 5.15. Spanwise vorticity fluctuations, $\sqrt{\overline{\omega_z'^2}}h/U_0$. —— , $x/h = -2.5$; ---- , $x/h = 5.0$; ····· , $x/h = 10.0$; —·— , $x/h = 18.0$.

5.6. Instantaneous Flow Field

Presented in this section are characteristics of the instantaneous flow fields, including the reverse flow region, velocity contours, and the flow three-dimensionality. Of particular interest is the oscillatory behavior of the flow behind the step.

5.6.1. Instantaneous Coefficient of Friction

Figure 5.16 shows instantaneous contours of the friction coefficient C_f at the bottom wall. For clarity, only contours of negative C_f (reverse flow) are plotted. The heavy lines are the zero-friction lines separating the forward and backward moving flows near the wall. The instantaneous reattachment boundaries are a set of contorted lines. The lines of separation divide the flow domain near the wall into four general regions with alternating C_f signs: forward flow region (positive C_f, $x/h > 7.0$); reverse flow region (negative C_f, $2.5 < x/h < 5.0$); secondary bubble (positive C_f, $0.05 < x/h < 1.0$); and very close to the step, a weak second

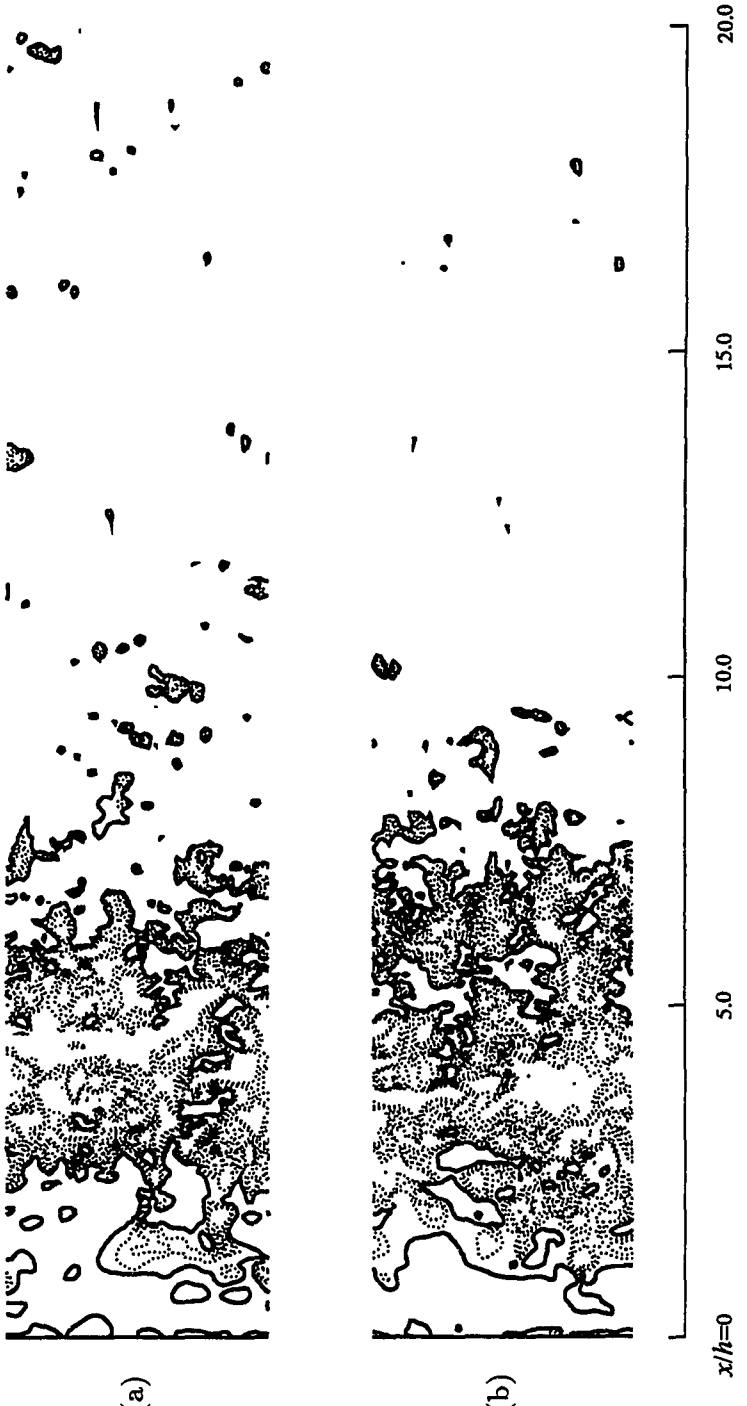

Figure 5.16. Instantaneous friction coefficient contours. ..... negative C_f; —— $C_f = 0$. (a) $t = 293h/U_0$; (b) $t = 300h/U_0$. Contours: -0.0005, -0.00075, -0.001, -0.002, -0.0025, -0.003.

reverse flow region extending to only about $0.05h$ (approximately one grid cell). These boundaries, of course, are not sharp. For example, the variation in the size of the main reverse flow region is clearly seen if Fig. 5.16. In fact these separation lines have a cyclical behavior which will be discussed in details in §5.6.3. There are patches of positive C_f even in the reverse flow region which were also observed by Friedrich & Arnal (1990) in their LES results. Pockets of locally high C_f values are seen in both positive and negative regions with magnitudes up to several times the mean values.

5.6.2. Instantaneous Velocity

The instantaneous contours of the velocity components in a typical x-y plane are shown in Fig. 5.17. All velocities are normalized by the inlet free-stream velocity U_0. The negative contours are plotted with dotted lines and positive contours with solid lines. The streamwise velocity contours indicate a shear layer emanating from the step corner and reaching the bottom wall near $x/h = 8.0$ (Fig. 5.17(a)). In Fig. 5.17(b), strong upward flow patches are concentrated within the shear layer inside the recirculation zone. The flow is mostly downward behind the reattachment, but alternating positive and negative v contours are observed indicating the presence of spanwise vortices; the motion of spanwise vortices will be presented in §5.6.3. High gradients are seen in both velocity components in the shear layer. Note that Fig. 5.17 is only representative of one vertical plane, and although contours of extreme values are omitted from the plots, numerical results indicate that the magnitudes of each velocity components can reach values much higher than shown in Fig. 5.17: $|u_{\max}| \approx 1.3U_0$, and $|v_{\max}| \approx 0.8U_0$. The maxima of v occur near reattachment, where the downward moving fluid interacts with the wall. The streamwise velocity also reaches its maximum value near reattachment but in the free shear layer.

Figure 5.18 shows the instantaneous velocity fluctuations. Again, contours of extreme values are omitted. At the instant shown, $|u'|$, $|v'|$ and $|w'|$ can reach as

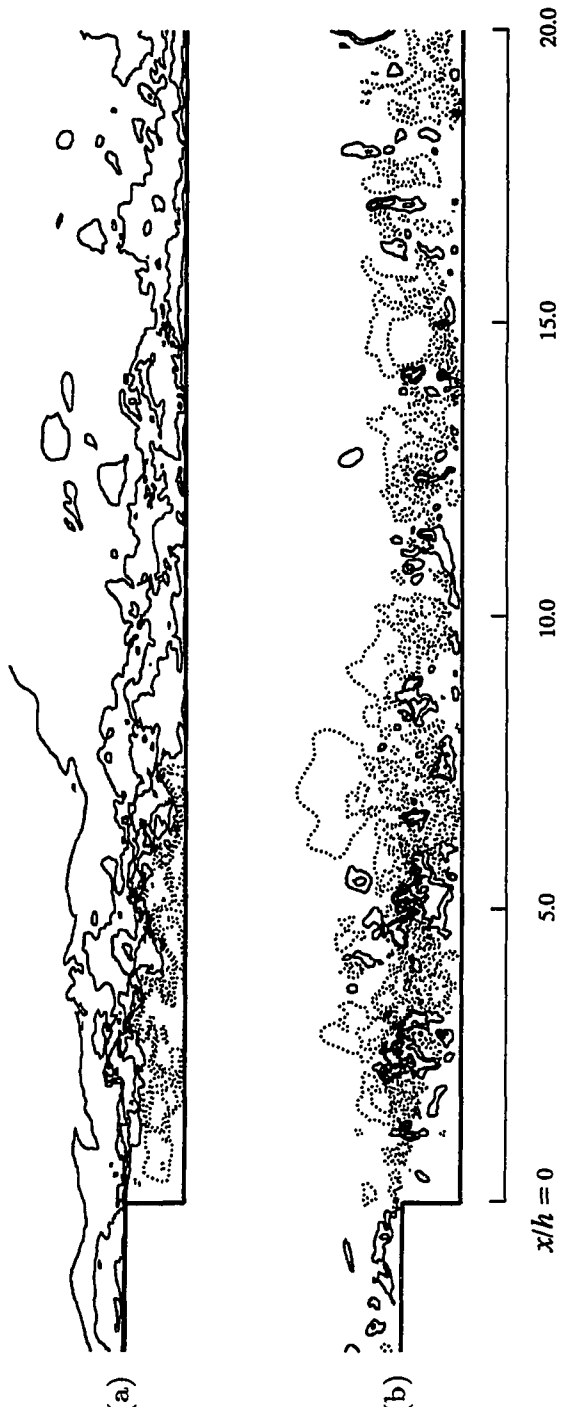

Figure 5.17. Instantaneous velocity contours. ..... negative; —— positive. (a) u/U_0, contours: -0.10, -0.05, -0.01, 0.10, 0.30, 0.50, 0.70, 0.90; (b) v/U_0, contours: -0.20, -0.10, -0.05, 0.05, 0.10, 0.20.

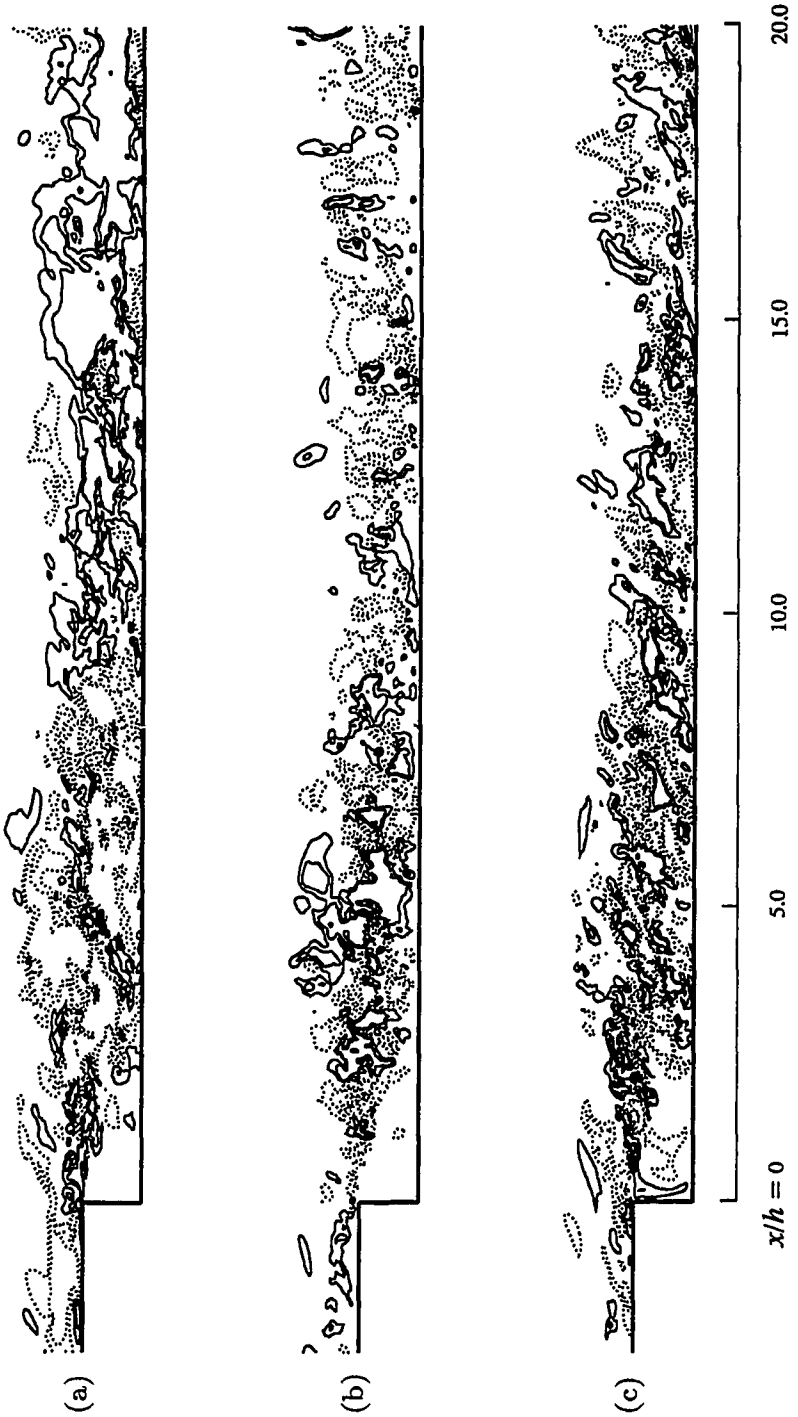

Figure 5.18. Instantaneous velocity fluctuation contours. ..... negative; —— positive. (a) u'/U_0, contours: -0.10, -0.05, 0.05, 0.10; (b) v'/U_0, contours: -0.10, -0.05, 0.05, 0.10; (c) w'/U_0, contours: -0.10, -0.05, 0.05, 0.10.

high as $0.4U_0$, $0.6U_0$ and $1.0U_0$, respectively, near reattachment. It appears that the fluctuations in the backflow region are relatively small (the maximum value of velocity fluctuations in this region is approximately $0.08U_0$). However, considering that the maximum mean streamwise velocity in this region is only $U_N \approx 0.18U_0$, the fluctuations can reach 40% of U_N, eventhough the mean flow is laminar-like near the wall (see §5.7.4.3). This is in accordance with Westphal *et al.*'s (1984) suggestion that the reverse flow is lamilar-like but with high unsteadiness imposed by the turbulent shear layer.

The locations of the maximum velocities from Figs. 5.17 and 5.18 indicate, as expected, that the most turbulent activities occur near reattachment. A spanwise cut through the flow at $x/h = 4.0$ (before the reattachment location) in Fig. 5.19 illustrates the high three-dimensionality of the flow with several imbedded streamwise vortices. The flow is virtually quiet above $y/h = 2$.

To examine the structural recovery to a normal turbulent boundary layer after reattachment, Fig. 5.20 presents the streamwise velocity fluctuation (u') contours in an x-z plane at $y^+ \approx 5$ (normalization for y^+ here uses the shear velocity $u_\tau = 0.038U_0$ at the exit). Near the exit, elongated, alternating positive and negative contour lines begin to appear. However, the wall streaks, characteristics of an attached turbulent boundary layer, are not yet present indicating that the flow has not fully recovered after 20 step heights.

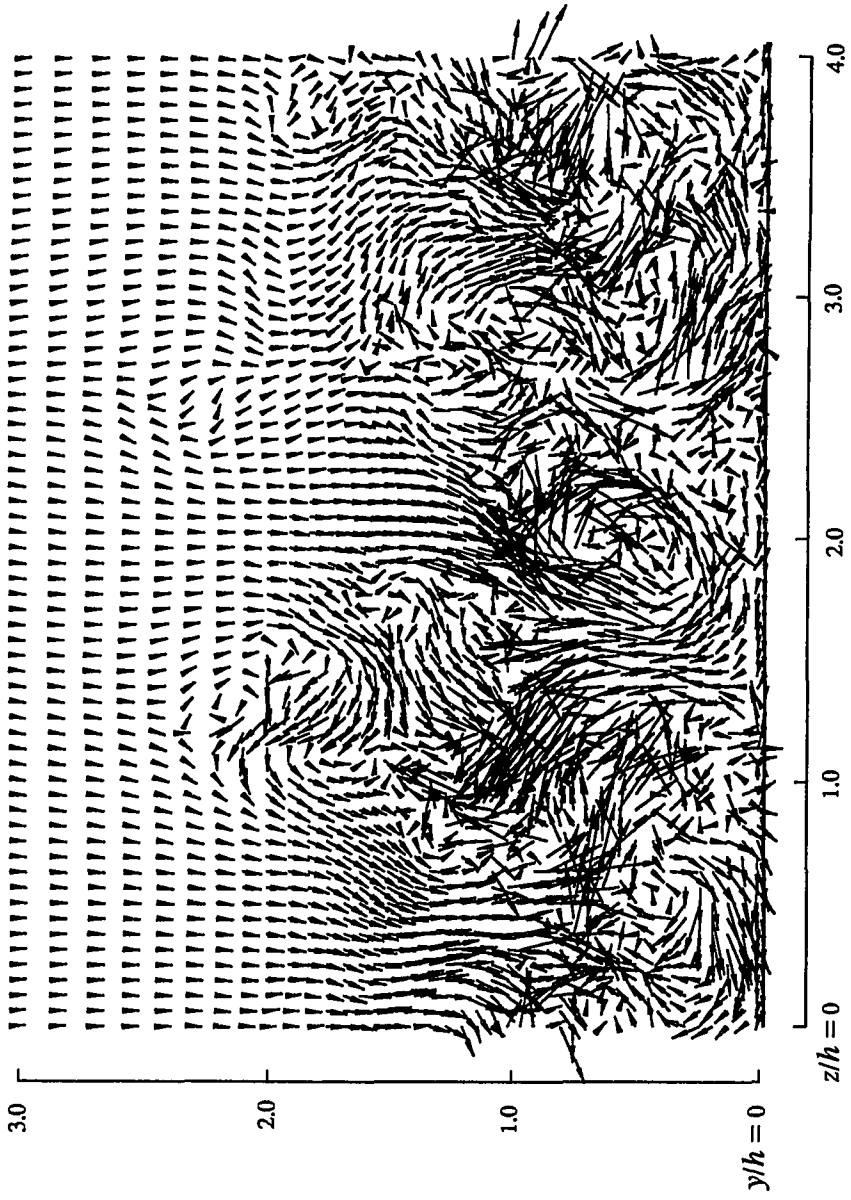

Figure 5.19. Instantaneous spanwise velocity vectors at $x/h = 4.0$.

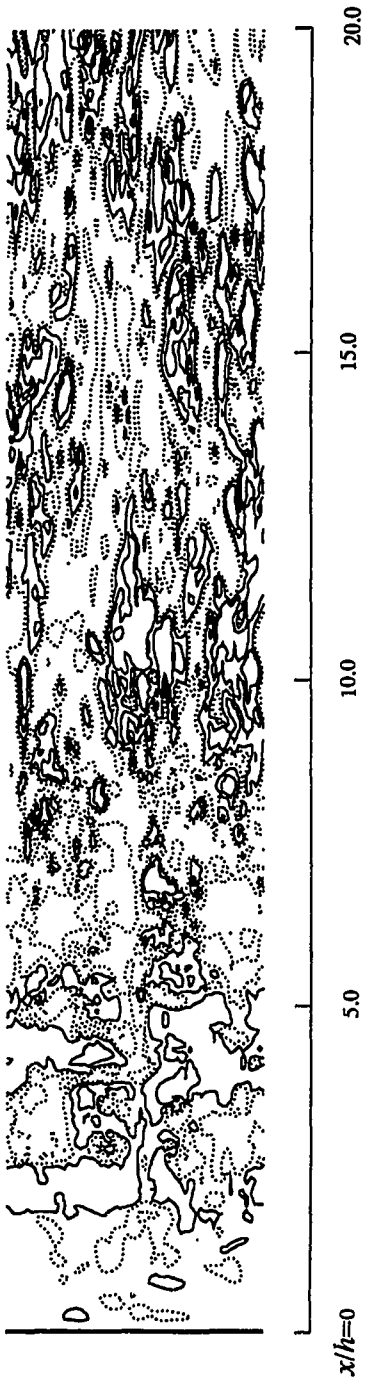

Figure 5.20. Instantaneous streamwise velocity fluctuations (u'/U_0) contours at $y^+ \approx 5$ (y^+ normalized to $u_\tau = 0.0384U_0$ at exit). ..... negative; —— positive. Contours: -0.10, -0.02, 0.02, 0.10; $t = 382h/U_0$.

5.6.3. Large Scale Temporal Oscillations

In Chapter 3, a limit cycle behavior of the backward-facing step flow is clearly observed in 2-D simulations at high Reynolds numbers. The motion of vortices shedding from the step and how their interaction with the wall induces the oscillatory motion of the reattachment length were elucidated with the spanwise vorticity contours (see §3.5). However, in similar plots for 3-D simulations, large scale vortical structures are obscured by the high intensity small scale structures. Figure 5.21 shows the instantaneous spanwise vorticity contours at a selected x-y plane. Similar to features seen in 2-D simulations (§3.5), there is an apparent large scale roll-up of the shear layer extending to the reattachment region. However, this large structure is not one large vortex but is composed of many small counter-rotating vortices. From their LES results, Friedrich & Arnal (1990) observed that the free-shear layer has a vertical motion causing the reattachment location to oscillate. A low frequency "flapping" motion of the flow was also reported by Eaton & Johnston (1980), and periodic vortical motions were observed by Driver *et al.* (1983, 1987). In the current simulation, such oscillatory behavior can not be seen clearly with successive snapshots of the spanwise vorticity contours.

One indicator of the oscillatory behavior is the motion of the reattachment location(s). Figure 5.22 displays the temporal movement of the reattachment locations which has a saw-tooth shape. Here, an instantaneous reattachment location is the location of zero C_f of the *spanwise-averaged* flow field. A likely scenario for the saw-tooth shape of the X_r vs. t plot is as follows. The shear layer rolls up forming a large-scale structure behind the step. As the large-scale structure grows, the reattachment location travels downstream at a constant speed, indicated by the linear positive slopes in Fig. 5.22. The large scale structure then collapses, causing a sudden drop of the reattachment location. At instances when the collapse of the large scale structure occurs, e.g., $t \approx 282h/U_0$ or $t \approx 300h/U_0$, a single reattachment "point" is not well defined; rather, small fragments of forward and reverse flow regions are scattered between $x/h \approx 5.0$ and $x/h \approx 7.5$. This cycle repeats

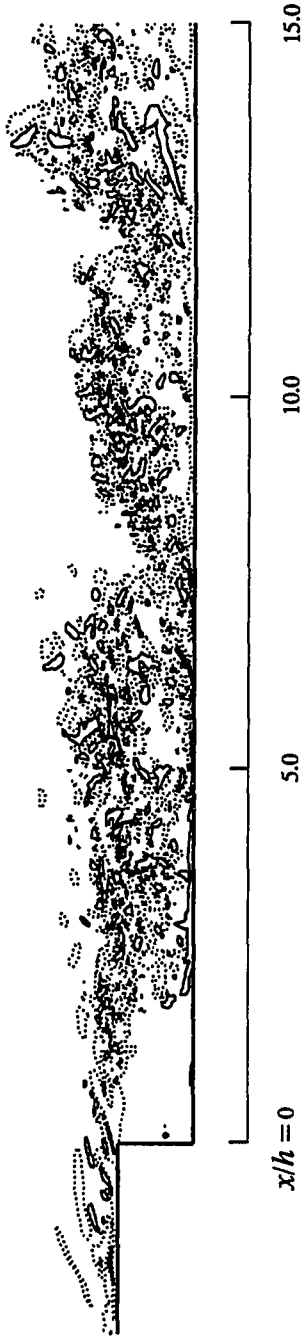

Figure 5.21. Instantanous spanwise vorticity (ω_z) contours. ..... $-1.0U_0/h$ contours; —— $1.0U_0/h$ contours.

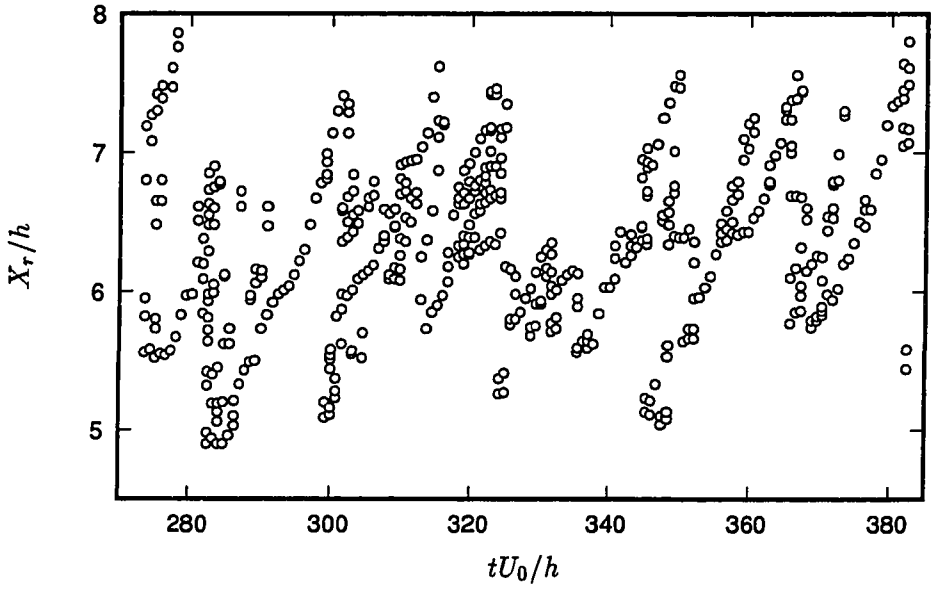

Figure 5.22. Motion of the spanwise-averaged reattachment locations.

itself with $5h < X_r < 7.5h$. The sudden decrease in X_r following a slow increase was also speculated by Eaton & Johnston (1980), but their data did not show this behavior.

The periodic behavior of the flow can be better elucidated by studying pressure fluctuations; low pressure regions have been shown to correspond to the center of turbulent vortices. The pressure fluctuations p' as a function of time at a location near the reattachment, $x/h = 6.0$ and $y/h = 0.055$ is shown in Fig. 5.23. Again, presented here are the spanwise averaged p' values. There is a very good correspondence between the p' minima and the preaks in Fig. 5.22. Similar oscillatory responses are also detected at other points in the flow field and in both vertical and streamwise velocity components (data analysis using BL6 results was provided by Mr. C. Pierce). The power density of the p' signal in Fig. 5.23 is shown in Fig. 5.24. The Strouhal number corresponding to the dominant frequency is $St = fh/U_0 \approx 0.06$, corresponding to period $T \approx 17h/U_0$. As discussed in Chapter 2, there is a characteristic period associated with the method of generating

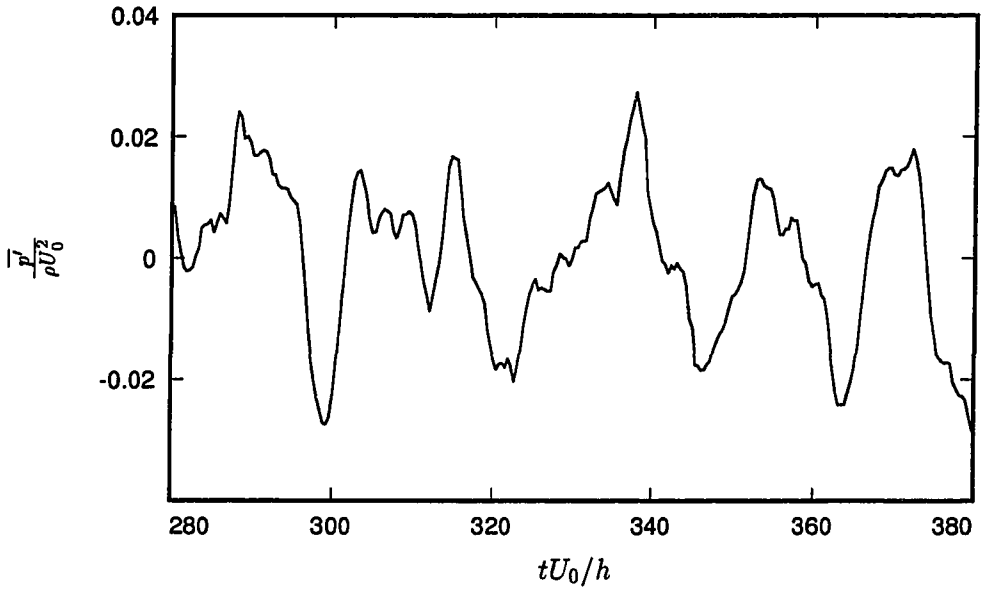

Figure 5.23. Spanwise-averaged pressure fluctuations at $x/h = 6.0$, $y/h = 0.055$.

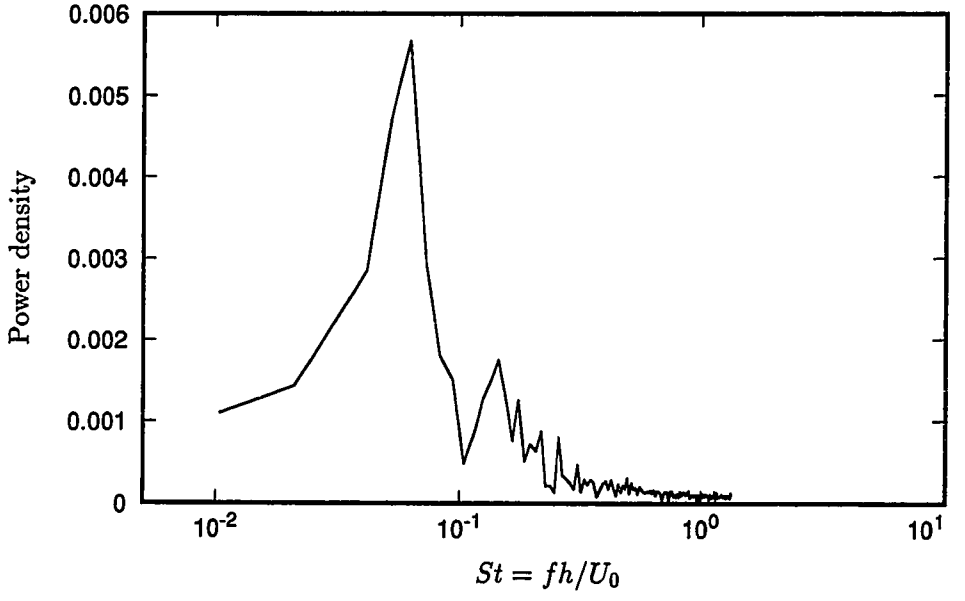

Figure 5.24. Power spectra of spanwise-averaged pressure fluctuations at $x/h = 6.0$, $y/h = 0.055$.

inflow turbulence. Although the imposed random phases destroy the periodicity of the inflow (§2.6.1), one must be certain that there is no correlation between the inflow frequency and the oscillation frequency. Studies of the flow oscillation in 2-D simulations, with and without inflow turbulence, have established the independence between the two frequencies (see §3.5). Nevertheless, in BL6, the flow oscillation period of $17h/U_0$ is several times larger than the inflow segment period ($T_f = 6.4h/U_0$, $St_f = 0.15$) indicating that it is not an artifact of the inflow condition. Compared to the 2-D oscillation, the BL6 oscillation period is approximately 30% longer. The difference is possibly due to a much lower expansion ratio in BL6. However, since only five periods are examined (Fig. 5.23), the averaged period, $17h/U_0$, should be considered as an approximation; more samples are needed to determine the exact frequency. In their experiment, Eaton & Johnston (1980) measured the energy spectra of the streamwise velocity fluctuations (u') at several locations and reported that the spectral peak occurs in the Strouhal number range $0.066 < fh/U_0 < 0.08$.

The motion of large scale vortices can be traced by the contour plots of the spanwise averaged pressure fluctuations in Fig. 5.25. Only the negative values are plotted for clarity. An animation of the 3-D constant-p' surfaces and calculations of the average speed of vortices (analysis was provided by Mr. C. Pierce) indicate that the vortices are generated at the step at approximately twice the frequency calculated above. These vortices slow down and either dissipate or merge near the reattachment region. The resulting large vortex has a higher convection speed after the reattachment. Evidence of this change in speed is seen in Fig. 5.25.

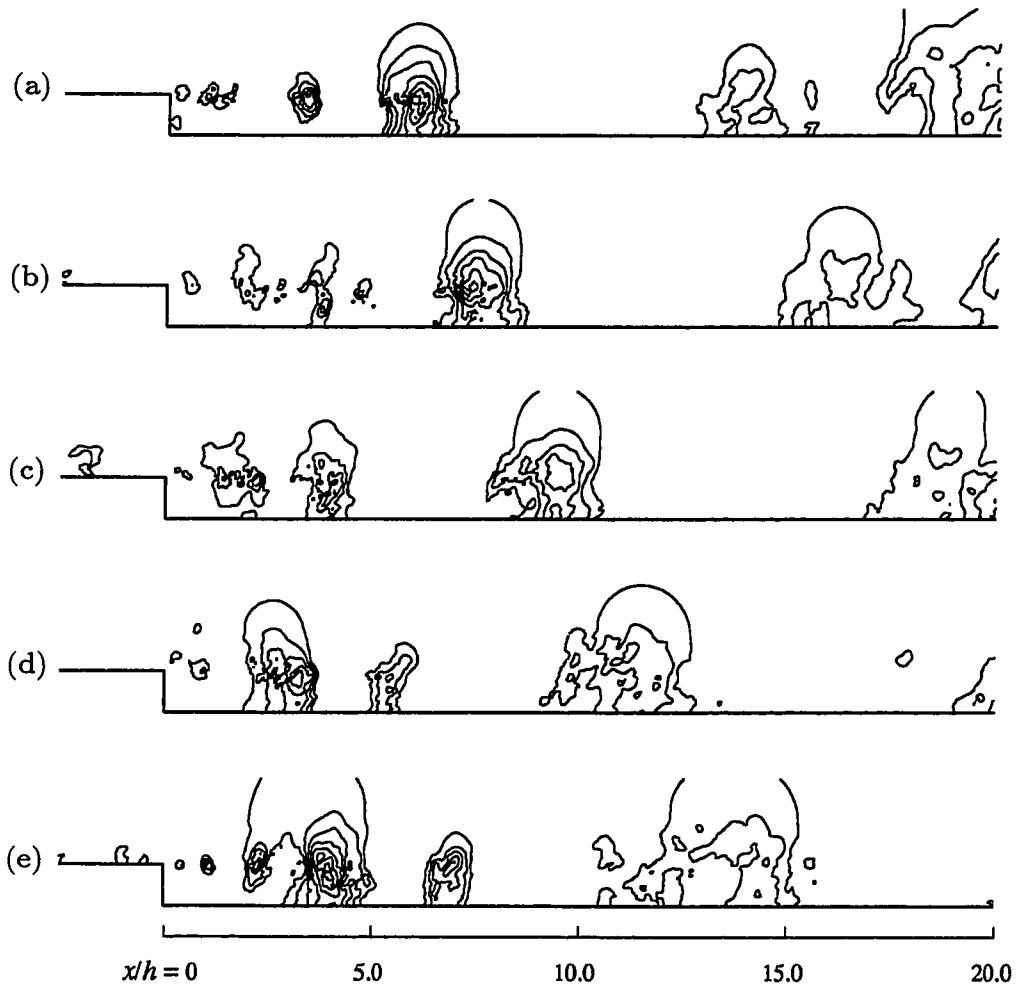

Figure 5.25. Spanwise averaged pressure fluctuations as a function of time; negative contours. (a) $t = 299U_0/h$; (b) $t = 303U_0/h$; (c) $t = 306U_0/h$; (d) $t = 310U_0/h$; (e) $t = 314U_0/h$.

5.7. Statistical Results

5.7.1. Reattachment Length

Several methods were used to determine the mean reattachment location, X_r: by (a) the location at which the mean velocity $U = 0$ at the first grid point away from the wall, (b) the location of zero wall-shear stress ($\tau_w = 0$), and (c) the location of the mean dividing streamline ($\psi = 0$). A *pdf* method was also used in which the mean reattachment point is indicated by the location of 50% forward flow fraction. The *pdf* method was also used experimentally by Westphal *et al.* (1984) and Adams *et al.* (1984). The results of the first three methods are within 0.1% of each other, and about 2% from the *pdf* result. The mean reattachment length is $6.28h$. (The reattachment length was reported in Le *et al.*, 1993, as $X_r = 6.0h$. However, the total simulation time at the time of that publication was only $t \approx 204h/U_0$.) The X_r measurements in the JD experiment vary between $6.0h$ and $6.1h$ (Jovic & Driver, 1994). Thus, there is a variation between 2 and 3% among all measured and computed X_r's. Figure 5.26 shows the average streamlines of the mean flow.

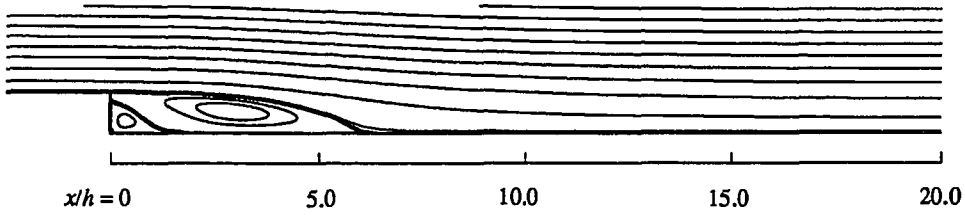

Figure 5.26. Contours of mean stream function ψ; reattachment length $X_r = 6.28h$.

A large secondary bubble is evident in the step corner, extending to $1.76h$ in the x-direction, and $0.8h$ in the y-direction. The secondary bubble size seems long compared to measurements ($\approx 0.9h$) by Durst & Schmitt (1985). However their studies were conducted at a much higher Reynolds number ($Re_h = 1.13 \times 10^5$) and

expansion ratio ($ER = 2$). It is unclear how these factors affect the secondary recirculation region. Friedrich & Arnal (1990) reported that the instantaneous secondary recirculation regions are three-dimensional bubbles, located in the corner. In the current computations, the secondary recirculation extends across the entire span as seen in Fig. 5.16. Not seen in Fig. 5.26 is a third corner vortex (Moffatt, 1964) of $0.042h$ in size.

Experimental studies have shown that the reattachment length is influenced by several parameters:

(a) Expansion ratio, ER. The reattachment length was demonstrated by Kuehn (1980) to increase as the expansion ratio increase. Durst & Tropea (1981) compiled data from a number of experiments to show that, although the increase in X_r is almost linear at high expansion ratio ($1.5 < ER < 2.0$), the most dramatic change is in the range $1.10 < ER < 1.30$ where X_r varies from $5h$ to $7h$. The X_r's from BL6 and the JD experiment are in this range. The effect of ER on the reattachment length was also verified in the preliminary 3-D simulations (see §4.2).

(b) Reynolds number, Re_h. Durst & Tropea (1981) and Armaly *et al.* (1983) demonstrated that X_r is strongly dependent on the Reynolds number at low Re_h values ($Re_h < 4500$). But in the Reynolds number range of the JD experiment ($Re_h = 5000$), and current simulation ($Re_h = 5100$), X_r only increases slightly with Re_h. This is consistent with the results from the preliminary 3-D simulations.

(c) Inlet turbulence intensities $\sqrt{\overline{u'^2}}/U_0$. The inlet turbulence is expected to influence the reattachment length (Eaton & Johnston,1981). Isomoto & Honami (1989) found that an increase in inlet turbulence intensities causes a decrease in X_r. However, results of all 3-D simulations are inconclusive because the inlet turbulence intensity was not one of the parameters varied in the parametric study in Chapter 4.

(d) Inlet boundary layer thickness, δ/h. Adams *et al.* (1984) studied the variation of X_r due to both the thickness of the inlet δ and its state (laminar or turbulent). For the same Reynolds number, they found X_r to increase with δ/h in laminar state. When δ/h increases at a fixed Reynolds number, the flow undergoes a transition from laminar to turbulent, and X_r increases. However, once the boundary layer becomes turbulent, the reattachment length decreases slightly as δ/h increases. Again, although 3-D simulations have been performed with different boundary layer thicknesses, there is insufficient computational data to either support or negate Adams *et al.*'s (1984) results.

5.7.2. Coefficient of Friction

The wall skin friction coefficient is normalized by the inlet velocity as follows:

$$C_f = \frac{\tau_w}{\frac{1}{2}\rho U_0^2}.$$

Figure 5.27 compares the mean friction coefficient from BL5 and BL6. The reattachment location is indicated by the point $C_f = 0$. Increasing the resolution shifts the C_f curve to the left, hence a lower reattachment length. The higher resolution also increases the skin friction in the recovery region by 8%. The computed C_f (BL6) is plotted against the JD data in Fig. 5.28. Excellent agreement is obtained between computational and experimental results.

A striking departure from previous measurements is the large peak negative skin friction in the recirculation region ($\approx -3 \times 10^{-3}$), seen in both computation and JD experiment. As shown Fig. 5.29, where C_f of BL6 and JD experiment are compared with data from previous experiments, the peak negative C_f is about 3 times larger than previously reported. It was established in the preliminary 3-D simulations (Chapter 4) that this high negative C_f is not a result of computational resolution, boundary or initial conditions; it is now confirmed by JD data to be a real characteristic of the flow.

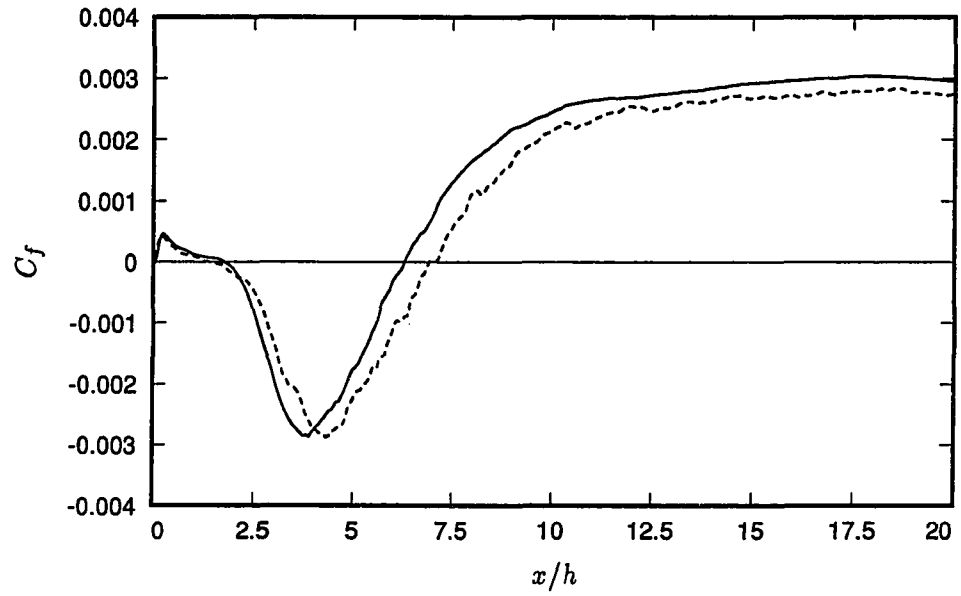

Figure 5.27. Effect of grid resolution on skin friction coefficient. —— case BL6 ($768 \times 192 \times 64$); ---- case BL5 ($480 \times 128 \times 32$).

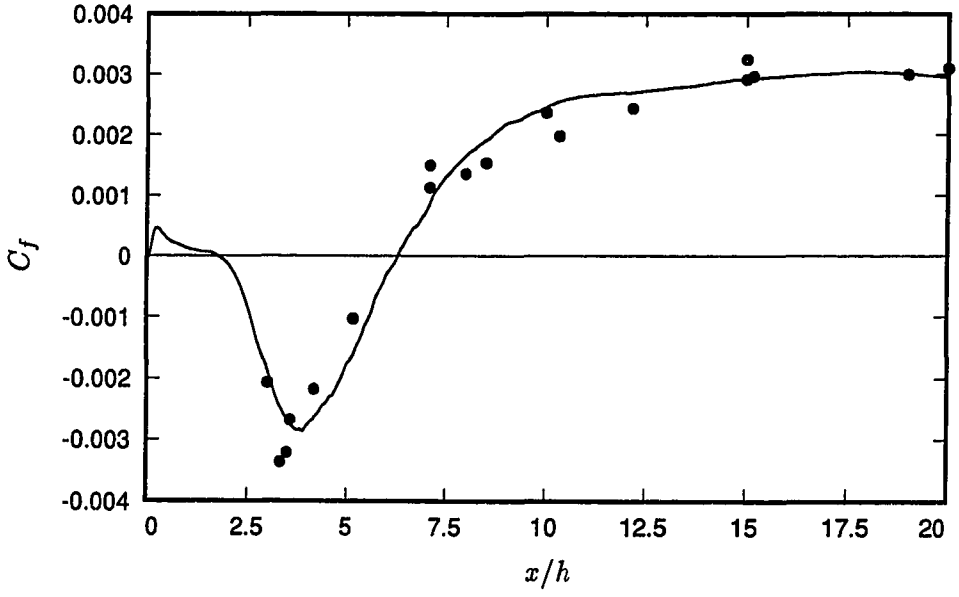

Figure 5.28. Comparison between BL6 and JD step-wall skin friction coefficient. —— case BL6; • Jovic & Driver (1994).

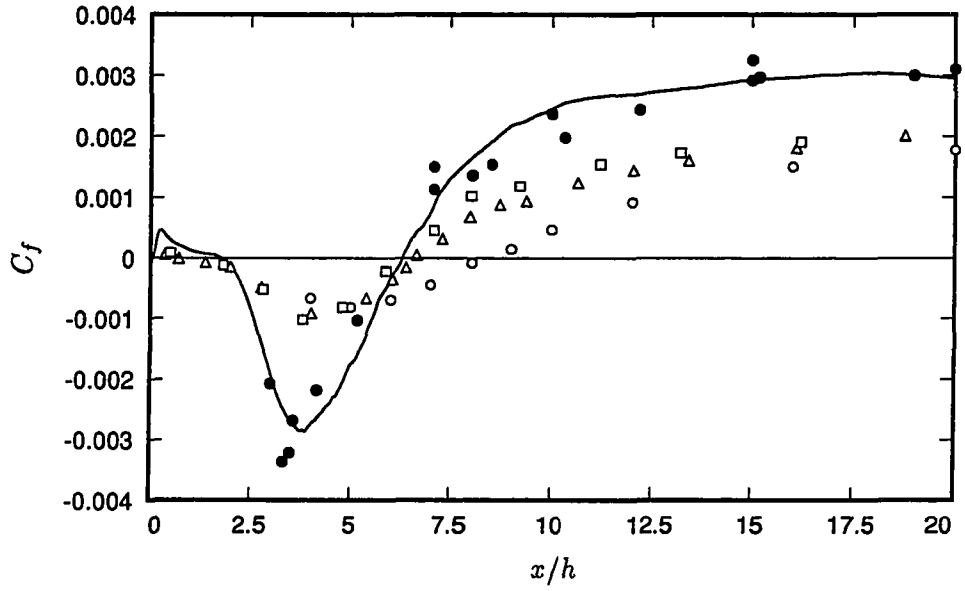

Figure 5.29. Comparison of BL6 and JD coefficient of friction with previous experiments. —— case BL6; • Jovic & Driver (1994); ▫ Driver & Seegmiller (1985); △ Adams *et al.* (1984); ○ Westphal *et al.* (1984) (CASE A).

Jovic & Driver (1995) also measured the skin friction in the reverse flow region for a wide range of Reynolds numbers. Their results show that the recirculation C_f decreases with increasing Reynolds number. This is shown in Fig. 5.30. The peak negative C_f reaches a value of approximately -1.0×10^{-3} at $Re_h \approx 20000$ which is the Reynolds number range used in many experiments. Thus the large negative skin friction in the current study and in the JD experiment is due to low Reynolds number effects. The low Reynolds number not only decreases the absolute value of the skin friction in the recirculation region, but also increases C_f in the recovery region as seen in Fig. 5.29. This high C_f in the recovery region results in a shift in the universal log-law of the near-wall velocity profiles which was previously observed in the preliminary 3-D results (§4.2). The discussion of the near-wall velocity profiles will be presented in §5.7.4.2.

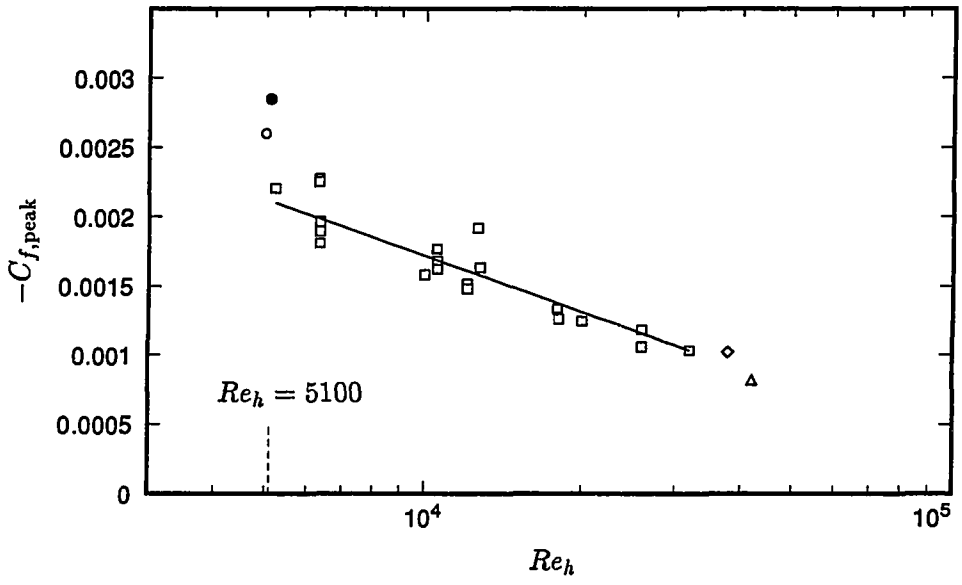

Figure 5.30. Peak negative C_f in recirculation region. △ Westphal *et al.* (1984) (CASE A); ◇ Driver & Seegmiller (1985); □ Jovic & Driver (1995); ○ Jovic & Driver (1994); • BL6.

5.7.3. Pressure Distribution

The mean static pressure distribution along the step wall is shown in Fig. 5.31. Also included in this figure is the pressure distribution from the coarse-grid case (BL5). The pressure coefficient C_p is defined as

$$C_p = \frac{P - P_0}{\frac{1}{2}\rho U_0^2},$$

where P_0 is the reference pressure taken at $2.5h$ before the step. The shift in C_p in the recirculation zone in Fig. 5.31(a) is related to the difference in reattachment lengths, X_r. Roshko & Lau (1965) and Westphal *et al.* (1984) suggested a renormalized streamwise coordinate to account for the difference in X_r: $x^* = (x - X_r)/X_r$. Figure 5.31(b) shows that the C_p curves become much closer in this normalized coordinate. It is evident from these figures that the grid resolution has very little effect on the pressure rise through the reattachment. The total pressure rise

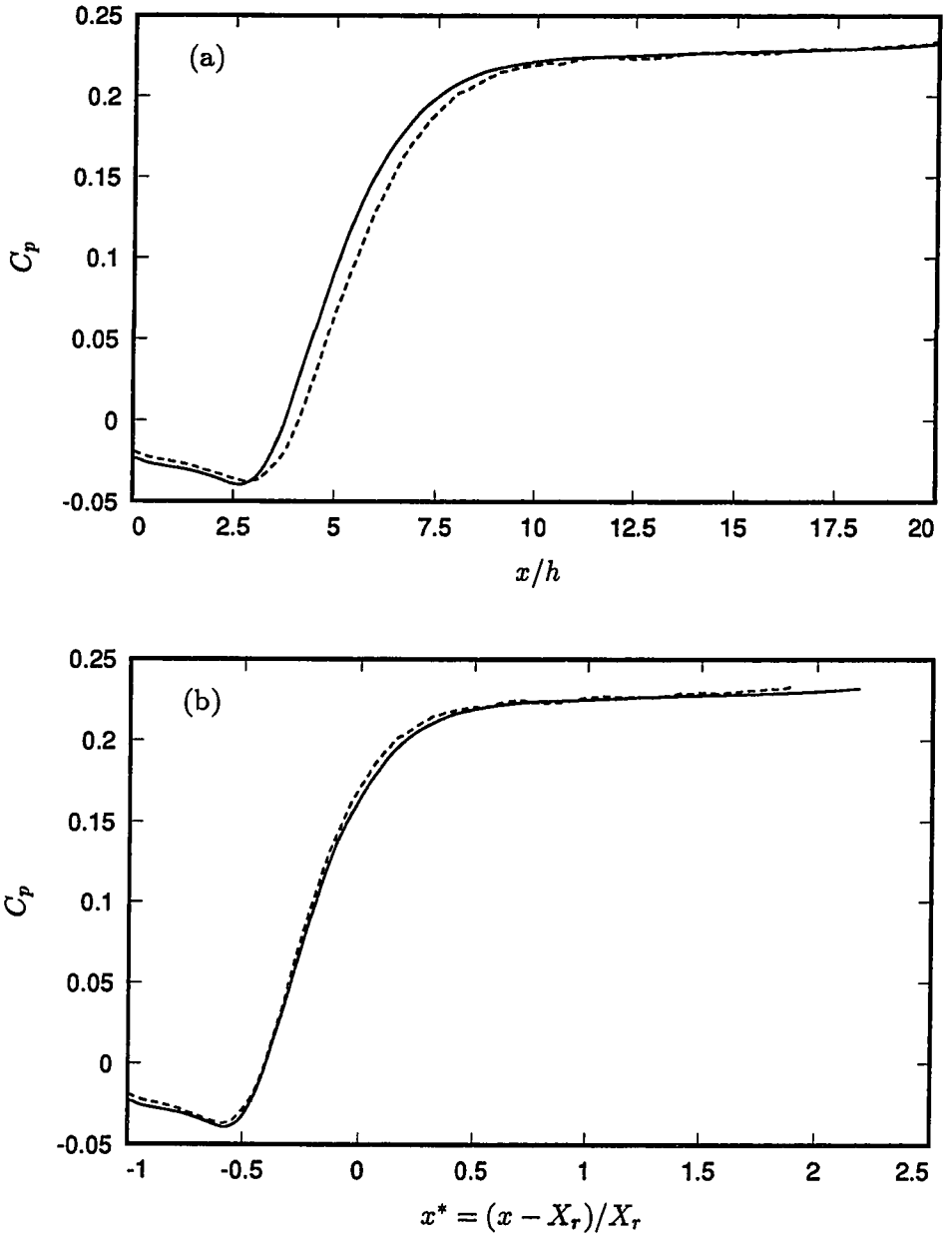

Figure 5.31. Step-wall pressure coefficient, DNS results. —— case BL6 ($768 \times 192 \times 64$); ---- case BL5 ($480 \times 128 \times 32$). (a) C_p as a function of x/h; (b) C_p as a function of $x^* = (x - X_r)/X_r$.

between the point of minimum pressure, $P_{\min}$, at $x^* = -0.60$ ($x/h = 2.52$) and $x^* = 0.59$ ($x/h = 10$) is $\Delta P = 0.26\rho U_0^2$.

The pressure coefficient is compared with results of several experiments in Fig. 5.32. All curves have nearly the same characteristic rise in pressure across

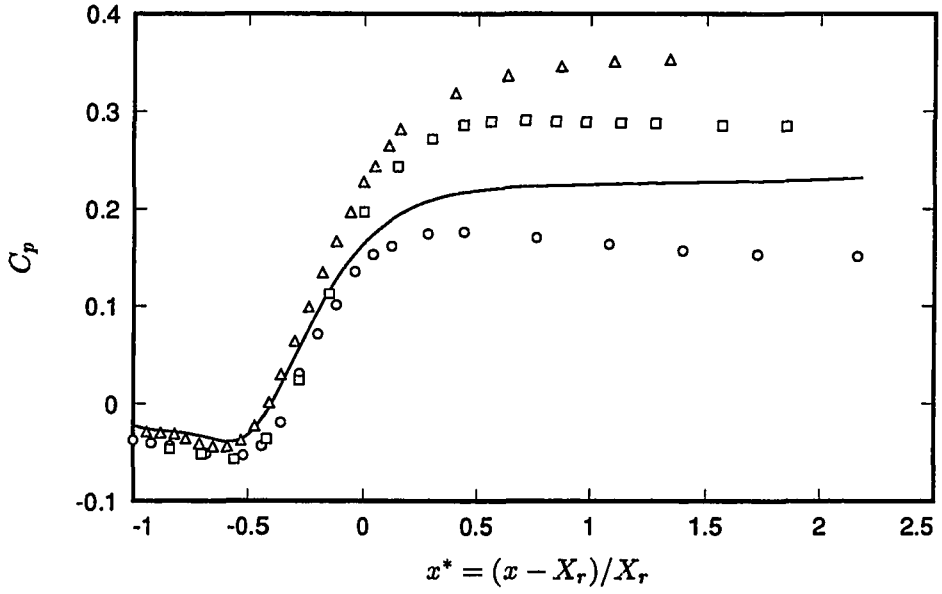

Figure 5.32. Step-wall pressure coefficient as a function of x^*. —— case BL6; o Driver and Seegmiller (1985); □ Kim *et al.* (1978) (STEP1); △ Westphal *et al.* (1984) (CASE A).

the recirculation zone, but diverge in the recovery region due to the differences in expansion ratio. As expected, the higher expansion ratios lead to a higher exit C_p (Driver & Seegmiller (1985) had the lowest expansion ratio of 1.125, and Westphal *et al.* (1984) had the highest, 1.67).

Several authors have suggested rescaling of C_p to collapse the pressure data from various geometries and inflow condition. Roshko and Lau (1965) used

$$\tilde{C}_p = \frac{C_p - C_{p,\min}}{1 - C_{p,\min}}$$

for incompressible flows. Another scaling, used by Kim *et al.* (1978), normalizes the pressure rise with the ideal pressure rise:

$$C_p^* = \frac{C_p - C_{p,\min}}{C_{p,BC} - C_{p,\min}},$$

where $C_{p,BC}$ is the ideal Borda-Carnot pressure recovery based only on the expansion ratio:

$$C_{p,BC} = \frac{2}{ER}\left(1 - \frac{1}{ER}\right).$$

Plots of C_p using these two scalings are shown in Fig. 5.33. The $\tilde{C}_p$ scaling collapses the data well near the step (Fig. 5.33(a)); and the C_p^* scaling works only in the recovery region (Fig. 5.33(b)). Neither method successfully collapses the data near and beyond the reattachment region.

Adams *et al.* (1984) examined the effect of various parameters on the pressure coefficient and concluded that the only upstream condition having significant effects on the pressure rise at reattachment is the boundary layer thickness δ/h. They also suggested that, if $\delta/h < 0.8$, the C_p curve will reach a peak value after the rise through the reattachment region, then decrease slightly in the recovery zone (e.g. data from Kim *et al.*, 1978); for larger δ/h, C_p will monotonically increase. However, this behavior does not hold for the data from Driver & Seegmiller (1985); although $\delta/h = 1.5$, their C_p curve has a peak at $x^* \approx 0.4$ (Fig. 5.33(b)).

In Fig. 5.34, the pressure coefficient of BL6 is compared to JD data. Since the JD experiment has a double expansion configuration (see §5.4), C_p values at both bottom and top walls are included in Fig. 5.34, showing symmetry in their experiment. The reference pressure P_0 is at $x/h = -5.0$ for both BL6 and the JD data. The agreement between computational and experimental results is excellent in the recirculation as well as reattachment regions. It should be noted that this agreement is achieved without relying on any normalization of data suggested earlier.

The *rms* wall pressure fluctuations is shown in Fig. 5.35. The wall pressure fluctuations peak near the reattachment location and decreases downstream, an observation made by Farabee & Casarella (1988). The deficiency of the convective

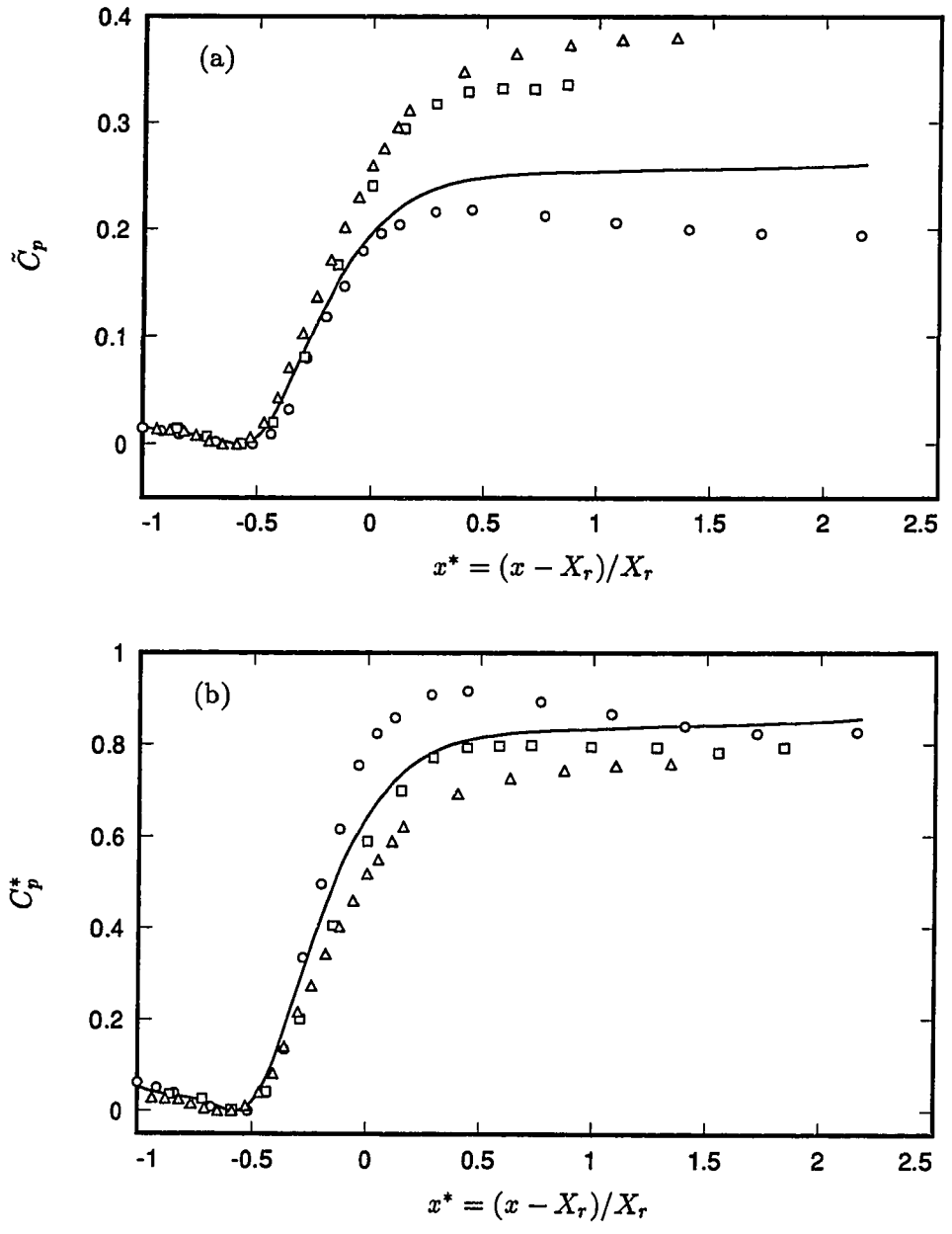

Figure 5.33. Normalized step-wall pressure coefficient as a function of x^*. —— case BL6; ○ Driver and Seegmiller (1985); □ Kim *et al.* (1978); △ Westphal *et al.* (1984). (a) $\tilde{C}_p = \frac{C_p - C_{p,\min}}{1 - C_{p,\min}}$; (b) $C_p^* = \frac{C_p - C_{p,\min}}{C_{p,BC} - C_{p,\min}}$.

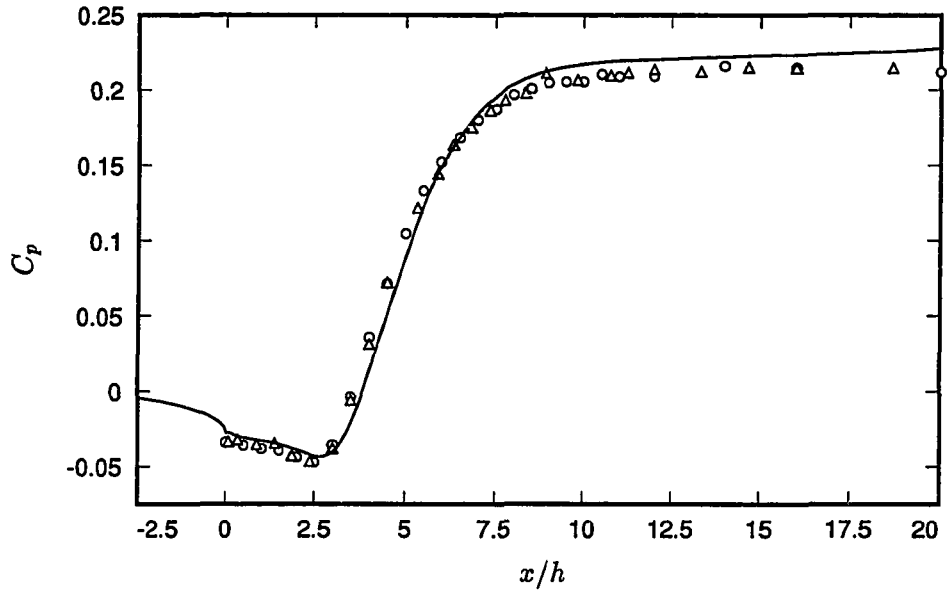

Figure 5.34. Comparison between BL6 and JD experiment step-wall pressure coefficient. —— case BL6; o Jovic & Driver (1994) bottom wall; △ Jovic & Driver (1994), top wall.

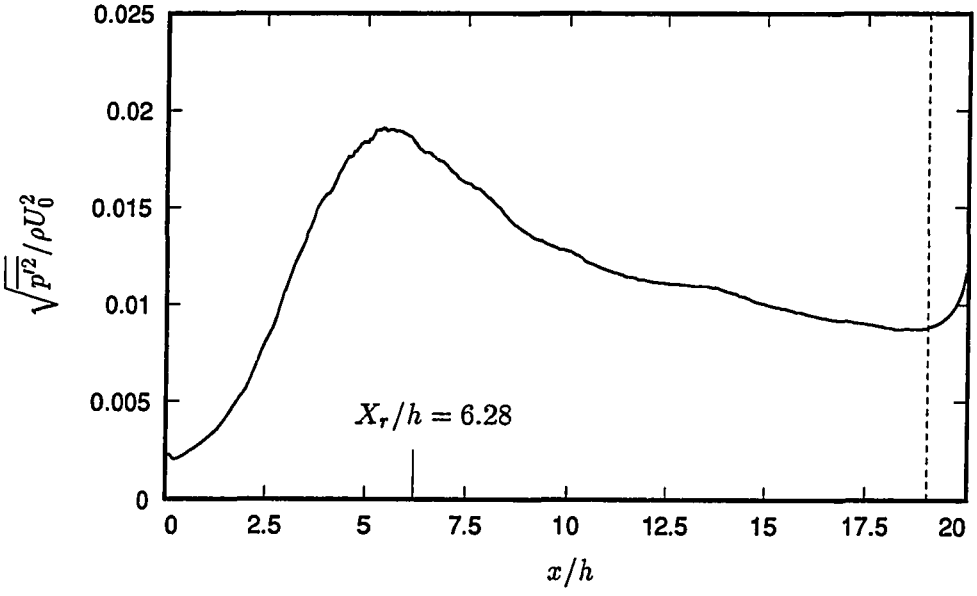

Figure 5.35. Root-mean-square pressure fluctuation at bottom wall.

outflow condition is evident in the behavior of $\sqrt{\overline{p'^2}}$ near the exit. Figure 5.35 indicates that $\overline{p'^2}$ within one step height from the exit is affected by the boundary condition.

The streamwise evolution and the contour plots of both the mean pressure and root-mean-square (*rms*) pressure fluctuations are shown in Figs. 5.36 through 5.39. The reference pressure P_0 is at $x/h = -5.0$ and $y/h = 1.0$ for both Figs. 5.36 and 5.37. Note that in the free stream ($y/h > 2.0$), the flow has a favorable pressure gradient up to $x/h \approx 2.5$. Similar to the LES results of Friedrich & Arnal (1990), the *rms* fluctuations are highest in the free-shear layer near the step.

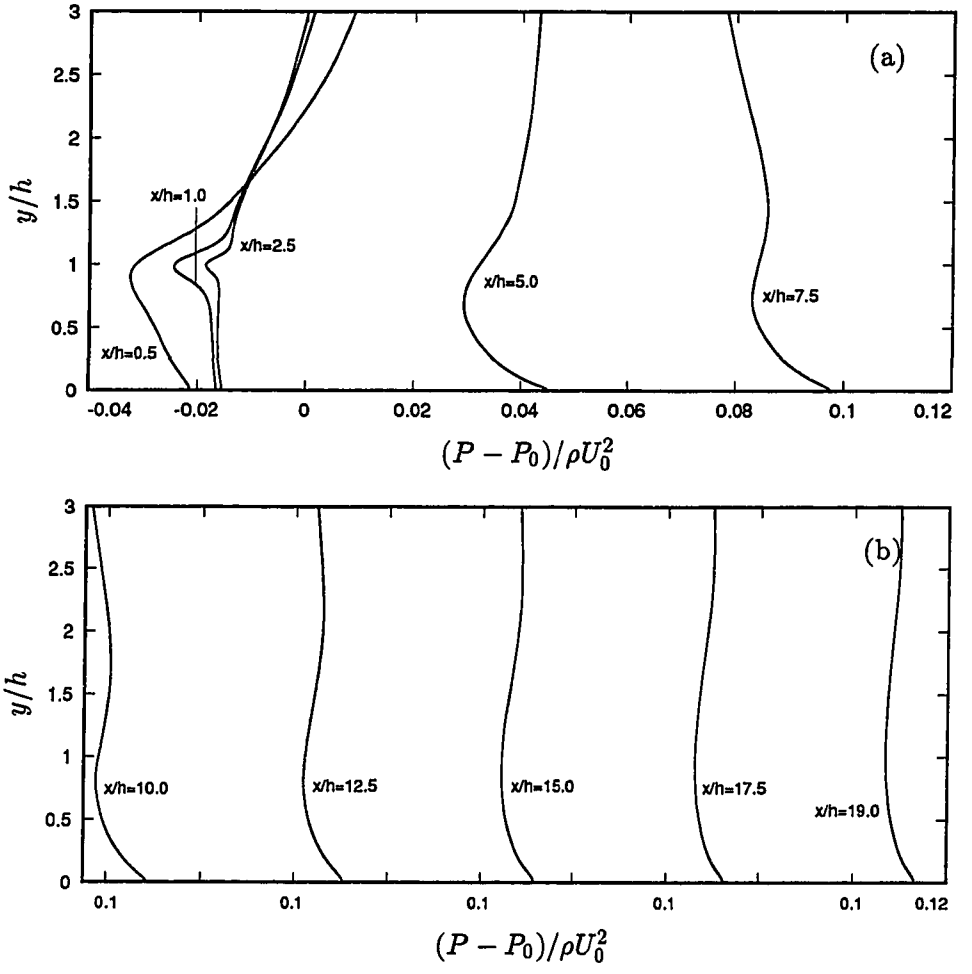

Figure 5.36. Mean pressure profiles, $(P - P_0)/\rho U_0^2$. (a) Recirculation and reattachment regions; (b) recovery region.

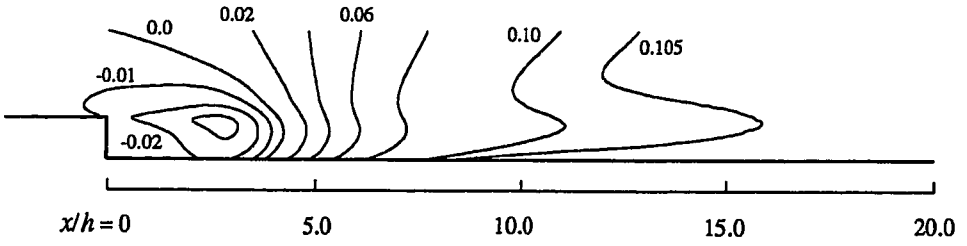

Figure 5.37. Contours of mean pressure, $(P - P_0)/\rho U_0^2$.

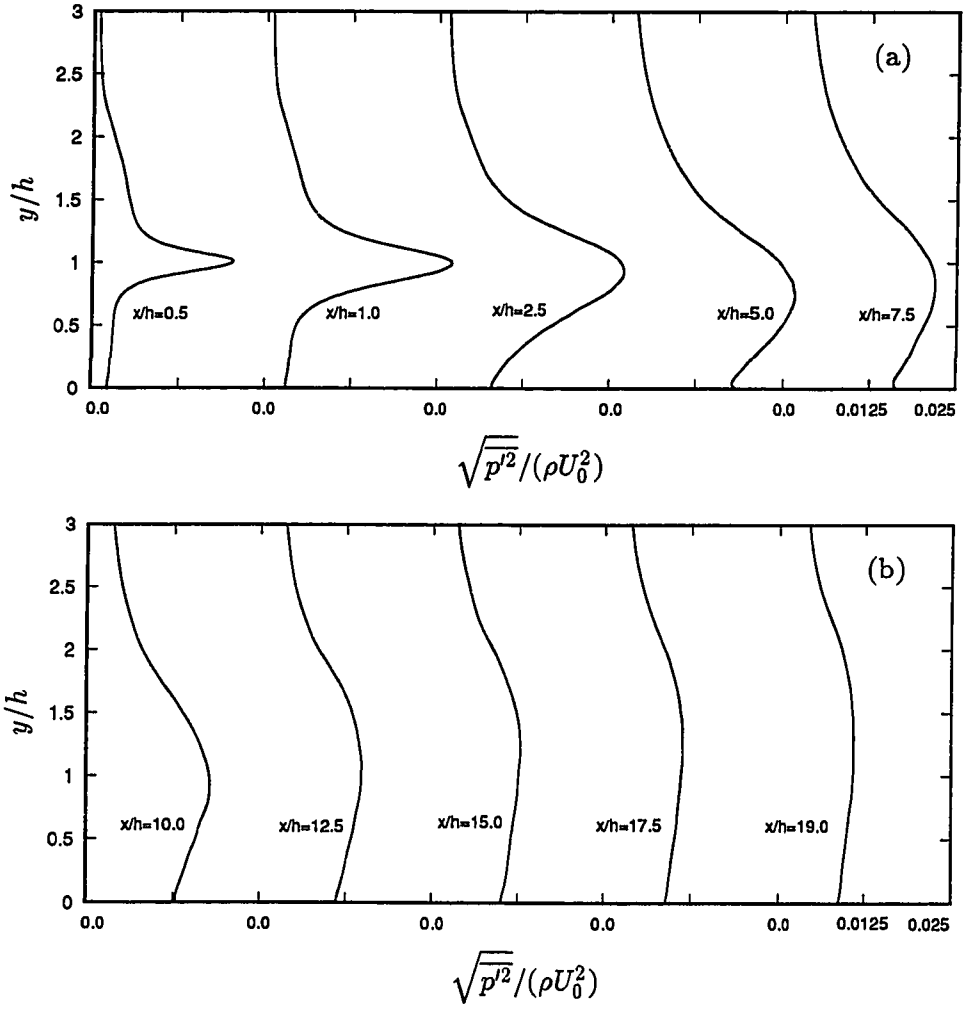

Figure 5.38. Profiles of *rms* pressure fluctuations. (a) Recirculation and reattachment regions; (b) recovery region.

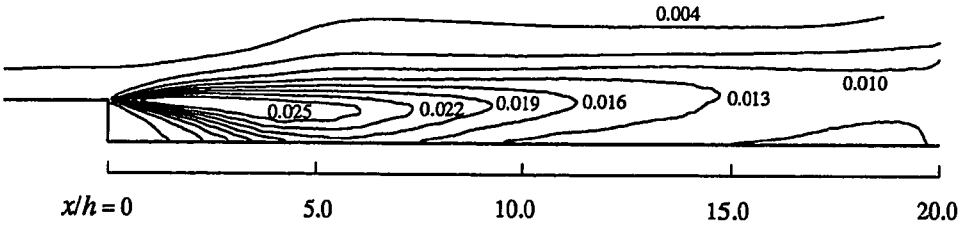

Figure 5.39. Contours of *rms* pressure fluctuations, $\sqrt{\overline{p'^2}}/\rho U_0^2$.

5.7.4. Velocity Field

This section presents several aspects of the mean velocity field. Quantities of interest are the mean streamwise velocity profiles and integral parameters, the near-wall behavior of the mean velocity profile behind the reattachment point, and the mean velocity in the recirculation region.

5.7.4.1. Mean and Defect Velocity Profiles

Figure 5.40 presents the comparison between BL6 results and JD experiment for the streamwise velocity profiles. The comparison is made at four representative locations in recirculation, reattachment and recovery regions. Excellent agreement between computational and experimental results is obtained at all locations.

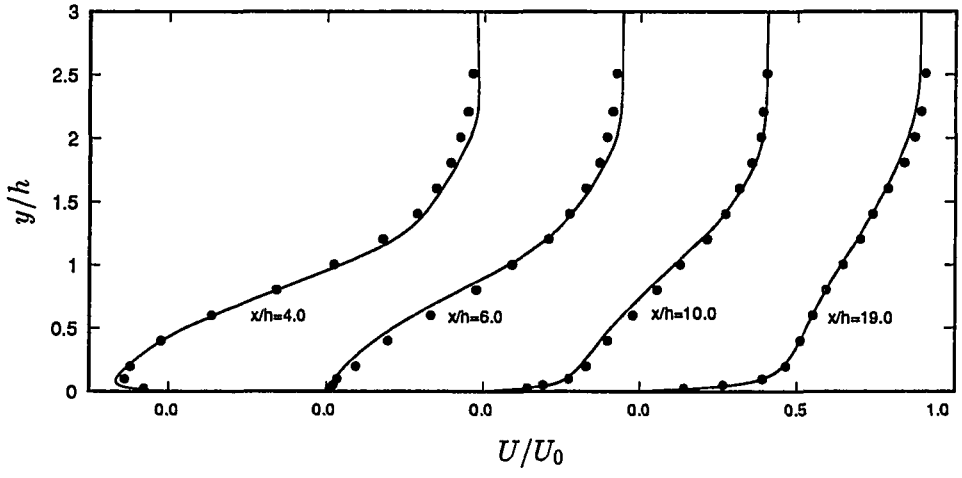

Figure 5.40. Comparison of mean streamwise velocity profiles, BL6 and JD experiment. —— case BL6; • Jovic & Driver (1994).

The mean streamwise velocity profiles at x-stations throughout the domain behind the step are shown in Fig. 5.41; and Fig. 5.42 presents the mean velocity contours. In the recovery region, the velocity at $x/h = 19.0$ has an inflection point indicating that an equilibrium boundary layer profile is not yet recovered. Bradshaw & Wong (1972) observed profiles with an inflection point at 50 step

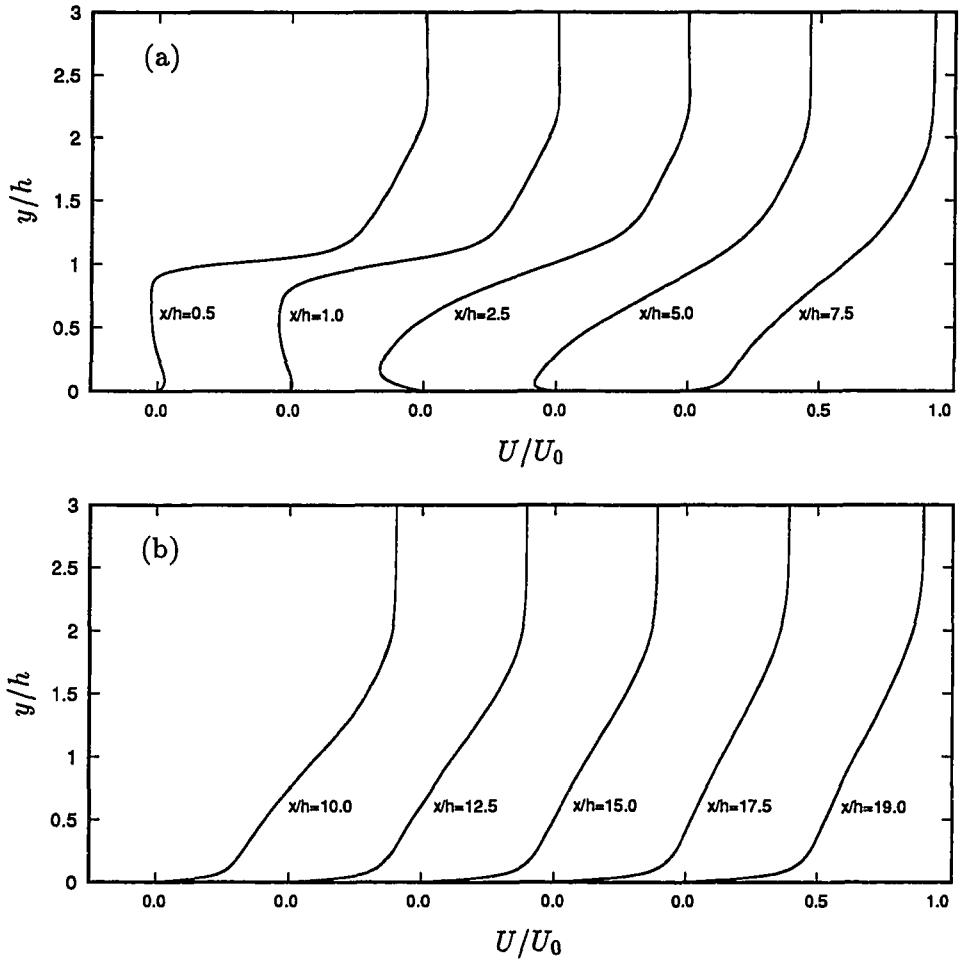

Figure 5.41. Mean streamwise velocity profiles. (a) Recirculation and reattachment regions; (b) recovery region.

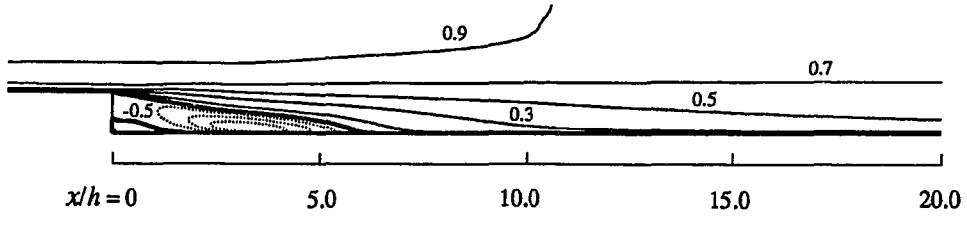

Figure 5.42. Mean streamwise velocity contours. ····· negative; —— positive; heavy line indicates contours of $U = 0.0$.

heights downstream from the step. Farabee & Casarella (1988) also found that even at $72h$ downstream of reattachment, the pressure field was not fully recovered.

The approach to equilibrium in the recovery region can be seen in Fig. 5.43, where U is plotted in the defect coordinates (Kays & Crawford, 1980) at three locations, $x/h = 10.0$, 15.0, and 19.0. The velocity defect coordinates are defined as:

$$\frac{U - U_e}{u_\tau} = f\left(\frac{y}{\delta_3}\right), \qquad \delta_3 = -\int_0^\infty \frac{U - U_e}{u_\tau} dy,$$

with U_e being the boundary layer edge velocity. In these coordinates, the outer-region similarity is attained independently of the streamwise locations if the boundary layer is in equilibrium. It is clear in Fig. 5.43 that the profiles are approaching

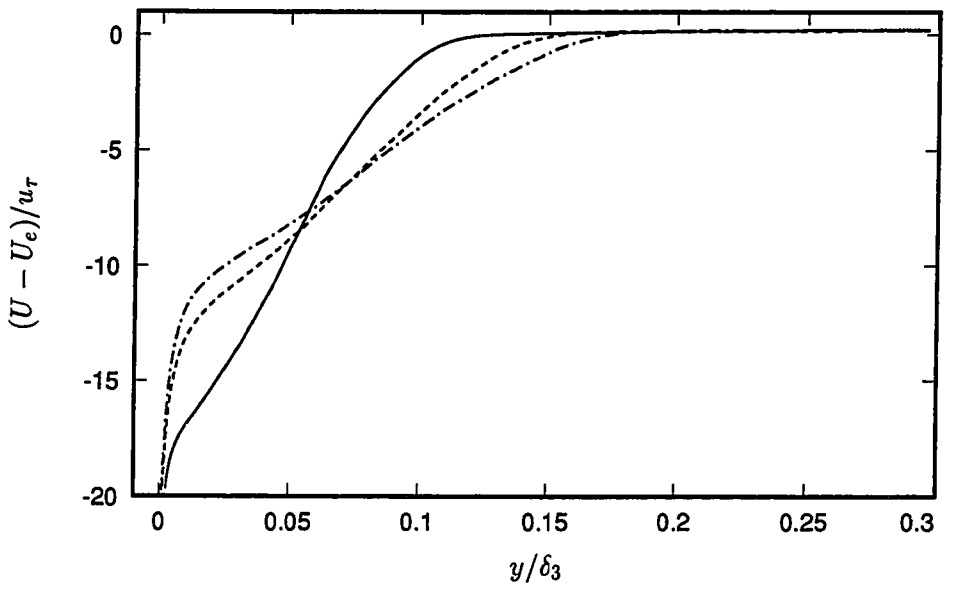

Figure 5.43. Velocity profiles in defect coordinates. —— $x/h = 10.0$; ---- $x/h = 15.0$; —·— $x/h = 19.0$.

but do not reach self-similarity at the exit. This is also the characteristic of boundary layer profiles in an adverse pressure gradient (APG) (see for example, Schraub & Kline, 1965, Kline *et al.*, 1967). The equilibrium condition may be determined

by the Clauser shape factor G, defined as:

$$G = \int_0^\infty \left(\frac{U - U_e}{u_\tau}\right)^2 d\left(\frac{y}{\delta_3}\right).$$

The streamwise variation of the Clauser shape factor G is shown in Fig. 5.44. Also shown is the shape factor $H = \delta^*/\theta$. The Clauser shape factor is ∞ at the reattachment point because $u_\tau = 0$, and decreases to ≈ 10 near the domain exit. In a study of APG flows having pressure gradient parameters similar to the exit conditions here, Andersen *et al.* (1972) measured values near $G \approx 7.1$.

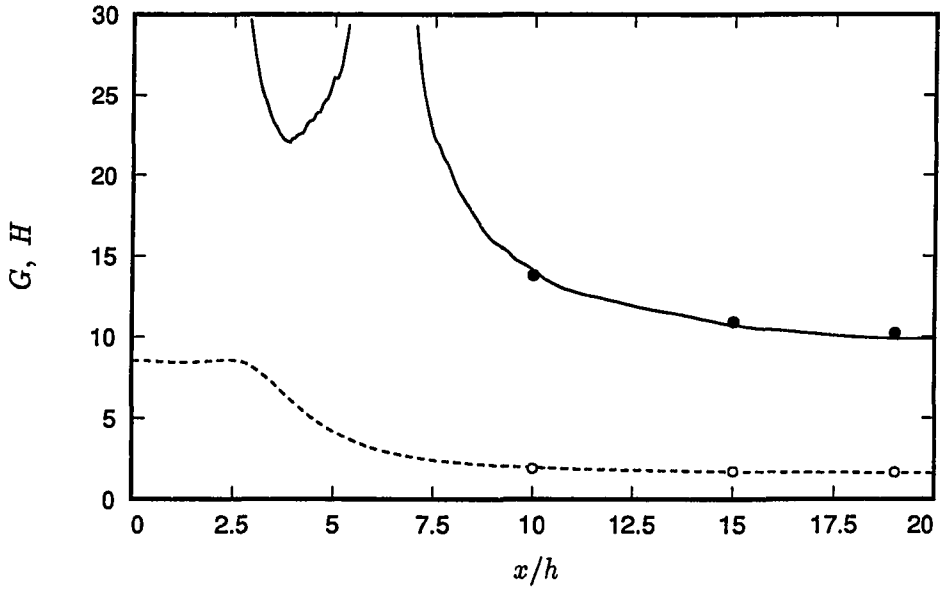

Figure 5.44. Shape factors. Clauser shape factor G: —— BL6; • Jovic & Driver (1994). H: ---- BL6; o Jovic & Driver (1994).

Finally, the displacement and momentum thicknesses from both BL6 and the JD experiment are plotted in Fig. 5.45. The agreements with the JD experiment are very good.

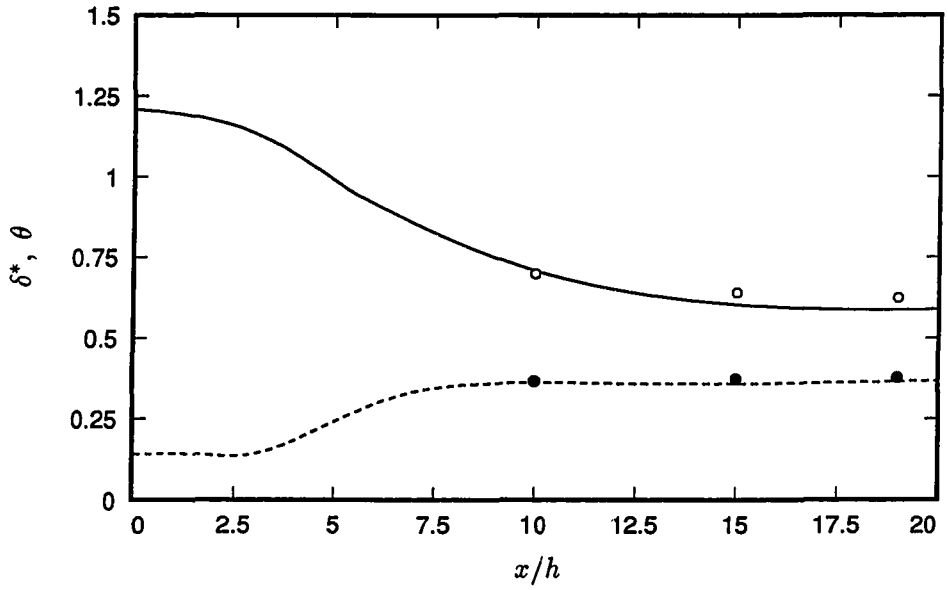

Figure 5.45. Displacement ant momentum thicknesses. δ^*: —— BL6; • Jovic & Driver (1994). θ: ---- BL6; o Jovic & Driver (1994).

5.7.4.2. Wall-Shear Velocity and the Law of the Wall

Figure 5.46 shows the progression of the near wall velocity profiles in the recovery region. The profiles are below the universal log-law even at $20h$ downstream of the step. Previous experimental studies reported a recovery of the log-law profile even as early as 6 step heights after the reattachment, e.g., Westphal *et al.* (1984), Kim *et al.* (1978), and Adams *et al.* (1984). The preliminary 3-D simulations (Chapter 4) indicated that, in the range considered, the grid resolution as well as the upstream conditions have no effect on the recovery profiles. The excellent agreement between the BL6 and JD profiles at $x/h = 19.0$, shown in Fig. 5.47, confirms that the deviation from the universal log-law is a real behavior in this flow. The apparent discrepancy between the present near-wall profiles and previous experiments is attributed to the method of obtaining the wall-shear velocity u_τ. In previous experiments, the wall-shear velocity was calculated using the Clauser chart with the inherent assumption that the log-law of the zero-pressure gradient

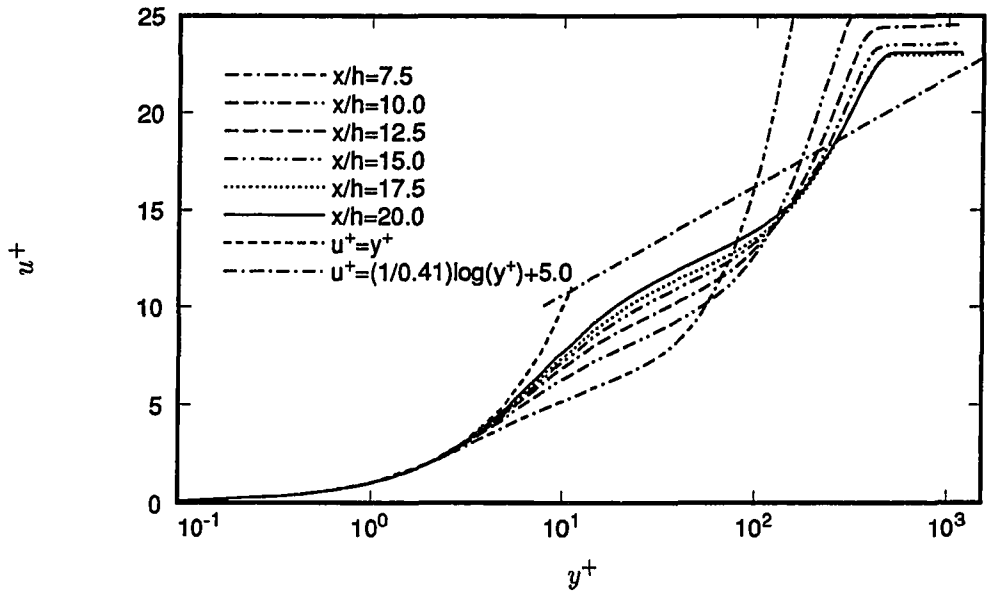

Figure 5.46. Progression of mean streamwise velocity profiles in wall coordinates.

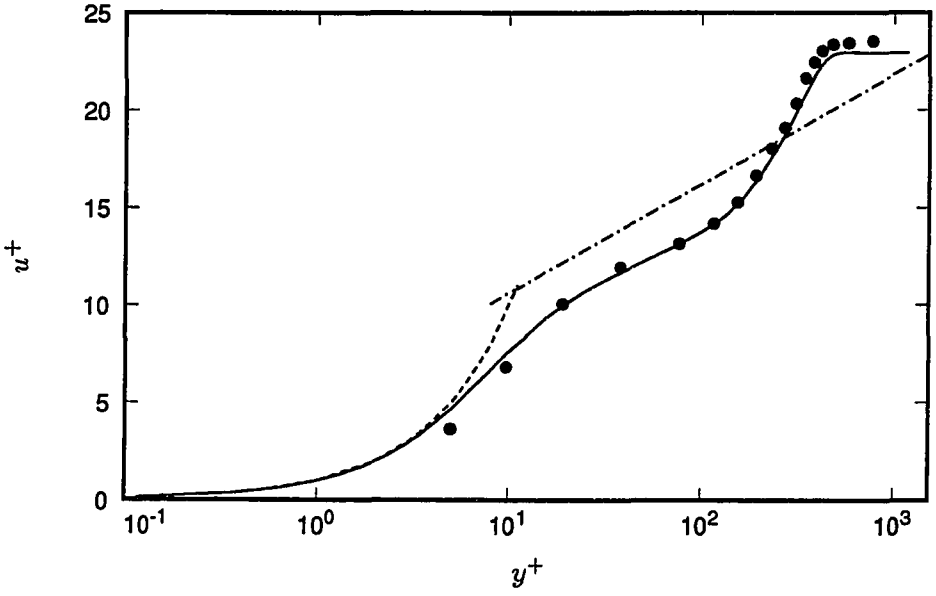

Figure 5.47. Mean streamwise velocity profiles in wall coordinates at $x/h = 19.0$. ---- $u^+ = y^+$; —·— $u^+ = \frac{1}{0.41}\log y^+ + 5.0$; —— computation (case BL6); • Jovic & Driver (1994).

turbulent boundary layer is applicable. The result was lower values of u_τ, hence higher u^+ values. The JD data in Fig. 5.47 were based on C_f directly measured by a laser interferometer, and not relying on the Clauser chart. Direct C_f measurements using a pulsed wall probe by Westphal *et al.* (1984) confirm that the correct shear velocity in this flow region is indeed higher than that predicted by the Clauser chart. In the present configuration, this discrepancy is as high as 17%, i.e., $U_\tau/u_{\tau_c} \approx 1.17$, where the subscript c denotes the value obtained using the Clauser chart. Westphal *et al.*'s (1984) velocity profiles with their directly measured u_τ are plotted in Fig. 5.48. Their profiles did fall below the log-law at $x/h = 12.0$ and 16.0 but recovered at $x/h = 20.0$. A much higher Reynolds number in Westphal *et al.*'s (1984) experiment ($Re_h = 4.2 \times 10^4$) appears to accelerate the recovery of the log-law.

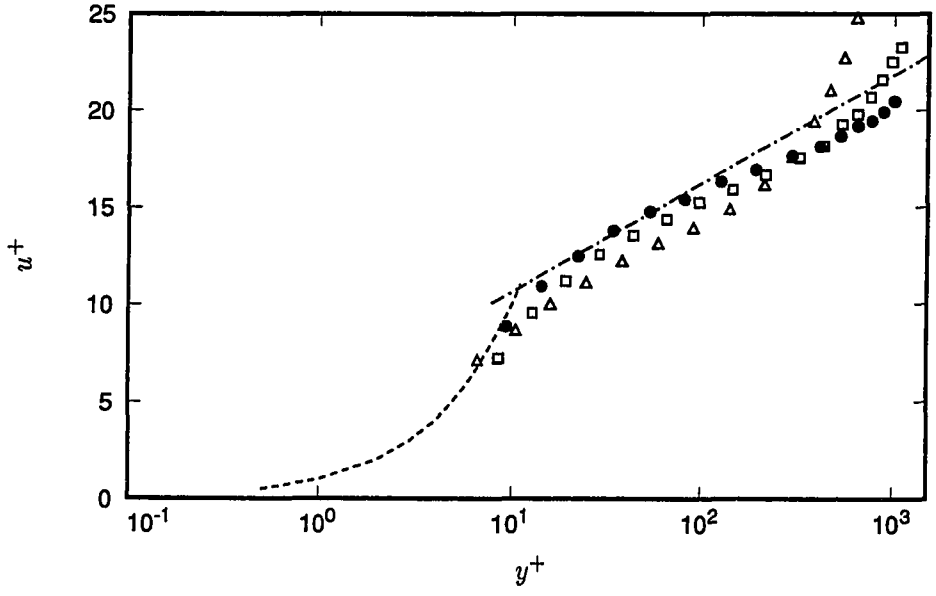

Figure 5.48. Mean streamwise velocity profiles in wall coordinates, Westphal *et al.* (1984). ---- $u^+ = y^+$; —·— $u^+ = \frac{1}{0.41}\log y^+ + 5.0$; △ $x/h = 12.0$; □ $x/h = 16.0$; • $x/h = 20.0$.

The deviation of the velocity profile from the log-law appears to be resulted from the strong streamwise adverse pressure gradient (APG) which is experienced by the flow following the sudden expansion. Although the effect of APG on a boundary layer has been studied by many authors, the universal log-law was still considered applicable because of the use of Clauser chart as mentioned above. A re-evaluation of the applicability of the log-law in non-zero pressure gradient flows was recently conducted by Nagano *et al.* (1991). They concluded that the mean velocity profile does indeed shift downward from the standard log-law in an APG. Figure 5.49 shows the velocity profile from Nagano *et al.*'s (1991) data at $P^+ = 2.5 \times 10^{-2}$, where P^+ is a non-dimensional pressure gradient parameter defined as:

$$P^+ = \frac{\nu}{u_\tau^3}\frac{\partial P}{\partial x}.$$

The same deviation from the log-law is observed in Fig. 5.49. Studies by Driver (1991) of flows with adverse pressure gradient also support this finding.

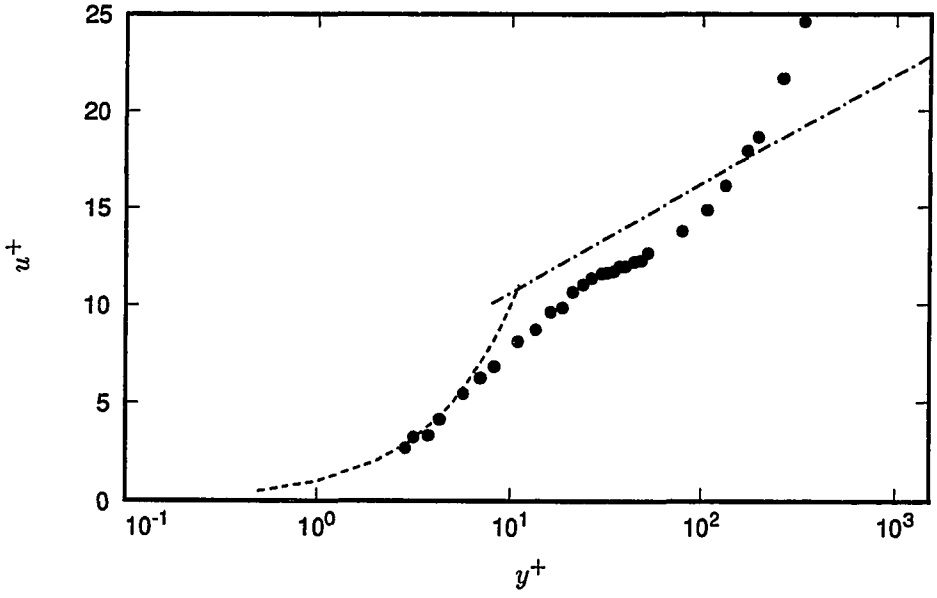

Figure 5.49. Mean streamwise velocity profiles subject to an APG in wall coordinates. ---- $u^+ = y^+$; —·— $u^+ = \frac{1}{0.41}\log y^+ + 5.0$; • Nagano *et al.* (1991), $P^+ = 2.5 \times 10^{-2}$.

Compared to the pressure gradient parameter P^+ in Nagano *et al.*'s (1991) data, the APG in the recovery region of JD experiment and of the current simulation is much less severe (P^+ decreases from 1×10^{-2} to 5×10^{-3} in the range $10.0 < x/h < 19.0$). On the other hand, Westphal *et al.*'s (1984) experiment, with a pressure gradient similar to BL6, shows a quicker recovery to the log-law. It should be noted that P^+, which represents the ratio of the axial pressure force to wall shear force, is inversely proportional to u_τ^3 or $C_f^{3/2}$. As shown in §5.7.2, the calculated C_f is high due to low Reynolds number effects; this contributes to the low P^+ values in the current simulation and JD experiment compared to Nagano *et al.*'s (1991) data. Recall that the velocity profiles in Westphal *et al.*'s (1984) experiment approach the log-law more quickly (Fig. 5.48) for a similar pressure gradient. Therefore, adverse pressure gradient alone does not fully account for the departure from the log-law, but the low Reynolds number also appears to have an effect on the rate of approach to recovery.

5.7.4.3. Recirculation Region

In the recirculation, the law of the wall for attached flows does not hold. The back flow appears to behave more like a laminar flow (Adams *et al.*, 1984). Simpson (1983) and Simpson *et al.* (1990) provided scaling parameters that collapsed the velocity profiles in a separated flow. Simpson (1983) proposed three layers for these profiles. The scaling distance is N, the distance from the wall to the maximum mean negative velocity U_N. The three layers are (a) the inner layer, $y/N < 0.02$, where viscous effects are important and $u^+ = y^+$ holds; (b) the outer layer, $y/N > 1$, which has a linear profile; and (c) the overlap layer, $0.02 < y/N < 1$. The proposed empirical relation for the overlap layer is:

$$\frac{U}{|U_N|} = A\left[\frac{y}{N} - \log\left(\frac{y}{N}\right) - 1\right] - 1, \tag{5.1}$$

where the constant A was selected to be 0.3 based on Simpson *et al.*'s (1990) data. Adams *et al.* (1984) applied this relation to their backward-facing step data but Eq. (5.1) did not provide a good representation of their data. Figure 5.50 presents

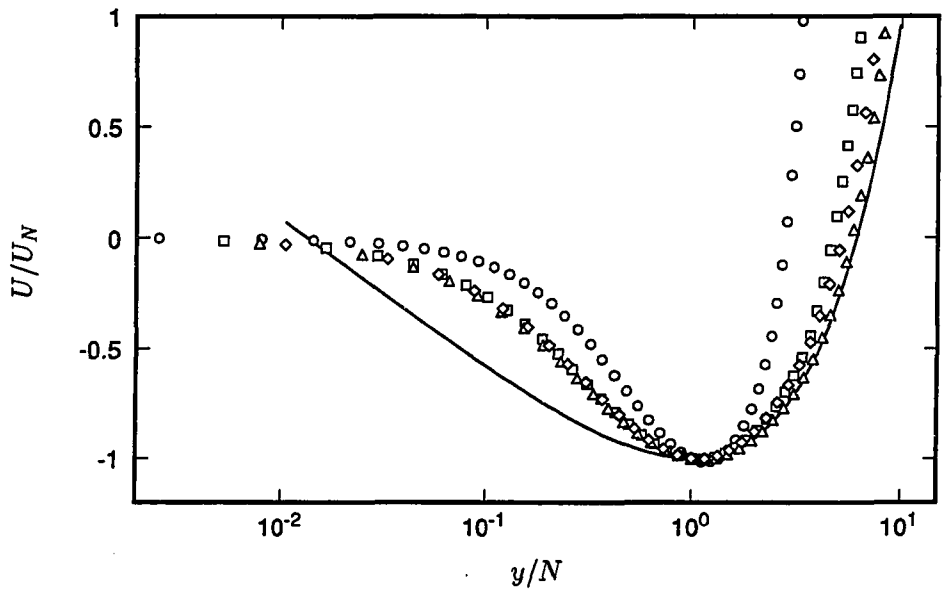

Figure 5.50. Normalized recirculation mean velocity profiles, U/U_N vs y/N. ○ $x/h = 2.0$; □ $x/h = 3.0$; △ $x/h = 4.0$; ◇ $x/h = 5.0$; —— Simpson's (1983) model, Eq. (5.1) with $A = 0.3$.

the velocity profiles at three locations in the recirculation, plotted in the coordinates suggested by Simpson *et al.* (1990). Also plotted for comparison is the relation in Eq. (5.1). Simpson's (1983) correlation with $A = 0.3$ deviate from the computed profiles by as much as 45% in the overlap layer ($0.02 < y/N < 1$). An adequate collapse is seen for locations in the range $3 < x/h < 5$. The similarity does not hold as one moves closer to the zero-velocity points (reattachment, $x/h = 6.28$, and secondary bubble, $x/h = 1.74$).

Adams *et al.* (1984) attempted to establish a skin friction law of the form $C_f = F(U, N)$. Assuming a universal profile does exist in the backflow region, i.e., $U/U_N = f(y/N)$, then one would obtain:

$$C_{f,U_N} = \frac{f'(0)}{Re_N}, \tag{5.2}$$

where C_{f,U_N} is the friction coefficient normalized by $\frac{1}{2}\rho U_N^2$, and Re_N is the Reynolds number based on U_N and N. In other words, $C_{f,U_N} \propto Re_N^{-1}$ which is typical for

laminar boundary layers. Data from the current simulation are shown in Fig. 5.51. The data do not quite follow the -1 slope (≈ -0.92) but are much closer to the laminar relation than shown by Adams *et al.* (1984). They speculated that the slope would be $-\frac{1}{2}$ instead of -1 based on their data. However, with high uncertainty level in the backflow C_f measurements, and too few available data points, clear conclusion could not be reached. The C_{f,U_N} correlation from the computational results is

$$C_{f,U_N} \approx 4.5 Re_N^{-0.92}. \tag{5.3}$$

It should be noted in Fig. 5.51 that this relation also holds even for locations in the secondary vortex.

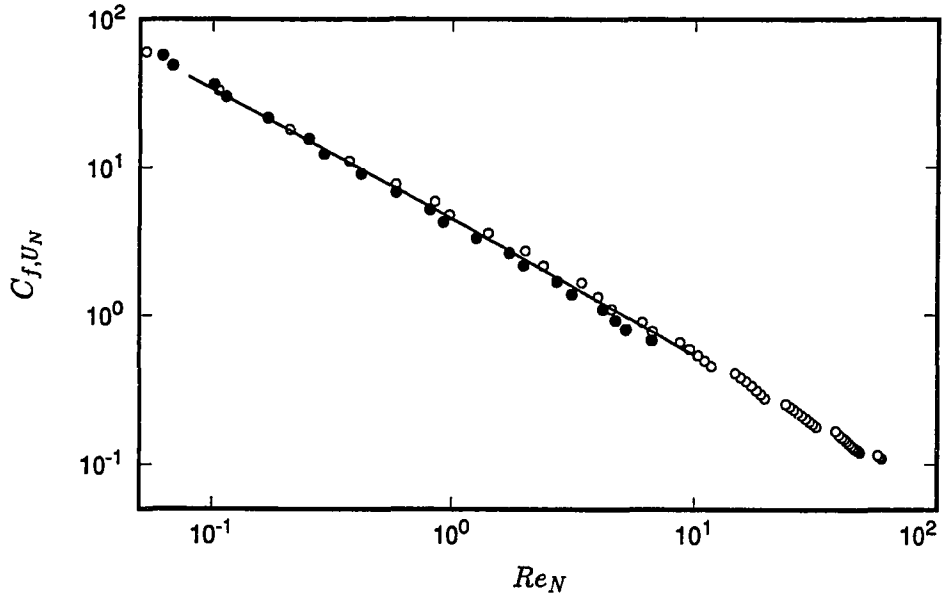

Figure 5.51. Skin friction in recirculation region as a function of wall-layer Reynolds number. o primary vortex; • secondary vortex; —— $C_{f,U_N} = 4.5 Re_N^{-0.92}$.

5.7.4.4. Vertical Velocity Profiles

The profiles of mean vertical component of the velocity, V, and its contours are plotted in Figs. 5.52 and 5.53, respectively. Inside the recirculation region, positive V (flow away from the wall) occurs in the region $x/h < 4.0$. The maximum positive V is approximately $0.04U_0$. The flow experiences the strongest downward turn just upstream of reattachment ($x/h \approx 5.0$). The maximum (negative) mean vertical velocity at this point is $V = -0.073U_0$. After $x/h \approx 15.0$, most of the mean vertical motion has diminished. At $x/h = 19.0$, there is still a very slight downward motion ($V_{\max} \approx -2.8 \times 10^{-3}U_0$). As mentioned in §5.6.2, although the mean vertical velocity is small, its instantaneous values can be up to 60% of inlet free stream velocity U_0 occurring at $0.5 < y/h < 0.9$ and $2.5 < x/h < 5.0$.

5.7.5. Turbulence Intensities and Reynolds Shear Stresses

The *rms* profiles of the longitudinal and vertical velocity fluctuations ($\sqrt{\overline{u'^2}}$, $\sqrt{\overline{v'^2}}$), and the Reynolds shear stress component ($\overline{u'v'}$) are compared with JD results at four streamwise locations in Figs. 5.54 and 5.55. The agreement between BL6 and JD results are excellent for all Reynolds stress components. Just after the reattachment zone, the near wall peak in the JD streamwise turbulence intensity appears to develop earlier than BL6 ($x/h = 10.0$).

The streamwise evolutions and contours of all four Reynolds stress components, $\sqrt{\overline{u'^2}}$, $\sqrt{\overline{v'^2}}$, $\sqrt{\overline{w'^2}}$ and $\overline{u'v'}$ are displayed in Figs. 5.56–5.63. All *rms* values are normalized to the inlet free-stream velocity U_0, and $\overline{u'v'}$ to U_0^2. For $x/h < 1.5$, the *rms* profiles in all three directions show a sharp increase at the step (Figs. 5.56–5.60). It will be shown later that, although these locations are very close to the step, the sharp rises are not a manifestation of the singular point at the step corner. Inside the recirculation region, the longitudinal turbulence intensity ($\sqrt{\overline{u'^2}}$) rises from zero at the wall to a first small peak at $y/h \approx 0.1$ (Fig. 5.56(a), $x/h = 2.5$). The distance from the wall to the first intensity peak is roughly the same distance N from the wall to the maximum reverse flow velocity U_N (see §5.7.4.3). The small

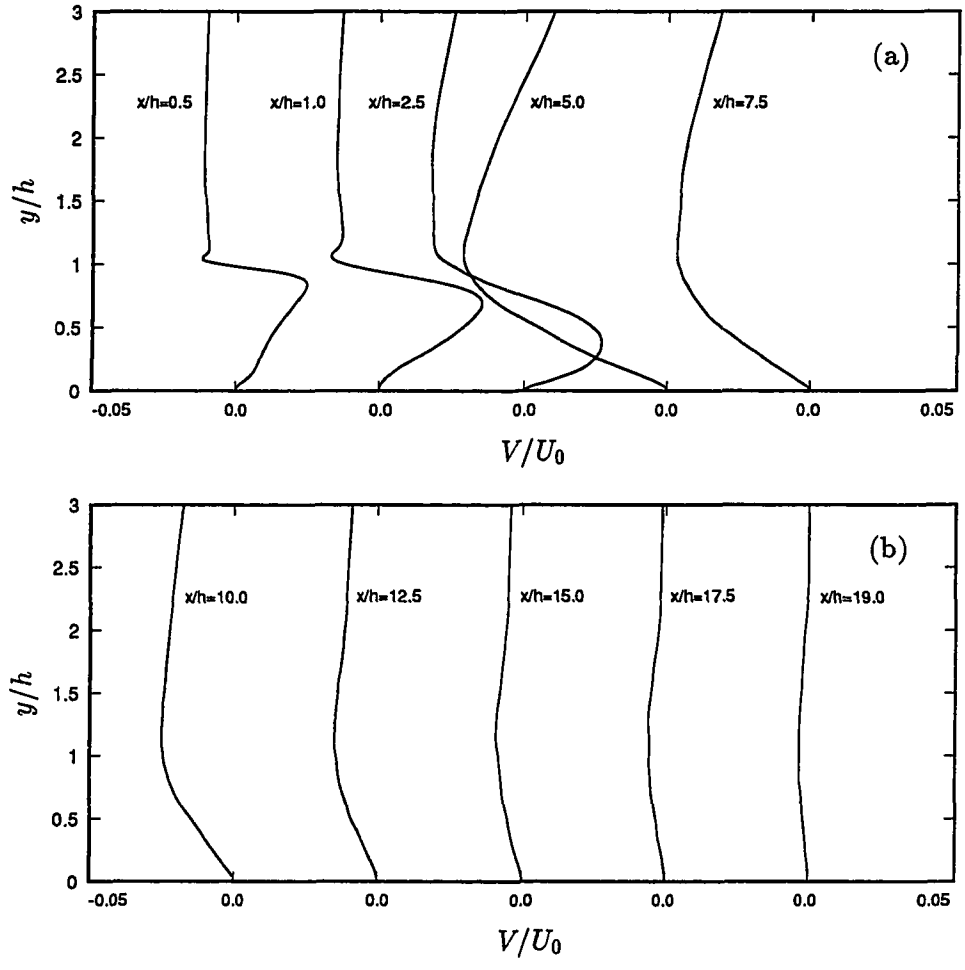

Figure 5.52. Mean vertical velocity profiles. (a) Recirculation and reattachment regions; (b) recovery region.

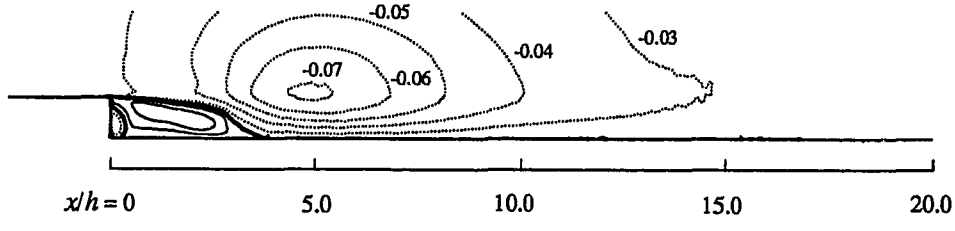

Figure 5.53. Mean vertical velocity contours. ····· negative; —— positive; heavy lines indicate contours of $V = 0.0$.

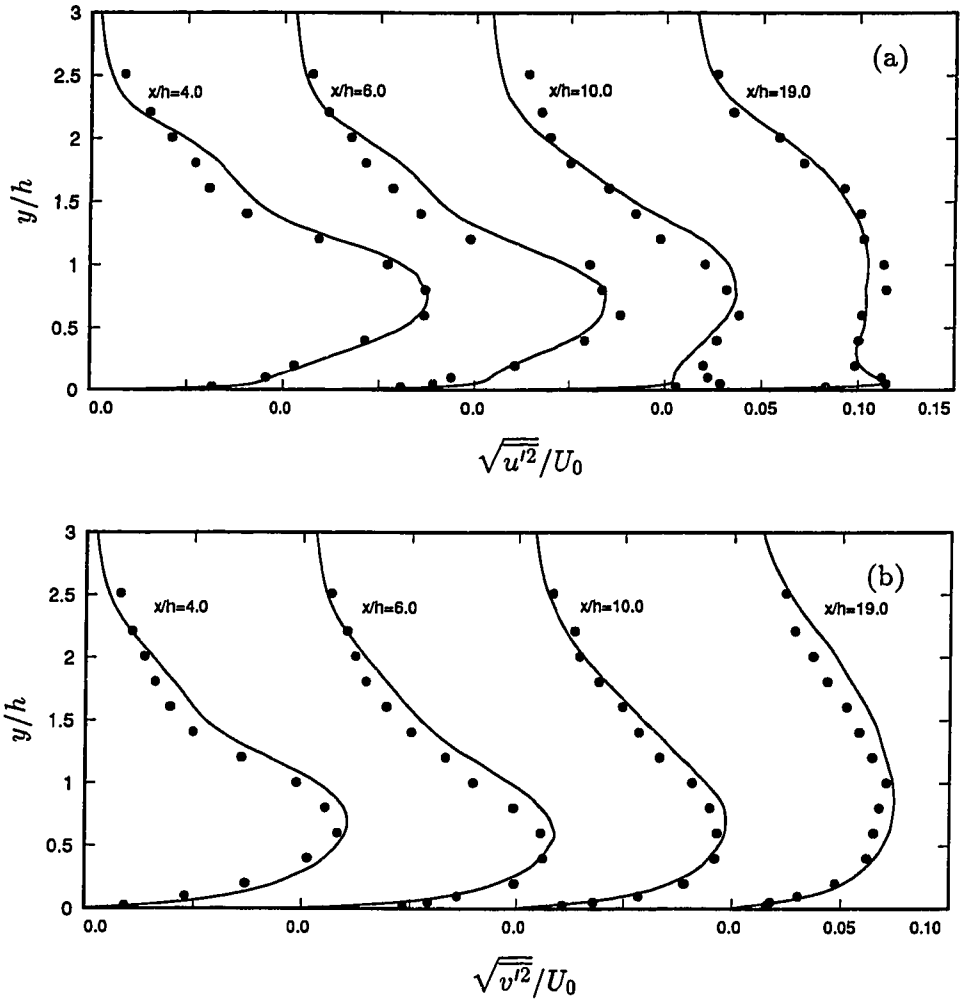

Figure 5.54. Comparison of BL6 and JD turbulence intensity profiles. —— BL6; • Jovic & Driver (1994). (a) $\sqrt{\overline{u'^2}}/U_0$; (b) $\sqrt{\overline{v'^2}}/U_0$.

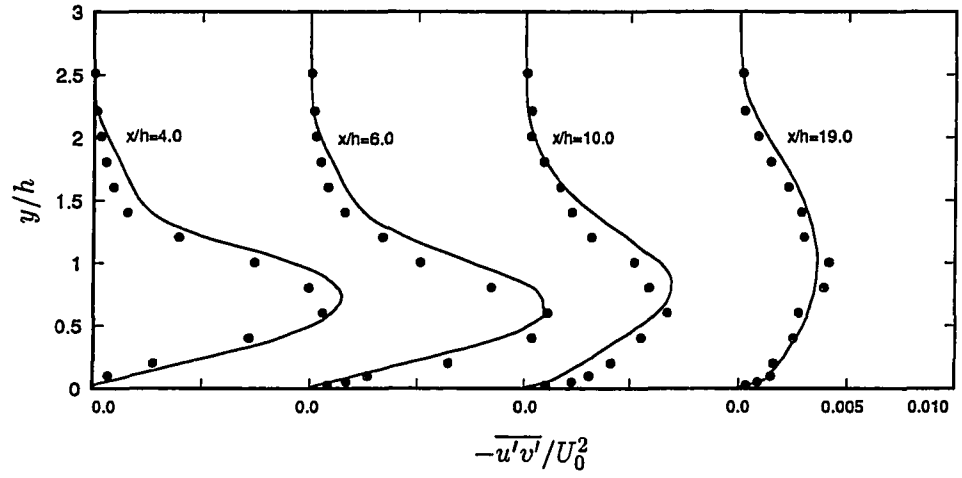

Figure 5.55. Comparison of BL6 and JD Reynolds shear stress profiles. —— BL6; • Jovic & Driver (1994).

peak near the wall, is dominated by the much larger peak in the free shear layer. After reattachment, the near-wall $\sqrt{\overline{u'^2}}$ peak re-emerges (Fig. 5.56(b)) at a distance $y/h \approx 0.06$; but this peak now is that of a re-developing turbulent boundary layer. Near the exit the near-wall peak grows to approximately 12% of the inlet free stream velocity. The evolutions of $\sqrt{\overline{v'^2}}$, $\sqrt{\overline{w'^2}}$ and $\overline{u'v'}$ are shown in Figs. 5.58, 5.60, and 5.62.

The maxima of all Reynolds stress components, at any streamwise location, occur in the free shear layer. The location of $\sqrt{\overline{u'^2}}_{\max}$ starts at $y/h = 1$ near the step, decreases to $y/h \approx 0.7$ at reattachment ($x/h \approx 6$), rises again to near $y/h = 1.0$ at $x/h \approx 12.0$ for the remaining recovery region (Figs. 5.56(b)). The locations of the streamwise intensity maxima coincide with the centerline of the free shear layer (the free shear layer centerline is the locus of the inflection points of the mean streamwise velocity profiles, Fig. 5.41). For the longitudinal component, $\sqrt{\overline{u'^2}}_{\max}$ reaches $0.18U_0$ at about one step height before the reattachment, then diminishes to approximately $0.10U_0$ at the exit. For the other components of the Reynolds stress tensor, the maximum values are: $\sqrt{\overline{v'^2}}_{\max} \approx 0.12U_0$, $\sqrt{\overline{w'^2}}_{\max} \approx 0.14U_0$, and

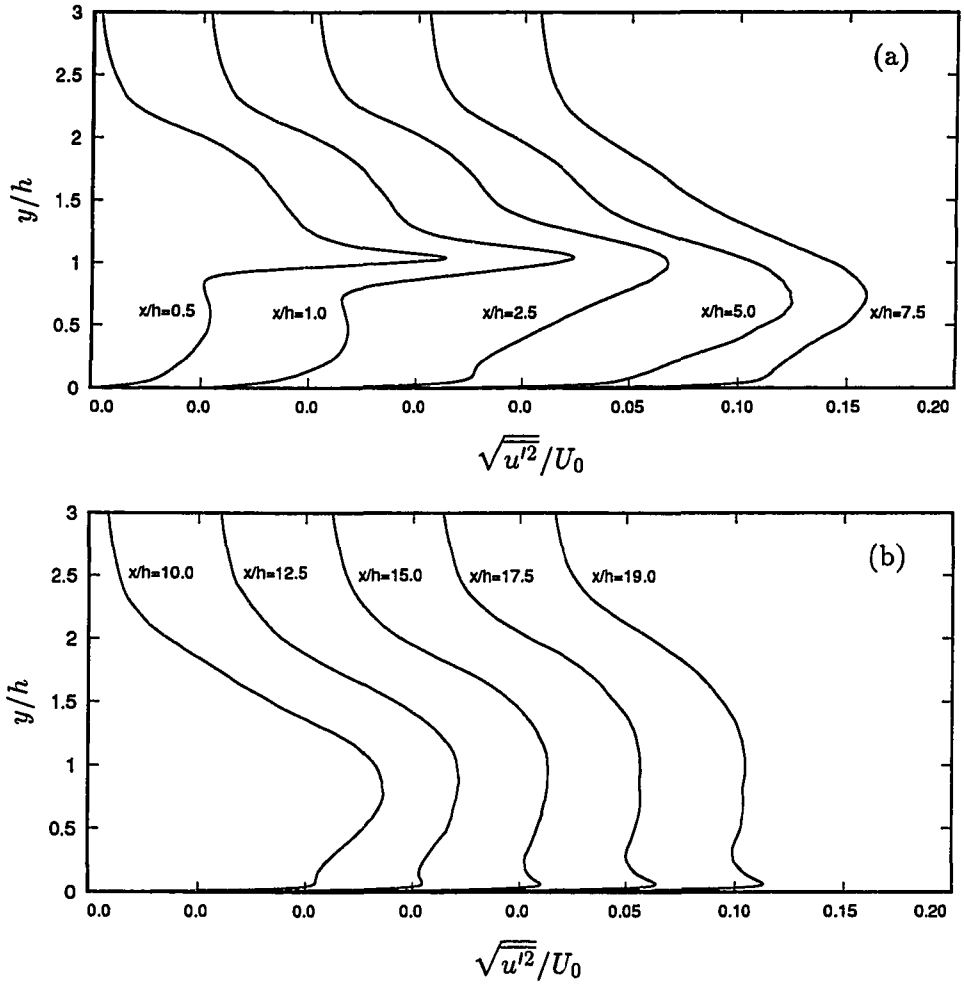

Figure 5.56. Longitudinal turbulence intensity profiles ($\sqrt{u'^2}/U_0$). (a) Recirculation and reattachment regions; (b) recovery region.

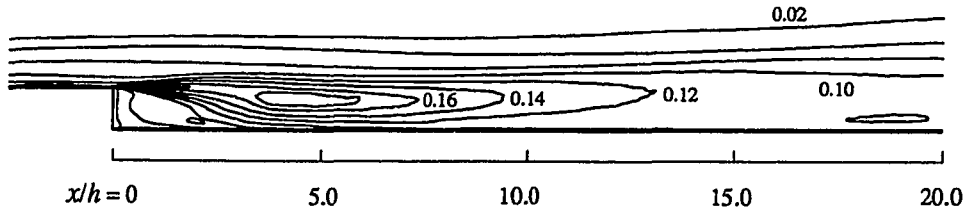

Figure 5.57. Longitudinal turbulence intensity contours ($\sqrt{u'^2}/U_0$).

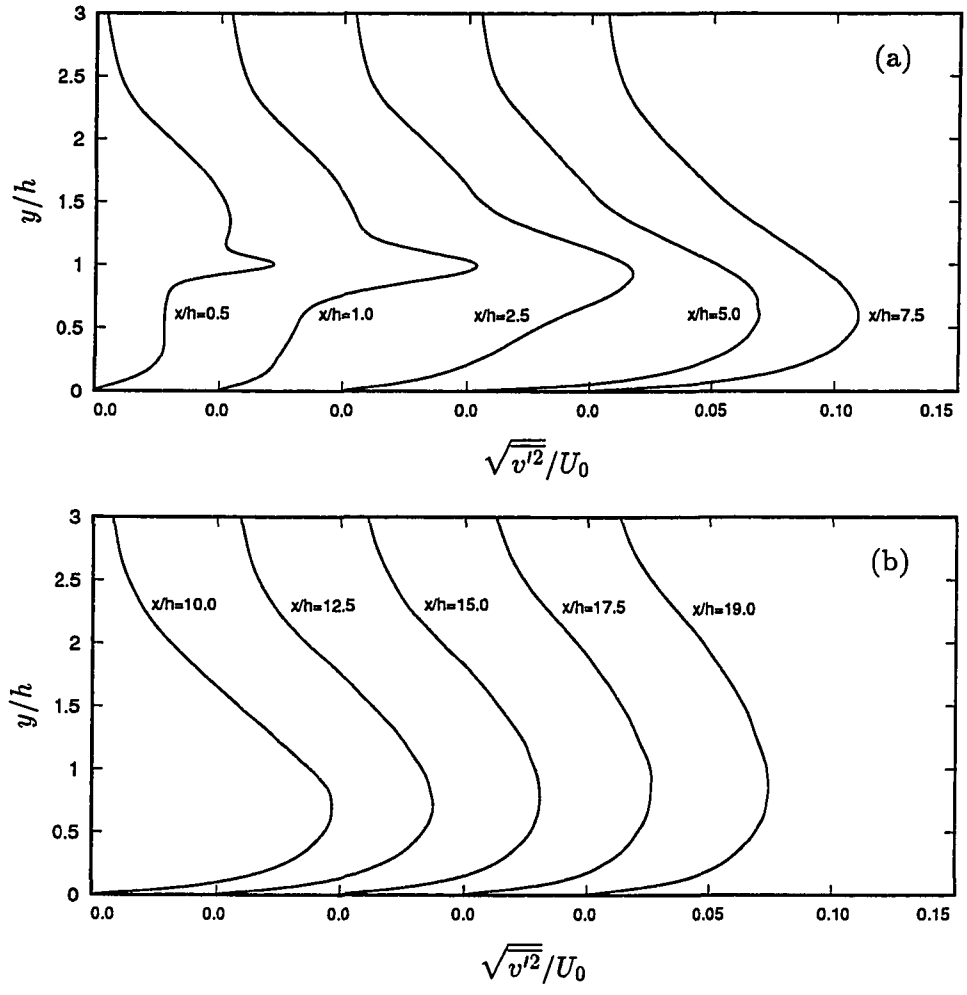

Figure 5.58. Vertical turbulence intensity profiles ($\sqrt{\overline{v'^2}}/U_0$). (a) Recirculation and reattachment regions; (b) recovery region.

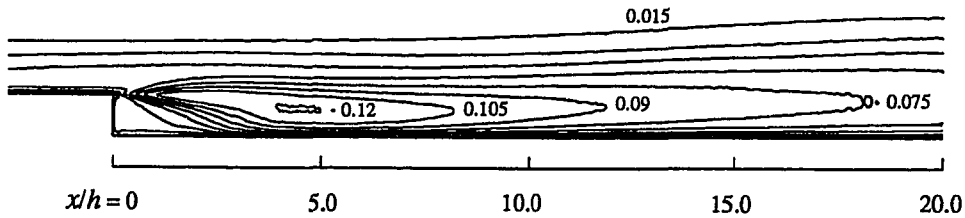

Figure 5.59. Vertical turbulence intensity contours ($\sqrt{\overline{v'^2}}/U_0$).

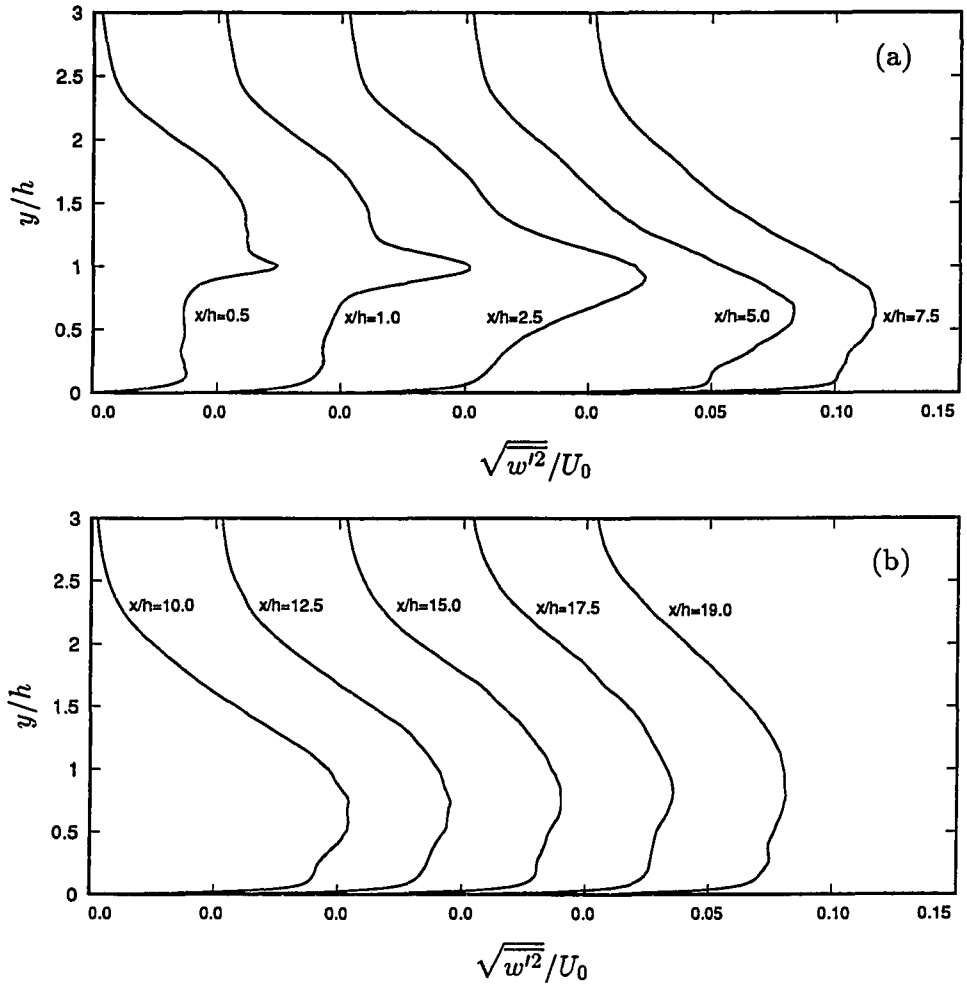

Figure 5.60. Spanwise turbulence intensity profiles ($\sqrt{\overline{w'^2}}/U_0$). (a) Recirculation and reattachment regions; (b) recovery region.

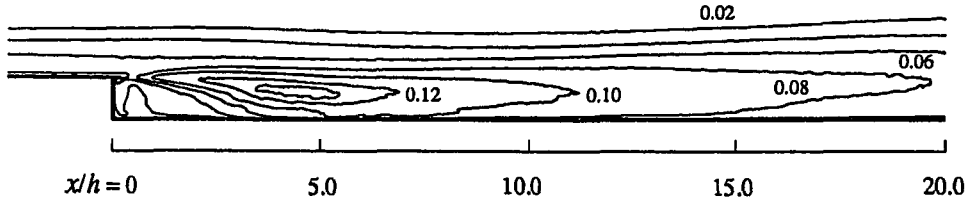

Figure 5.61. Spanwise turbulence intensity contours ($\sqrt{\overline{w'^2}}/U_0$).

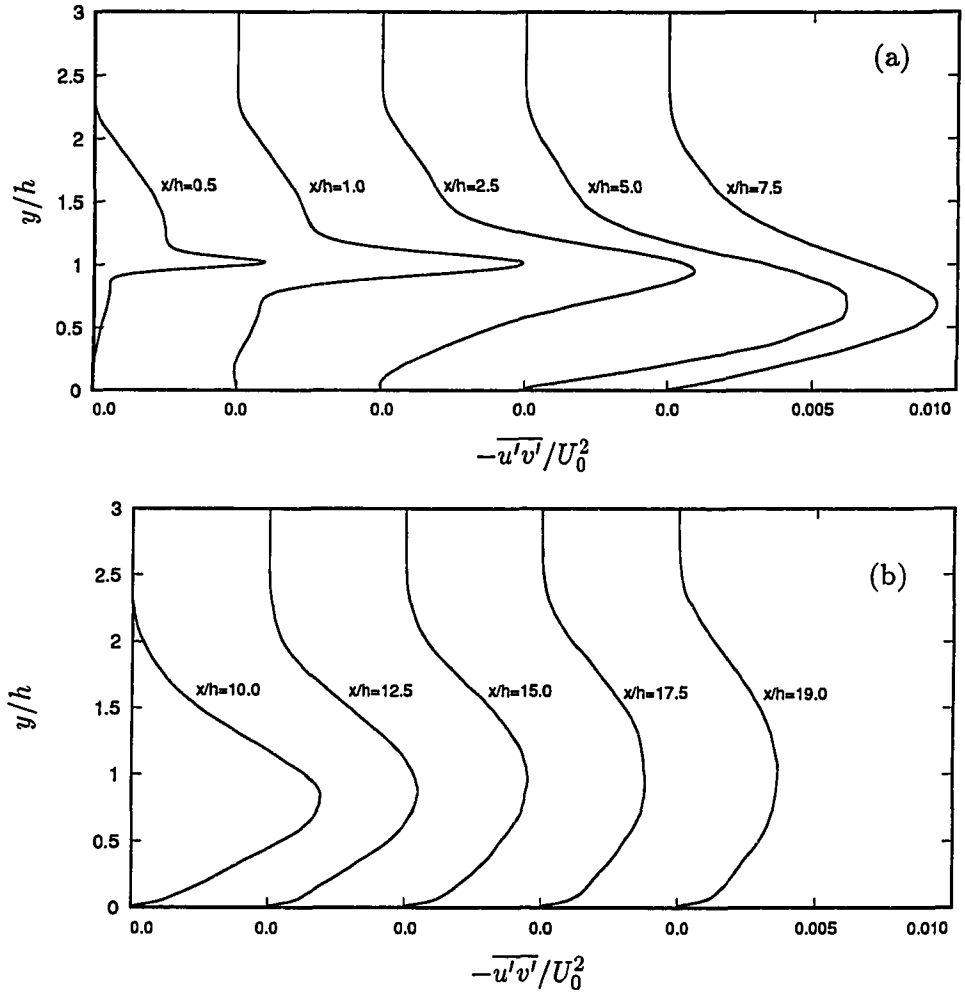

Figure 5.62. Reynolds shear stress profiles ($-\overline{u'v'}/U_0^2$). (a) Recirculation and reattachment regions; (b) recovery region.

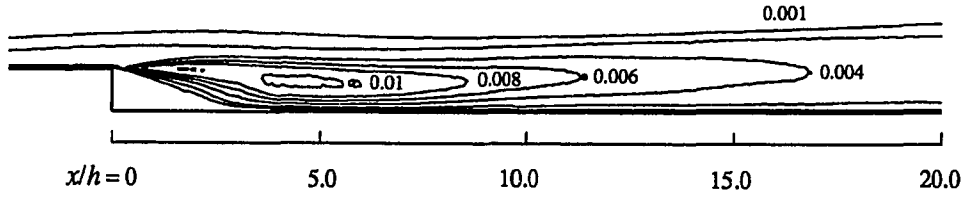

Figure 5.63. Reynolds shear stress contours ($-\overline{u'v'}/U_0^2$).

$\overline{u'v'}_{\max} \approx -0.011U_0^2$; all occur in the free shear layer just before the reattachment, $x/h \approx 5.0$ (Figs. 5.57, 5.59, 5.61 and 5.63).

The rise and fall in maximum values of all four Reynolds stress components with streamwise distance are shown in Fig. 5.64. For clarity, the $(-\overline{u'v'})_{\max}$ values are multiplied by 10. Note also that the near-wall peak of $\sqrt{\overline{u'^2}}$ is not presented here, although it is actually larger than the values in the free shear layer for $x/h > 15$ (see Fig. 5.56). A comparison with $\sqrt{\overline{u'^2}}_{\max}$ from the coarse grid case (BL5, chain-dot-dot line in Fig. 5.64) indicates that the magnitude of the peak of the streamwise intensity remains about the same with grid refinement.

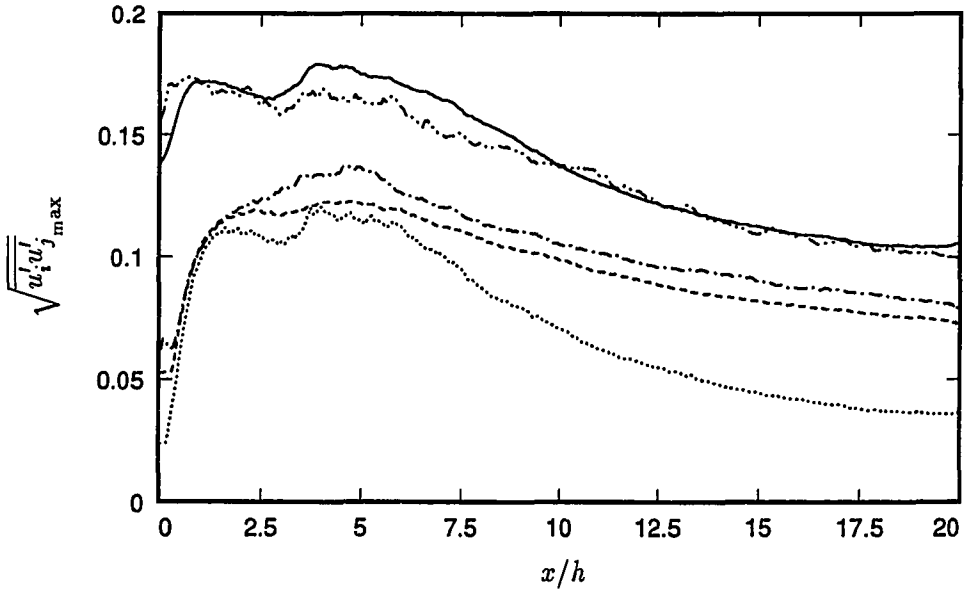

Figure 5.64. Maxima of Reynolds stress components. —— $\sqrt{\overline{u'^2}}_{\max}$; ---- $\sqrt{\overline{v'^2}}_{\max}$; —·— $\sqrt{\overline{w'^2}}_{\max}$; ····· $(-\overline{u'v'})_{\max} \times 10$; —··— $\sqrt{\overline{u'^2}}_{\max}$, case BL5.

5.8. Momentum Budgets

The mean momentum equation for incompressible flow is

$$\frac{\partial U_i}{\partial t} = \underbrace{-(U_i U_k)_{,k}}_{\text{(I)}} \underbrace{-\overline{(u_i' u_k')}_{,k}}_{\text{(II)}} + \underbrace{\frac{1}{Re} U_{i,kk}}_{\text{(III)}} \underbrace{- P_{,i}}_{\text{(IV)}}. \tag{5.4}$$

The four terms in the right hand side of Eq. (5.4) are identified below.

(I) = Convection term,

(II) = Reynolds stress term,

(III) = Viscous term,

(IV) = Pressure gradient term.

As described in §5.3, the budgets were evaluated using 6070 samples over an averaging time period $\Delta T_{\text{ave}} \approx 109h/U_0$. This represents about 4.3 flow-through times using a mean convective speed $U_c = 0.8U_0$ and a post-expansion length of $20h$. Figures 5.65–5.69 present the streamwise and normal momentum budgets at five representative locations in the streamwise direction: $x/h = -2.0$, 4.0, 7.0, 10.0 and 18.0. All quantities are normalized by U_0^2/h. As described in §5.3, a piecewise least-square fit is applied to budgets at $x/h = 4.0$, 7.0, 10.0 and 18.0.

Before the step, there is a slight favorable pressure gradient in the region $-3.0 < x/h < 0.0$. $\partial P/\partial x \approx -2.1 \times 10^{-3} \rho U_0^2$ at $x/h = -2.0$ as shown in Fig. 5.65(a). At the wall, the decrease in pressure is balanced by the viscous term. In the outer region, the viscous term is negligible, and the Reynolds shear stress is balanced by the pressure gradient and convection terms. In the normal momentum equation the pressure gradient and Reynolds stress terms are dominant.

In the backflow region, a severe adverse pressure gradient exists which is balanced at the wall by the viscous term (Fig. 5.66(a)). Unlike the zero pressure gradient boundary layer, both $\partial(UU)/\partial x$ and $\partial(UV)/\partial y$ have significant contributions to the momentum balance. The streamwise pressure gradient is not uniform in the y-direction; $\partial P/\partial x \approx 0.04\rho U_0^2/h$ at the wall and decreases to approximately

$0.017\rho U_0^2/h$. The Reynolds stress term is made up mainly from $\partial\overline{u'v'}/\partial y$ which changes its sign at $y/h \approx 0.6$.

Beyond the reattachment, the streamwise pressure gradient is virtually uniform in y; the Reynolds stress term increases significantly very close to the wall (Fig. 5.67(a)–5.68(a)). There is less downward flow downstream from the reattachment, thus in a role reversal, $\partial(UU)/\partial x$ becomes significantly larger then $\partial(UV)/\partial y$. This trend continues throughout the recovery region.

The dominant terms in the V momentum equation are the pressure gradient and the Reynolds stress terms. The equation

$$\frac{\partial P}{\partial y} \approx -\frac{\partial \overline{v'^2}}{\partial y}$$

is a reasonable approximation to the normal mean momentum equation. The convection term attains a more significant role near and beyond the reattachment point. It also changes sign from largely positive in the recirculation zone to negative in the recovery region.

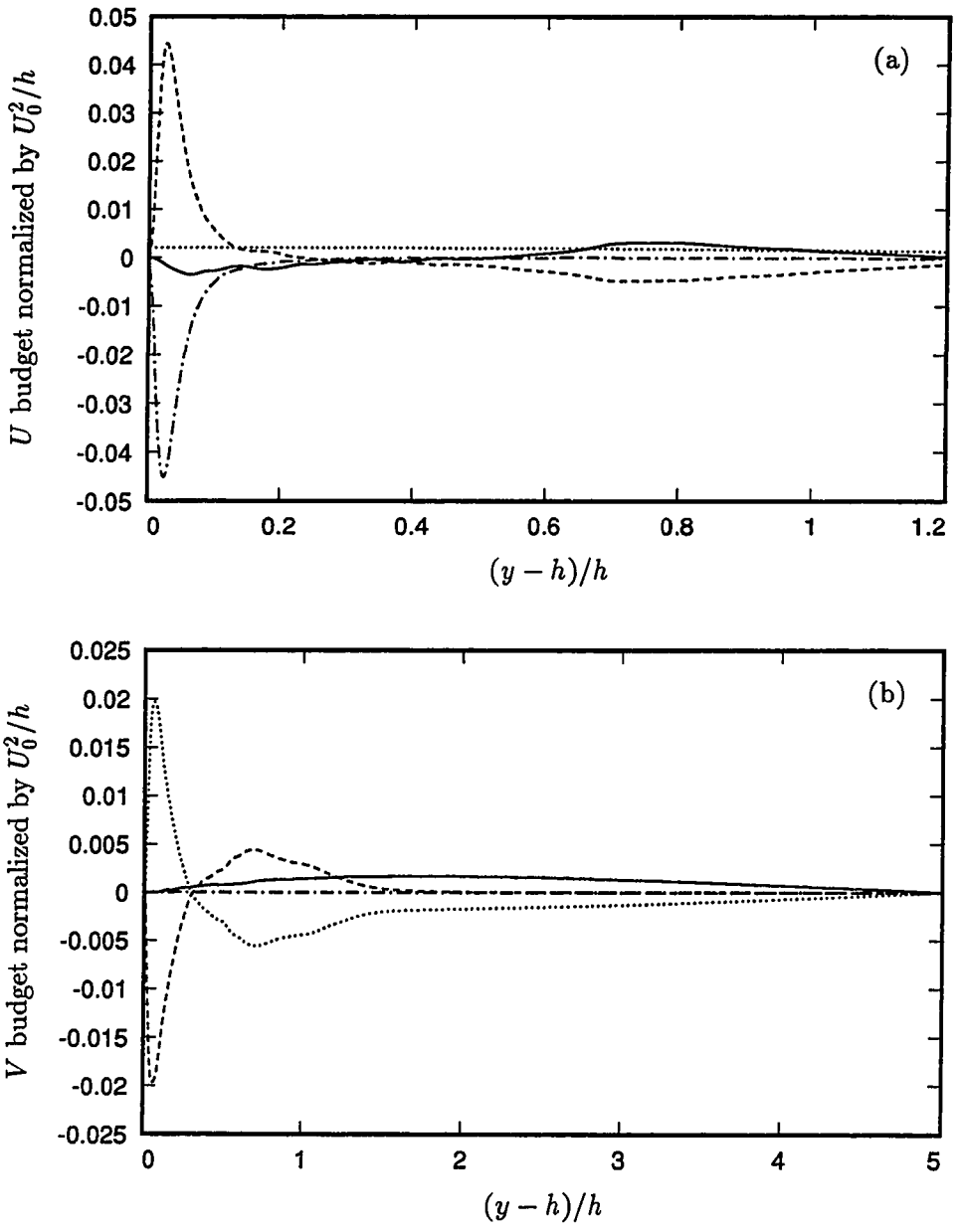

Figure 5.65. Momentum budget at $x/h = -2.0$, normalized by U_0^2/h. —— convection term; ---- Reynolds stress term; —·— viscous term; ····· pressure gradient term. (a) U momentum equation; (b) V momentum equation.

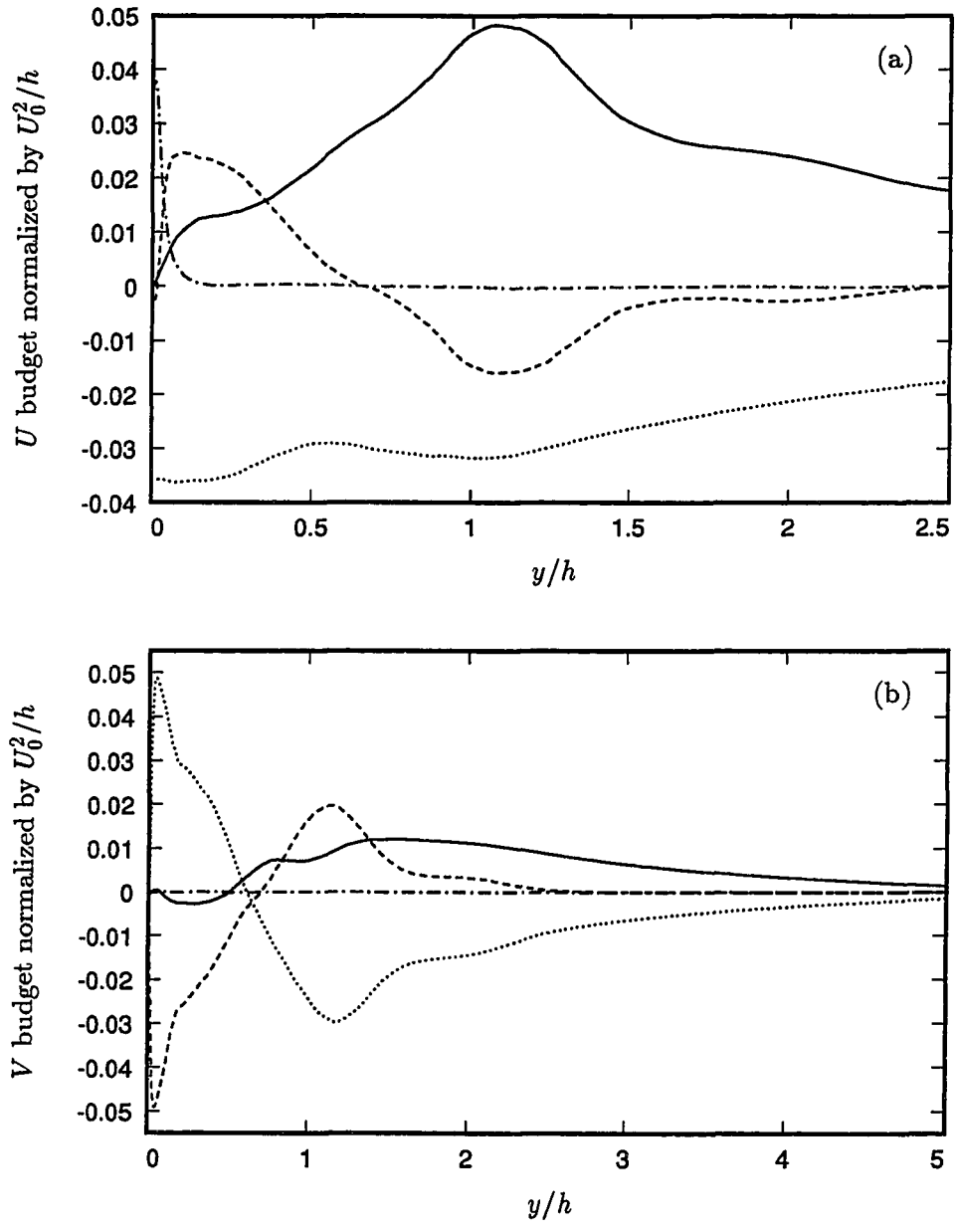

Figure 5.66. Momentum budget at $x/h = 4.0$, normalized by U_0^2/h (least-square fit). —— convection term; ---- Reynolds stress term; —·— viscous term; ····· pressure gradient term. (a) U momentum equation; (b) V momentum equation.

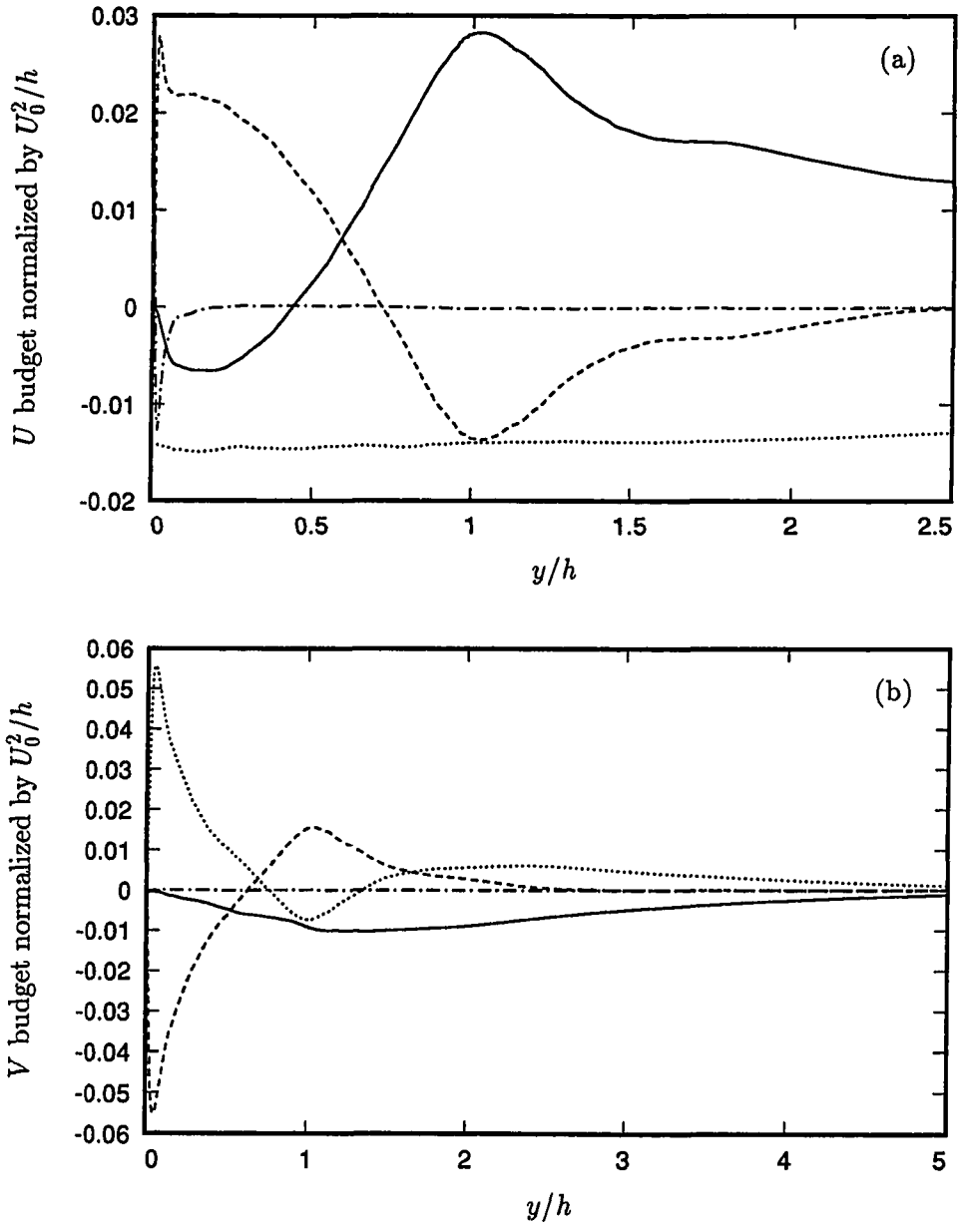

Figure 5.67. Momentum budget at $x/h = 7.0$, normalized by U_0^2/h (least-square fit). —— convection term; ---- Reynolds stress term; —·— viscous term; ····· pressure gradient term. (a) U momentum equation; (b) V momentum equation.

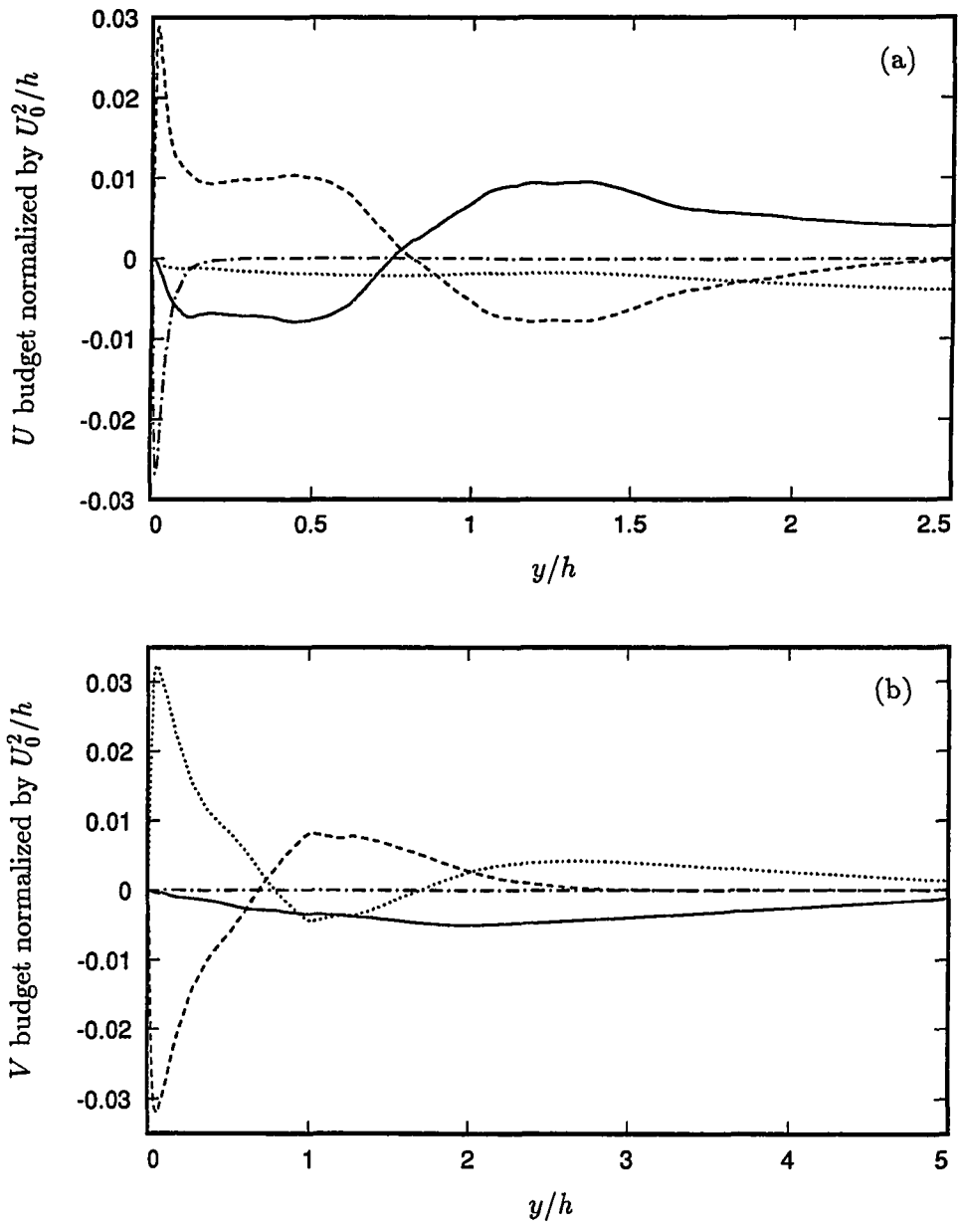

Figure 5.68. Momentum budget at $x/h = 10.0$, normalized by U_0^2/h (least-square fit). —— convection term; ---- Reynolds stress term; —·— viscous term; ····· pressure gradient term. (a) U momentum equation; (b) V momentum equation.

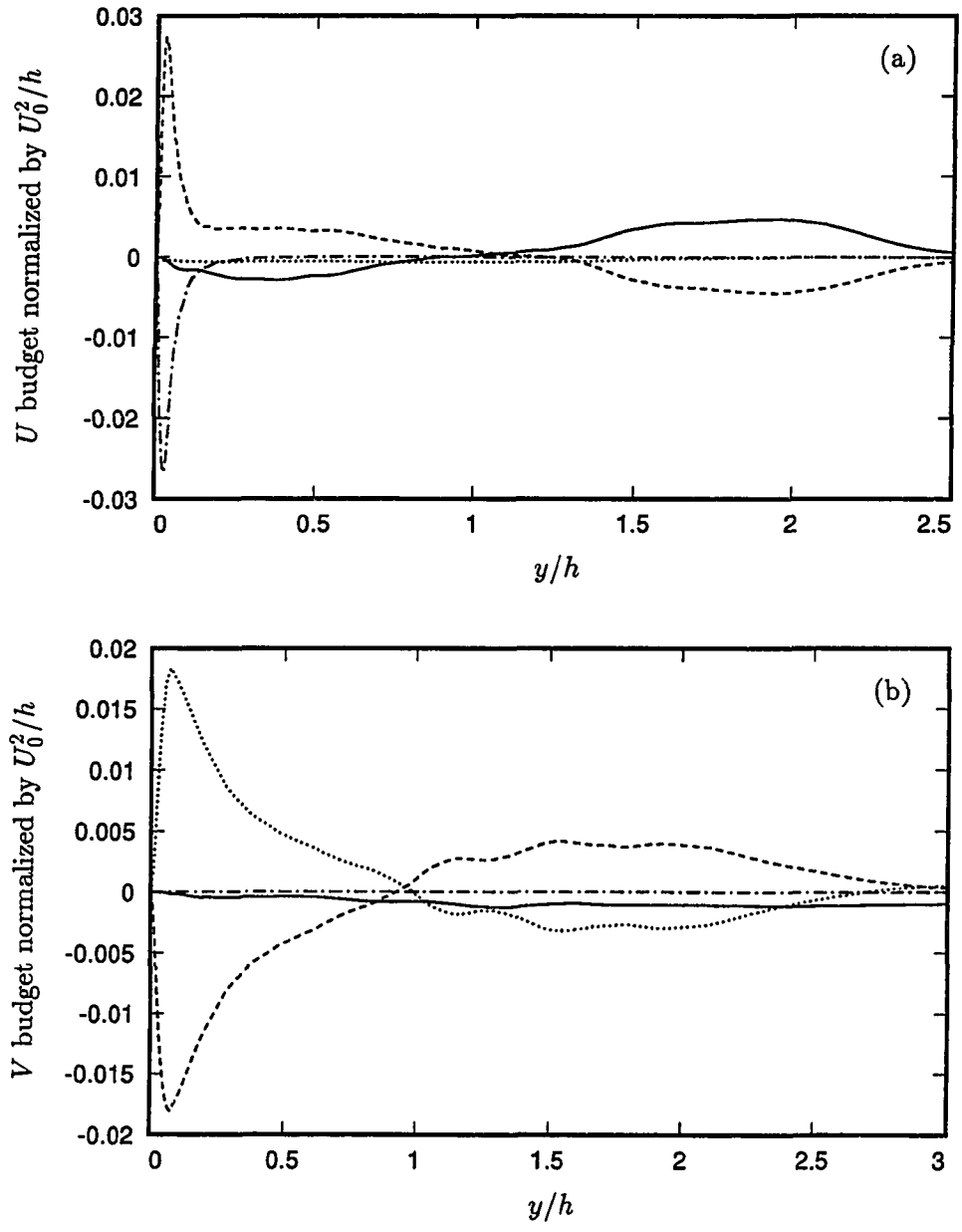

Figure 5.69. Momentum budget at $x/h = 18.0$, normalized by U_0^2/h (least-square fit). —— convection term; ---- Reynolds stress term; —·— viscous term; ····· pressure gradient term. (a) U momentum equation; (b) V momentum equation.

5.9. Reynolds Stress Budgets

5.9.1. Transport Equations and Averaging Method

Because momentum equations are numerically solved on a staggered grid, two forms of the Reynolds stress transport equation are considered. The first is more primitive and is a straight forward moment of the fluctuating momentum equation defined at the appropriate velocity grid points.

$$\begin{aligned}\frac{\partial \overline{u_i' u_j'}}{\partial t} = & \underbrace{-\overline{u_i'\left(u_j' U_k\right)_{,k}} - \overline{u_j'\left(u_i' U_k\right)_{,k}}}_{C_{ij}} \underbrace{-\overline{u_i'\left(U_j u_k'\right)_{,k}} - \overline{u_j'\left(U_i u_k'\right)_{,k}}}_{P_{ij}} \\ & \underbrace{-\overline{u_i'\left(u_j' u_k'\right)_{,k}} - \overline{u_j'\left(u_i' u_k'\right)_{,k}}}_{T_{ij}} + \underbrace{\frac{1}{Re}\overline{\left(u_i' u_j'\right)_{,kk}}}_{D_{ij}} \\ & \underbrace{-\frac{2}{Re}\overline{u_{i,k}' u_{j,k}'}}_{\epsilon_{ij}} \underbrace{-\overline{u_i' p_{,j}'} - \overline{u_j' p_{,i}'}}_{\Pi_{ij}}. \end{aligned} \tag{5.5}$$

The terms on the right hand side of Eq. (5.5) are identified as follows:

C_{ij} = Convection,

P_{ij} = Production,

T_{ij} = Turbulence Transport,

D_{ij} = Viscous Diffusion,

ϵ_{ij} = Viscous Dissipation,

Π_{ij} = Velocity Pressure-Gradient.

The relevant non-zero stresses are $\overline{u_1' u_1'}$, $\overline{u_2' u_2'}$, $\overline{u_3' u_3'}$, and $\overline{u_1' u_2'}$.

The continuity equations $U_{k,k} = u_{k,k}' = 0$ can be applied to Eq. (5.5) to obtain a more compact form:

$$\frac{\partial \overline{u_i' u_j'}}{\partial t} = \underbrace{-U_k\overline{\left(u_i' u_j'\right)_{,k}}}_{C_{ij}} \underbrace{-\overline{u_i' u_k'} U_{j,k} - \overline{u_j' u_k'} U_{i,k}}_{P_{ij}} \underbrace{-\overline{\left(u_i' u_j' u_k'\right)_{,k}}}_{T_{ij}}$$

$$+\underbrace{\frac{1}{Re}\overline{\left(u_i'u_j'\right)}_{,kk}}_{D_{ij}}-\underbrace{\frac{2}{Re}\overline{u_{i,k}'u_{j,k}'}}_{\epsilon_{ij}}\underbrace{-\overline{u_i'p_{,j}'}-\overline{u_j'p_{,i}'}}_{\Pi_{ij}}. \tag{5.6}$$

In Eq. (5.5), each term is computed at the node points corresponding to each velocity component. For example, in the $\partial\overline{u_1'u_1'}/\partial t$ equation, all terms are evaluated at the East and West surfaces of the cells; similar procedure is applied at other cell surfaces for the remaining components. Equation (5.5) requires 71 statistical variables for every x-y location. On the other hand, all variables in Eq. (5.6) are interpolated to the cell centers before statistics are computed; which reduces the number of variables per x-y node to 24. The budget resulted from Eq. (5.5) is more accurate because this is the primitive form employed in the computations. Nevertheless, there is less that 5% difference between the results of Eqs. (5.5) and (5.6). Both data sets were sampled at equal time intervals of $\Delta t_s = 0.018h/U_0$ apart.

The sections below examine the budget for each Reynolds stress component and the turbulent kinetic energy, $q^2/2 = \frac{1}{2}(\overline{u_1'u_1'} + \overline{u_2'u_2'} + \overline{u_3'u_3'})$. The budgets were averaged over $\Delta T_{\text{ave}} = 109h/U_0$. In subsequent discussions, all terms in the Reynolds stress transport equations are non-dimensionalized by U_0^3/h for regions away from the wall. Near the wall ($y^+ < 25$), the transport equations are non-dimensionalized by u_τ^4/ν, where u_τ is the local wall shear velocity, and ν is the kinematic viscosity. Least-square fit is applied only to budget terms away from the wall ($y^+ > 50$) and for locations behind the step.

5.9.2. Longitudinal Stress Budget

The streamwise Reynolds stress transport equation is

$$\frac{\partial \overline{u_1' u_1'}}{\partial t} = \underbrace{-U_k \overline{(u_1' u_1')}_{,k}}_{C_{11}} \underbrace{-2\overline{u_1' u_k'} U_{1,k}}_{P_{11}} \underbrace{-\overline{(u_1' u_1' u_k')}_{,k}}_{T_{11}} + \underbrace{\frac{1}{Re}\overline{(u_1' u_1')}_{,kk}}_{D_{11}} \underbrace{-\frac{2}{Re}\overline{u_{1,k}' u_{1,k}'}}_{\epsilon_{11}} \underbrace{-2\overline{u_1' p_{,1}'}}_{\Pi_{11}}. \tag{5.7}$$

The $\overline{u'^2}$ budget for five representative locations along the streamwise direction are shown in Figs. 5.70–5.74. At two step heights prior to separation, the budget terms are qualitatively similar to those of Spalart (1988) and of turbulent channel flow, Mansour *et al.* (1988). However, the viscous diffusion (D_{11}) and dissipation (ϵ_{11}) here are about 40% higher near the wall. This is possibly due a mild favorable pressure gradient in the region before the step. No significant differences in the remaining terms are discernible compared to a zero pressure gradient boundary layer.

Figures 5.71–5.73 show the longitudinal stress budgets in the free-shear layer across the recirculation and reattachment regions. In the recirculation region, the production, P_{11}, reaches its maximum in the shear layer. As discussed in §5.7.5, although both $\overline{u'^2}$ and $\overline{u'v'}$ have maxima at this location, only the term $\overline{u'v'}\partial U/\partial y$ contributes significantly to P_{11}. Although ϵ_{11} peaks in the shear layer at the same location as P_{11}, it accounts for approximately 30% of the energy production. The velocity pressure-gradient, Π_{11}, is appreciably larger than dissipation.

The turbulence transport, T_{11}, is made up of two triple products:

$$T_{11} = -\frac{\partial \overline{u'^3}}{\partial x} - \frac{\partial \overline{u'^2 v'}}{\partial y}.$$

The streamwise variation of these triple correlations is shown in Fig. 5.75. Inside the recirculation zone, $\partial\overline{u'^3}/\partial x \ll \partial\overline{u'^2 v'}/\partial y$. Similar to observations by Chandrsuda & Bradshaw (1981), $\overline{u'^2 v'}$ is anti-symmetric in the shear layer. The turbulence

transport term thus removes energy from the shear layer region ($0.3 < y/h < 1.1$) and deposits it near the wall and in the high-speed side of the layer.

Figure 5.73(a) shows that all terms decay rapidly through the reattachment region. But the transport (T_{11}) and convection (C_{11}) terms become relatively more prominent. As expected, in the low-speed side of the layer, the convection term is positive whereas it is negative in the high-speed side.

Very near the wall, turbulence production becomes negative in the recirculation zone (Fig. 5.71(b)) because of the reverse flow below $y^+ \approx 25$. The velocity pressure-gradient term (Π_{11}) becomes positive for $y^+ < 15$. As the adverse pressure gradient decreases after reattachment, the near wall Π_{11} diminishes and the features of a normal turbulent boundary layer re-emerge as seen in Fig. 5.73(b). However, the viscous terms (D_{11} and ϵ_{11}) are still dominant; the viscous diffusion and dissipation at the wall are about 3 times larger than the peak production. It should be noted that, compared to the location inside the recirculation region, D_{11} and ϵ_{11} at the wall are virtually unchanged; but this is not obvious from Figs. 5.71(b) and 5.73(b) because the terms are normalized using local u_τ's.

In the recovery region, the near wall profiles are very much similar to those of a standard turbulent boundary layer (Fig. 5.74(b)) although there remains some discrepancy between the production peak and the wall viscous dissipation and diffusion. Moreover, after reattachment, the turbulence transport becomes a very significant term near the wall (Fig. 5.75).

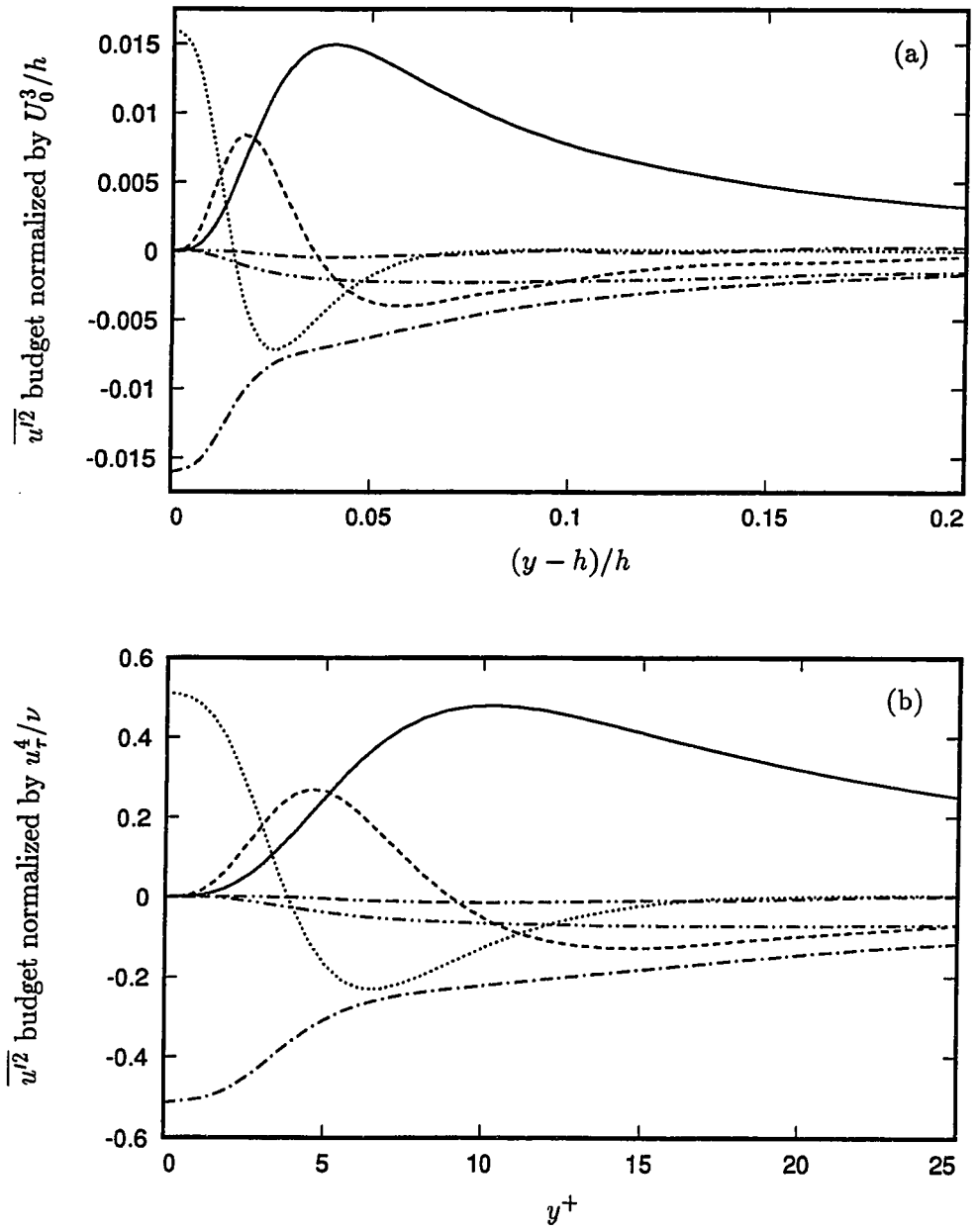

Figure 5.70. Longitudinal Reynolds-stress budget at $x/h = -2.0$. -·-· convection; —— production; ---- turbulence transport; ····· viscous diffusion; —·— viscous dissipation; —··— velocity pressure-gradient. (a) Away from the wall; (b) near the wall.

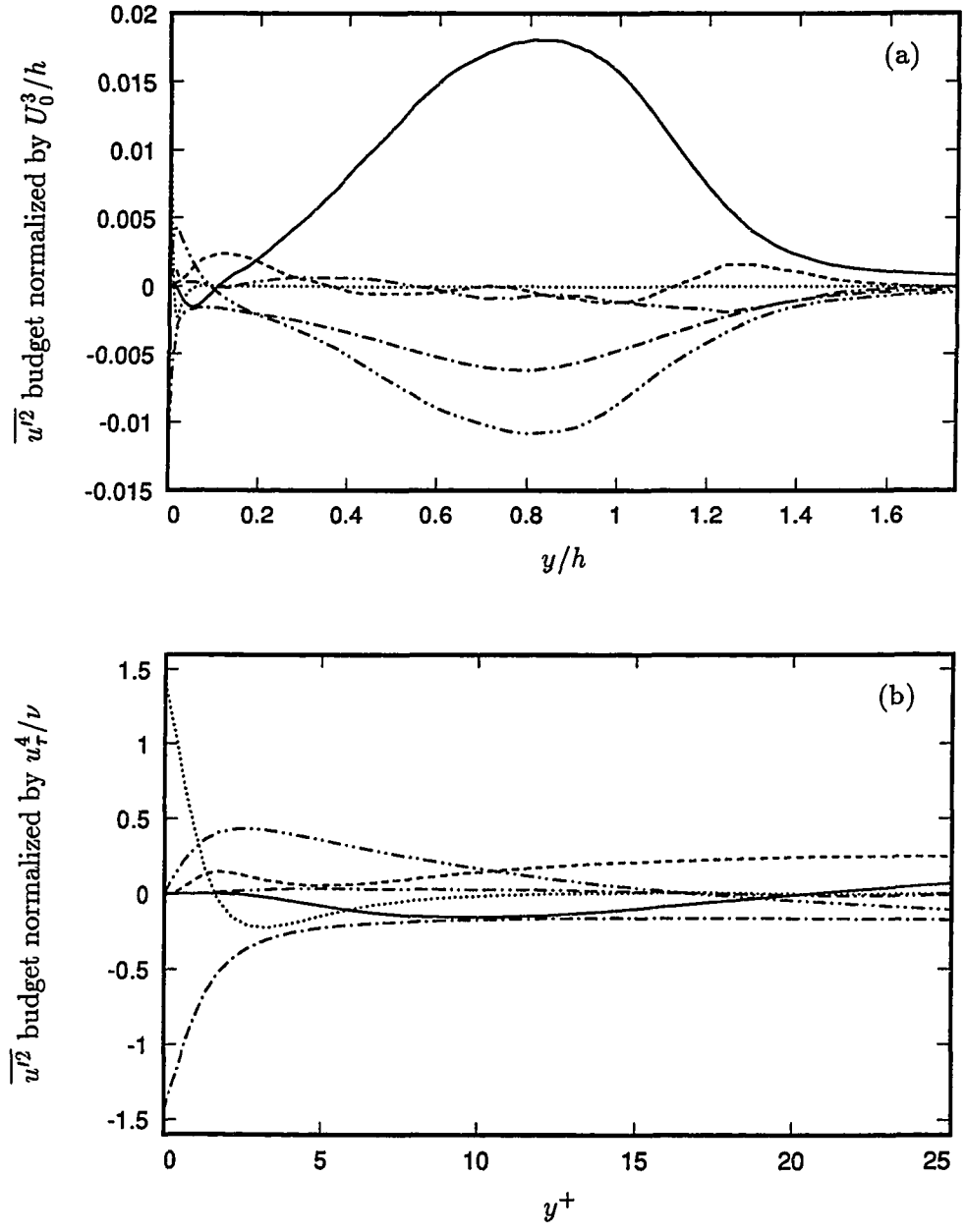

Figure 5.71. Longitudinal Reynolds-stress budget at $x/h = 4.0$. -·-· convection; —— production; ---- turbulence transport; ····· viscous diffusion; —·— viscous dissipation; —·—· velocity pressure-gradient. (a) Away from the wall (least-square fit); (b) near the wall.

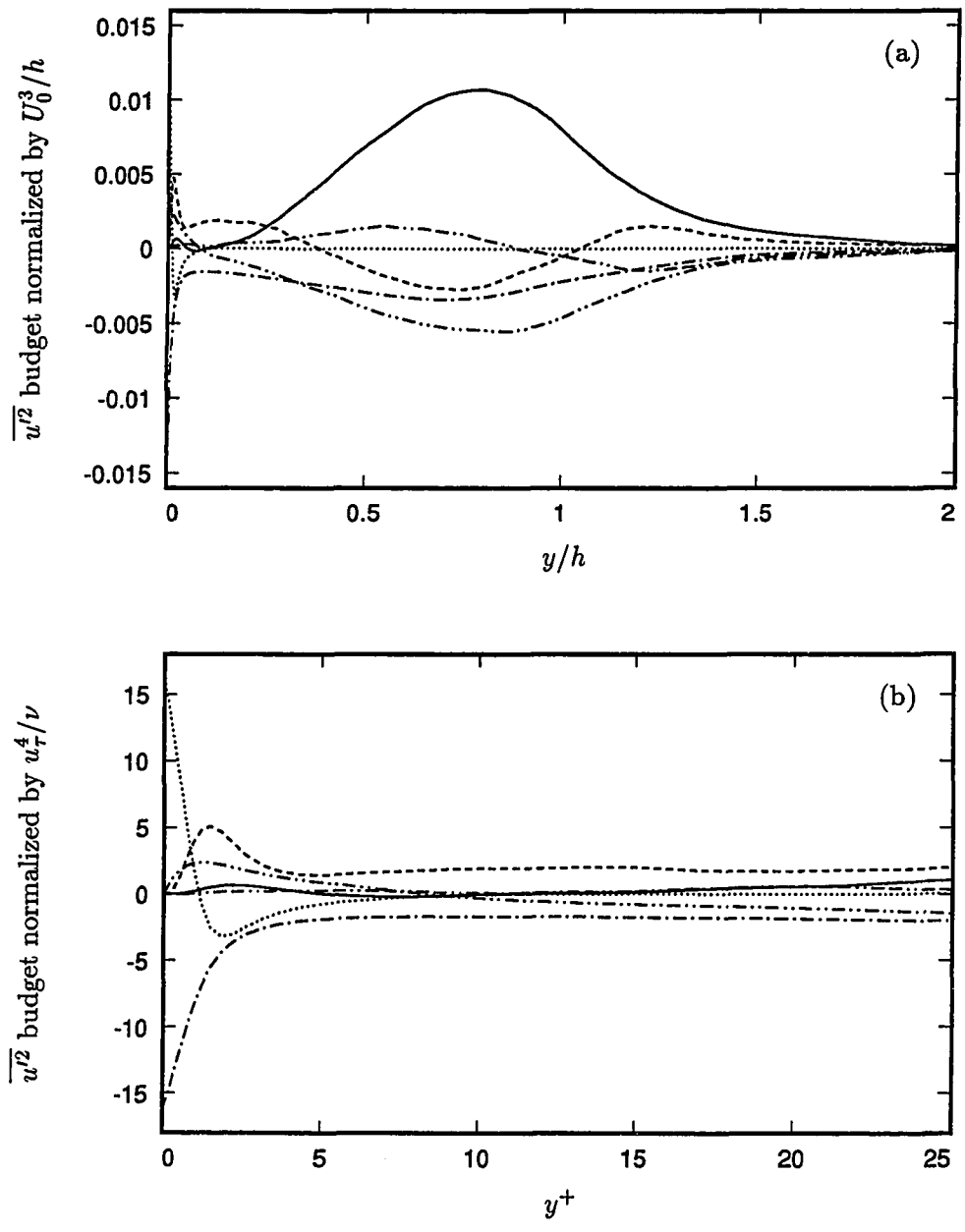

Figure 5.72. Longitudinal Reynolds-stress budget at $x/h = 7.0$. ---- convection; —— production; ---- turbulence transport; ····· viscous diffusion; —·— viscous dissipation; —··— velocity pressure-gradient. (a) Away from the wall (least-square fit); (b) near the wall.

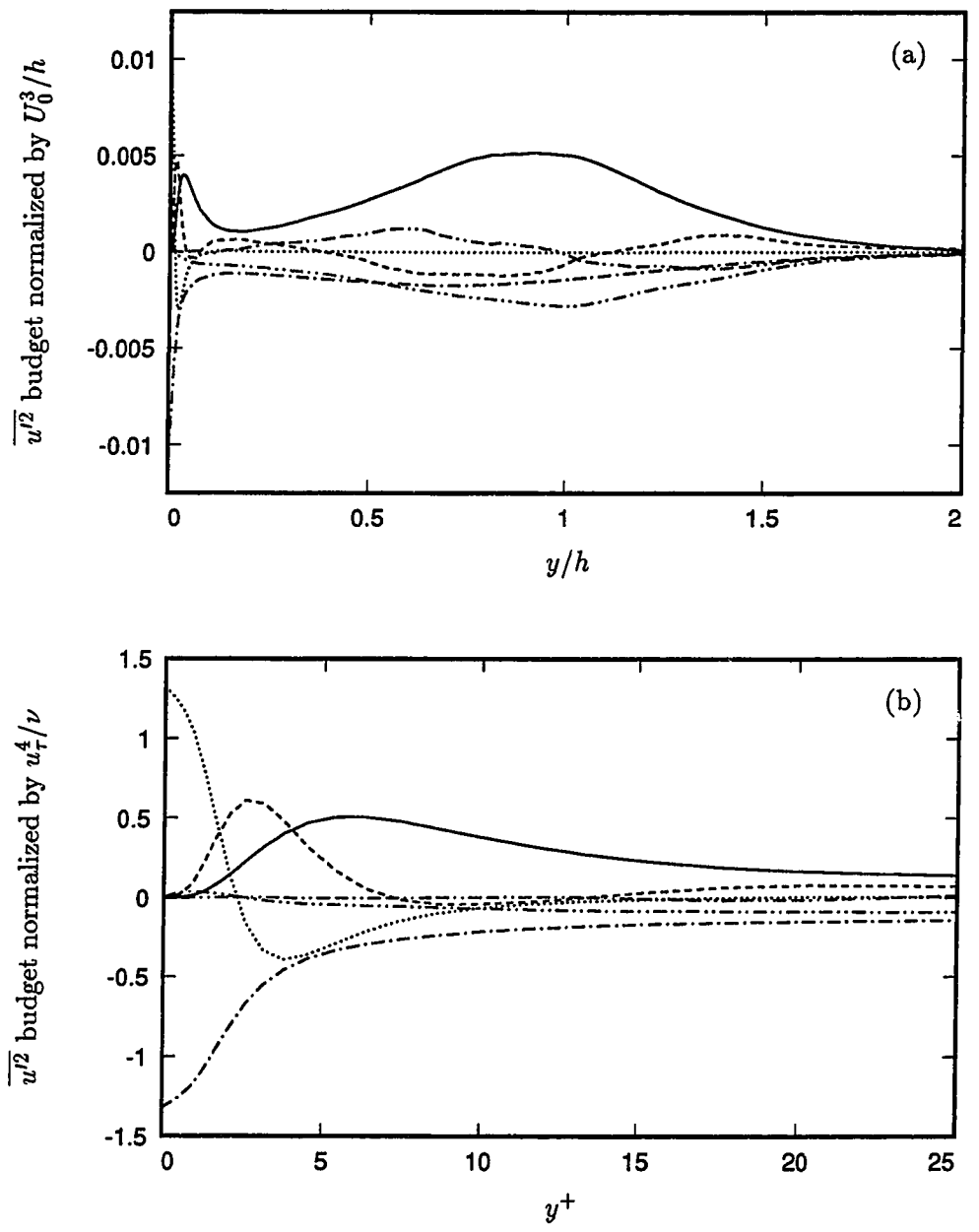

Figure 5.73. Longitudinal Reynolds-stress budget at $x/h = 10.0$. -·-· convection; —— production; ---- turbulence transport; ····· viscous diffusion; —·— viscous dissipation; —··— velocity pressure-gradient. (a) Away from the wall (least-square fit); (b) near the wall.

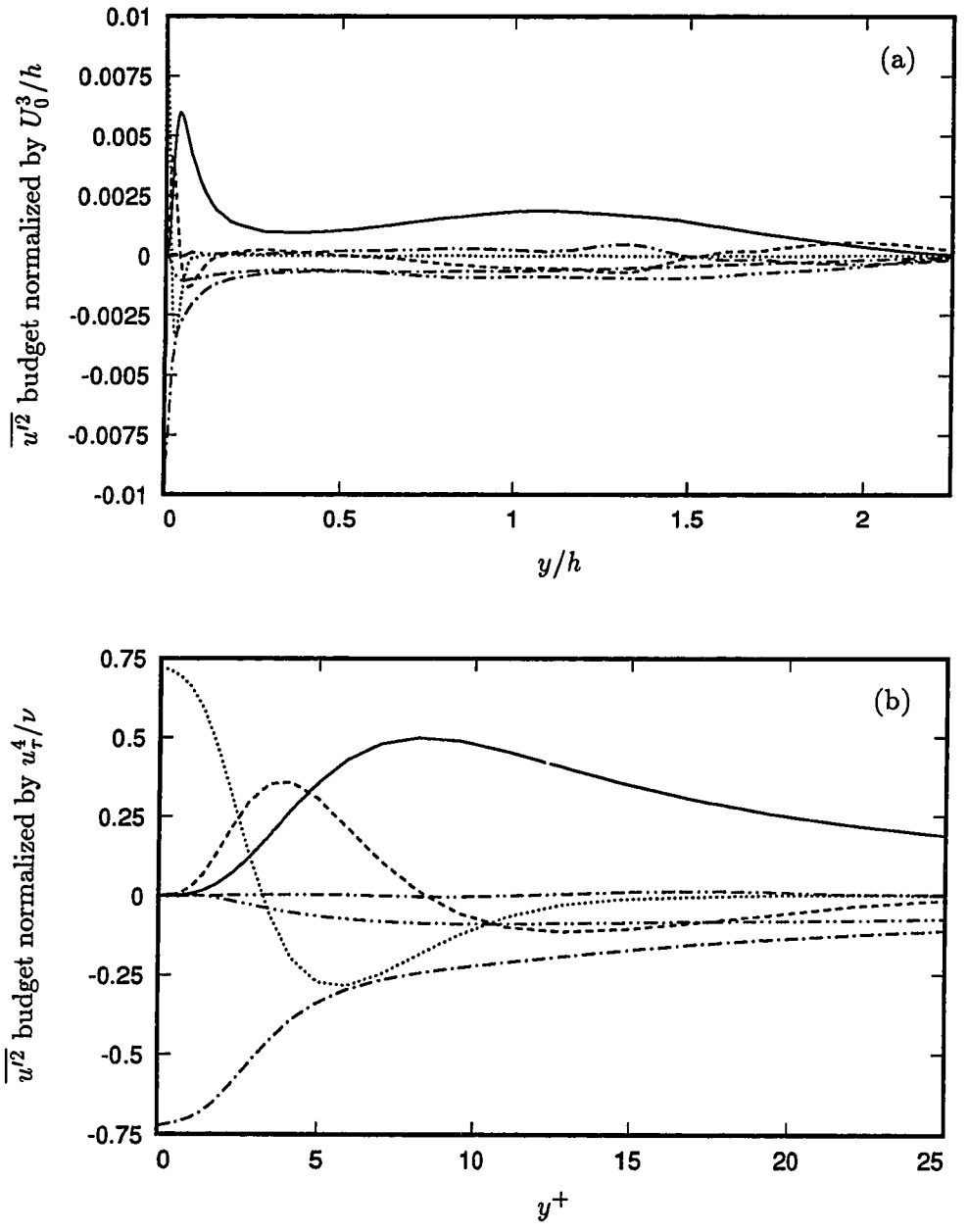

Figure 5.74. Longitudinal Reynolds-stress budget at $x/h = 18.0$. -·-· convection; —— production; ---- turbulence transport; ····· viscous diffusion; —·— viscous dissipation; —··— velocity pressure-gradient. (a) Away from the wall (least-square fit); (b) near the wall.

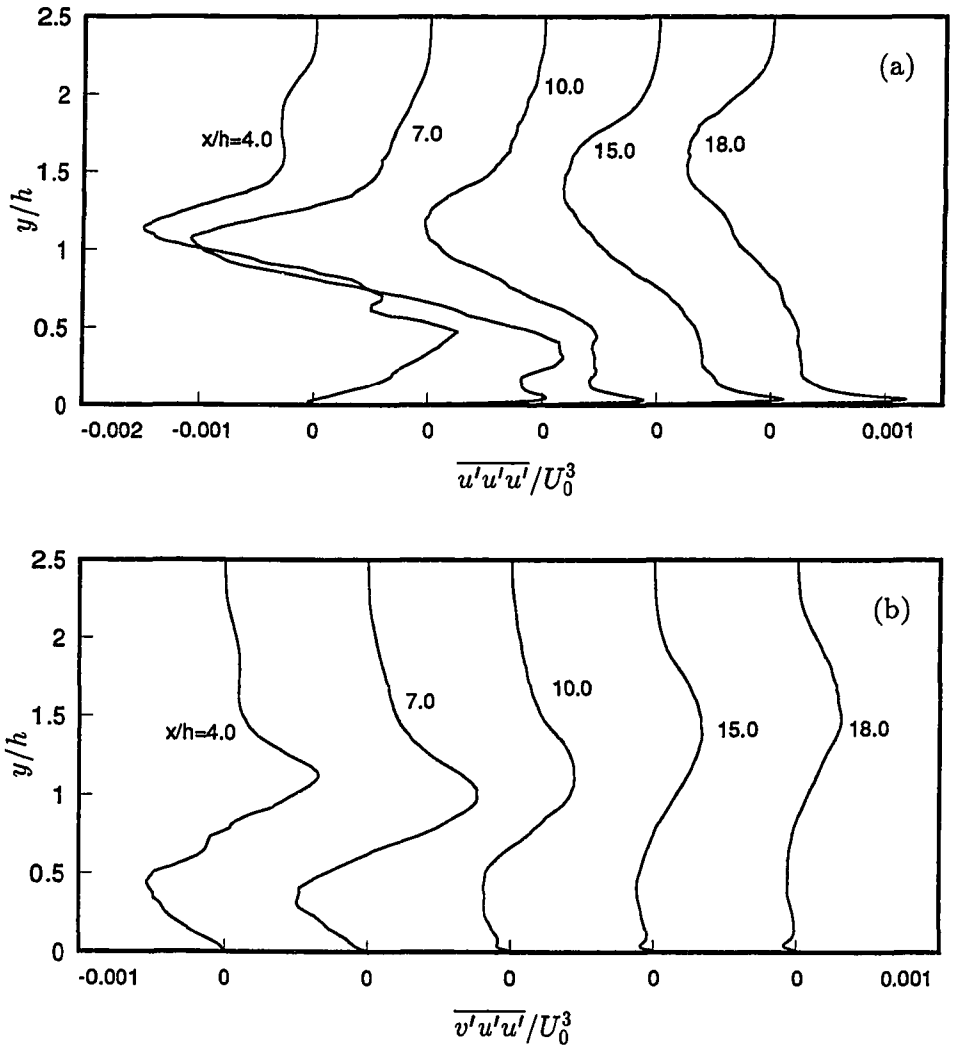

Figure 5.75. Triple products. (a) $\overline{u'u'u'}$; (b) $\overline{v'u'u'}$.

5.9.3. Vertical Stress Budget

The budgets of the wall-normal stress component are shown in Figs. 5.76–5.80 according to the following transport equation:

$$\frac{\partial \overline{u_2' u_2'}}{\partial t} = \underbrace{-U_k \overline{(u_2' u_2')}_{,k}}_{C_{22}} \underbrace{-2\overline{u_2' u_k'} U_{2,k}}_{P_{22}} \underbrace{-\overline{(u_2' u_2' u_k')}_{,k}}_{T_{22}} + \underbrace{\frac{1}{Re}\overline{(u_2' u_2')}_{,kk}}_{D_{22}} \underbrace{-\frac{2}{Re}\overline{u_{2,k}' u_{2,k}'}}_{\epsilon_{22}} \underbrace{-2\overline{u_2' p_{,2}'}}_{\Pi_{22}}. \tag{5.8}$$

Before the separation ($x/h = -2.0$), the vertical stress budget terms are somewhat different than in the zero pressure gradient turbulent boundary layer (Spalart, 1988). The convection term (C_{22}) is negligible near the wall (Fig. 5.76), but becomes dominant in the outer region of the boundary layer, absorbing most of the energy transported by the turbulence transport term, T_{22}. Owing to the splatting effect, the velocity pressure-gradient term becomes negative in the immediate vicinity of the wall and is compensated by the turbulence transport term.

The qualitative features of the budget of $\overline{v'^2}$ does not change significantly through the recirculation and reattachment regions (Figs. 5.77 and 5.79) although all terms decay in magnitudes. The turbulence transport term is one of the dominant terms in the budget, transporting normal stress away from the region below the shear layer to the near wall region and the high-speed side of the shear layer. Similar to the streamwise component, the triple products that make up the turbulence transport term T_{22} are anti-symmetric in the shear layer. These are plotted in Fig. 5.81. Note that the triple correlation $\overline{v'^3}$ has about the same relative magnitude as $\overline{u'^2 v'}$ (Fig. 5.75).

Unlike the standard turbulent boundary layer, the vertical velocity gradient, $\partial V/\partial y$, is very large in the vicinity of the reattachment. The production of $\overline{v'^2}$ thus becomes significant below the step.

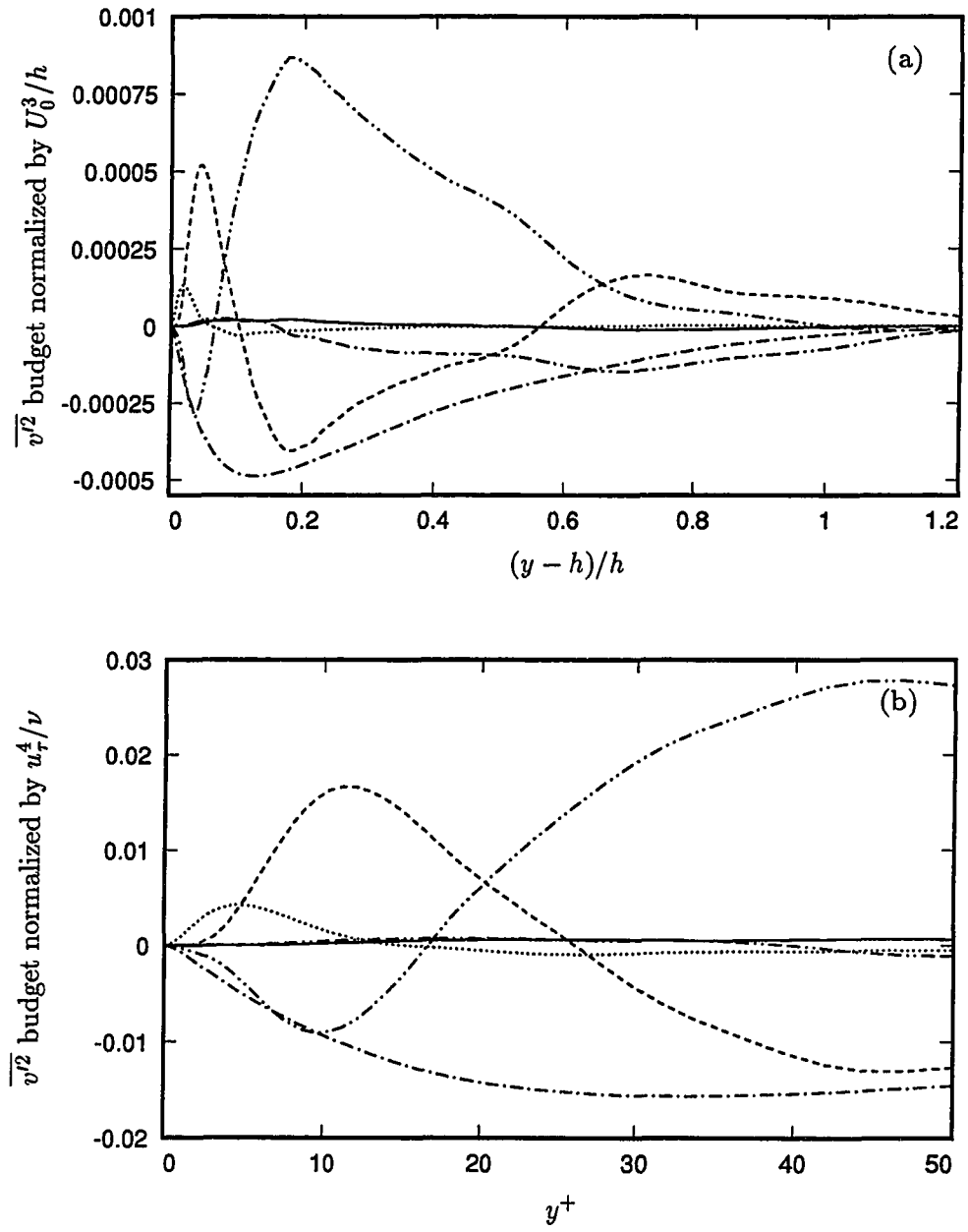

Figure 5.76. Vertical Reynolds-stress budget at $x/h = -2.0$. ---- convection; —— production; ---- turbulence transport; ····· viscous diffusion; —·— viscous dissipation; —··— velocity pressure-gradient. (a) Away from the wall; (b) near the wall.

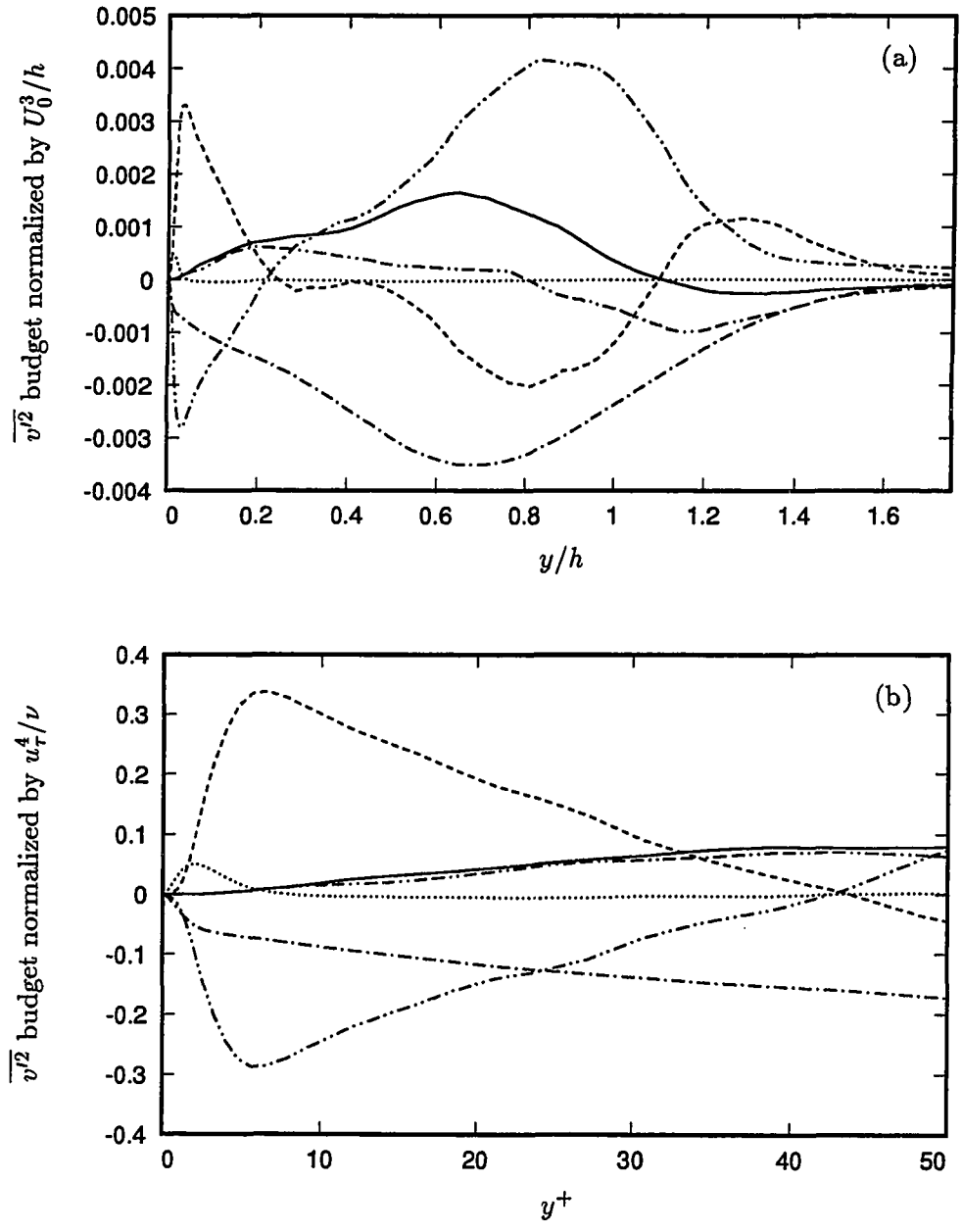

Figure 5.77. Vertical Reynolds-stress budget at $x/h = 4.0$. -·-· convection; —— production; ---- turbulence transport; ····· viscous diffusion; —·— viscous dissipation; —··— velocity pressure-gradient. (a) Away from the wall (least-square fit); (b) near the wall.

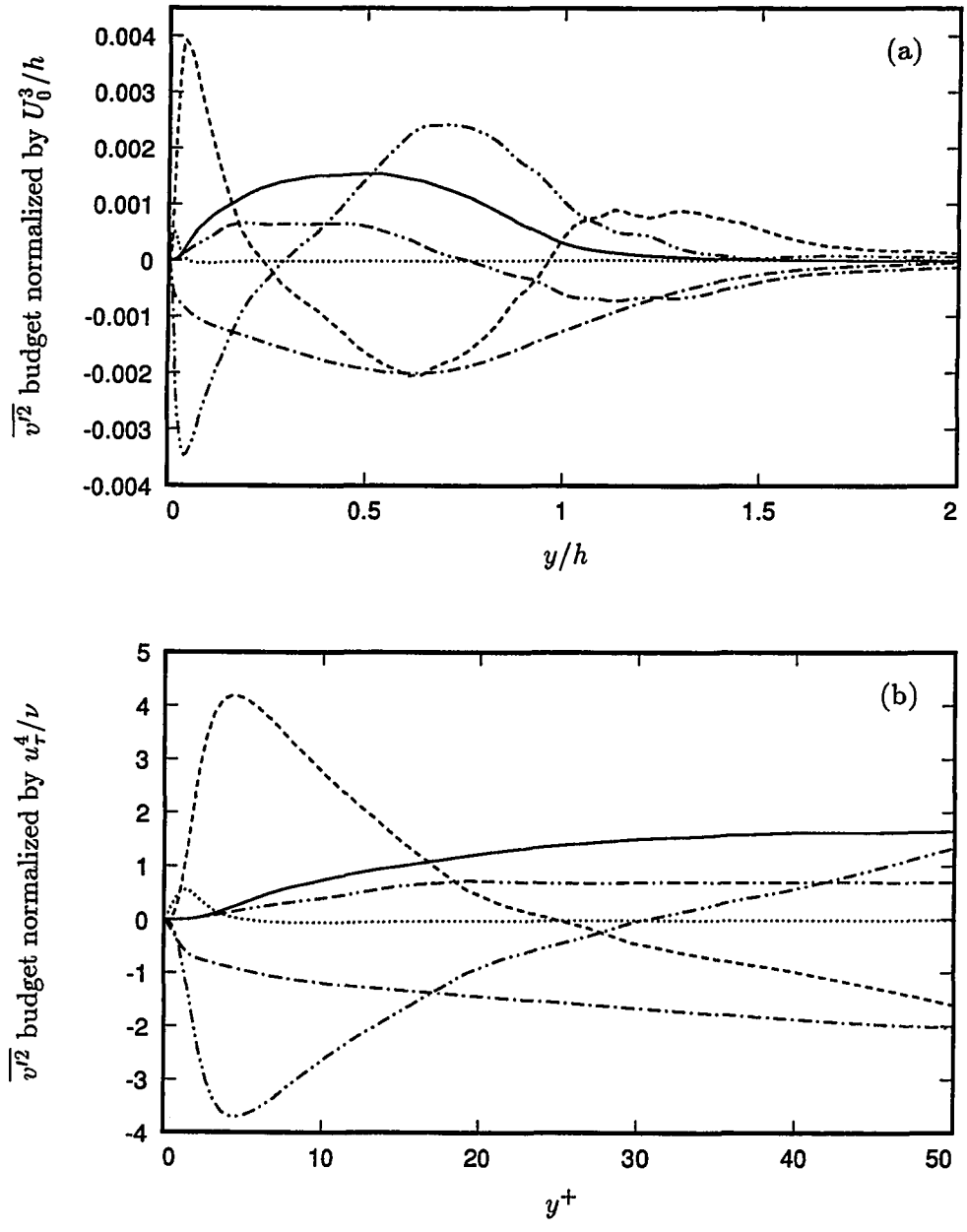

Figure 5.78. Vertical Reynolds-stress budget at $x/h = 7.0$. —·— convection; —— production; ---- turbulence transport; ····· viscous diffusion; —·— viscous dissipation; —··— velocity pressure-gradient. (a) Away from the wall (least-square fit); (b) near the wall.

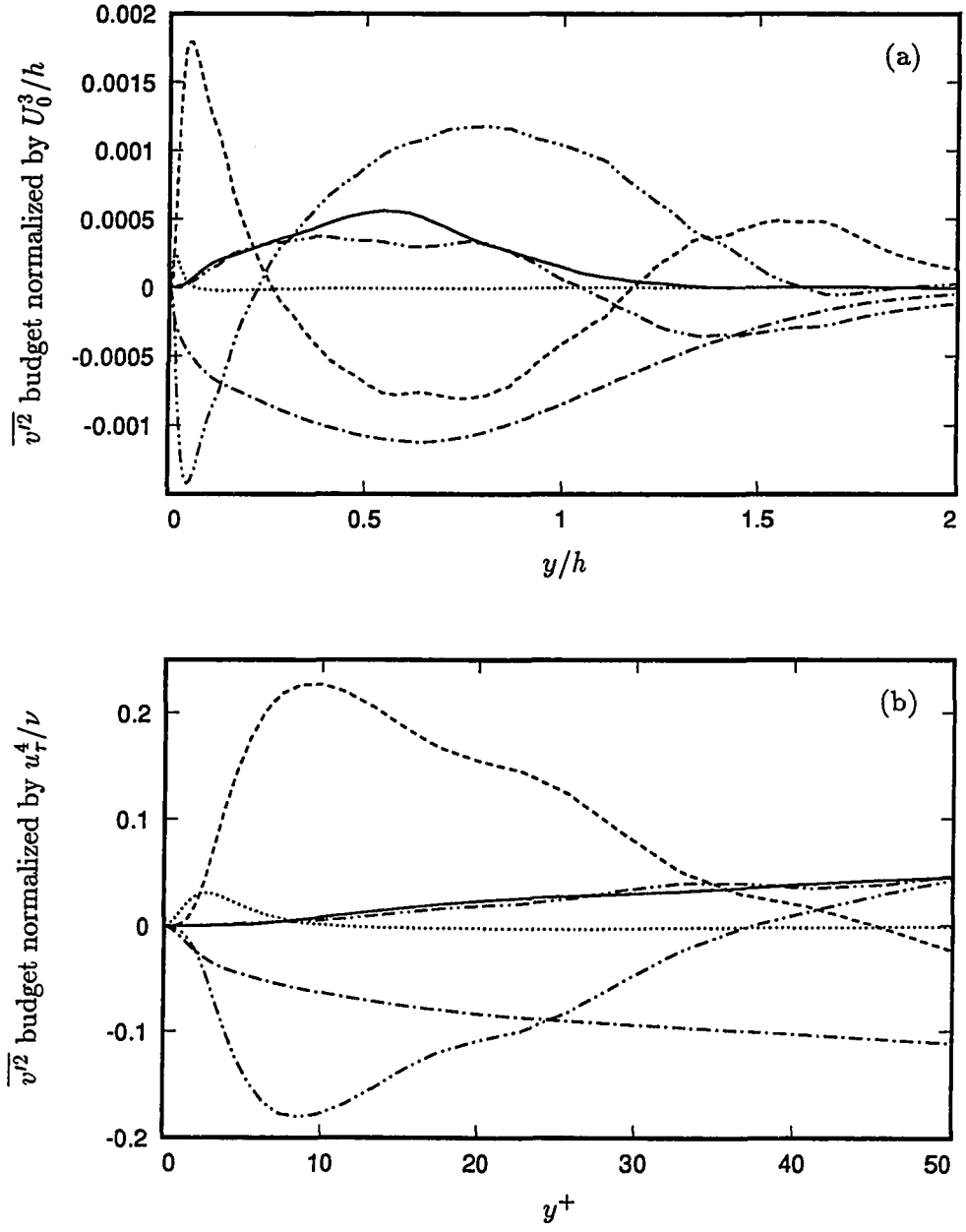

Figure 5.79. Vertical Reynolds-stress budget at $x/h = 10.0$. -·-· convection; —— production; ---- turbulence transport; ····· viscous diffusion; —·— viscous dissipation; —·— velocity pressure-gradient. (a) Away from the wall (least-square fit); (b) near the wall.

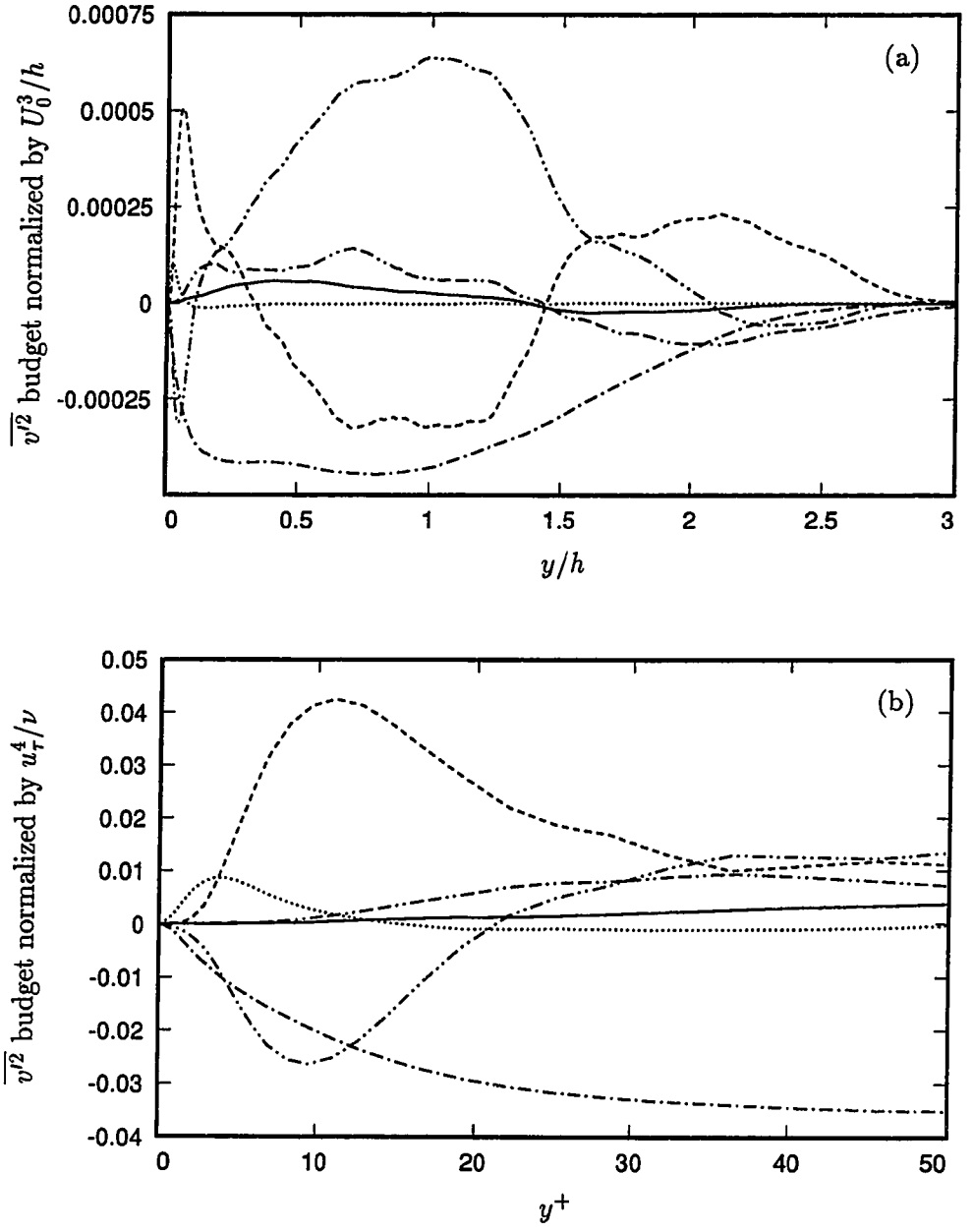

Figure 5.80. Vertical Reynolds-stress budget at $x/h = 18.0$. -·-· convection; —— production; ---- turbulence transport; ····· viscous diffusion; —·— viscous dissipation; —··— velocity pressure-gradient. (a) Away from the wall (least-square fit); (b) near the wall.

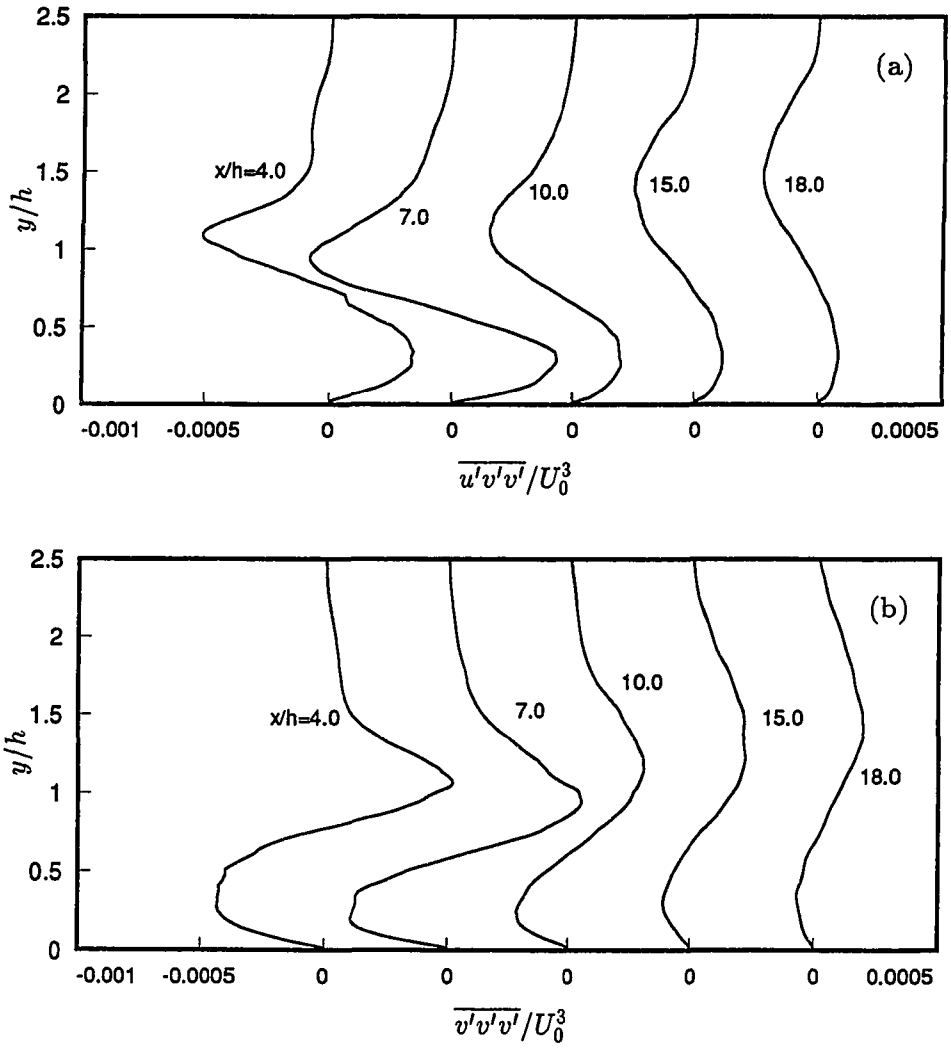

Figure 5.81. Triple products. (a) $\overline{u'v'v'}$; (b) $\overline{v'v'v'}$.

5.9.4. Spanwise Stress Budget

The budget of the spanwise component of the Reynolds-stress is given by

$$\frac{\partial \overline{u_3' u_3'}}{\partial t} = \underbrace{-U_k \overline{(u_3' u_3')}_{,k}}_{C_{33}} \underbrace{-\overline{(u_3' u_3' u_k')}_{,k}}_{T_{33}} + \underbrace{\frac{1}{Re}\overline{(u_3' u_3')}_{,kk}}_{D_{33}} \underbrace{-\frac{2}{Re}\overline{u_{3,k}' u_{3,k}'}}_{\epsilon_{33}} \underbrace{-2\overline{u_3' p_{,3}'}}_{\Pi_{33}}. \quad (5.9)$$

The budgets for $\overline{u_3' u_3'}$ in the shear layer and near the wall are presented in Figs. 5.82–5.86. Also plotted are profiles of the two triple products $\overline{w'^2 u'}$ and $\overline{w'^2 v'}$ in Fig. 5.87. It is apparent from Fig. 5.87 that more statistical samples are needed for the convergence of $\overline{w'^2 u'}$ and $\overline{w'^2 v'}$.

At $x/h = -2.0$, the $\overline{w'^2}$ budget is very similar to that of a zero pressure gradient boundary layer (Spalart, 1988). The flow acceleration, however, leads to a slight increase in the turbulence convection, C_{33}, at $0.2 < y/h < 0.4$.

As in the budgets of $\overline{u'^2}$ and $\overline{v'^2}$, the triple products are anti-symmetric in the recirculation region (Fig. 5.87); hence the turbulence transport removes energy from the shear layer region and adds it to the near wall region and to the high-speed side of the layer. T_{33} remains small across the shear layer. The velocity pressure-gradient term increases rapidly, reaching its peak in the shear layer where it is mostly balanced by the viscous dissipation. Below $y^+ = 5$, however, all terms except the turbulence convection are significant. Compared to the budget upstream of the step, the near-wall peak of Π_{33} is doubled. The two viscous terms, D_{33} and ϵ_{33}, attain their maxima at the wall which are about four times that in a zero pressure gradient boundary layer. Another departure from a standard turbulent boundary layer is that the dissipation term monotonically decreases in the region $0 < y^+ < 20$ and does not have a near wall peak at $y^+ \approx 10$.

Behind the reattachment, Π_{33} and ϵ_{33} decrease in relative magnitude in the shear layer, but the transport and convection of turbulence remain about the same as in the recirculation zone (Fig. 5.85). The terms now become significant near the wall as the features of the turbulent boundary layer re-emerge. The same trend continues into the recovery region (Fig. 5.86).

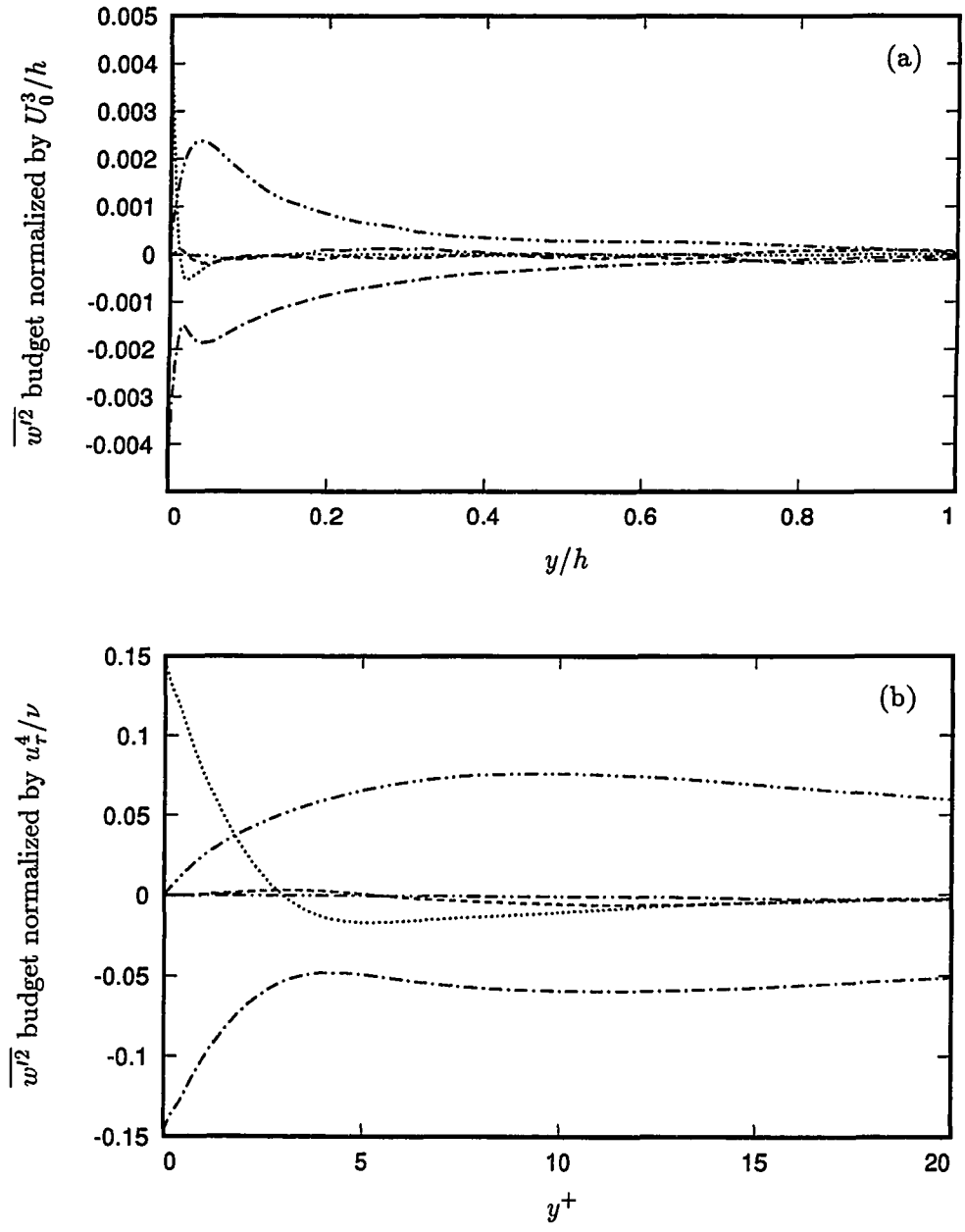

Figure 5.82. Spanwise Reynolds-stress budget at $x/h = -2.0$. -·-· convection; ---- turbulence transport; ····· viscous diffusion; —·— viscous dissipation; ——— velocity pressure-gradient. (a) Away from the wall; (b) near the wall.

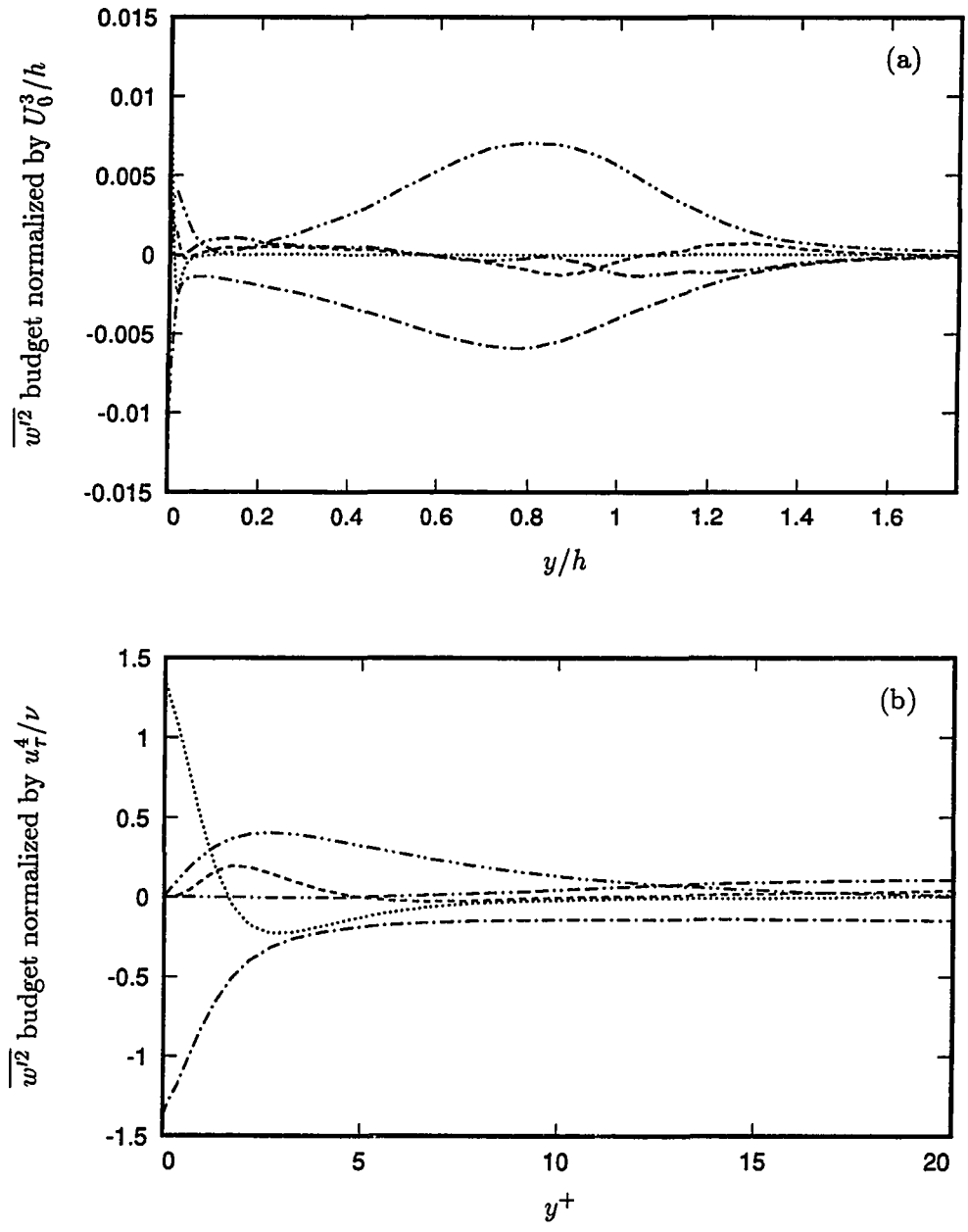

Figure 5.83. Spanwise Reynolds-stress budget at $x/h = 4.0$. -·-· convection; ---- turbulence transport; ····· viscous diffusion; —·— viscous dissipation; —··— velocity pressure-gradient. (a) Away from the wall (least-square fit); (b) near the wall.

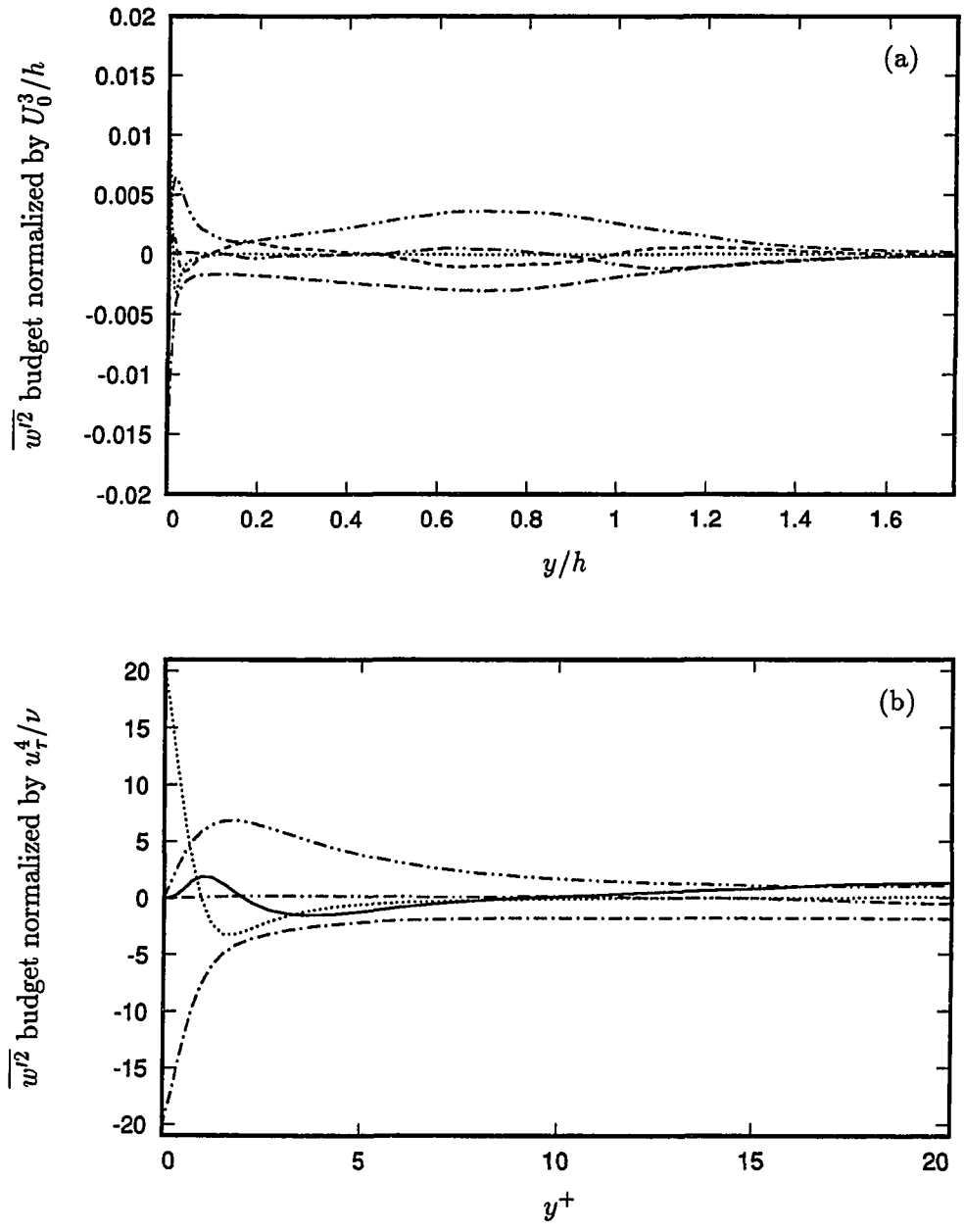

Figure 5.84. Spanwise Reynolds-stress budget at $x/h = 7.0$. ·—· convection; ---- turbulence transport; ····· viscous diffusion; —·— viscous dissipation; —··— velocity pressure-gradient. (a) Away from the wall (least-square fit); (b) near the wall.

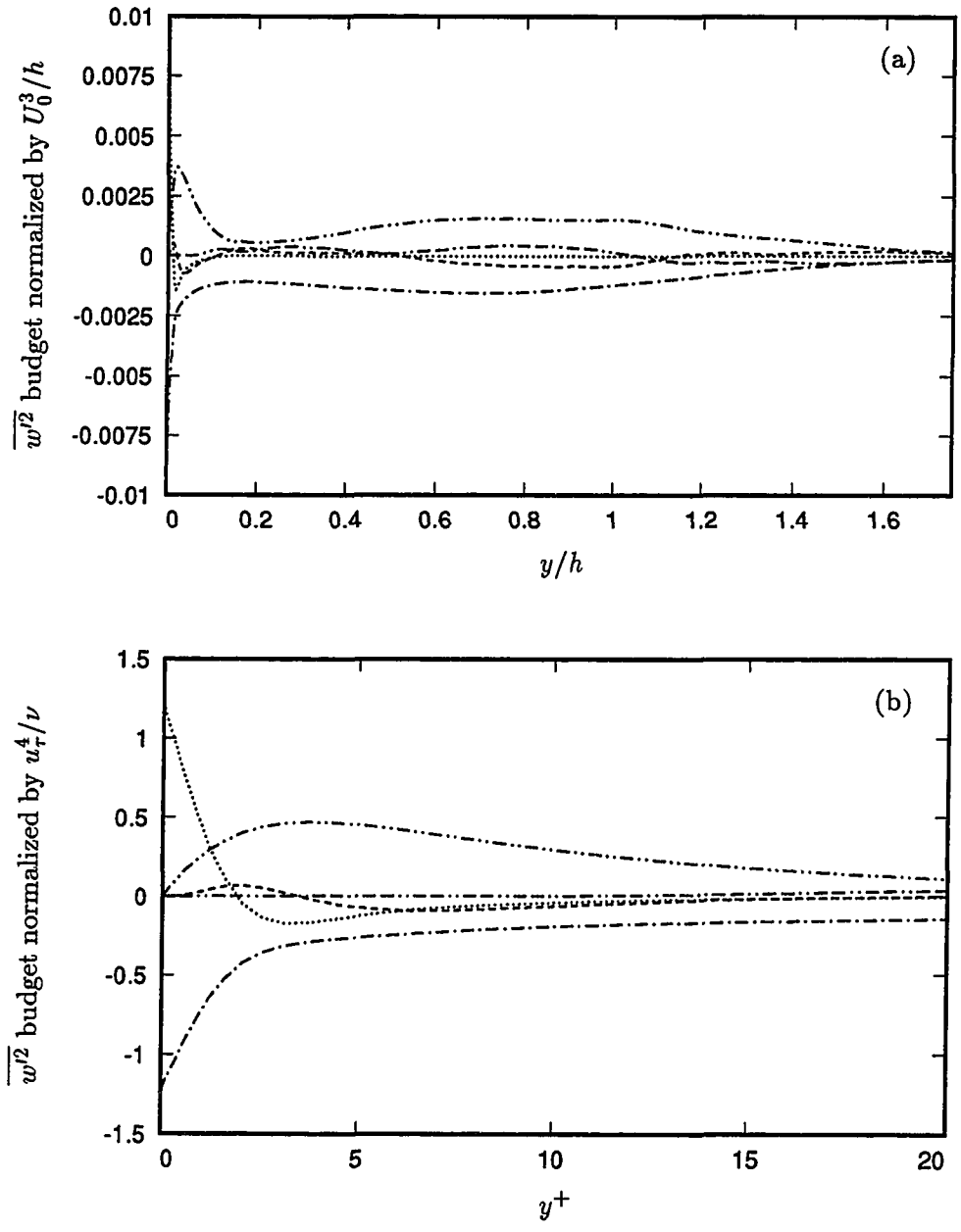

Figure 5.85. Spanwise Reynolds-stress budget at $x/h = 10.0$. ---·--- convection; ---- turbulence transport; ····· viscous diffusion; —·— viscous dissipation; —··— velocity pressure-gradient. (a) Away from the wall (least-square fit); (b) near the wall.

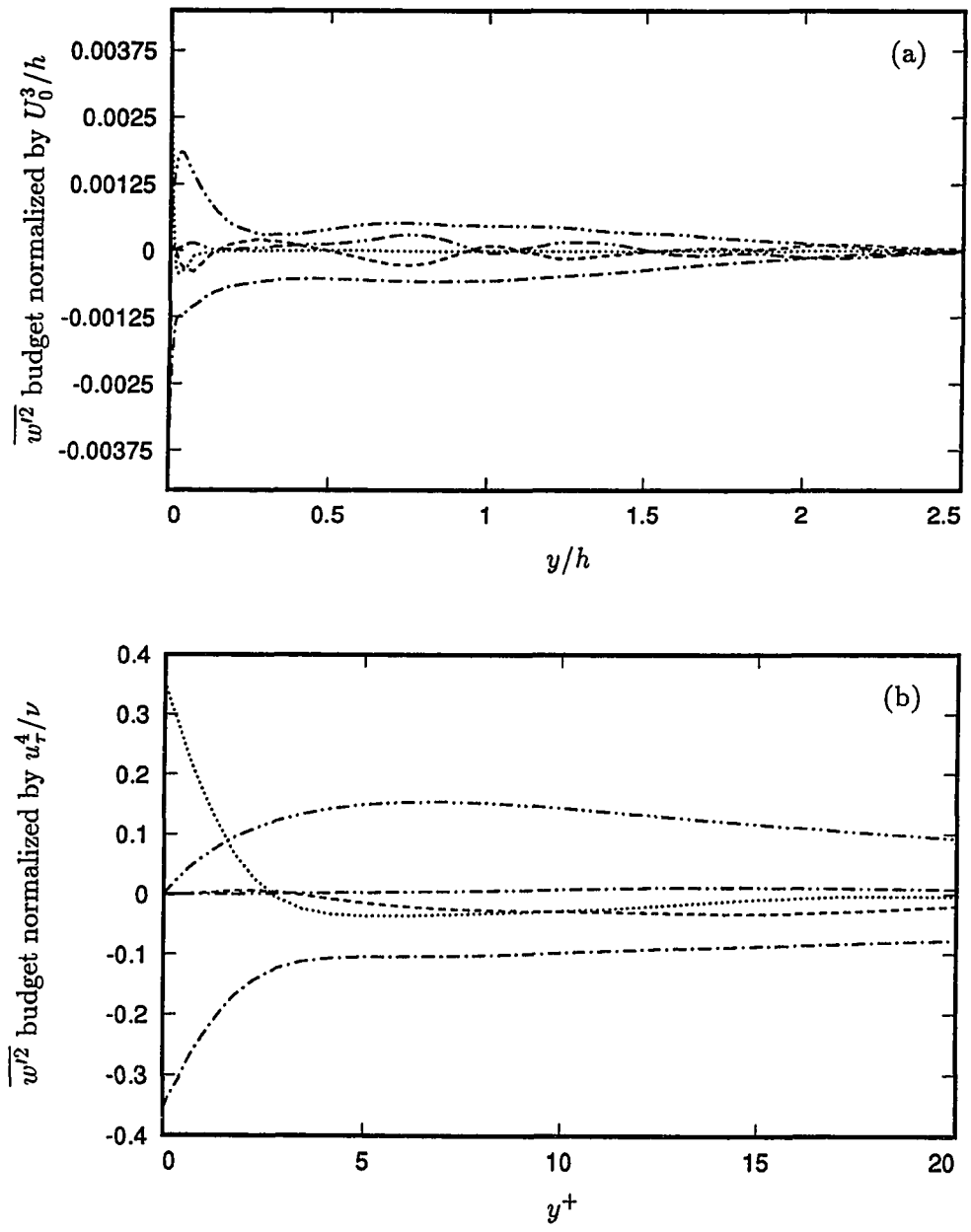

Figure 5.86. Spanwise Reynolds-stress budget at $x/h = 18.0$. -·-· convection; ---- turbulence transport; ····· viscous diffusion; —·— viscous dissipation; —··— velocity pressure-gradient. (a) Away from the wall (least-square fit); (b) near the wall.

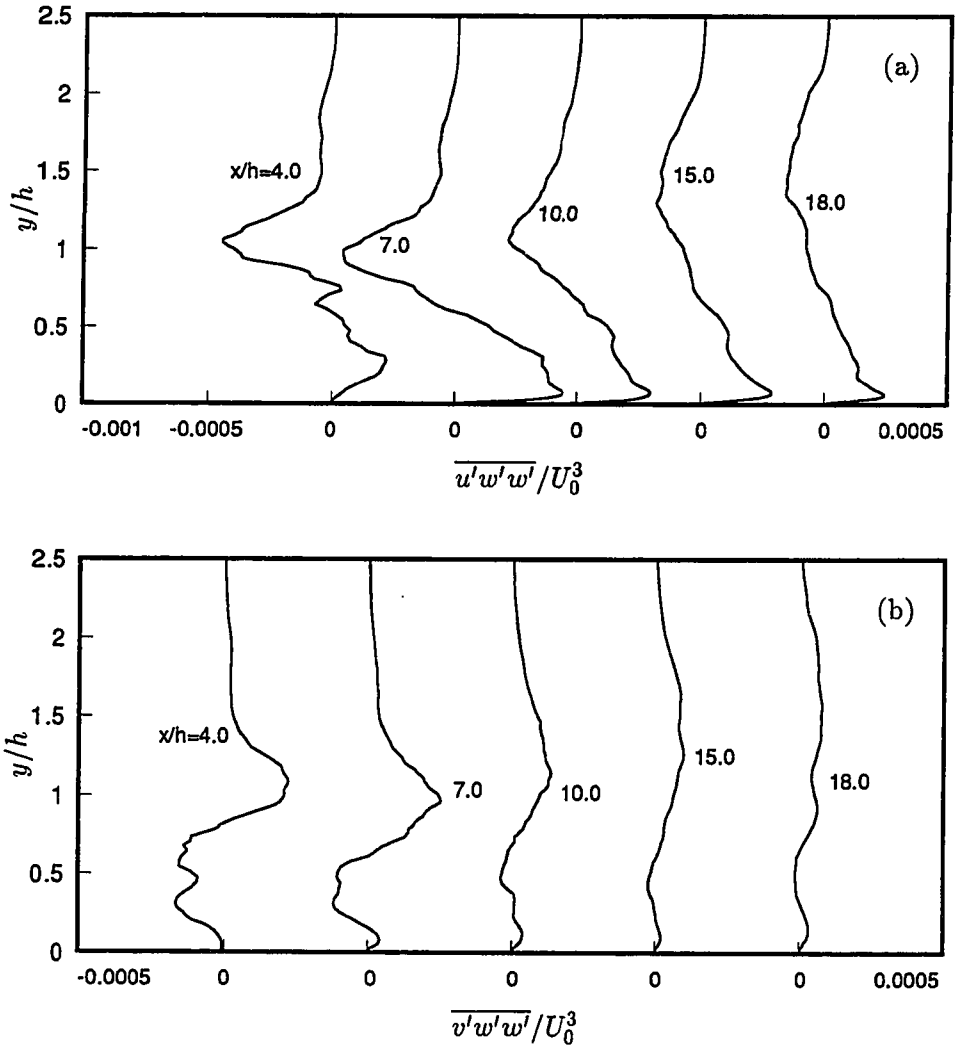

Figure 5.87. Triple products. (a) $\overline{u'w'w'}$; (b) $\overline{v'w'w'}$.

5.9.5. Reynolds Shear Stress Budget

The governing equation for the Reynolds shear stress is

$$\frac{\partial \overline{u_1' u_2'}}{\partial t} = \underbrace{-U_k \overline{(u_1' u_2')}_{,k}}_{C_{12}} \underbrace{-\overline{u_1' u_1'} U_{2,1} - \overline{u_2' u_2'} U_{1,2}}_{P_{12}} \underbrace{-\overline{(u_1' u_2' u_k')}_{,k}}_{T_{12}} + \underbrace{\frac{1}{Re} \overline{(u_1' u_2')}_{,kk}}_{D_{12}} \underbrace{-\frac{2}{Re} \overline{u_{1,k}' u_{2,k}'}}_{\epsilon_{12}} \underbrace{-2\overline{u_1' p_{,2}'} - 2\overline{u_2' p_{,1}'}}_{\Pi_{12}}. \tag{5.10}$$

The budget of the Reynolds shear stress is dominated by the production and velocity pressure-gradient terms in all streamwise locations. Unlike the zero pressure gradient boundary layer, the convection of the shear stress (C_{12}) is significant in the outer region ($(y-h)/h > 0.5$).

In the recirculation region (Fig. 5.89), the production peaks in the shear layer. The velocity pressure-gradient term also peaks in the shear layer, but only accounts for about 75% of P_{12}. The turbulence transport is a significant dissipating term in the shear layer (20% of P_{12}). Viscous dissipation amounts to only 5% of production. Close to the wall, the production of $\overline{u'v'}$ becomes positive due to the negative gradient of the mean velocity U in the reverse flow, and it is balanced by T_{12}.

As the flow progresses downstream through the reattachment and recovery zones, the profile peaks shift from the shear layer to the wall region. The near-wall distribution of the budget in these regions are similar to that of a standard turbulent boundary layer (Figs. 5.91(b) and 5.92(b), $y^+ < 20$) except for much higher levels of turbulence transport. At $x/h = 18.0$, the effects of the shear layer are still much more present in the dynamics of the Reynolds shear stress than in other components as seen in Fig. 5.92(a).

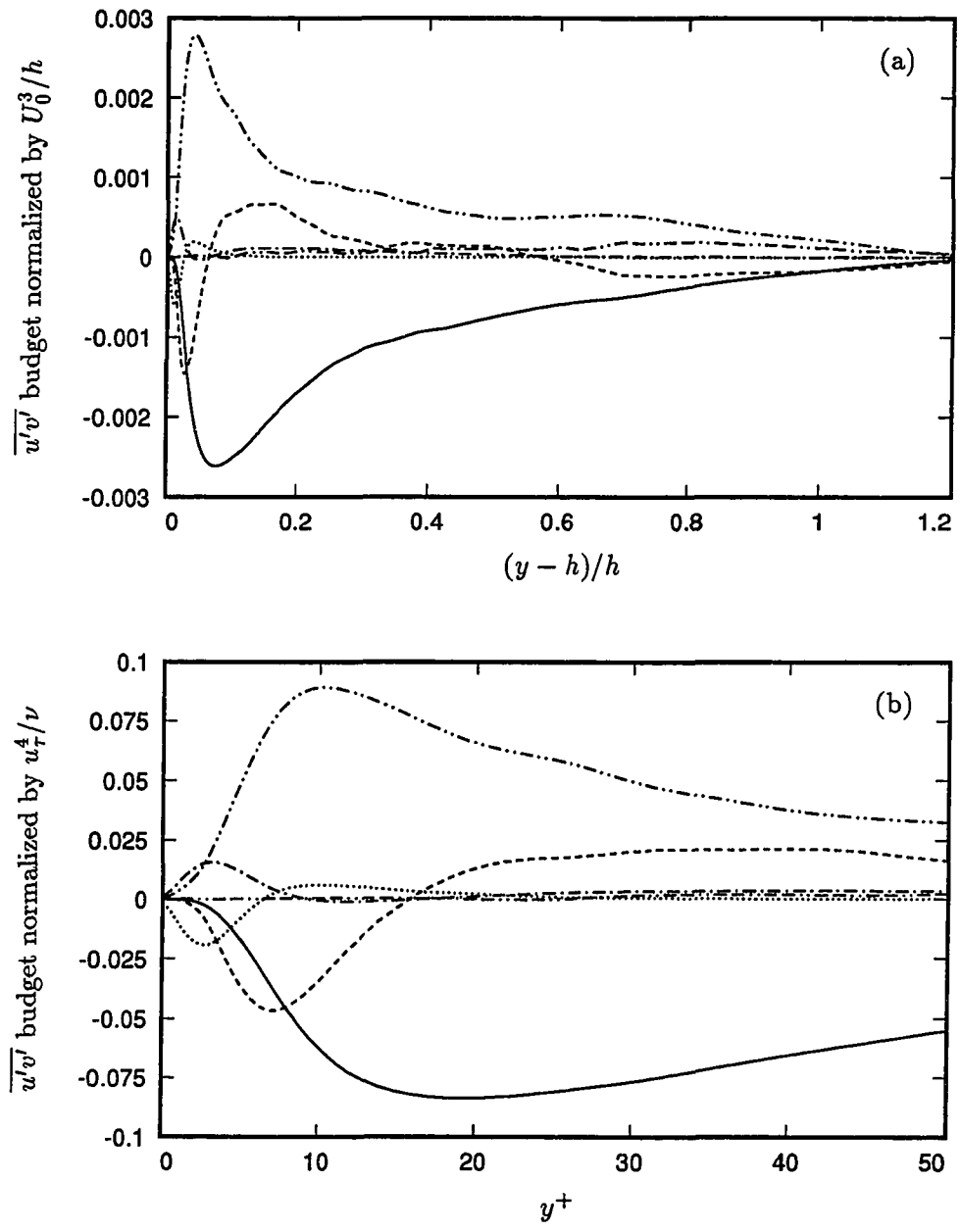

Figure 5.88. Reynolds shear stress budget at $x/h = -2.0$. -·-· convection; —— production; ---- turbulence transport; ····· viscous diffusion; —·— viscous dissipation; —··— velocity pressure-gradient. (a) Away from the wall; (b) near the wall.

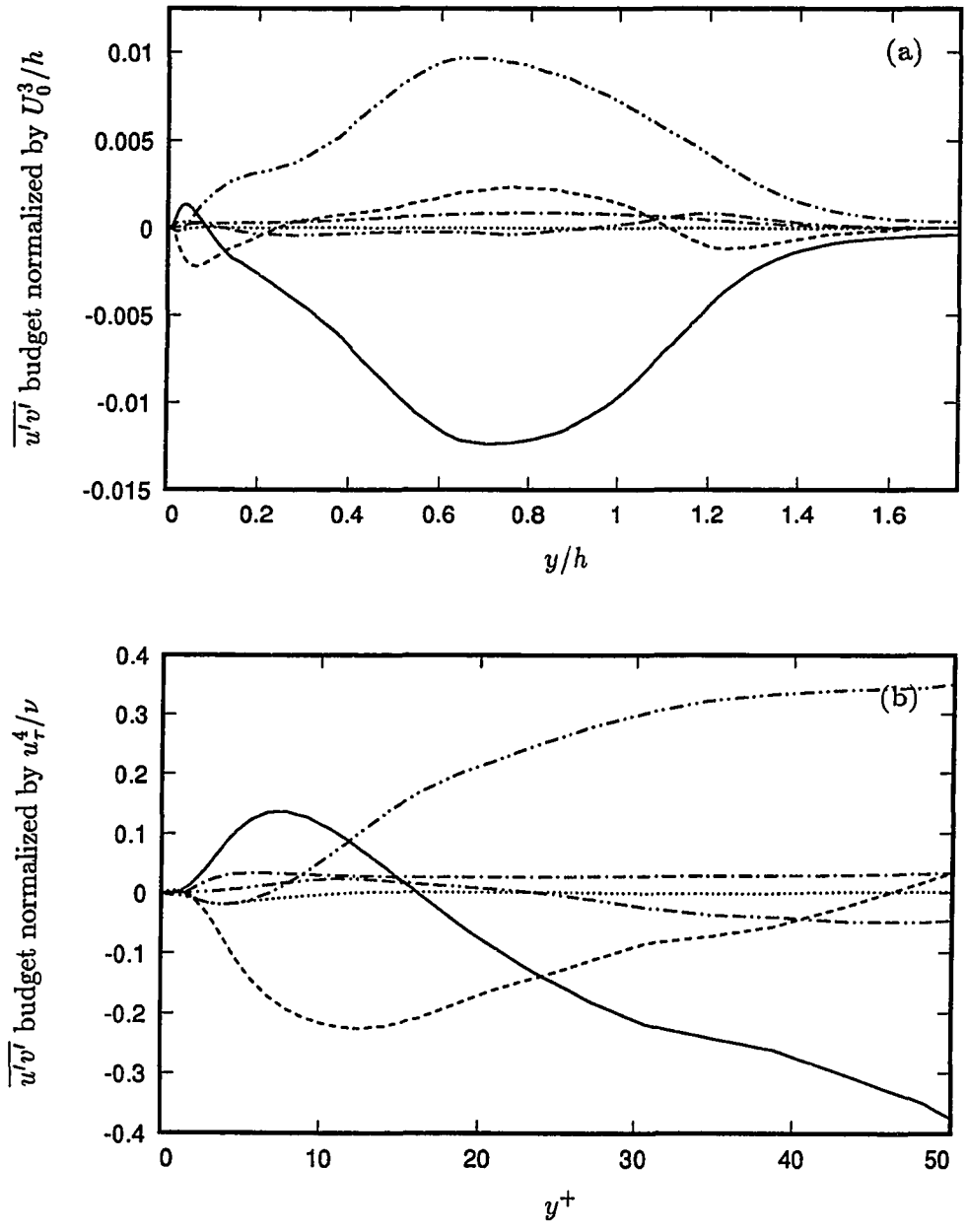

Figure 5.89. Reynolds shear stress budget at $x/h = 4.0$. ——· convection; —— production; ---- turbulence transport; ····· viscous diffusion; —·— viscous dissipation; —··— velocity pressure-gradient. (a) Away from the wall (least-square fit); (b) near the wall.

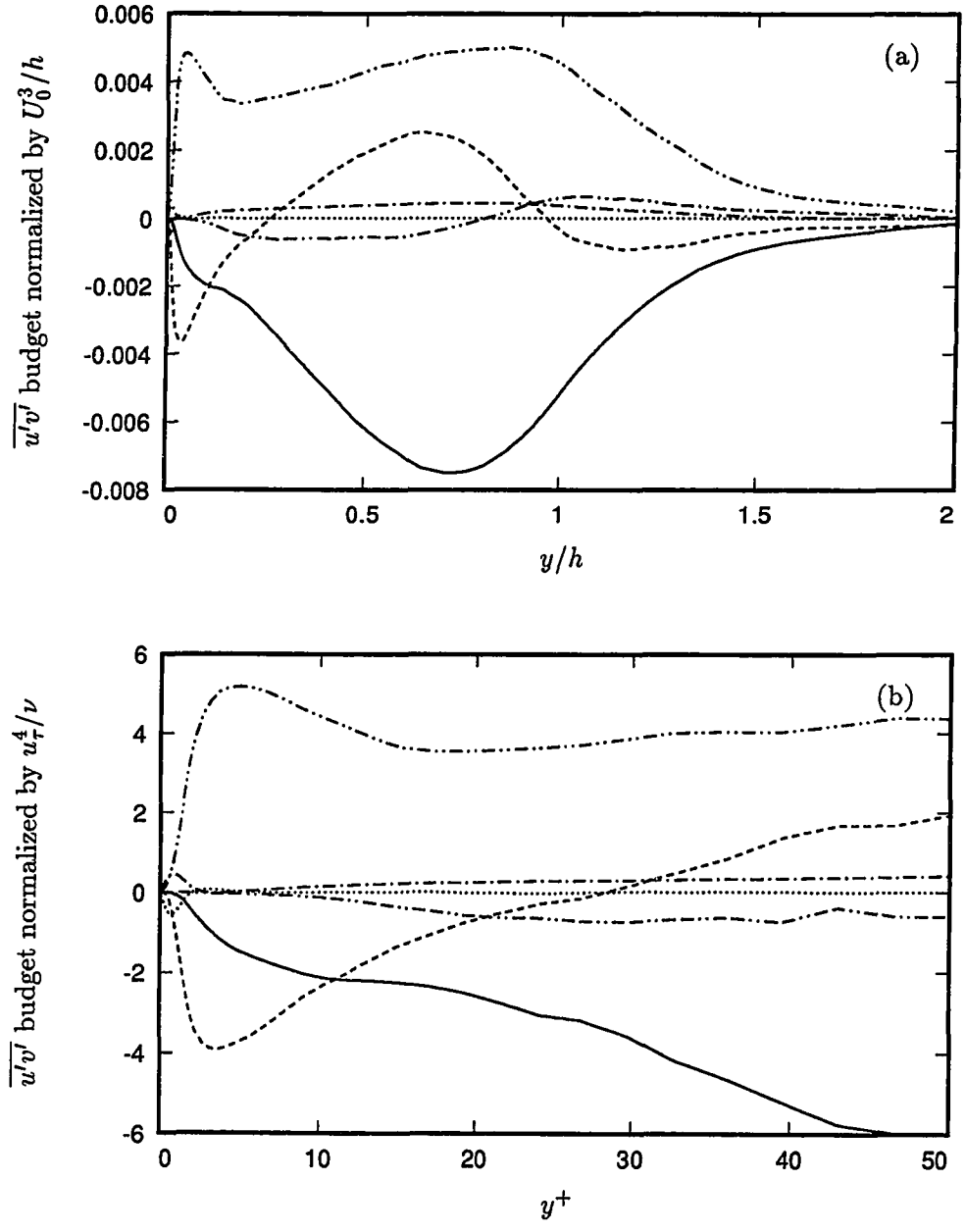

Figure 5.90. Reynolds shear stress budget at $x/h = 7.0$. —·— convection; —— production; ---- turbulence transport; ····· viscous diffusion; —·— viscous dissipation; —··— velocity pressure-gradient. (a) Away from the wall (least-square fit); (b) near the wall.

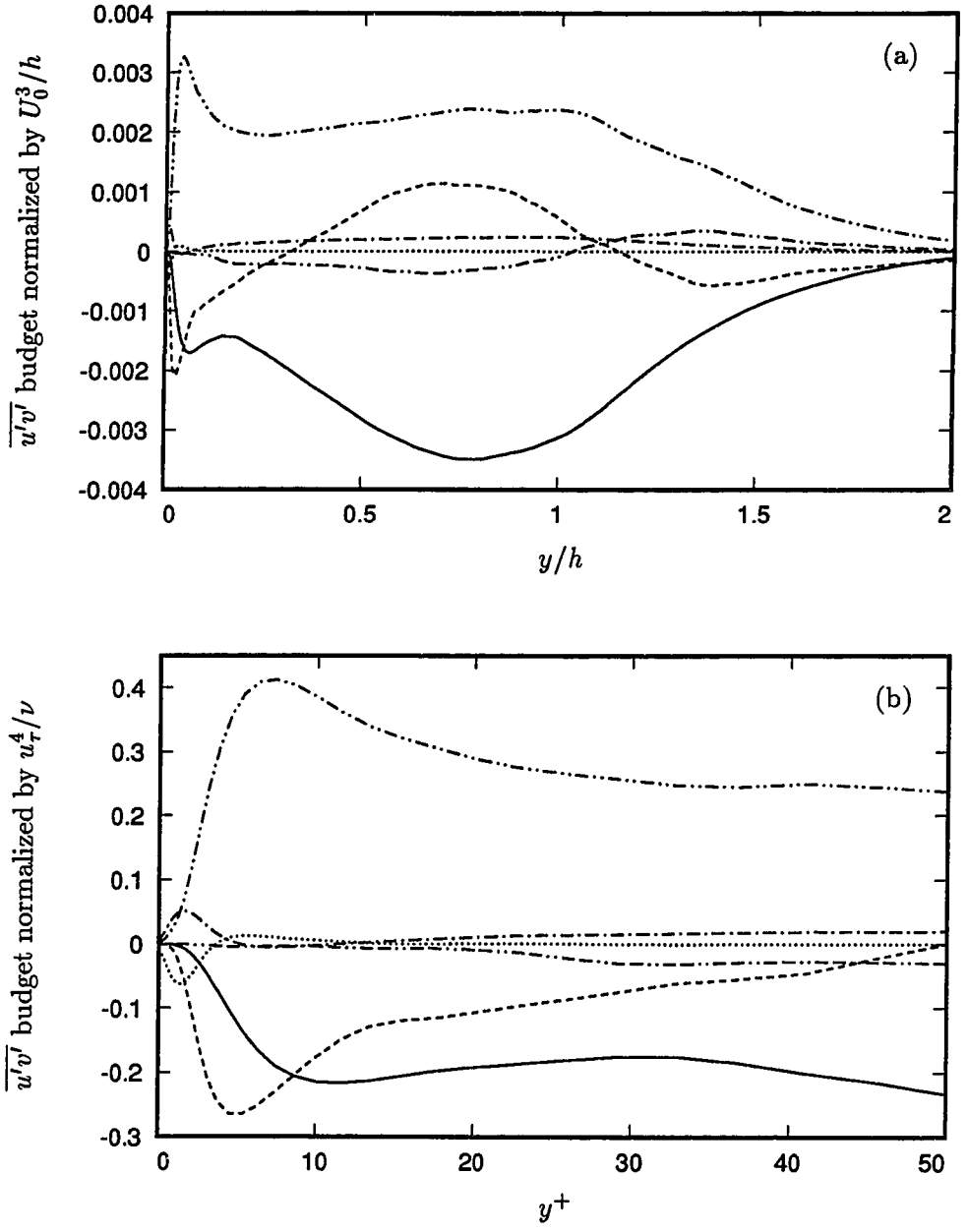

Figure 5.91. Reynolds shear stress budget at $x/h = 10.0$. ---·--- convection; ——— production; ---- turbulence transport; ····· viscous diffusion; —·— viscous dissipation; —··— velocity pressure-gradient. (a) Away from the wall (least-square fit); (b) near the wall.

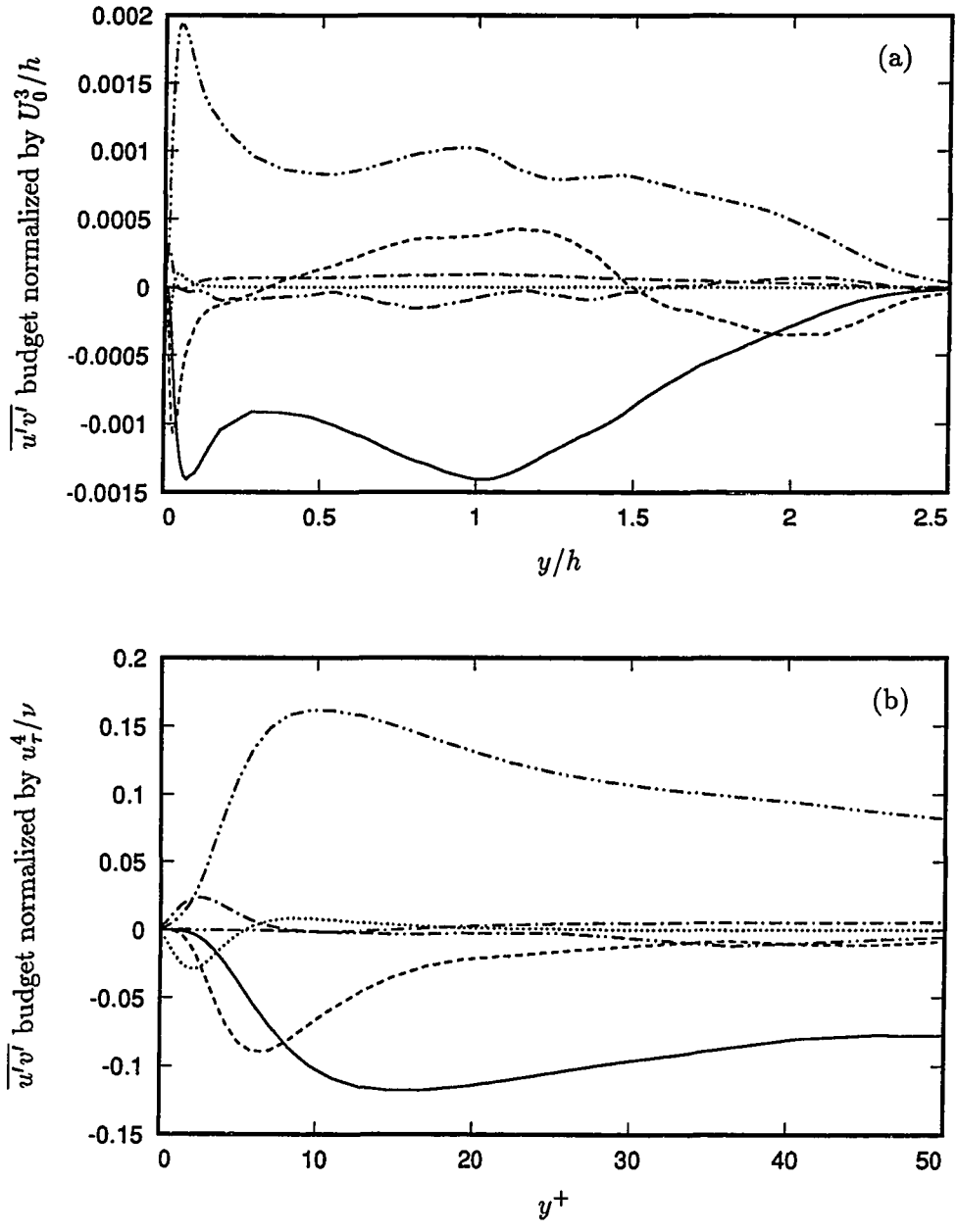

Figure 5.92. Reynolds shear stress budget at $x/h = 18.0$. -·-· convection; —— production; ---- turbulence transport; ····· viscous diffusion; —·— viscous dissipation; —·—· velocity pressure-gradient. (a) Away from the wall (least-square fit); (b) near the wall.

5.9.6. Turbulent Kinetic Energy Budget

The turbulent kinetic energy budget is given by

$$\frac{\partial (q^2/2)}{\partial t} = \underbrace{-\tfrac{1}{2}U_k\overline{(u_l'u_l')}_{,k}}_{C_k} \underbrace{-\overline{u_l'u_k'}U_{l,k}}_{P_k} \underbrace{-\tfrac{1}{2}\overline{(u_l'u_l'u_k')}_{,k}}_{T_k} + \underbrace{\frac{1}{2Re}\overline{(u_l'u_l')}_{,kk}}_{D_k} \underbrace{-\frac{1}{Re}\overline{u_{l,k}'u_{l,k}'}}_{\epsilon_k} \underbrace{-\overline{u_l'p_{,l}'}}_{\Pi_k}, \tag{5.11}$$

where,

$$\frac{q^2}{2} = \frac{1}{2}\left(\overline{u'^2} + \overline{v'^2} + \overline{w'^2}\right).$$

The budget for the turbulent kinetic energy is shown in Figs. 5.93–5.97. At two step heights before the separation, the energy budget (Figs. 5.93) is similar to that of a zero pressure gradient turbulent boundary layer (Spalart, 1988) although there is an enhancement of the viscous terms near the wall (as in the longitudinal turbulence intensity) and also higher levels of turbulence transport.

In the recirculation region, P_k is mostly due to the production of the longitudinal stress: $P_k \approx P_{11}$. The turbulence transport term removes energy from the shear layer region, $0.3 < y/h < 1.1$, and delivers it to regions near the wall and away from the shear layer.

The turbulent kinetic energy budget in the recirculation region is very similar to that of a plane mixing layer (Bradshaw & Ferriss, 1965 and Roger & Moser, 1993). This budget also agrees qualitatively with the measurements by Chandrsuda & Bradshaw (1981) for a backward-facing step flow. Both production P_k and viscous dissipation ϵ_k have maximum values at the same point in the free-shear layer. The peak ϵ_k is approximately 60% of the production peak. Thus, the commonly used assumption leading to eddy viscosity parameterization, that production is balanced with dissipation is not applicable in the recirculation region.

As one approaches the wall, production becomes a consuming term because of the negative gradient of the mean reverse flow (Fig. 5.94(b)) although its magnitude is relatively small. Very close to the wall, the two viscous terms, D_k and ϵ_k, grow

rapidly due the high intensities in all three directions (their value at the wall is about 40% higher than the peak production in the shear layer). The velocity pressure-gradient is very significant in the region $y^+ < 10$ where it balances the dissipation and turbulence transport terms.

All terms decay with x except near the wall. Near the flow exit, $y/h = 18$, the turbulent kinetic energy budget resembles that of a turbulent boundary layer. However, the effects of the free-shear layer are still present, e.g., T_k is still large at $y/h = 1$. The relative magnitudes of the viscous terms near the wall are much larger than in a zero pressure gradient boundary layer.

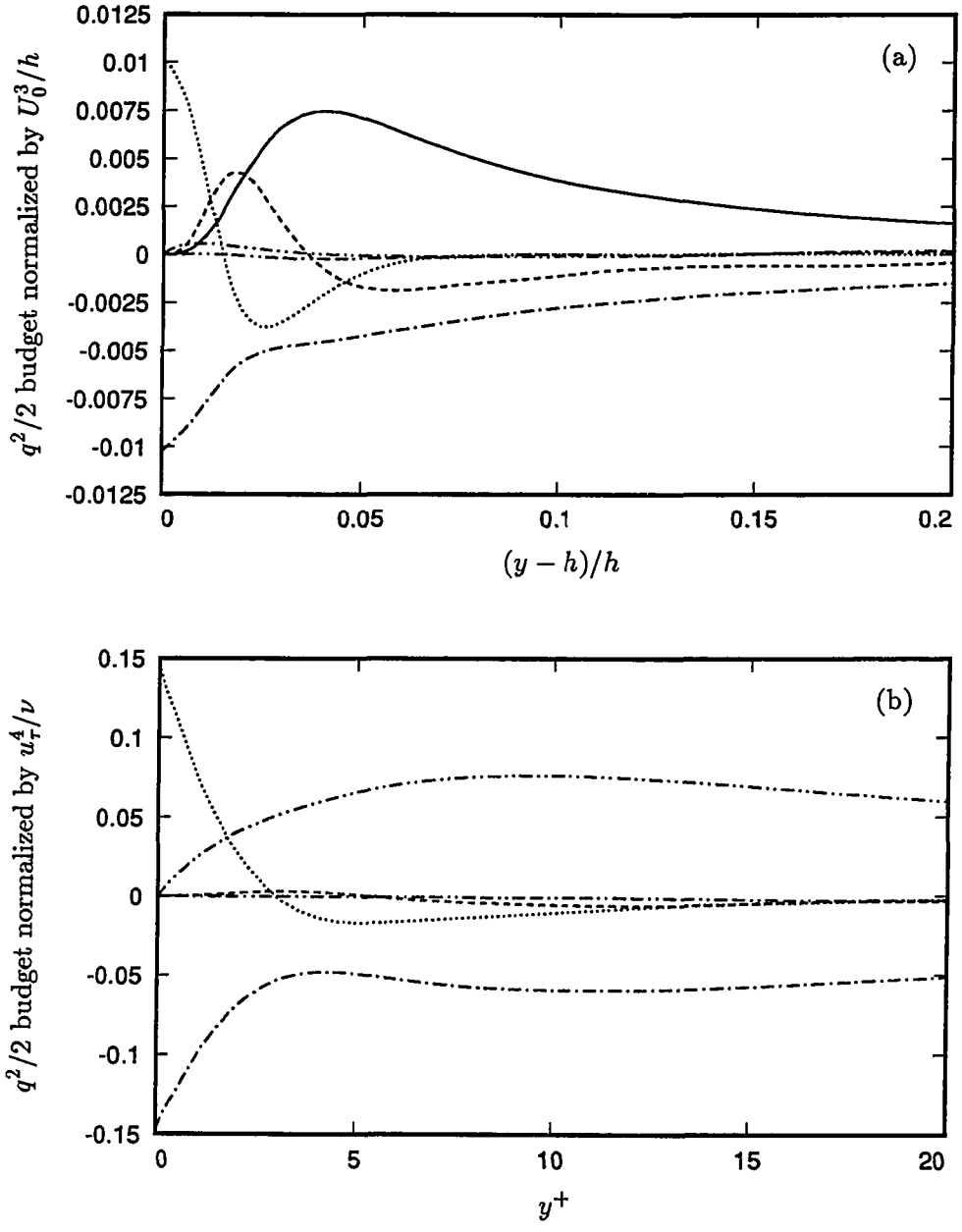

Figure 5.93. Turbulent kinetic energy budget at $x/h = -2.0$. -·-· convection; —— production; ---- turbulence transport; ····· viscous diffusion; —·— viscous dissipation; —··— velocity pressure-gradient. (a) Away from the wall; (b) near the wall.

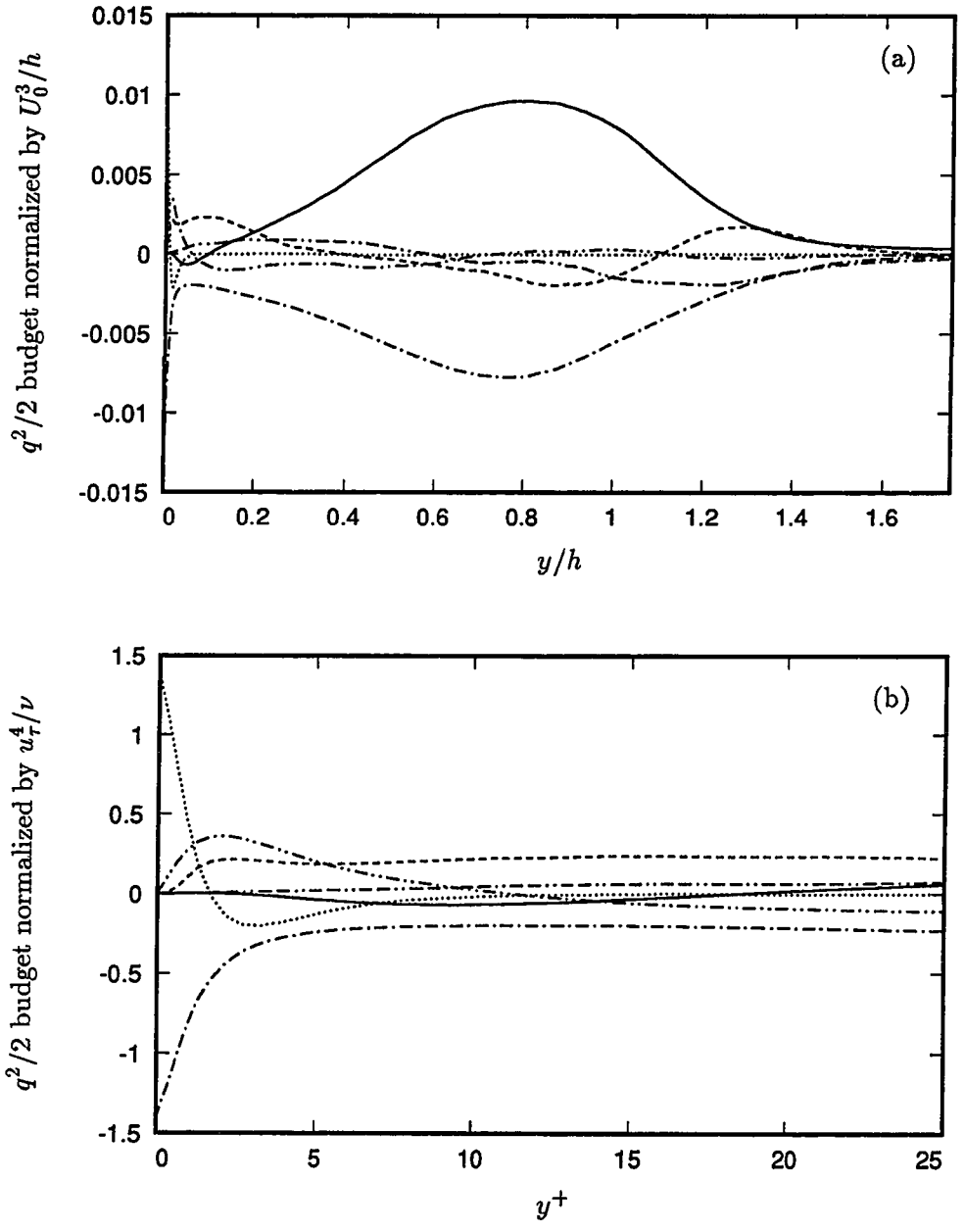

Figure 5.94. Turbulent kinetic energy budget at $x/h = 4.0$. -·-· convection; —— production; ---- turbulence transport; ····· viscous diffusion; —·— viscous dissipation; —·— velocity pressure-gradient. (a) Away from the wall (least-square fit); (b) near the wall.

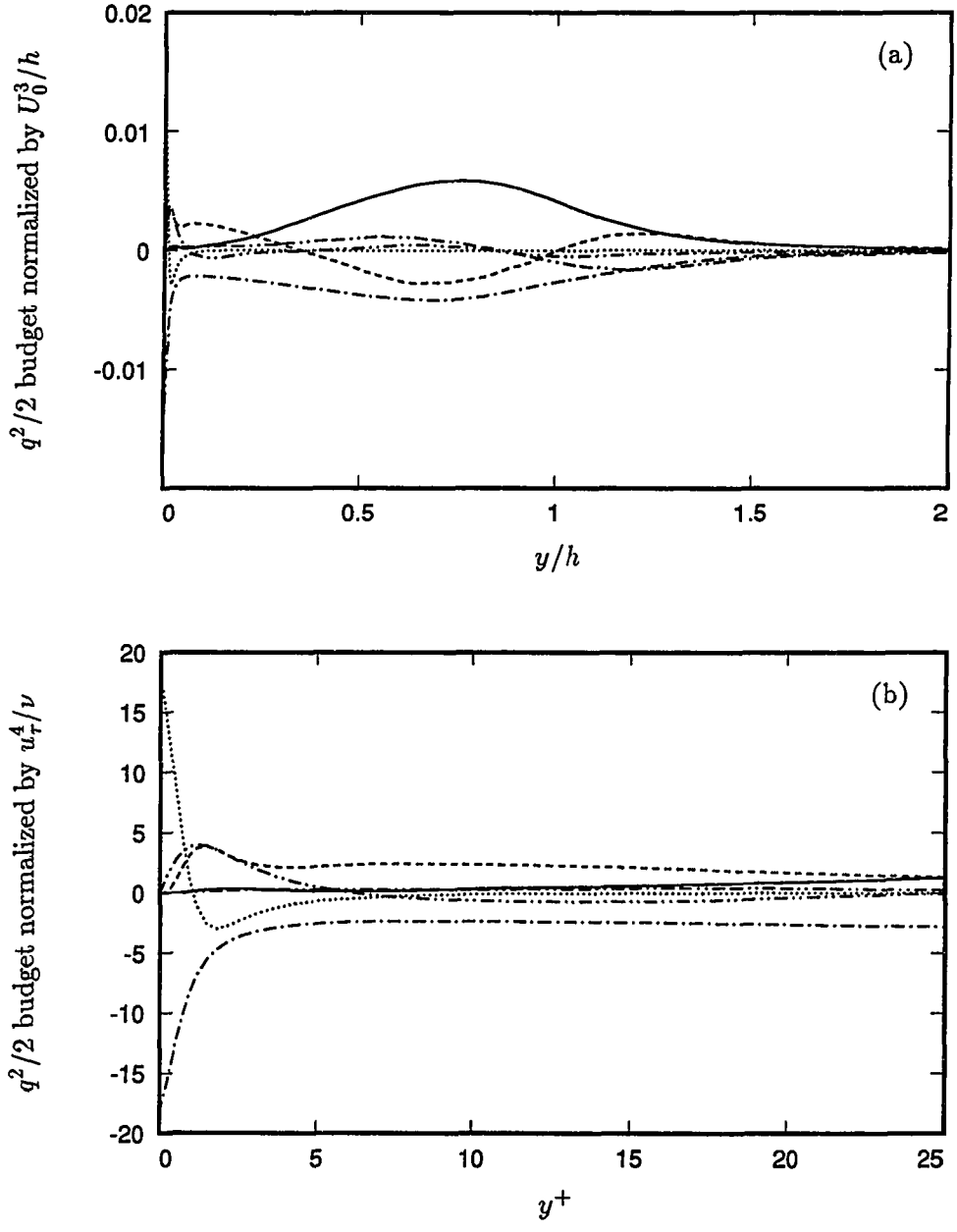

Figure 5.95. Turbulent kinetic energy budget at $x/h = 7.0$. -·-· convection; —— production; ---- turbulence transport; ····· viscous diffusion; —·— viscous dissipation; —·— velocity pressure-gradient. (a) Away from the wall (least-square fit); (b) near the wall.

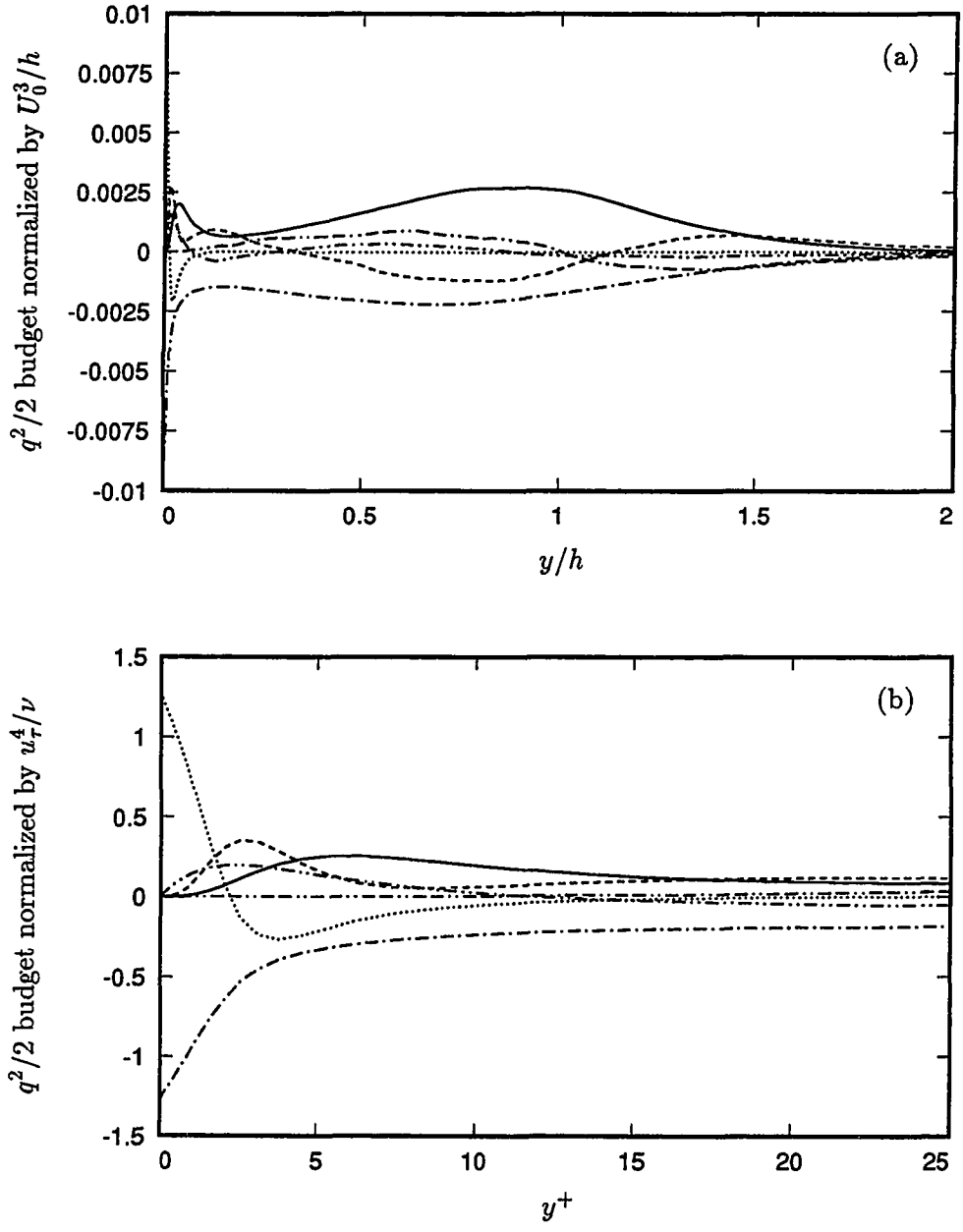

Figure 5.96. Turbulent kinetic energy budget at $x/h = 10.0$. -·-· convection; —— production; ---- turbulence transport; ····· viscous diffusion; —·— viscous dissipation; —·— velocity pressure-gradient. (a) Away from the wall (least-square fit); (b) near the wall.

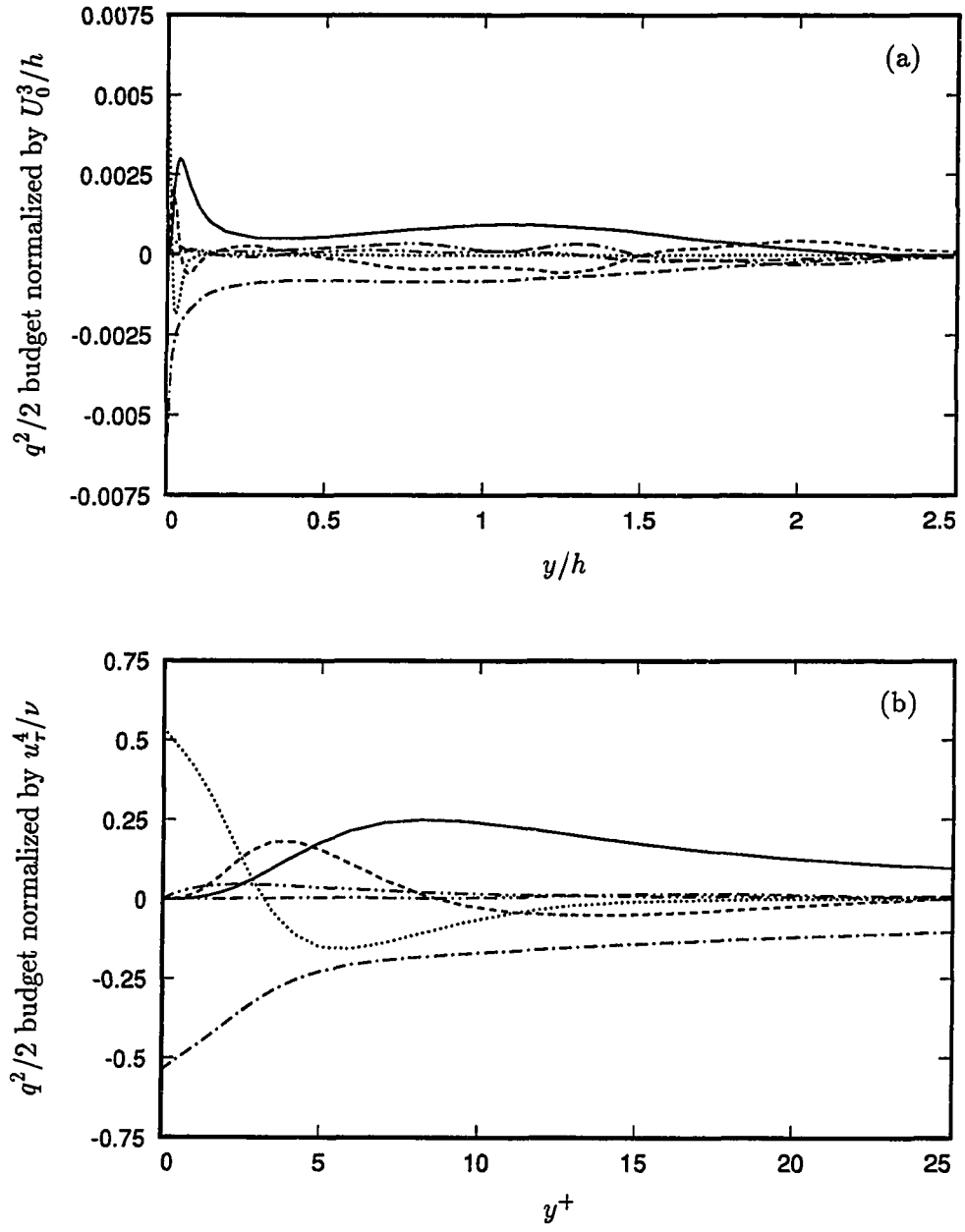

Figure 5.97. Turbulent kinetic energy budget at $x/h = 18.0$. —·— convection; —— production; ---- turbulence transport; ····· viscous diffusion; —·— viscous dissipation; —··— velocity pressure-gradient. (a) Away from the wall (least-square fit); (b) near the wall.

Chapter 6
CONCLUSIONS

Direct numerical simulations of turbulent flows over a backward-facing step were performed with the objective of developing a simulation method with turbulent inflow and outflow, and generating a comprehensive database for turbulence modeling. The statistical results compare well with data from the concurrent experiment by Jovic & Driver (1994). A large data base from this simulation has been archived. It contains up to third-order statistics, and the budgets of the Reynolds stress tensor. The main conclusions from this study are divided into two categories. The first category describes the lessons learned from the successive steps in developing the DNS method. In the second category, conclusions are drawn from the observed characteristics of the flow.

6.1. Computational Method

Resolution

Both 2-D and 3-D simulations were performed. For the Reynolds number range considered and with uniform grid spacing, the adequate mesh spacing in the streamwise direction in wall coordinates is $\Delta x^+ \approx 10$ based on the inlet friction velocity. In the vertical direction, fine mesh is needed at both the lower wall and at the step with a minimum grid spacing of $\Delta y^+ \approx 0.3$. For the spanwise direction, although it was shown that $\Delta z^+ \approx 15$ is adequate for the first-order statistics, the spectra and two-point correlations indicate a higher spanwise resolution is desirable.

No-Stress Boundary Condition

The no-stress boundary condition, which simulates the plane of symmetry in the vertical direction, must be located sufficiently far from the turbulent region which grows as the flow proceeds downstream. The minimum height at which the no-stress boundary condition can be applied for the domain length considered in

this study is $4h$. That is, the expansion ratio should be less than 1.33 regardless of the inlet boundary layer thickness.

Inflow Condition

The turbulent inflow condition was successfully applied using a modification of the method by Lee *et al.* (1992). However application of random phases for the Fourier coefficients of the velocity fluctuations leads to the loss of the imposed statistical correlations of the fluctuations within a few step heights from the inlet. Thus, a development section of approximately $7h$ must be included in the domain to allow the flow to regain its turbulence structures.

Outflow Condition

In both 2-D and 3-D simulations, the convective boundary condition successfully convects vortical structures through the exit plane with minimal distortions. The exit boundary condition does not appear to have adverse effects on the solution in regions more than one step height away from the exit. In the formulation of the convective boundary condition, a constant convection speed U_c is used in all simulations. An instantaneous convection velocity which varies in the exit y-z plane and in time was also tested. Tests show that instabilities develop if $U_c < 0$. For variable $U_c \geq 0$, there is no appreciable difference in statistical results compared to simulations with constant U_c.

6.2. Flow Characteristics

The results from the fine grid 3-D simulation at $Re_h = 5100$ show excellent agreements with concurrent experimental data by Jovic & Driver (1994). Good agreement was obtained in comparison of pressure coefficient, skin friction coefficient, mean velocity profiles, turbulence intensities and Reynolds shear stress profiles.

Skin Friction Coefficient

In the low Reynolds number range considered in this study, large negative skin friction is observed in the recirculation region. The peak negative C_f is approximately 2.5 times larger than the value measured in experiments with higher Reynolds numbers ($Re_h \approx 30000$). Higher skin friction is also seen in the recovery region. Additional experiments by Jovic & Driver (1995) with varying Reynolds numbers confirm that the high skin friction is due to the low Reynolds number effects.

Mean Velocity Profiles

In the recovery region, both DNS and experimental mean velocity profiles indicate a shift downward from the universal log-law. The intercept C of the logarithmic profile is about 2.54 compared to 5.0 of the universal log-law. The deviation from the log-law is observed even at the domain exit ($x/h = 20$) although previous experiments reported a recovery of the universal log-law as early as 6 step heights downstream from the reattachment. The difference is due to the method of calculating the wall shear velocity u_τ. Previous authors used the Clauser chart to calculate u_τ which assumes that the universal log-law is applicable. Experiments by Nagano *et al.* (1991) and Jovic & Driver (1994) show that u_τ in a boundary layer under adverse pressure gradient is higher than that predicted by the Clauser chart (17% higher in the current simulation). The Clauser shape factor G indicates that the velocity profile has not reached equilibrium at $x/h = 20$ which is in part due to low Reynolds number effects. Therefore, it can be concluded that the deviation from the universal log-law in the recovery region is due to the combined effects of the low Reynolds number and adverse pressure gradient.

Reattachment Length

The mean reattachment length X_r is 6.2 step heights from the separation. This agrees to within 3% of Jovic & Driver's (1994) measurements. The preliminary simulations confirm previous experimental findings that the reattachment length

increases with an increase in Reynolds number or expansion ratio. However, at the low Reynolds number range considered, the expansion ratio effect is dominant.

Oscillatory Behavior

In 2-D simulations, flows with steady inlet velocity profile at high Reynolds numbers exhibit limit cycle behavior. The time history of the streamwise velocity component shows an oscillation at a Strouhal number $St = fh/U_0 \approx 0.08$, where f is the frequency of oscillation. Imposing broad band fluctuations at the inlet also induces an oscillatory response of the same frequency. Varying the Reynolds number or inlet velocity profile has little effects on the oscillation frequency.

In the 3-D simulation, the spanwise averaged reattachment length shows quasi periodic behavior with Strouhal number $St \approx 0.06$.

Reynolds Stress Budgets

The budgets of all components of the Reynolds stress tensor were computed. The budgets were evaluated using 6070 samples over an averaging time period $\Delta t_{\text{ave}} \approx 193h/U_0$. Up to third-order statistics are documented in a database allowing evaluation of the budgets at all locations in the flow field.

In the recirculation region, the $\overline{u'u'}$ budgets show that the production term is balanced by dissipation and velocity pressure-gradient terms; all three terms peak in the shear layer. Near the wall, however, the production and velocity pressure-gradient terms change sign due to the reverse flow. The viscous diffusion and dissipation become dominant at the wall, reaching approximately 3 times larger than the peak production. The wall viscous diffusion and dissipation terms remain larger than the production peak near the exit.

In the $\overline{v'v'}$ budgets, all terms except viscous diffusion are significant. Unlike the standard turbulent boundary layer, the production is significant throughout the recirculation and reattachment regions. Also in contrast to the standard turbulent boundary layer near the wall, turbulence transport and viscous dissipation are dominant.

Similar to the streamwise and wall-normal components, the spanwise stress budgets also exhibit peaks in velocity pressure-gradient and viscous dissipation in the shear layer, but other terms are negligible. Below $y^+ \approx 5$, all terms except the turbulence convection become significant. Unlike the standard turbulent boundary layer, the viscous dissipation term decreases monotonically in the region $0 < y^+ < 20$. Both viscous terms attain their maxima at the wall which are about four times that in a zero pressure gradient boundary layer.

The shear stress production and velocity pressure-gradient terms are dominant at all streamwise locations. In the recirculation region, these two terms peak in the shear layer. The relative magnitude of the turbulence transport term remains high in the recovery region.

The turbulent kinetic energy budget in the recirculation region is similar to that of a turbulent mixing layer. In the shear layer, the peak energy production and dissipation are near the step $y/h \approx 1$. The peak dissipation is approximately 60% of the turbulent production. The turbulence diffusion is a consuming term in the range $0.3 < y/h < 1$ but becomes a 'producing' term outside of this range. The velocity pressure-gradient and viscous diffusion are negligible in the shear layer, but both are significant in the near-wall region ($y^+ \approx 4$). Near the domain exit ($x/h = 20$), the energy budget still shows a strong effect of the shear layer near $y/h = 1$, indicating that the flow has not fully recovered.

Appendix A
Non-Uniform Vertical Grid Spacing

In the domain $[0, L_y]$, the following coordinate transform maps a uniform grid in $\tilde{y}$ onto a non-uniform grid in y.

$$y = \xi \left[1 - \frac{\tanh \gamma (\xi - \tilde{y})}{\tanh \gamma \xi} \right], \qquad 0 \leq \tilde{y}, y \leq L_y, \tag{A.1}$$

where γ determines the slope and ξ the inflection point of the function. Equation (A.1) is applicable if a grid compression is only needed at $y = \tilde{y} = 0$ and/or $y = \tilde{y} = L_y$. In simulations of flows over a backward-facing step, fine grid spacing is also desired at the step ($y = h$). The following derivation develops a smooth transform function based on a set of parameters described below:

N	Number of grid points in $[0, L_y]$ including two end points,
$\Delta\tilde{y}$	Uniform grid spacing in $\tilde{y}$: $\Delta\tilde{y} = L_y/(N-1)$,
Δy_j	Grid spacing at j^{th} node (non-uniform) in y,
N_s	Number of grid points to be included in the step, $0 \leq y \leq h$,
η	Value of $\tilde{y}$ at node $j = N_s$: $\eta = (N_s - 1)\Delta\tilde{y}$. Thus, $y = h$ at $\tilde{y} = \eta$.

Two hyperbolic tangent functions f_1 and f_2 are combined to transform a uniform mesh in $\tilde{y}$ to a non-uniform mesh in y:

$$y_1 = f_1(\tilde{y}), \qquad 0 \leq \tilde{y} \leq \eta,$$
$$y_2 = f_2(\tilde{y}), \qquad \eta < \tilde{y} \leq L_y.$$

The following criteria are imposed on y_1 and y_2:

(i) $y_1 = 0$ at $\tilde{y} = 0$: lower boundary condition.

(ii) $y_1 = y_2 = h$ at $\tilde{y} = \eta$: continuity of function at $y = h$.

(iii) $y_2 = L_y$ at $\tilde{y} = L_y$: upper boundary condition.

(iv) $dy_1/d\tilde{y} = dy_2/d\tilde{y}$ at $\tilde{y} = \eta$: continuity of first derivative of function at $y = h$.

The two functions $f_1(\tilde{y})$ and $f_2(\tilde{y})$ take the following forms:

$$y_1 = K_1\xi_1\left[1 - \frac{\tanh\gamma_1(\xi_1 - \tilde{y})}{\tanh\gamma_1\xi_1}\right], \qquad 0 \le \tilde{y} \le \eta, \tag{A.2}$$

$$y_2 = h + K_2(\xi_2 - \eta)\left[1 - \frac{\tanh\gamma_2(\xi_2 - \tilde{y})}{\tanh\gamma_2(\xi_2 - \eta)}\right], \qquad \eta < \tilde{y} \le L_y. \tag{A.3}$$

Criterion (i) is naturally satisfied by the first function y_1, and Eq. (A.3) also satisfies criterion (ii) on y_2. The remaining criteria are accommodated by adjusting the parameters K_1, K_2, ξ_1, ξ_2, and γ_1.

γ_1 determines the slope of y_1 at $\tilde{y} = 0$, hence the degree of compression at the bottom wall.

ξ_1 is the location of the inflection point of the function $f_1(\tilde{y})$,

$$\frac{\eta}{2} \le \xi_1 \le \eta.$$

The grid spacing will be finest at $\tilde{y} = 0$ and $\tilde{y} = 2\xi_1$, and largest at $\tilde{y} = \xi_1$. If ξ_1 is selected to be $\frac{\eta}{2}$, the grid spacing is symmetric between $\tilde{y} = 0$ and $\tilde{y} = \eta$ (corresponding to $y_1 = 0$ and $y_1 = h$). However, the computational stability constraint is most restrictive near the step ($y = h$) where the vertical velocity component v is largest. Thus to ease this restriction, ξ_1 can be selected slightly larger than $\frac{\eta}{2}$ so that Δy_j is small near $y = h$ but not as fine as at $y = 0$. On the other hand, if ξ_1 is close to η, the grid spacing near the step will be large.

K_1 is a scaling factor. This factor is necessary to satisfy criterion (ii) on y_1 above. Applying (ii) to Eq. (A.2) gives

$$K_1 = \frac{\eta}{\xi_1\left[1 - \frac{\tanh\gamma_1(\xi_1 - \eta)}{\tanh\gamma_1\xi_1}\right]}. \tag{A.4}$$

ξ_2 is the inflection point of y_2 where Δy_j will be largest. If a no-slip wall is located at $y = L_y$, ξ_2 will be the midpoint between $\tilde{y} = \eta$ and $\tilde{y} = L_y$ (symmetric function),

$$\xi_2 = \frac{L_y + \eta}{2}.$$

If a no-stress wall is at $y = L_y$, then the inflection point is placed at $\tilde{y} = L_y$,

$$\xi_2 = L_y.$$

K_2 is a scaling factor imposed to satisfy criterion (iii) on y_2,

$$K_2 = \frac{L_y - h}{L_y - \eta}.$$

γ_2 determines the curvature of y_2 which is unknown and must be calculated based on criterion (iv). Taking derivatives of y_1 and y_2 gives:

$$\frac{dy_1}{d\tilde{y}} = \frac{K_1\gamma_1\xi_1}{\tanh\gamma_1\xi_1}\mathrm{sech}^2\gamma_1(\xi_1 - \tilde{y}), \qquad 0 \le \tilde{y} \le \eta, \tag{A.5}$$

$$\frac{dy_2}{d\tilde{y}} = \frac{K_2\gamma_2(\xi_2 - \eta)}{\tanh\gamma_2(\xi_2 - \eta)}\mathrm{sech}^2\gamma_2(\xi_2 - \tilde{y}), \qquad \eta \le \tilde{y} \le L_y. \tag{A.6}$$

At $\tilde{y} = \eta$, Eqs. (A.5) and (A.6) are equated to satisfied criterion (iv), yielding

$$K_2[2\gamma_2(\xi_2 - \eta)] = \lambda\sinh[2\gamma_2(\xi_2 - \eta)], \tag{A.7}$$

where

$$\lambda = \frac{K_1\gamma_1\xi_1}{\tanh\gamma_1\xi_1}\mathrm{sech}^2\gamma_1(\xi_1 - \eta). \tag{A.8}$$

Let $\theta = 2\gamma_2(\xi_2 - \eta)$, Eq. (A.7) becomes a function of θ:

$$g(\theta) = K_2\theta - \lambda\sinh\theta = 0. \tag{A.9}$$

The root of Eq. (A.9) is calculated by Newton-Raphson's method.

Listed below are several options for determining the type of grid compression in the y-direction.

(a) One double-sided tanh transform (symmetric), Eq. (A.1) with $\xi = L_y/2$: fine mesh at both $y = 0$ and L_y. Application: plain channel flows.

(b) One single-sided tanh transform, Eq. (A.1) with $\xi = L_y$: fine mesh at $y = 0$ only. Application: flat-plate turbulent flows.

(c) Two double-sided tanh transforms, Eqs. (A.2) and (A.3): fine mesh at $y = 0$, h, and L_y. Application: flows over a backward-facing step with a no-slip wall at $y = L_y$.

(d) One double-sided and one single-sided tanh transforms, Eqs. (A.2) and (A.3): fine mesh at $y = 0$ and h. Application: flows over a backward-facing step with a no-stress wall at $y = L_y$.

Figure A.1 shows an example of the transform function and the resulting grid spacing using option (d) above. Option (d) is applied in the 3-D backward facing step simulation presented in Chapter 5, with the following selected parameters:

$$L_y/h = 6.0, \quad N = 193, \quad N_s = 71, \quad \eta/h = 2.1875,$$
$$\xi_1/h = 1.10, \quad \gamma_1 = 2.20, \quad \xi_2/h = 6.0, \quad \gamma_2 = 0.7963.$$

This gives:

$$\Delta y_{\min} = 0.001165h \quad \text{at } y = 0,$$
$$\Delta y = 0.001177h \quad \text{at } y = h,$$
$$\Delta y_{\max} = 0.124970h \quad \text{at } y = L_y.$$

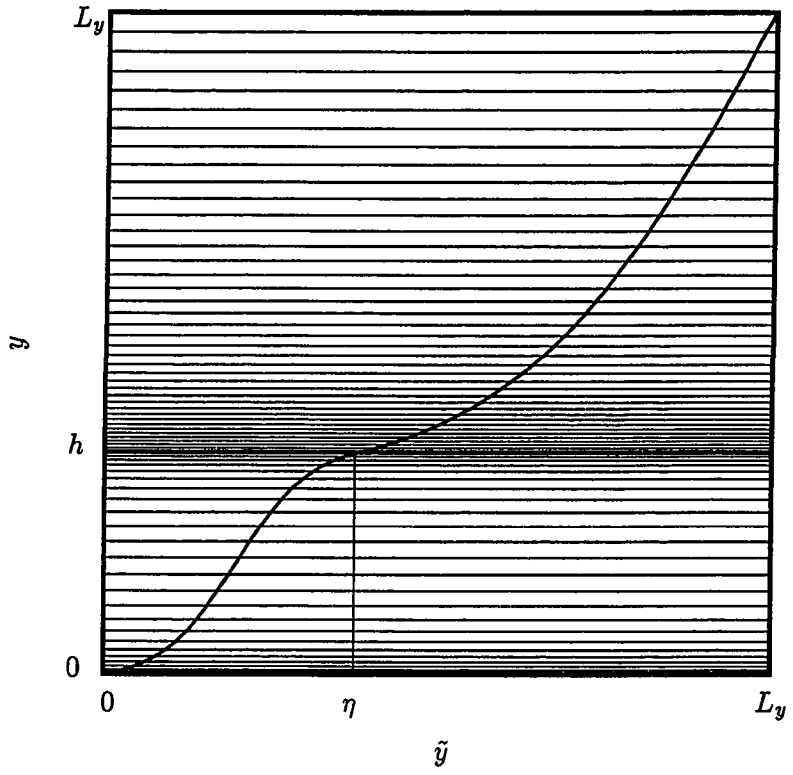

Figure A.1. Mesh refinement at $y = 0$ (bottom wall) and $y = h$ (step) using hyperbolic tangent transform function.

Appendix B
Numerical Discretization Of Equations

Presented in this Appendix is the discretization of all terms in the Navier-Stokes, and Poisson equations for computations on a staggered grid. Inversion of tridiagonal matrices are also presented.

B.1. Nodal Assignment

On a staggered grid, the cell centers, where the pressure points are defined, are customarily denoted by integer subscripts $[i, j, k]$, and the half-index shift ($i \pm \frac{1}{2}$, $j \pm \frac{1}{2}$, $k \pm \frac{1}{2}$) denotes the velocity points at the cell surfaces. For programming purposes, an $[i, j, k]$ tetrahedron is defined on each cell where the velocities and pressure are defined at the vertices: $p_{i,j,k}$ at the cell center, $u_{i,j,k}$, $v_{i,j,k}$ and $w_{i,j,k}$ at the right, top and front surfaces, respectively. This is shown in Fig. B.1.

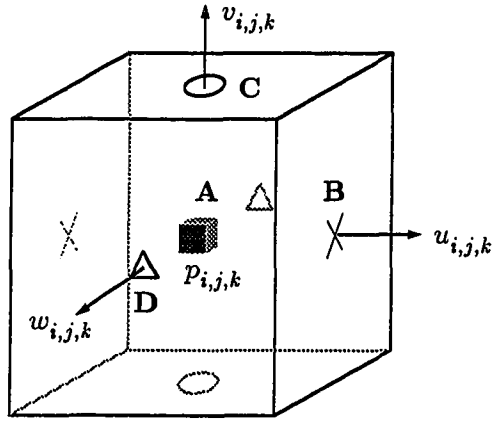

Figure B.1. Nodal assignment for a 3-D staggered grid. × u locations; o v locations; △ w locations; ▫ p location.

In each direction, the velocities and pressure do not have the same number of node points. Figure B.2 shows the nodal distribution of u, v, w and p in the x- and

y-directions. The nodal distribution is the same for all variables in the z-direction due to the periodic boundary condition. The nodal assignment in Fig. B.2 is based on N_x, N_y and N_z, the number of *cells* in the x-, y- and z-directions, respectively. The extents of the domain in these three directions are L_x, L_y, and L_z.

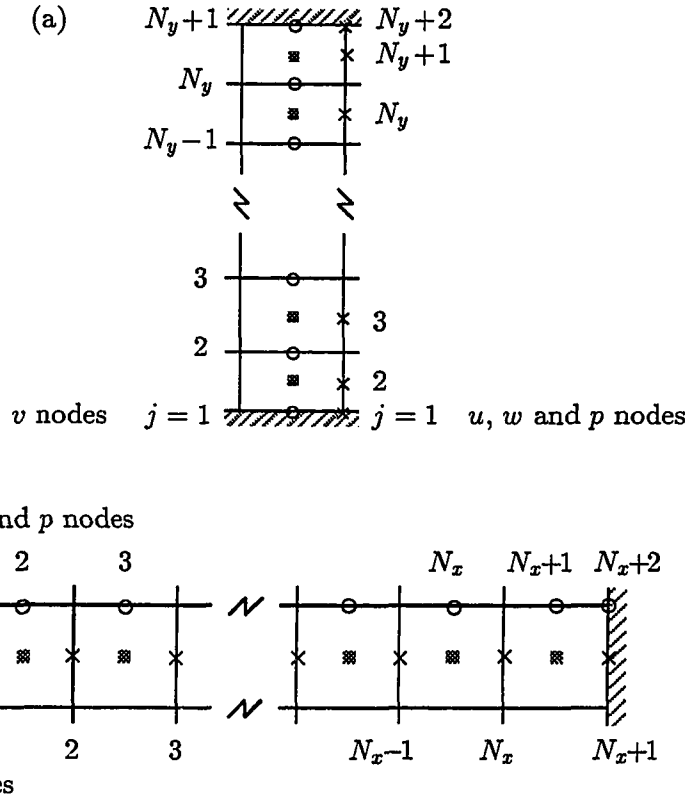

Figure B.2. Nodal distribution for velocities and pressure in the computational domain. (a) y-direction. (b) x-direction.

In all subsequent formulae, y_j denotes the vertical distance at the v node of the $[i,j,k]$ tetrahedron.

B.2. Momentum Equations

At substep l of the Runge-Kutta scheme, the intermediate velocities $\tilde{u}^{(l)}$, $\tilde{v}^{(l)}$ and $\tilde{w}^{(l)}$ are evaluated from equations below.

$$\left(1-\frac{\Delta t\beta_l}{Re}\frac{\delta^2}{\delta x^2}\right)\left(1-\frac{\Delta t\beta_l}{Re}\frac{\delta^2}{\delta y^2}\right)\left(1-\frac{\Delta t\beta_l}{Re}\frac{\delta^2}{\delta z^2}\right)\left(\tilde{\vartheta}^{(l)}-\tilde{\vartheta}^{(l-1)}\right)=$$
$$+\Delta t\left(\alpha_l+\beta_l\right)L\left(\tilde{\vartheta}^{(l-1)}\right)-\frac{\Delta t\beta_l}{Re}\frac{\delta}{\delta x}D^{(l-1)}$$
$$+\Delta t\left[-\gamma_l N\left(\vartheta^{*(l-1)}\right)-\zeta_l N\left(\vartheta^{*(l-2)}\right)\right], \qquad \text{(B.1)}$$

where:

ϑ	indicates any of the three velocity components: $\vartheta \equiv u$ in the streamwise direction; $\vartheta \equiv v$ in the vertical direction; $\vartheta \equiv w$ in the spanwise direction;
$\delta/\delta x$, $\delta/\delta y$, $\delta/\delta z$	are finite difference operators;
$L()$	is the linear viscous term;
$N()$	is the non-linear convective term;
$D^{(l)}$	is the divergence at substep l.

Using the nodal assignment shown in Fig. B.1, the x-, y- and z-momentum equations will be evaluated at points B, C and D, respectively. If velocity values are required at points where they are not defined, e.g., at the cell corners, the linear interpolation of two adjacent points will be taken.

B.2.1. Viscous Terms

$$L(\vartheta)=\frac{1}{Re}\left[\frac{\delta^2\vartheta}{\delta x^2}+\frac{\delta^2\vartheta}{\delta y^2}+\frac{\delta^2\vartheta}{\delta z^2}\right]$$
$$=\frac{1}{Re\Delta x^2}\left[\vartheta_{i-1,j,k}-2\vartheta_{i,j,k}+\vartheta_{i+1,j,k}\right]+$$
$$\frac{1}{Re}\left[\mathcal{A}_j^{(\vartheta)}\vartheta_{i,j-1,k}+\mathcal{B}_j^{(\vartheta)}\vartheta_{i,j,k}+\mathcal{C}_j^{(\vartheta)}\vartheta_{i,j+1,k}\right]+ \qquad \text{(B.2)}$$
$$\frac{1}{Re\Delta z^2}\left[\vartheta_{i,j,k-1}-2\vartheta_{i,j,k}+\vartheta_{i,j,k+1}\right].$$

Equation (B.2) is evaluated at point B for $\vartheta \equiv u$, C for $\vartheta \equiv v$ and D for $\vartheta \equiv w$. $\mathcal{A}_j^{(\vartheta)}$, $\mathcal{B}_j^{(\vartheta)}$, and $\mathcal{C}_j^{(\vartheta)}$ are the coefficients derived for the second-derivatives $\delta^2/\delta y^2$ using central difference over a non-uniform grid.

For $\vartheta \equiv u, w$:

$$\begin{aligned}
\mathcal{A}_j^{(\vartheta)} = \mathcal{A}_j^{(h)} &= \frac{8}{(y_j - y_{j-2})(y_{j+1} - y_{j-1} + y_j - y_{j-2})}; \\
\mathcal{B}_j^{(\vartheta)} = \mathcal{B}_j^{(h)} &= -\frac{8}{(y_j - y_{j-2})(y_{j+1} - y_{j-1})}; \\
\mathcal{C}_j^{(\vartheta)} = \mathcal{C}_j^{(h)} &= \frac{8}{(y_{j+1} - y_{j-1})(y_{j+1} - y_{j-1} + y_j - y_{j-2})}.
\end{aligned} \tag{B.3}$$

For $\vartheta \equiv v$:

$$\begin{aligned}
\mathcal{A}_j^{(\vartheta)} = \mathcal{A}_j^{(v)} &= \frac{2}{(y_j - y_{j-1})(y_{j+1} - y_{j-1})}; \\
\mathcal{B}_j^{(\vartheta)} = \mathcal{B}_j^{(v)} &= -\frac{2}{(y_j - y_{j-1})(y_{j+1} - y_j)}; \\
\mathcal{C}_j^{(\vartheta)} = \mathcal{C}_j^{(v)} &= \frac{2}{(y_{j+1} - y_j)(y_{j+1} - y_{j-1})}.
\end{aligned} \tag{B.4}$$

B.2.2. Convective Terms

$$N(u) = \left.\frac{\delta uu}{\delta x} + \frac{\delta uv}{\delta y} + \frac{\delta uw}{\delta z}\right|_{\mathrm{B}} = \tag{B.5}$$

$$\frac{1}{4\Delta x}\left[(u_{i+1,j,k} + u_{i,j,k})^2 - (u_{i,j,k} + u_{i-1,j,k})^2\right] +$$

$$\frac{1}{2(y_j - y_{j-1})}\left[\left(\frac{(y_j - y_{j-1})u_{i,j+1,k} + (y_{j+1} - y_j)u_{i,j,k}}{y_{j+1} - y_{j-1}}\right)(v_{i+1,j,k} + v_{i,j,k}) - \right.$$

$$\left.\left(\frac{(y_{j-1} - y_{j-2})u_{i,j,k} + (y_j - y_{j-1})u_{i,j-1,k}}{y_j - y_{j-2}}\right)(v_{i,j-1,k} + v_{i+1,j-1,k})\right] +$$

$$\frac{1}{4\Delta z}\left[(u_{i,j,k+1} + u_{i,j,k})(w_{i+1,j,k} + w_{i,j,k}) - (u_{i,j,k} + u_{i,j,k-1})(w_{i+1,j,k-1} + w_{i,j,k-1})\right].$$

$$N(v) = \left.\frac{\delta vu}{\delta x} + \frac{\delta vv}{\delta y} + \frac{\delta vw}{\delta z}\right|_{\mathrm{C}} = \tag{B.6}$$

$$\frac{1}{2\Delta x}\left[\left(\frac{(y_j - y_{j-1})u_{i,j+1,k} + (y_{j+1} - y_j)u_{i,j,k}}{y_{j+1} - y_{j-1}}\right)(v_{i+1,j,k} + v_{i,j,k}) - \right.$$

$$\left.\left(\frac{(y_j - y_{j-1})u_{i-1,j+1,k} + (y_{j+1} - y_j)u_{i-1,j,k}}{y_{j+1} - y_{j-1}}\right)(v_{i,j,k} + v_{i-1,j,k})\right] +$$

$$\frac{1}{2(y_{j+1} - y_{j-1})}\left[(v_{i,j+1,k} + v_{i,j,k})^2 - (v_{i,j,k} + v_{i,j-1,k})^2\right] +$$

$$\frac{1}{3\Delta x}\left[\left(\frac{(y_j - y_{j-1})w_{i,j+1,k} + (y_{j+1} - y_j)w_{i,j,k}}{y_{j+1} - y_{j-1}}\right)(v_{i,j,k+1} + v_{i,j,k}) - \right.$$

$$\left.\left(\frac{(y_j - y_{j-1})w_{i,j+1,k-1} + (y_{j+1} - y_j)w_{i,j,k-1}}{y_{j+1} - y_{j-1}}\right)(v_{i,j,k} + v_{i,j,k-1})\right].$$

$$N(w) = \left.\frac{\delta wu}{\delta x} + \frac{\delta wv}{\delta y} + \frac{\delta ww}{\delta z}\right|_{\mathrm{D}} = \tag{B.7}$$

$$\frac{1}{4\Delta x}\left[(w_{i+1,j,k} + w_{i,j,k})(u_{i,j,k+1} + u_{i,j,k}) - (w_{i,j,k} + w_{i-1,j,k})(u_{i-1,j,k+1} + u_{i-1,j,k})\right] +$$

$$\frac{1}{2(y_j - y_{j-1})}\left[\left(\frac{(y_j - y_{j-1})w_{i,j+1,k} + (y_{j+1} - y_j)w_{i,j,k}}{y_{j+1} - y_{j-1}}\right)(v_{i,j,k+1} + v_{i,j,k}) - \right.$$

$$\left.\left(\frac{(y_{j-1} - y_{j-2})w_{i,j,k} + (y_j - y_{j-1})w_{i,j-1,k}}{y_j - y_{j-2}}\right)(v_{i,j-1,k} + v_{i,j-1,k+1})\right] +$$

$$\frac{1}{4\Delta z}\left[(w_{i,j,k+1} + w_{i,j,k})^2 - (w_{i,j,k} + w_{i,j,k-1})^2\right].$$

B.2.3. Pressure Terms

$$\left.\frac{\delta p}{\delta x}\right|_{\mathrm{B}} = \frac{1}{\Delta x}\left(p_{i+1,j,k} - p_{i,j,k}\right). \tag{B.8}$$

$$\left.\frac{\delta p}{\delta y}\right|_{\mathrm{C}} = \frac{2}{y_{j+1} - y_{j-1}} \left(p_{i,j+1,k} - p_{i,j,k}\right). \tag{B.9}$$

$$\left.\frac{\delta p}{\delta z}\right|_{\mathrm{D}} = \frac{1}{\Delta z} \left(p_{i,j,k+1} - p_{i,j,k}\right). \tag{B.10}$$

B.3. Poisson Equation

$$\mathcal{L}(\phi) = \frac{1}{\Delta t} D^{(3)}, \tag{B.11}$$

where

$\mathcal{L}()$ is the discrete Laplace operator;

$D^{(3)}$ is the divergence at substep 3.

The Poisson equation is evaluated at the cell center (point A, Fig. B.1).

B.3.1. Divergence

$$\begin{aligned} D &= \left.\frac{\delta u}{\delta x} + \frac{\delta v}{\delta y} + \frac{\delta w}{\delta z}\right|_{\mathrm{A}} \\ &= \frac{1}{\Delta x}\left(u_{i,j,k} - u_{i-1,j,k}\right) + \frac{1}{y_j - y_{j-1}}\left(v_{i,j,k} - v_{i,j-1,k}\right) + \\ &\quad \frac{1}{\Delta z}\left(w_{i,j,k} - w_{i,j,k-1}\right); \\ &\quad i = 2, \ldots, N_x + 1; \quad j = 2, \ldots, N_y + 1; \quad k = 2, \ldots, N_z + 1. \end{aligned} \tag{B.12}$$

B.3.2. Laplace Operator

$$\mathcal{L}(\phi) = \left.\frac{\delta^2}{\delta x^2}\phi + \frac{\delta^2}{\delta y^2}\phi + \frac{\delta^2}{\delta z^2}\phi\right|_{\mathrm{A}}$$

$$
\begin{aligned}
=&\frac{1}{\Delta x^2}\left[\phi_{i-1,j,k}-2\phi_{i,j,k}+\phi_{i+1,j,k}\right]+\\
&\left[\mathcal{A}_j^{(\phi)}\phi_{i,j-1,k}+\mathcal{B}_j^{(\phi)}\phi_{i,j,k}+\mathcal{C}_j^{(\phi)}\phi_{i,j+1,k}\right]+\\
&\frac{1}{\Delta z^2}\left[\phi_{i,j,k-1}-2\phi_{i,j,k}+\phi_{i,j,k+1}\right];\\
&i=2,\ldots,N_x+1;\quad j=2,\ldots,N_y+1;\quad k=2,\ldots,N_z+1.
\end{aligned}
\tag{B.13}
$$

where $\mathcal{A}_j^{(\phi)}$, $\mathcal{B}_j^{(\phi)}$ and $\mathcal{C}_j^{(\phi)}$ are the discrete representation of $\partial^2/\partial y^2$ at node j:

$$
\begin{aligned}
\mathcal{A}_j^{(\phi)}=&\frac{2}{(y_j-y_{j-1})(y_j-y_{j-2})};\\
\mathcal{B}_j^{(\phi)}=&-\frac{2}{y_j-y_{j-1}}\left[\frac{1}{y_{j+1}-y_{j-1}}+\frac{1}{y_j-y_{j-2}}\right];\\
\mathcal{C}_j^{(\phi)}=&\frac{2}{(y_j-y_{j-1})(y_{j+1}-y_{j-1})}.
\end{aligned}
\tag{B.14}
$$

Appendix C
Capacitance Matrix

The formulation of the capacitance matrix is presented in this Appendix. For each wave number, the capacitance matrix is a full matrix; and is also singular for the zero wave number.

The basis for the capacitance matrix is Eq. (2.38) in §2.7.3.2 which is presented below.

$$\Delta\phi_\ell^{(\mathrm{II})} - \Delta\eta_\ell \frac{\tilde{\vartheta}_\ell^{(\mathrm{II})}}{\Delta t} = -\Delta\phi_\ell^{(\mathrm{I})}; \tag{C.1}$$

where

- $\Delta\phi_\ell^{(\mathrm{II})}$ is the difference in ϕ across the boundary Γ at location ℓ in the second pass of the Poisson solver (unknown);
- $\tilde{\vartheta}_\ell^{(\mathrm{II})}$ is the desired velocity to be applied in the second pass (unknown);
- $\Delta\phi_\ell^{(\mathrm{I})}$ is the error from the first pass.

A new variable, $\rho_\ell^{(\mathrm{II})}$, is now defined to absorb the constant Δt in to $\tilde{\vartheta}_\ell^{(\mathrm{II})}$: $\rho_\ell^{(\mathrm{II})} = \tilde{\vartheta}_\ell^{(\mathrm{II})}/\Delta t$. Thus,

$$\Delta\phi_\ell^{(\mathrm{II})} - \Delta\eta_\ell \rho_\ell^{(\mathrm{II})} = -\Delta\phi_\ell^{(\mathrm{I})}; \tag{C.2}$$

$\Delta\phi_\ell^{(\mathrm{II})}$ is the solution of the Poisson equation if $\rho_\ell^{(\mathrm{II})}$, $\ell = 1, \ldots, N_c$, *are placed along* Γ *and zero elsewhere in the domain.* $\rho_\ell^{(\mathrm{II})}$, $\ell = 1, \ldots, N_c$, are thus the *sources* and $\Delta\phi_\ell^{(\mathrm{II})}$ can be expressed in terms of $\rho_\ell^{(\mathrm{II})}$.

If the Poisson equation is solved with a right-hand-side value $\rho_{\ell'} = 1$, a unit source, placed at location ℓ' on Γ, and zero elsewhere, the resulting $\Delta\phi_\ell$ ($\ell = 1, \ldots, N_c$) on Γ will be (see Fig. C.1)

$$\begin{pmatrix} \Delta\phi_{1,\ell'} \\ \Delta\phi_{2,\ell'} \\ \vdots \\ \Delta\phi_{\ell,\ell'} \\ \vdots \\ \Delta\phi_{N_c,\ell'} \end{pmatrix}. \tag{C.3}$$

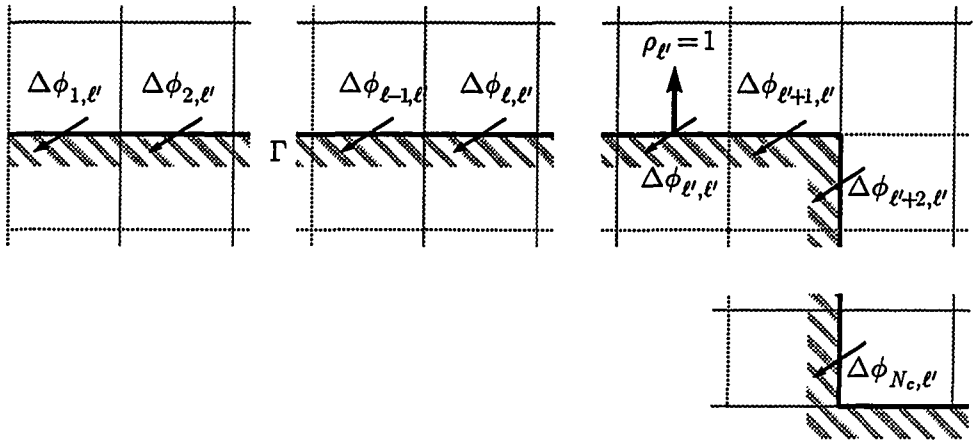

Figure C.1. Responses $\Delta\phi_\ell$ due to a unit source at location ℓ' on Γ.

Thus, $\Delta\phi_{\ell,\ell'}$ is a response vector at locations $\ell = 1,\ldots,N_c$ due to a unit source placed at location ℓ'. To extend this further, if a velocity of magnitude $\rho_{\ell'}^{(\mathrm{II})} \neq 1$ is placed at ℓ', the corresponding response vector will be:

$$\begin{pmatrix} \Delta\phi_1^{(\mathrm{II})} \\ \Delta\phi_2^{(\mathrm{II})} \\ \vdots \\ \Delta\phi_\ell^{(\mathrm{II})} \\ \vdots \\ \Delta\phi_{N_c}^{(\mathrm{II})} \end{pmatrix}_{\ell'} = \begin{pmatrix} \Delta\phi_{1,\ell'} \\ \Delta\phi_{2,\ell'} \\ \vdots \\ \Delta\phi_{\ell,\ell'} \\ \vdots \\ \Delta\phi_{N_c,\ell'} \end{pmatrix} \rho_{\ell'}^{(\mathrm{II})}. \tag{C.4}$$

Equation (C.4) is the responses due to only one $\rho^{(\mathrm{II})}$ placed at location ℓ', and zero everywhere else. If all $\rho_{\ell'}^{(\mathrm{II})}$ ($\ell' = 1,\ldots,N_c$), are present, the total responses will then be the superposition of all individual response vectors:

$$\begin{pmatrix} \Delta\phi_1^{(\mathrm{II})} \\ \Delta\phi_2^{(\mathrm{II})} \\ \vdots \\ \Delta\phi_\ell^{(\mathrm{II})} \\ \vdots \\ \Delta\phi_{N_c}^{(\mathrm{II})} \end{pmatrix} = \begin{pmatrix} \Delta\phi_{1,1} \\ \Delta\phi_{2,1} \\ \vdots \\ \Delta\phi_{\ell,1} \\ \vdots \\ \Delta\phi_{N_c,1} \end{pmatrix} \rho_1^{(\mathrm{II})} + \ldots + \begin{pmatrix} \Delta\phi_{1,\ell} \\ \Delta\phi_{2,\ell} \\ \vdots \\ \Delta\phi_{\ell,\ell} \\ \vdots \\ \Delta\phi_{N_c,\ell} \end{pmatrix} \rho_\ell^{(\mathrm{II})} + \ldots + \begin{pmatrix} \Delta\phi_{1,N_c} \\ \Delta\phi_{2,N_c} \\ \vdots \\ \Delta\phi_{\ell,N_c} \\ \vdots \\ \Delta\phi_{N_c,N_c} \end{pmatrix} \rho_{N_c}^{(\mathrm{II})}, \tag{C.5}$$

or

$$\underbrace{\begin{pmatrix} \Delta\phi_1^{(\mathrm{II})} \\ \Delta\phi_2^{(\mathrm{II})} \\ \vdots \\ \Delta\phi_\ell^{(\mathrm{II})} \\ \vdots \\ \Delta\phi_{N_c}^{(\mathrm{II})} \end{pmatrix}}_{\Delta\mathbf{\Phi}^{(\mathrm{II})}} = \underbrace{\begin{pmatrix} \Delta\phi_{1,1} & \Delta\phi_{1,2} & \cdots & \Delta\phi_{1,N_c} \\ \Delta\phi_{2,1} & \Delta\phi_{2,2} & \cdots & \Delta\phi_{2,N_c} \\ \vdots & & & \\ \Delta\phi_{\ell,1} & \Delta\phi_{\ell,2} & \cdots & \Delta\phi_{\ell,N_c} \\ \vdots & & & \\ \Delta\phi_{N_c,1} & \Delta\phi_{N_c,2} & \cdots & \Delta\phi_{N_c,N_c} \end{pmatrix}}_{\mathbf{G}} \underbrace{\begin{pmatrix} \rho_1^{(\mathrm{II})} \\ \rho_2^{(\mathrm{II})} \\ \vdots \\ \rho_\ell^{(\mathrm{II})} \\ \vdots \\ \rho_{N_c}^{(\mathrm{II})} \end{pmatrix}}_{\mathbf{r}^{(\mathrm{II})}}. \tag{C.6}$$

From Eq. (C.6), $\Delta\phi_\ell^{(\mathrm{II})}$, $\ell = 1, \ldots, N_c$, is

$$\Delta\phi_\ell^{(\mathrm{II})} = \sum_{\ell'=1}^{N_c} \Delta\phi_{\ell,\ell'}\rho_{\ell'}^{(\mathrm{II})}. \tag{C.7}$$

Substituting Eq. (C.7) into Eq. (C.2) gives

$$\sum_{\ell'=1}^{N_c} \Delta\phi_{\ell,\ell'}\rho_{\ell'}^{(\mathrm{II})} - \Delta\eta\rho_\ell^{(\mathrm{II})} = -\Delta\phi_\ell^{(\mathrm{I})}. \tag{C.8}$$

Equation (C.8) can be written in matrix form:

$$[\mathbf{G} + \mathbf{d}]\,\mathbf{r}^{(\mathrm{II})} = -\Delta\mathbf{\Phi}^{(\mathrm{I})}, \tag{C.9}$$

where $\mathbf{d}$ is an $N_c \times N_c$ diagonal matrix with elements $-\Delta\eta_\ell$, and $\mathbf{r}^{(\mathrm{II})}$ is the unknown vector $\rho^{(\mathrm{II})}$.

The $N_c \times N_c$ matrix $\mathbf{C}$=$\mathbf{G}$+$\mathbf{d}$ is called the *capacitance matrix.* Its elements are unchanged with time. It should be noted that $\mathbf{G}$ may not be a symmetric matrix if the grid spacing is non-uniform. Matrix $\mathbf{G}$ is computed by solving the Poisson equation N_c times; each time a unit value is assigned to $\rho_{\ell'}$ and zero at all other locations in the flow field, and a column $\Delta\phi_{\ell'}$ of $\mathbf{G}$ is calculated. Elements of $\mathbf{C}$ depend only on the geometry and mesh spacing of the domain.

REFERENCES

ABBOTT, D. E. and KLINE, S. J. (1961), "Theoretical and experimental investigation of flow over single and double backward facing steps," *Report No. MD-5*, Dept. of Mech. Eng., Stanford University.

ADAMS, E. W. and EATON, J. K. (1988), "An LDA study of the backward-facing step flow, including the effects of velocity bias," *J. of Fluids Eng.*, **110**, pp. 275–282.

ADAMS, E. W. and JOHNSTON, J. P. (1985), "Experimental studies of high Reynolds number backward-facing step flow," *Proc. of the Fifth International Symposium on Turbulent Shear Flows*, Cornell University, pp. 5.1–5.6.

ADAMS, E. W. and JOHNSTON, J. P. (1988), "Effects of the separating shear layer on the reattachment flow structure. Part 2: reattachment length and wall shear stress," *Experiments in Fluids*, **6**, pp. 493–499.

ADAMS, E. W., JOHNSTON, J. P. and EATON, J. K. (1984), "Experiments on the structure of turbulent reattaching flow," *Report No. MD-43*, Thermosciences Division, Dept. of Mech. Eng., Stanford University.

ANDERSEN, P. S., KAYS, W. M. and MOFFAT, R. J. (1972), "The turbulent boundary layer on a porous plate: An experimental study of the fluid mechanics for adverse free-stream pressure gradients," *Report No. HMT-15*, Thermosciences Division, Dept. of Mech. Eng., Stanford University.

ARMALY, B. F., DURST, F., PEREIRA, J. C. F. and SCHÖNUNG, B. (1983), "Experimental and theoretical investigation of backward-facing step," *J. of Fluid Mech.*, **127**, pp. 473–496.

ARNAL, M. and FRIEDRICH, R. (1991), "On the effects of spatial resolution and subgrid-scale modeling in the large eddy simulation of a recirculating flow," *Proc. of the 9th GAMM-Conference on Num. Methods in Fluid Mech.*, Lausanne.

BRADSHAW, P. (1967), "Irrotational fluctuations near a turbulent boundary layer," *J. Fluid Mech.*, **27**, part 2, pp. 209–230.

BRADSHAW, P. and FERRISS, D. H. (1965), "The spectral energy balance in a turbulent mixing layer," *AERO Report 1144*, National Physical Laboratory, England.

BRADSHAW, P. and WONG, F. Y. F. (1972), "The reattachment and relaxation of a turbulent shear layer," *J. of Fluid Mech.*, **52**, part 1, pp. 113–135.

BUZBEE, B. L., GOLUB, G. H. and NIELSON, C. W. (1970), "On direct methods for solving Poisson's equations," *SIAM J. Num. Anal.*, **7**, pp. 627–656.

BUZBEE, B. L., DOOR, F. W., GEORGE, J. A. and GOLUB, G. H. (1971), "The direct solution of the discrete Poisson equation on irregular regions," *SIAM J. Num. Anal.*, **8**, pp. 722–736.

CHANDRSUDA, C. and BRADSHAW, P. (1981), "Turbulence structure of a reattaching mixing layer," *J. of Fluid Mech.*, **110**, pp. 171–194.

DOOR, F. W. (1970), "The direct solution of the discrete Poisson equation on a rectangle," *SIAM Review*, **12**, pp. 248–263.

DOOR, F. W. (1973), "Direct methods for the solution of Poisson's equation on a staggered grid," *J. Comp. Phys.*, **12**, pp. 422–428.

DRIVER, D. M. (1991), "Reynolds shear stress measurements in a separated boundary layer flow," *AIAA Paper 91-1787.*

DRIVER, D. M. and SEEGMILLER, H. L. (1982), "Features of a reattaching turbulent shear layer subject to an adverse pressure gradient," *AIAA Paper 82-1029.*

DRIVER, D. M. and SEEGMILLER, H. L. (1985), "Features of a reattaching turbulent shear layer in divergent channel flow," *AIAA J.*, **23**, pp. 163–171.

DRYJA, M. (1978), "Capacitance matrix method for the difference parabolic problem," *Warsaw Computation Centre Reports No. 73*, Sprawozdania Instytutu Informatyki Uniwersytetu Warszawskiego.

DURST, F. and PEREIRA, J. C. F. (1988), "Time-dependent laminar backward-facing step flow in a two-dimensional duct," *J. of Fluids Eng.*, **110**, pp. 289–296.

DURST, F. and SCHMITT, F. (1985), "Experimental studies of high Reynolds number backward-facing step flow," *Proc. of the Fifth International Symposium on Turbulent Shear Flows*, Cornell University, pp. 5.19–5.24.

DURST, F. and TROPEA, C. (1981), "Turbulent, backward-facing step flows in two-dimensional ducts and channels," *Proc. of the Third International Symposium on Turbulent Shear Flows*, University of California, Davis, pp. 18.1–18.5.

EATON, J. K. and JOHNSTON, J. P. (1980), "Turbulent flow reattachment: An experimental study of the flow and structure behind a backward-facing step," *Report No. MD-39*, Thermosciences Division, Dept. of Mech. Eng., Stanford University.

EATON, J. K. and JOHNSTON, J. P. (1981), "A review of research on subsonic turbulent flow reattachment," *AIAA J.*, **19**, pp. 1093–1100.

FARABEE, T. M. and CASARELLA, M. J. (1988), "Wall pressure fluctuations beneath a disturbed turbulent boundary layer," *International Symposium on Flow Induced Vibration and Noise: Acoustic Phenomena and Interaction in Shear Flows over Compliant and Vibrating Surfaces*, New York, pp. 121–135.

FRIEDRICH, R. and ARNAL, M. (1990), "Analysing turbulent backward-facing step flow with the lowpass-filtered Navier-Stokes equations," *J. of Wind Engineering and Industrial Aerodynamics*, **35**, pp. 101–128.

GOLDSTEIN, R. J., ERIKSEN, V. L., OLSON, R. M. and ECKERT, E. R. G. (1970), "Laminar separation, reattachment, and transition of the flow over a downstream-facing step," *J. of Basic Eng.*, **92**, pp. 732–741.

GRESHO, P. M., GARTLING, D. K., CLIFFE, K. A., GARRATT, T. J., SPENCE, A., WINTERS, K. H., GOODRICH, J. W. and TORCZYNSKI, J. R. (1993),

"Is the steady viscous incompressible two-dimensional flow over a backward-facing step at $Re = 800$ stable?" *Int. J. for Num. Methods in Fluids*, **17**, No. 6, pp. 501-541.

HAN, T. Y., MENG, J. C. S. and INNIS, G. E. (1983), "An open boundary condition for incompressible stratified flows," *J. of Comp. Phys.*, **49**, pp. 276–297.

HARLOW, F. H. and WELCH, J. E. (1965), "Numerical calculation of time-dependent viscous incompressible flow of fluid with free surface," *Phys. of Fluids*, **8**, pp. 2182–2189.

HOCKNEY, R. W. (1965), "A fast direct solution of Poisson's equation using Fourier analysis," *J. Assoc. Computing Machinery*, **12**, pp. 95–113.

HOCKNEY, R. W. (1970), "The potential calculation and some applications," *Method in Comp. Phys.*, **9**, pp. 135–211.

ISOMOTO, K. and HONAMI, S. (1989), "The effect of inlet turbulence intensity on the reattachment process over a backward-facing step," *J. of Fluids Eng.*, **111**, pp. 87–92.

JOVIC, S. and DRIVER, D. M. (1994), "Backward-facing step measurement at low Reynolds number, $Re_h = 5000$," *NASA Technical Memorandum*, No. 108807.

JOVIC, S. and DRIVER, D. M. (1995), "Reynolds number effects on the skin friction in separated flows behind a backward facing step," accepted for publication in *Experiments in Fluids.*

KAIKTSIS, L., KARNIADAKIS, G. E. and ORSZAG, S. A. (1991), "Onset of three-dimensionality, equilibria, and early transition in flow over a backward-facing step," *J. of Fluid Mech.*, **231**, pp. 501–528.

KAYS, W. M. and CRAWFORD, M. E. (1980), *Convective heat and mass transfer*, 2nd Ed., McGraw-Hill, pp. 166–173.

KASAGI, N., MATSUNAGA, A. and KAWARA, S. (1992), "Turbulence measurement in a separated and reattaching flow over a backward-facing step with the

aid of three-dimensional particle tracking velocimetry," *J. of Wind Eng.*, **52**, pp. 523–528.

KIM, J., KLINE, S. J. and JOHNSTON, J. P. (1978), "Investigation of separation and reattachment of a turbulent shear layer: Flow over a backward-facing step," *Report No. MD-37*, Thermosciences Division, Dept. of Mech. Eng., Stanford University.

KIM, J., KLINE, S. J. and JOHNSTON, J. P. (1980), "Investigation of a reattaching turbulent shear layer: Flow over a backward-facing step," *J. of Fluids Eng.*, **102**, pp. 302–308.

KIM, J. and MOIN, P. (1985), "Application of a fractional-step method to incompressible Navier-Stokes equations," *J. of Comp. Phys.*, **59**, pp. 308–323.

KIM, J., MOIN, P. and MOSER, R. (1987), "Turbulence statistics in fully developed channel flow at low Reynolds number," *J. of Fluid Mech.*, **177**, pp. 133–166.

KLINE, S. J., REYNOLDS, W. C., SCHRAUB, F. A. and RUNSTADLER, P. W. (1967), "The structure of turbulent boundary layers," *J. of Fluid Mech.*, **30**, pp. 741–773.

KUEHN, D. M. (1980), "Some effects of adverse pressure gradient on the incompressible reattaching flow over a rearward-facing step," *AIAA J.*, **18**, pp. 343–344.

LE, H. and MOIN, P. (1991), "An improvement of fractional step methods for the incompressible Navier-Stokes equations," *J. of Comp. Phys.*, **92**, pp. 369–379.

LE, H., MOIN, P. and KIM, J. (1993), "Direct simulations of turbulent flow over a backward-facing step," *Proc. of the Nineth Symposium on Turbulent Shear Flows*, Kyoto University, pp. 13-2-1–13-2-5.

LEE, S., LELE, S. K. and MOIN, P. (1992), "Simulation of spatially evolving turbulence and the applicability of Taylor's hypothesis in compressible flow," *Phys. Fluids A*, 4, pp. 1521–1530.

LOWERY, P. S. and REYNOLDS, W. C. (1986), "Numerical simulation of a spatially-developing, forced, plane mixing layer," *Report No. TF-26*, Thermosciences Division, Dept. of Mech. Eng., Stanford University.

MANSOUR, N. N., KIM, J. and MOIN, P. (1988), "Reynolds-stress and dissipation-rate budgets in a turbulent channel flow," *J. of Fluid Mech.*, **194**, pp. 15–44.

MOFFATT, M. K. (1964), "Viscous and resistive eddies near a sharp corner," *J. Fluid Mech.*, **18**, pp. 1–18.

NAGANO, Y., TAGAWA, M. and TSUJI, T. (1991), "Effects of adverse pressure gradients on mean flows and turbulence statistics in a boundary layer," *Proc. of the Eighth Symposium on Turbulent Shear Flows*, Technical University of Munich, pp. 2-3-1–2-3-6.

ÖTÜGEN, M. V. (1991), "Expansion ratio effects on the separated shear layer and reattachment downstream of a backward-facing step," *Experiments in Fluids*, **10**, pp. 273–280.

PAULEY, L. L., MOIN, P. and REYNOLDS, W. C. (1988), "A numerical study of unsteady laminar boundary layer separation," *Report No. TF-34*, Thermosciences Division, Dept. of Mech. Eng., Stanford University.

PRESS, W. H., TEUKOLSKY, S. A., VETTERLING, W. T. and FLANNERY, B. P. (1992), *Numerical recipes in FORTRAN - The art of scientific computing*, 2nd Ed., Cambridge Univ. Press, pp. 644–649.

PROSKUROWSKI, W. and WIDLUND, O. (1976), "On the numerical solution of Helmholtz's equation by the capacitance matrix method," *Math. Comp.*, **30**, pp. 433–468.

RA, S. H. and CHANG, P. K. (1990), "Effects of pressure gradient on reattaching flow downstream of a rearward-facing step," *J. of Aircraft*, **27**, pp. 93–95.

ROGERS, M. and MOSER, R. (1993), "Direct simulations of a self similar turbulent mixing layer," *Phys. of Fluids A*, **6**, No. 2, Part 2, pp. 903–923.

ROSHKO, A. and LAU, J. C. (1965), "Some observations on transition and reattachment of a free shear layer in incompressible flow," *Proc. of the 1965 Heat Transfer and Fluid Mech. Inst.*, Stanford University Press, pp. 157–167.

SCHUMANN, U. and BENNER, J. (1982), "Direct solution of the discretized Poisson-Neumann problem on a domain composed of rectangles," *J. of Comp. Phys.*, **46**, pp. 1–14.

SCHUMANN, U. and SWEET, R. A. (1988), "Fast Fourier transforms for direct solution of Poisson's equation with staggered boundary conditions," *J. of Comp. Phys.*, **75**, pp. 123–137.

SIMPSON, R. L. (1983), "A model for the backflow mean velocity profile," *AIAA J.*, **21**, pp. 142–143.

SIMPSON, R. L., AGARWAL, N. K., NAGABUSHANA, K. A. and OLCMEN, S. (1990), "Spectral measurements and other features of separating turbulent flows," *AIAA J.*, **28**, pp. 446–452.

SINHA, S. N., GUPTA, A. K. and OBERAI, M. M. (1981), "Laminar separating flow over backsteps and cavities part I: backsteps," *AIAA J.*, **19**, pp. 1527–1530.

SPALART, P. R. (1987), "Hybrid RKW3 + Crank-Nicolson scheme," private communication, NASA-Ames Research Center, Moffett Field, CA.

SPALART, P. R. (1988), "Direct simulation of a turbulent boundary layer up to $R_\theta = 1410$," *J. Fluid Mech.*, **187**, pp. 61–98.

SPALART, P. R., MOSER, R. D., and ROGERS, M. M. (1991), "Spectral methods for the Navier-Stokes equations with one infinite and two periodic directions," *J. Comp. Phys.*, **96**, pp. 297–324.

VOGEL, J. C. and EATON, J. K. (1985), "Combined heat transfer and fluid dynamic measurements downstream of a backward-facing step," *J. of Heat Transfer*, **107**, pp. 922–929.

WESTPHAL, R. V., EATON, J. K. and JOHNSTON, J. P. (1981), "A new probe for measurement of velocity and wall shear stress in unsteady, reversing flow," *J. of Fluids Eng.*, **103**, pp. 478–482.

WESTPHAL, R. V., JOHNSTON, J. P. and EATON, J. K. (1984), "Experimental study of flow reattachment in a single-sided sudden expansion," *Report No. MD-41*, Thermosciences Division, Dept. of Mech. Eng., Stanford University.